



TECHNISCHE  
UNIVERSITÄT  
DARMSTADT

**Coupled Thermal-Hydraulic-Mechanical (THM)  
modelling of underground gas storage – A case study  
from the Molasse Basin, South Germany**

**Vom Fachbereich Material- und Geowissenschaften  
der Technische Universität Darmstadt**

zur Erlangung des akademischen Grades

Doktor Ingenieur

(Dr. Ing)

Dissertation

**Von**

**M.Sc. M.Sc. Muhammad Zain-Ul-Abedin**

geboren am 21. November 1989 in Lahore, Pakistan

Erstgutachter: Prof. Dr. Andreas Henk

Zweitgutachterin: Prof. Dr. Eva Schill

Darmstadt 2022

---

Zain-Ul-Abedin, Muhammad: Coupled Thermal Hydraulic-Mechanical (THM) modelling of underground gas storage – A case study from the Molasse Basin, South Germany.

Darmstadt Technische Universität Darmstadt,

Jahr der Veröffentlichung der Dissertation auf TUprints: 2022

URN: urn:nbn:de:tuda-tuprints-225379

Tag der mündlichen Prüfung: 04.07.2022

Veröffentlicht unter CC BY-SA 4.0 International

<https://creativecommons.org/licenses/>

## Abstract

Thermal-hydraulic-mechanical (THM) models of gas storage in porous media provide valuable information for various applications. The range of these applications varies from prediction of ground surface displacements, determination of stress path changes, and maximum reservoir pressure to storage capacity for maintaining fault stability and overburden integrity. The study, conducted in collaboration with research institutes and storage companies in Germany, addresses the numerical modelling of geomechanical effects caused by the storage of methane in a depleted gas field. The geomechanical assessment focuses on a former gas reservoir in the Bavarian Molasse Basin east of Munich, for which a hypothetical conversion into underground gas storage (UGS) is considered.

The target reservoir is of Late Oligocene age, i.e., the Chattian Hauptsand with three gas bearing layers having a total thickness of 85 m. The reservoir formation is highly porous with an average porosity of 23% and permeability is in the range between 20 mD and 80 mD. The reservoir has produced natural gas from 1958 till 1978 and has been in a shut-in phase ever since. The storage operations require precise understanding of reservoir mechanics and stresses; therefore, the selected methodology helps to analyze these issues in detail.

The geomechanical analysis is performed with the help of a state-of-the-art THM model with the following objectives: (1) analyze the variation of principal stress field induced by the field activities (2) analyze the effective stress changes with changing pore pressure in short-term as well as long-term using hypothetical injection-production schedule cases (3) prediction of ground surface displacements over the field, (4) analyze the possible reactivation of faults and fractures as well as the safe storage capacity of the reservoir; and (5) thermal stress changes with injection of colder foreign gas in underground reservoir.

The methodology comprises 1D mechanical earth modelling (MEM) to calculate elastic properties as well as a first estimate for the vertical and horizontal stresses at well locations by using log data. This modelling phase provide complete analyses of log, core and laboratory data which leads to detailed 1D MEM of all the wells available for case study reservoir.

This information is then used to populate a 3D finite element MEM) which has been built from seismic data and comprises not only the reservoir but the entire overburden up to the earth's surface as well as part of the underburden. The size of this model is  $30 \times 24 \times 5 \text{ km}^3$  and 3D property modelling has been done by applying geostatistical approach for property inter-/extrapolation.

The behavior of pore pressure in the field has been derived from dynamic fluid flow simulation through history matching for the production and subsequent shut-down phases of the field. Subsequently, changes in the pore pressure field during injection-production and subsequent shut-down phases are analyzed for weekly and seasonal loading and unloading scenario cases. The resulting pore pressure changes are coupled with 3D geomechanical model in order to have complete understanding of stress changes during these operations.

In two scenario cases, the surplus electricity in Germany from renewable energy sources such as solar and wind from the year 2017 is considered. It results that the German surplus electricity can be stored in underground gas storage facilities with a Power-to-Gas (PtG) concept and that the stored gas can be reused again.

Additionally, fault reactivation and thermal stress analyses are also performed on THM model in order to evaluate maximum threshold (injection) pressure as well as safe storage capacity of the reservoir. The fault reactivation already occurs at 1.25 times the initial reservoir pressure which provides a safe storage rate of 100,000-150,000 m<sup>3</sup>/day in the case study reservoir. The validated THM model is ready to be used for analyzing new wells for future field development and testing further arbitrary injection-production schedules, among others. The methodology can be applied on to any UGS facility not only in German Molasse Basin but anywhere in the world.

## Zusammenfassung

Thermohydromechanische (THM) Modelle der Gasspeicherung in porösen Medien liefern wertvolle Informationen für verschiedene Anwendungen, die von der Vorhersage von Verschiebungen an der Bodenoberfläche über die Bestimmung des maximalen Lagerstättendrucks bis hin zur Speicherkapazität zur Aufrechterhaltung der Störungsstabilität und der Integrität des Deckgebirges reichen. Die in Zusammenarbeit mit Forschungsinstituten und Untertage-Gasspeicherunternehmen in Deutschland durchgeführte Studie befasst sich mit der numerischen Modellierung von geomechanischen Effekten, die durch die Speicherung von Erdgas (potenziell Wasserstoff) in einem unterirdischen, erschöpften Gasfeld verursacht werden. Die geomechanische Bewertung konzentriert sich auf ein ehemaliges Gasfeld im Bayerischen Molassebecken östlich von München, für das eine hypothetische Umwandlung in einen unterirdischen Gasspeicher (UGS) betrachtet wird.

Das Zielreservoir ist der Chatt Hauptsand aus dem oberen Oligozän mit drei gasführenden Schichten mit einer Gesamtdicke von 85 m. Die Reservoirformation ist hochporös mit einer durchschnittlichen Porosität von 23 % und einer Permeabilität im Bereich zwischen 20 mD und 80 mD. Die Lagerstätte hat von 1958 bis 1978 Erdgas produziert und befindet sich seither in einer Shut-in-Phase. Der Speicherbetrieb erfordert ein genaues Verständnis der Reservoirmechanik und der Spannungen; daher hilft die gewählte Methodik, diese Fragen im Detail zu analysieren.

Die geomechanische Analyse wird mit Hilfe eines modernen THM-Modells mit den folgenden Zielen durchgeführt: (1) Analyse der Variation des Hauptspannungsfeldes, die durch die Feldaktivitäten induziert wird, (2) Analyse der effektiven Spannungsänderungen mit sich änderndem Porendruck in kurz- und langfristigen, auch unregelmäßigen Injektions-/Produktionsplan-Fällen, (3) Vorhersage der Verschiebung der Erdoberfläche über dem Feld, (4) Analyse der möglichen Aktivierung von Verwerfungen und Brüchen und der sicheren Speicherkapazität des Reservoirs, und (5) thermische Spannungsänderungen mit der Injektion von kälterem Fremdgas in das unterirdische Reservoir.

Die Methodik umfasst eine 1D mechanische Erdmodellierung (1D MEM) zur Berechnung der elastischen Eigenschaften sowie eine erste Abschätzung der vertikalen und horizontalen Spannungen an den Bohrlochstandorten anhand von Logdaten. Diese Modellierungsphase bietet vollständige Analysen von Log-, Kern- und Labordaten, die zu detaillierten 1D-MEM aller für das Fallstudienreservoir verfügbaren Bohrungen führen.

Diese Informationen werden dann verwendet, um ein 3D-Finite-Elemente-Modell (3D MEM) aufzubauen, das aus seismischen Daten erstellt wurde und nicht nur das Reservoir, sondern das gesamte Deckgebirge bis zur Erdoberfläche sowie einen Teil des Unterlagers umfasst. Die Größe dieses Modells beträgt  $30 \times 24 \times 5 \text{ km}^3$  und die 3D- Parametrisierung wurde durch Anwendung eines geostatistischen Ansatzes für die Inter-/Extrapolation von Eigenschaften durchgeführt.

Das Verhalten des Porendrucks in dem Feld wurde aus der dynamischen Strömungssimulation durch History Matching für die Produktions- und anschließenden Shut-down-Phase des Feldes abgeleitet. Anschließend werden die Veränderungen im Porendruckfeld während der Injektions- und Produktionsphase und der anschließenden Shut-down-Phase für wöchentliche und saisonale Testsszenarien analysiert. Die daraus resultierenden Porendruckänderungen werden mit einem geomechanischen 3D-Modell gekoppelt, um ein vollständiges Verständnis der Spannungsänderungen während dieser Vorgänge zu erhalten.

In zwei Szenarien wird der Stromüberschuss in Deutschland aus erneuerbaren Energiequellen wie Sonne und Wind aus dem Jahr 2017 berücksichtigt. Es zeigt sich, dass der Deutsche Überschussstrom in unterirdischen Gasspeichern mit einem Power-to-Gas (PtG)-Konzept gespeichert werden kann und dass das gespeicherte Gas wiederverwendet werden kann.

Zusätzlich werden am THM-Modell auch Störungsreaktivierungs- und thermische Spannungsanalysen durchgeführt, um den maximalen Schwellenwert (Injektionsdruck) sowie die sichere Speicherkapazität des Reservoirs zu bewerten. Die Störungsreaktivierung erfolgt bereits beim 1,25 fachen des anfänglichen Reservoirdrucks, was eine sichere Speicherrate von 100.000-150.000 m<sup>3</sup>/Tag im Fallstudienreservoir ermöglicht. Das validierte THM-Modell kann u. a. für die Analyse neuer Bohrungen für die zukünftige Feldentwicklung und das Testen weiterer beliebiger Injektions-Produktionspläne verwendet werden. Die Methodik kann auf jede UGS-Anlage nicht nur im Molassebecken, sondern überall auf der Welt angewendet werden.

## Acknowledgements

“I dedicate this thesis to my beloved late mother Najma Khanum and my beloved late father Muhammad Saeed”.

The work of this study was carried out within the SUBI project, which was funded by the German Federal Ministry of Education and Research (BMBF). There are various research institutes, universities and German companies are involved in this project. The support from the entire SUBI team was essential and is greatly appreciated. I would like to thank especially the consortium partner Uniper SE for providing the essential data to accomplish this study. I would like to thank Dr. Tobias Rudolph, Mr. Béla Tihamér Szócs and Mr. Joseph Hölwart for their support and discussions regarding methodology of this work.

I would like to thank Prof. Dr. Andreas Henk for showing trust in me to participate in the project and continue my PhD under his supervision. I am very grateful for his invaluable expertise in formulating the research questions and methodology. He always encouraged me to work independently and encouraged me to share my ideas in meetings, conferences and workshops. His kindness and encouragement will remain forever with me.

My special thanks go to the Schlumberger Geomechanics Centre of Excellence in the UK for technical support. In particular, Dr. Karsten Fischer and Ivan Diaz Granados are thanked to teach me about geomechanics software.

I really appreciate the company of the entire staff of the Institute of Applied Geosciences at TU Darmstadt. To my group: Karsten, Tobias, Torben, Stephan, Reimund, Dominique, Constantin. Special thanks to Steffi, who always helped me in administrative work.

I would also like to thank my friends: Tanveer, Muqtadir, Waqas, Shehzad, Bilal, Ahsan, Ali and Sarwar. My special thanks go to my friends, Sammar, Jawad, Nadeem and Khizar for their moral support especially in the later stages of my thesis.

Finally, my deep and sincere gratitude to my family for their continuous and unparalleled love, help and support. I am grateful to my wife Dr. Amara Saud for always being there for me as a friend. Thank you for being there for me in all circumstances and for being a great inspiration to me.

# Contents

<b>ABSTRACT</b>	<b>II</b>
<b>ZUSAMMENFASSUNG</b>	<b>IV</b>
<b>ACKNOWLEDGEMENTS</b>	<b>VI</b>
<b>CONTENTS</b>	<b>VII</b>
<b>LIST OF FIGURES</b>	<b>X</b>
<b>LIST OF TABLES</b>	<b>XVI</b>
<b>LIST OF ABBREVIATIONS AND SYMBOLS</b>	<b>XVII</b>
<b>CHAPTER 1 INTRODUCTION</b>	<b>1</b>
1.1 MOTIVATION AND OBJECTIVES	1
1.2 SUBI PROJECT	2
1.3 THESIS OVERVIEW	3
1.4 POROUS UGS AND IMPORTANCE OF THM MODELLING	5
<b>CHAPTER 2 POWER-TO-GAS</b>	<b>8</b>
2.1 PERCEIVED ROLE OF POWER-TO-GAS AND GAS-TO-POWER	8
2.2 ELECTROLYSIS AND METHANATION	10
2.3 POWER-TO-GAS IN GERMANY	11
2.4 ECONOMIC CONDITIONS OF POWER-TO-GAS IN GERMANY	13
2.5 SYNERGY BETWEEN POWER-TO-GAS AND GAS-TO-POWER	13
<b>CHAPTER 3 METHODOLOGY</b>	<b>15</b>
3.1 1D MECHANICAL EARTH MODELLING (1D MEM)	16
3.1.1 VERTICAL (OVERBURDEN) STRESS	16
3.1.2 PORE PRESSURE	17
3.1.3 ELASTIC PROPERTIES	19
3.1.4 STRENGTH PARAMETERS	21
3.1.5 HORIZONTAL STRESSES	22
3.2 3D MECHANICAL EARTH MODELLING (3D MEM)	24
3.3 HYDRAULIC MODEL	25
3.4 THERMAL MODEL	26
3.5 COUPLED THERMAL-HYDRAULIC-MECHANICAL (THM) MODELLING	26
3.5.1 SIMULATION CONCEPT AND GOVERNING EQUATIONS	29
3.6 ECLIPSE™-VISAGE™ THM MODELLING	30
<b>CHAPTER 4 CASE STUDY</b>	<b>32</b>
4.1 GEOLOGICAL SETTING	32
4.1.1 HYDROCARBON SYSTEM	34



4.1.2	PRESENT DAY STRESS STATE IN GERMAN MOLASSE BASIN	36
<b>4.2</b>	<b>GEOLOGY AND DATA SET</b>	<b>36</b>
4.2.1	WELL DATA	36
4.2.2	CALIBRATION DATA	37
4.2.3	STATIC GEOLOGICAL MODEL	38
4.2.4	HYDRAULIC MODEL	39
<b>4.3</b>	<b>THERMAL MODEL</b>	<b>43</b>
4.3.1	INPUT DATA FOR FLUID AND ROCK THERMAL PROPERTIES	43
<b><u>CHAPTER 5 CALCULATION AND CALIBRATION OF THE MECHANICAL PROPERTIES</u></b>		<b>48</b>
<b>5.1</b>	<b>1D MECHANICAL EARTH MODEL</b>	<b>48</b>
<b>5.2</b>	<b>RESULTS</b>	<b>48</b>
5.2.1	OVERBURDEN STRESS	48
5.2.2	ELASTIC PROPERTIES	49
5.2.3	ROCK STRENGTH	49
5.2.4	PORE PRESSURE	49
<b><u>CHAPTER 6 CALCULATION AND CALIBRATION OF THE STRESS STATE</u></b>		<b>53</b>
<b>6.1</b>	<b>3D MECHANICAL EARTH MODEL</b>	<b>53</b>
6.1.1	BOUNDARY CONDITIONS AND STRESS ORIENTATIONS	54
<b>6.2</b>	<b>RESULTS</b>	<b>55</b>
<b><u>CHAPTER 7 HYDRAULIC MODEL</u></b>		<b>59</b>
<b>7.1</b>	<b>MODEL SETUP</b>	<b>59</b>
<b>7.2</b>	<b>RESULTS</b>	<b>60</b>
7.2.1	LONG-TERM (SEASONAL) CASE	60
7.2.2	SHORT-TERM CASES	62
<b><u>CHAPTER 8 THERMAL MODEL</u></b>		<b>74</b>
<b>8.1</b>	<b>MODEL SETUP</b>	<b>74</b>
8.1.1	THERMAL STRESSES	74
<b>8.2</b>	<b>THERMAL ANALYSIS</b>	<b>74</b>
<b><u>CHAPTER 9 THM COUPLED MODEL</u></b>		<b>76</b>
<b>9.1</b>	<b>RESULTS</b>	<b>76</b>
<b>9.2</b>	<b>SURFACE DISPLACEMENT</b>	<b>76</b>
9.2.1	FUTURE SCENARIO TESTING CASES	77
<b><u>CHAPTER 10 POTENTIAL FAULT REACTIVATION ANALYSES</u></b>		<b>88</b>
<b>10.1</b>	<b>MODEL SETUP</b>	<b>88</b>
<b>10.2</b>	<b>RESULTS</b>	<b>89</b>
<b>10.3</b>	<b>SAFE INJECTION RATE FOR SAFE STORAGE CAPACITY</b>	<b>90</b>
<b>10.4</b>	<b>STORAGE CAPACITY OF POWER-TO-GAS AND GAS-TO-POWER</b>	<b>90</b>
<b><u>CHAPTER 11 SUMMARY AND DISCUSSION</u></b>		<b>92</b>
<b>11.1</b>	<b>1D MECHANICAL EARTH MODEL</b>	<b>92</b>

	<b>Contents</b>
<b>11.2 HYDRAULIC MODEL</b>	<b>93</b>
<b>11.3 3D MECHANICAL EARTH MODEL</b>	<b>95</b>
<b>11.4 THM COUPLED MODELLING</b>	<b>96</b>
<b><u>CHAPTER 12 CONCLUSIONS AND PERSPECTIVES</u></b>	<b><u>100</u></b>
<b>12.1 CONCLUSIONS</b>	<b>100</b>
<b>12.2 PERSPECTIVES</b>	<b>102</b>
<b><u>REFERENCES</u></b>	<b><u>104</u></b>
<b><u>APPENDIX</u></b>	<b><u>110</u></b>
<b>1D MEM FOR ALL THE WELLS</b>	<b>110</b>
<b>DISSERTATION IN PDF FORMAT</b>	<b>114</b>
<b>1D MECHANICAL EARTH MODELS FOR ALL THE WELLS IN PDF FORMAT</b>	<b>114</b>
<b>PETREL MODEL GENERATION 2D MAP – STUDENT GUIDE</b>	<b>114</b>
<b>FLUID FLOW MODELLING USING ECLIPSE™ 100 – STUDENT GUIDE</b>	<b>114</b>
<b><u>STATEMENT OF AUTHORSHIP</u></b>	<b><u>115</u></b>
<b><u>RESUME/CV</u></b>	<b><u>116</u></b>

# List of Figures

Figure 1-1: Thesis flowchart. ....	5
Figure 2-1: Schematic diagram of PtG concept [29]. ....	9
Figure 2-2: Concept of PtG and its usage in various industries [32]. ....	9
Figure 2-3: Working principle of PtG and governing chemical processes of electrolysis and methanation [34]. ....	11
Figure 2-4: Power-to-Gas development in Europe [34]. ....	12
Figure 2-5: Coupling interface for gas, power and heat Systems [30]. ....	14
Figure 3-1: Flowchart illustrating the complete THM modelling workflow [36]. ....	15
Figure 3-2: Step by step 1D MEM workflow for computing material properties, pore pressure and stresses for a single well [36]. ....	16
Figure 3-3: The relationship between effective stress, overburden stress and pore pressure with respect to compaction along with depth [43]. ....	18
Figure 3-4: The illustration of stresses in three dimensions along with tensor transformation and principal stress tensor [53]. ....	23
Figure 3-5: The relation of principal stresses in different faulting regimes [53]. ....	23
Figure 3-6: 3D geomechanical modelling workflow including input data sources, validation and calibration. Modified after Henk et al. [27] [36]. ....	25
Figure 4-1: Location (blue square) and structure of the study area along with other small hydrocarbon fields in the area. Red dots indicate drilled wells in the area. (Provided by Uniper SE) ....	33
Figure 4-2: (a) Map of the Swiss-German Molasse basin along with main geological structures. Contour lines indicate the depth of the base of the Cenozoic sediments [24]. The grey area represents the Molasse Basin proper. The study area is indicated as red box. (b) N-S cross section of the profile shown in (a) representing the subsurface structures [24]. The case study reservoir is located near one of the north-dipping normal faults. ....	33
Figure 4-3: Stratigraphic overview of the Bavarian Molasse Basin along with the Mesozoic sub- Molasse succession [90]. The lithology fill and high sedimentation rates correspond to different ages and tectonic events of the Molasse Basin in Bavaria [28] [87] [91] [92]. ....	34
Figure 4-4: Hydrocarbon system of the Swiss-German Molasse Basin with key source rocks, reservoir formation and seal formation. The diagram represents also the hydrocarbons generation/- tectonic history as well as migration. [94]. ....	35
Figure 4-5: Present day orientation of maximum horizontal stresses ( $S_{Hmax}$ ) in the Molasse Basin	

derived from borehole breakouts and drilling induced fractures. The box represents the area of interest (modified after [24]).	36
Figure 4-6: Magnitudes and orientations of the total in situ principal normal stresses at the time of core extraction in the analyzed sections of the reservoir X6 well [95].	38
Figure 4-7: 3D structural model of the case study reservoir with three main faults. (a) is oblique view, (b) is top map view at depth of 1200 m below sea level, and (c) is east-west cross-sectional view. The model shows the porosity distribution throughout the reservoir area [36].	39
Figure 4-8: Horizons along with intervening lithostratigraphic units used to build up the 3D MEM down to a depth of 5 km [36].	39
Figure 4-9: Reservoir pressure prediction with base ECLIPSE™, E100-temp and E300-Thermal models [96].	45
Figure 4-10: Time steps of the three models [96].	46
Figure 4-11: Production prediction of the gas with all three models [96].	46
Figure 4-12: Prediction of field gas injection rate with the three models [96].	47
Figure 5-1: Summary of density calculations along with extrapolated overburden stress and mud weight profiles for Well X6. Section 1 represents bulk density ( $\rho_b$ ) for two sections along with combined extrapolated and bulk density profile ( $\rho_b\_COM\_Extra.$ ), section 2 represent only extrapolated density profile, section 3 consists of extrapolated overburden mud weight (OBMW_Extra.) and section 4 shows extrapolated overburden or vertical stress profile ( $S_v\_Extra.$ ).	48
Figure 5-2: Conversion of compressional velocity ( $V_p$ ) to shear velocity ( $V_s$ ) by using Greenberg and Castagna correlation (for Well X6) [46].	50
Figure 5-3: Computed dynamic Bulk modulus ( $K_d$ ) and Shear modulus ( $G_d$ ) (left) from dynamic Young's modulus and static Bulk ( $K_s$ ) and static Shear ( $G_s$ ) moduli (right) from dynamic Bulk and Shear moduli by using Bradford correlation (for Well X6).	51
Figure 5-4: Summary of calculated mechanical properties along with input log data for Well X6. Input data comprises shear and compressional slowness as well as extrapolated density and output data includes mechanical properties and pore pressure. Section 1 contains shear slowness ( $\Delta t_s$ ) and compressional slowness ( $\Delta t_c$ ), section 2 is bulk density ( $\rho_b$ ) and extrapolated density ( $\rho_b\_Extra.$ ), section 3 consists of calculated dynamic Young's modulus ( $E_d$ ) and static Young's modulus ( $E_s$ ), section 4 is dynamic Poisson ratio ( $\nu_d$ ) and static Poisson ratio ( $\nu_s$ ), section 5 shows unconfined compressive strength (UCS) and friction angle (FANG) and section 6 represents hydrostatic pressure	52
Figure 6-1: Reservoir model proper embedded in 3D geomechanical model with reservoir, overburden, underburden and sideburden zones. (a) is the top view and (b) is the oblique view [36].	53
Figure 6-2: Static Young's modulus ( $E_s$ ) distribution through upscaled computed log properties (1D MEM) with wells: Oblique view of overburden and underburden of reservoir area [36].	55

Figure 6-3: Calculated stress profile at well X6 showing vertical ( $S_v$ ), maximum ( $SH_{max}$ ) and minimum horizontal ( $Sh_{min}$ ) stresses with calibration data. ....56

Figure 6-4: Map view of the computed principal stresses on top of the reservoir. a=magnitude of the maximum horizontal stress ( $SH_{max}$ ), b= orientation of  $SH_{max}$ , c= magnitude of the minimum horizontal stress ( $Sh_{min}$ ) and d= magnitude of the vertical stress ( $S_v$ ). Color scale is in MPa. ....57

Figure 6-5: Stress state of randomly proposed well with principal stresses: maximum horizontal stress ( $SH_{max}$ ), minimum horizontal stress ( $Sh_{min}$ ) and vertical stress ( $S_v$ ).....58

Figure 7-1: Pressure profile during production history of the case study reservoir at well X6. The curve declines during production phase and increase during shut-in phase (replenishment phase) which is present day pore-pressure and starting point of further scenario testing. Continuous blue line represents pressure profile as a result of history match from the flow simulation. Red dots are the observed pressure data which can be used as calibration points on the pressure profile. ....59

Figure 7-2: Seasonal scenario testing case that represents six months injection and six months production cycle for Well X6. (a) Field pressure (FPR) profile for these cycles, (b) Well bottom hole pressure (WBHP), (c) Well water production rate (WWPR) and (d) Well gas injection rate (WGIR) and well gas production rate (WGPR). ....61

Figure 7-3: Short-term case characterizes 1 week injection-1 week shut in and two weeks production and 1 week shut in phases (1wkInj-1wkShut-2wkProd-1wkShut) for one year with one vertical well X6. (a) Field pressure (FPR) profile for these cycles, (b) Well bottom hole pressure (WBHP), (c) Well water production rate (WWPR) and (d) Injection (WGIR) and production (WGPR) gas rates.....63

Figure 7-4: Short-term case exemplifies 1wkInj-1wkShut-2wkProd-1wkShut schedule of two wells (1 vertical well X6 and 1horizontal well H1) for 1 year. (a) is field pressure (FPR) profile for these cycles, (b) Well bottom hole pressure (WBHP)of both wells X6 and H1, (c) Well water production rate (WWPR) for well H1 and (d) Injection (WGIR) and production (WGPR) gas rates for well H1.....64

Figure 7-5: Field pressure (FPR) profile of all three well (X2, X6 and H1) with schedule 1wkInj-1wkShut-2wkProd-1wkShut for 1 year.....65

Figure 7-6: Well properties comparison of three wells case scenario with short-term schedule 1wkInj-1wkShut-2wkProd-1wkShut for 1 year. X2 and X6 are vertical wells and H1 is the horizontal well. (a) Well bottom hole pressure (WBHP) of all wells, (b) production gas rates (WGPR) for all three wells, (c) Injection gas rates (WGIR) for all three wells and (d) Well water production rate (WWPR) for all the wells.....66

Figure 7-7: The properties of short-term case without water cut describes (1wkInj-1wkShut-2wkProd-1wkShut) schedule for one year with one vertical well X6. (a) field pressure (FPR) profile for these cycles, (b) Well bottom hole pressure (WBHP), (c) Well water production rate (WWPR) and (d) Injection (WGIR) and production (WGPR) gas rates.....67

Figure 7-8: Short-term case demonstrates 1wkInj-1wkShut-2wkProd-1wkShut schedule of two wells (1 vertical well X6 and 1horizontal well H1) for 1 year without water cut.. (a) is field pressure (FPR) profile for these cycles, (b) is Well bottom hole pressure (WBHP) of both wells X6 and

- H1, (c) is Well water production rate (WWPR) well water production rate (WWPR) for well H1 and (d) is Injection (WGIR) and production (WGPR) gas rates for well H1.....68
- Figure 7-9: Field pressure (FPR) profile of all three well (X2, X6 and H1) with schedule 1wkInj-1wkShut-2wkProd-1wkShut for 1 year without water cut-off.....69
- Figure 7-10: Well properties comparison of three wells case scenario with short-term schedule 1wkInj-1wkShut-2wkProd-1wkShut 1 year without water cut. X2 and X6 are vertical wells and H1 is the horizontal well. (a) Well bottom hole pressure (WBHP) of all wells, (b) production gas rate (WGPR) for all three wells, (c) Injection gas rate (WGIR) for all three wells and (d) Well water production rate (WWPR) for all the wells. ....70
- Figure 7-11: Data shows the consumption of total electricity in Germany along with electricity produced from renewable energy sources (such as wind, either offshore or onshore and solar) in the Calendar year 2017 [99] [100]. ....71
- Figure 7-12: The fluctuation of electricity produced in Germany from renewable sources in 2017 is modeled in to future scenario testing case with limited water cut-off ( $5 \text{ m}^3/\text{day}$ ). The excess of energy can be stored in UGS and can be used when needed. This schedule is helpful to understand which month of the year energy can be stored as gas in UGS and in which month of the year this energy can be utilized when shortage occurs. (a) Field pressure (FPR) profile for these cycles, (b) Well bottom hole pressure (WBHP)of well X6, (c) well water production rate (WWPR) for well X6 and (d) Well gas injection rate (WGIR) and well gas production rate (WGPR) for well X6. ....72
- Figure 7-13: The fluctuation of electricity produced in German from renewable sources in 2017 is modeled in to future scenario testing case without limited water cut-off. The excess of energy can be stored in UGS reservoirs and can be used when needed. This schedule is helpful to understand which month of the year energy can be stored as gas in UGS and in which month of the year this energy can be utilized when shortage occurs. (a) Field pressure (FPR) profile for these cycles, (b)Well bottom hole pressure (WBHP) of well X6, (c) well water production rate (WWPR) for well X6 and (d) Injection (WGIR) and production (WGPR) gas rates for well X6. ..73
- Figure 8-1: Temperature changes around Well X2 and X6 by injecting colder foreign gas at different time steps ( $t_1$ ,  $t_2$ ,  $t_3$  and  $t_4$ ). Time steps  $t_1$ ,  $t_2$ ,  $t_3$ ,  $t_4$  correspond to 01/01/20, 01/07/20, 01/01/21 and 01/07/21 respectively. The arrows show the exact location of significant temperature difference while injection/production phases. The color scale is in  $^{\circ}\text{C}$ , whereas the arrows with N show northward direction.....75
- Figure 9-1: Subsidence predicted at the ground surface above reservoir during depletion ( $t_1$ ) and replenishment ( $t_2$ ) relative to pre-production time (which was 0 mm displacement). The area in the box represents the ground surface right above reservoir area and rest area is ground surface of sideburden. Color scale is in millimeters.....77
- Figure 9-2: Pore pressure ( $P_p$ ) and effective stress ( $Seffec$ ) changes from  $t_1$  (01/01/26) to  $t_2$  (01/07/26) in long-term (seasonal) case with one well (X6). The arrows show the location of maximum observed fluctuation in  $P_p$  and  $Seffec$  from  $t_1$  to  $t_2$ . The color scale is in MPa. ....78
- Figure 9-3: Pore pressure ( $P_p$ ) and effective stress ( $Seffec$ ) changes from  $t_1$  (01/01/20) to  $t_2$  (22/09/20) in short-term case with one well (X6) with water cut-off rate of  $5 \text{ m}^3/\text{day}$ . The arrows show the location of maximum observed fluctuation in  $P_p$  and  $Seffec$  from  $t_1$  to  $t_2$ . The color

scale is in MPa. ....	79
Figure 9-4: Pore pressure ( $P_p$ ) and effective stress ( $Seffec$ ) changes from t1 (22/07/20) to t2 (05/08/20) in short-term case with two wells (X6 and H1) with water cut-off rate of 5 m <sup>3</sup> /day. The arrows show the location of maximum observed fluctuation in $P_p$ and $Seffec$ from t1 to t2. The color scale is in MPa. ....	80
Figure 9-5: Pore pressure ( $P_p$ ) and effective stress ( $Seffec$ ) changes from t1 (16/12/20) to t2 (23/12/20) in short-term case with three wells (X2, X6 and H1) with water cut-off rate of 5 m <sup>3</sup> /day. The arrows show the location of maximum observed fluctuation in $P_p$ and $Seffec$ from t1 to t2. The color scale is in MPa. ....	81
Figure 9-6: Pore pressure ( $P_p$ ) and effective stress ( $Seffec$ ) changes from t1 (01/01/20) to t2 (31/12/20) in short-term case with one (X6) with water cut-off rate of 5 m <sup>3</sup> /day with random schedule. The arrows show the location of maximum observed fluctuation in $P_p$ and $Seffec$ from t1 to t2. The color scale is in MPa. ....	82
Figure 9-7: Pore pressure ( $P_p$ ) and effective stress ( $Seffec$ ) changes from t1 (22/07/20) to t2 (12/08/20) in short-term case with one well (X6) without water cut-off rate of 5 m <sup>3</sup> /day. The arrows show the location of maximum observed fluctuation in $P_p$ and $Seffec$ from t1 to t2. The color scale is in MPa. ....	83
Figure 9-8: Pore pressure ( $P_p$ ) and effective stress ( $Seffec$ ) changes from t1 (22/07/20) to t2 (05/08/20) in short-term case with two wells (X6 and H1) without water cut-off rate of 5 m <sup>3</sup> /day. The arrows show the location of maximum observed variation in $P_p$ and $Seffec$ from t1 to t2. The color scale is in MPa. ....	84
Figure 9-9: Pore pressure ( $P_p$ ) and effective stress ( $Seffec$ ) changes from t1 (09/12/20) to t2 (23/12/20) in short-term case with three wells (X2, X6 and H1) without water cut-off rate of 5 m <sup>3</sup> /day. The arrows show the location of maximum observed change in $P_p$ and $Seffec$ from t1 to t2. The color scale is in MPa. ....	85
Figure 9-10: Pore pressure ( $P_p$ ) and effective stress ( $Seffec$ ) changes from t1 (01/01/20) to t2 (31/12/20) in short-term case with one well (X6) without water cut-off rate of 5 m <sup>3</sup> /day with random schedule. The arrows show the location of maximum observed fluctuation in $P_p$ and $Seffec$ from t1 to t2. The color scale is in MPa. ....	86
Figure 10-1: Pressure profiles for the history matching scenario and scenarios multiplied by a fixed factors ( $P_p$ , $P_p \times 1.15$ , $P_p \times 1.25$ and $P_p \times 1.5$ ) controlled by gas injection rates until fault reactivation occurs. ....	89
Figure 10-2: The computation of fault reactivation through numerical analysis for pressure multiplied by a factor of 1 (a) and 1.15 (b) on the left side of figure. White dots show the cells whose stress state exceeds the failure criterion (arrows show northward direction). On the right side of figure is the shear stress $S_s$ vs. normal stress $S_n$ diagrams, showing the Mohr-Coulomb failure criterion at well X6 location (which is nearest to the main fault of the reservoir). (a) is the Mohr-Coulomb diagram for $P_p$ and (b) is the Mohr-Coulomb diagram for $P_p \times 1.15$ . Time steps t1 and t2 correspond to starting (01/01/20) and final (01/01/21) time steps of the tested cases. An increase in pore pressure leads to a decrease in effective stresses from (a) to (b). This causes the corresponding Mohr circle to shift to the left in the direction of the tensile failure	

line. If the failure line is finally touched, plastic straining occurs and - in case of a fault zone - fault reactivation occurs. ....	89
Figure 10-3: The computation of fault reactivation through numerical analysis for pressure multiplied by a factor of 1.25 (c) and 1.5 (d) on the left side of figure. White dots show the cells whose stress state exceeds the failure criterion (arrows show northward direction). On the right side of figure is the shear stress $S_s$ vs. normal stress $S_n$ diagrams, showing the Mohr-Coulomb failure criterion at well X6 location (which is nearest to the main fault of the reservoir). (c) is the Mohr-Coulomb diagram for $P_p \times 1.25$ and (d) is the Mohr-Coulomb diagram for $P_p \times 1.5$ . Time steps $t_1$ and $t_2$ correspond to starting (01/01/20) and final (01/01/21) time steps of the tested cases. An increase in pore pressure leads to a decrease in effective stresses from (c) to (d). This causes the corresponding Mohr circle to shift to the left in the direction of the tensile failure line. If the failure line is finally touched, plastic straining occurs and - in case of a fault zone - fault reactivation occurs. ....	90
Figure 11-1: Gas saturation (%) during injection-production cycles. ....	93



## List of Tables

Table 2-1: Energy Requirements in the GHGND Scenario for Germany [35]. .....	12
Table 3-1: Various empirical correlations for calculating elastic Young’s modulus [45].....	20
Table 3-2: Various correlations to estimate unconfined compressive strength (UCS) depending upon the lithology of rock formation [49].....	21
Table 3-3: Coupled THM processes, modified after Jalali et al. [62] [67].....	28
Table 4-1: Summary of the available well logs for all the wells.....	37
Table 4-2: Magnitude of total stresses e.g. total vertical, total maximum horizontal and total minimum horizontal stress in well X6 [24]. .....	37
Table 4-3: Pressure, formation volume factor and viscosity data of fluid as part of PVT data used for reservoir (flow) simulation.....	40
Table 4-4: Temperature versus water viscosity data used as part of PVT data for reservoir simulation. ..	41
Table 4-5: Water properties used in the ECLIPSE™ model.....	41
Table 4-6: Saturation functions for gas phase .....	42
Table 4-7: Saturation functions of water phase .....	42
Table 4-8: Equilibration data specification for initialization.....	43
Table 4-9: Reservoir fluids initially in place (predicted) [96].....	44
Table 6-1: Material properties of the case study reservoir along with overburden and underburden units of 3D geomechanical model.....	54
Table 7-1: All future testing scenario cases with input parameters. WBHP is well bottom hole pressure, WGIR is well gas injection rate, and WGPR is well gas production rate.....	60
Table 9-1: Summary of results for all future test scenarios. The sign + in the pore pressure changes determines the positive change or increase in pore pressure from time step t1 to t2, while the sign - in the changes in effective stresses denotes the decrease in magnitudes of effective stresses fro time step t1 to t2. These two quantities are inversely proportional to each other and are expressed in MPa and KPa for a better understanding of the changes.....	86
Table 10-1: Power-to-Gas and gas-to-power convertible units.....	91

## List of abbreviations and symbols

### List of symbols

$A_0$	<i>Fitting parameter</i>
$\alpha_f$	<i>Fitting parameter</i>
$\alpha_E$	<i>Eaton factor</i>
$\alpha$	<i>Biot coefficient</i>
$\alpha_t$	<i>Thermal coefficient</i>
$B$	<i>Volume factor for gas</i>
$\beta$	<i>Coefficient of linear thermal expansion (<math>1/^\circ\text{C}</math>)</i>
$c_s$	<i>Specific heat capacities of the formation</i>
$c_f$	<i>Specific heat capacities of the fluid</i>
$c$	<i>Gas specific heat capacity</i>
$DTCO$	<i>Compressional slowness</i>
$E$	<i>Young's modulus</i>
$e$	<i>Exponent determined experimentally</i>
$E_d$	<i>Dynamic Young's modulus</i>
$\varepsilon_H$	<i>Maximum horizontal strain magnitudes</i>
$\varepsilon_h$	<i>Minimum horizontal strain magnitudes</i>
$E_s$	<i>Static Young's modulus</i>
$FANG$	<i>Friction angle</i>
$F_{E100}$	<i>Fluids in place calculated with E-100 models</i>
$F_{E300}$	<i>Fluids in place calculated with E-300 model</i>
$f_i$	<i>Body force</i>
$GWh$	<i>Giga Watt hours</i>
$CH_4$	<i>Methane</i>
$\phi$	<i>Porosity</i>

## List of abbreviations and symbols

$\phi_0$	<i>Porosity at zero stress</i>
$g$	<i>Gravitational acceleration</i>
$G_{dyn}$	<i>Dynamic shear modulus</i>
$G$	<i>Shear modulus</i>
$H_g$	<i>Hydrostatic gradient</i>
$H$	<i>Fluid height</i>
$i, j, k$	<i>Directions</i>
$K$	<i>Bulk modulus</i>
$k$	<i>Permeability</i>
$K_B$	<i>Bulk modulus of the rock</i>
$K_{dry}$	<i>Static bulk modulus of the dry skeletal frame</i>
$k_f$	<i>Thermal conductivity of the fluid</i>
$K_{ij}$	<i>Permeability tensor</i>
$k_0$	<i>Permeability at zero stress</i>
$K_{sotid}$	<i>Static bulk modulus of the rock material</i>
$K_r$	<i>Relative gas permeability</i>
$K_{rg}$	<i>Relative permeability of gas</i>
$K_{rw}$	<i>Relative permeability of water</i>
$k_s$	<i>Thermal conductivity of the formation</i>
$k_t$	<i>Thermal conductivity</i>
$k_{total}$	<i>Total thermal conductivity</i>
$kWh/d$	<i>Killowatt hours per day</i>
$m^3/day$	<i>Cubic meter per day</i>
$m$	<i>Meter</i>
$M$	<i>Molar mass of air</i>
$mD$	<i>Milli Darcy</i>
$MPa$	<i>Mega pascal</i>
$MWh$	<i>Mega Watt hours</i>

$n$	<i>Eaton exponent</i>
$\theta$	<i>Angle between dip line of the fault</i>
$P_p$	<i>Pore pressure</i>
$P$	<i>Fluid pressure for gas</i>
$(\rho c)_t$	<i>Total heat capacity of the solid and fluid phase</i>
$\bar{\rho}$	<i>Average density of the total overlying rock formation</i>
$\rho_b$	<i>Bulk density</i>
$\rho_{extra.}$	<i>Extrapolated synthetic density</i>
$\rho_f$	<i>Density of the fluid</i>
$\rho_g$	<i>Gas density</i>
$\rho_{mudline}$	<i>Density at the sea floor (offshore) or ground level (onshore)</i>
$\rho_s$	<i>Density of the formation</i>
$\rho(z)$	<i>Bulk density at depth <math>z</math> below the earth's surface</i>
$q$	<i>Fluid source or sink</i>
$q_h$	<i>Heat flux density</i>
$q_t$	<i>Intensity of the internal heat source</i>
$R$	<i>Ideal gas constant</i>
$R_{log}$	<i>Resistivity log</i>
$S$	<i>Saturation for gas</i>
$S_1, S_2, S_3$	<i>Principal stresses</i>
$S_{Hmax}$	<i>Maximum horizontal stress</i>
$S_{hmin}$	<i>Minimum or least horizontal stress</i>
$S_{i,j,j}$	<i>Total stress tensor</i>
$S_M$	<i>Effective stress</i>
$S_n$	<i>Normal stress</i>
$S_s$	<i>Shear stress</i>
$S_{m(total)}$	<i>Mean total stress</i>
$S_t$	<i>Thermal stress</i>

## List of abbreviations and symbols

$S_v$	<i>Overburden stress</i>
$T$	<i>Temperature</i>
$T_f$	<i>Final temperature of the reservoir</i>
$T_0$	<i>Original temperature of the reservoir</i>
$\Delta T$	<i>Temperature difference in the reservoir</i>
$TWh$	<i>Terra Watt hours</i>
$TVD$	<i>True vertical depth</i>
$\Delta t_c$	<i>Compressional wave interval transit time</i>
$\Delta t_s$	<i>Shear wave interval transit time (shear wave slowness)</i>
$\Delta t_n$	<i>Compressional slowness in shales at normal pressure</i>
$-\nabla T$	<i>Negative local temperature gradient</i>
$UCS$	<i>Unconfined compressive strength</i>
$\mu_g$	<i>Gas viscosity</i>
$\mu$	<i>Coefficient of friction</i>
$\nu$	<i>Poisson's ratio of the rock mass</i>
$\nu_s$	<i>Static Poisson's ratio</i>
$V_{clay}$	<i>Volume of clay</i>
$\nu_d$	<i>Dynamic Poisson's ratio</i>
$v_i$	<i>Fluid velocity</i>
$V_s$	<i>Shear wave velocity</i>
$V_p$	<i>Compressional wave velocity</i>
$Z$	<i>Depth</i>

## List of abbreviations

<i>1D MEM</i>	<i>1D mechanical earth modelling</i>
<i>3D MEM</i>	<i>3D finite element model</i>
<i>AEC</i>	<i>Alkaline Electrolysis Cells</i>

<i>AVO</i>	<i>Amplitude versus offset</i>
<i>BMBF</i>	<i>German Federal Ministry of Education and Research</i>
<i>BSL</i>	<i>Below sea level</i>
<i>BHP</i>	<i>Bottom hole pressure</i>
<i>CAPEX</i>	<i>Capital Expenditures</i>
<i>CHP</i>	<i>Combined heat and power</i>
<i>CO2</i>	<i>Carbon Dioxide</i>
<i>DEN</i>	<i>Bulk density</i>
<i>DEN_extra</i>	<i>Extrapolated density</i>
<i>DIF's</i>	<i>Drilling-induced fractures</i>
<i>DTCO</i>	<i>Compressional slowness</i>
<i>EU</i>	<i>European Union</i>
<i>FANG</i>	<i>Friction angle</i>
<i>FMI</i>	<i>Formation micro imager</i>
<i>FMS</i>	<i>Formation micro scanner</i>
<i>FE</i>	<i>Finite element</i>
<i>FIPNUM</i>	<i>Fluid in place region number</i>
<i>FPR</i>	<i>Field pressure</i>
<i>FVF</i>	<i>Formation volume factor <math>rm^3/sm^3</math></i>
<i>GHGND</i>	<i>Greenhouse gas neutral land</i>
<i>Gt</i>	<i>Giga ton</i>
<i>HM</i>	<i>Poroelasticity</i>
<i>IoT</i>	<i>Internet of Things</i>
<i>LNG</i>	<i>Liquefied natural gas</i>
<i>LOT</i>	<i>Leak-off test</i>
<i>M</i>	<i>Molar mass</i>
<i>MEM</i>	<i>Mechanical earth model</i>
<i>MINPV</i>	<i>Minimum pore volume</i>

## List of abbreviations and symbols

---

<i>Mt</i>	<i>Megatonne</i>
<i>OBMW</i>	<i>Overburden mud weight</i>
<i>PEM-EC</i>	<i>Proton Exchange Membrane Electrolysis Cells</i>
<i>PtG</i>	<i>Power-to-Gas</i>
<i>PtG-M</i>	<i>Power-to-Gas methane</i>
<i>PVT</i>	<i>Pressure Volume Temperature</i>
<i>R&amp;D</i>	<i>Research &amp; Development</i>
<i>SCAL</i>	<i>Special core analysis</i>
<i>Seffec</i>	<i>Effective stress</i>
<i>Sg</i>	<i>Gas saturation</i>
<i>SOEC</i>	<i>Solid Oxide Electrolysis Cells</i>
<i>Sw</i>	<i>Water saturation</i>
<i>THM</i>	<i>Thermal-hydraulic-mechanical</i>
<i>TM</i>	<i>Thermoelasticity</i>
<i>TVD</i>	<i>True vertical depth</i>
<i>UBA</i>	<i>Umweltbundesamt</i>
<i>UCS</i>	<i>Unconfined compressive strength</i>
<i>UGS</i>	<i>Underground gas storage (Unterirdische Gasspeicherung)</i>
<i>WBHP</i>	<i>Well bottom hole pressure</i>
<i>WGIR</i>	<i>Well gas injection rate</i>
<i>WGPR</i>	<i>Well gas production rate</i>
<i>WSM</i>	<i>World Stress Map</i>
<i>WVA</i>	<i>Wave velocity analyses</i>
<i>WWPR</i>	<i>Well water production rate</i>

# Chapter 1 Introduction

## 1.1 Motivation and objectives

High energy demand requires more and more research in the “Underground Gas Storage” (UGS) discipline [1]. As a result, both long-term (seasonal) and short-term (weekly) gas storage projects have gained the attention of UGS researchers [1]. The combination of long-term and short-term storage can be an emphasis to use the same storage reservoir for long-term along with short-term storage [1]. The idea is to use the same UGS reservoir for “Power-to-Gas” from excessive electricity from renewable sources such as solar and wind. In addition, the stored gas can be reused for power generation when needed.

Short-term and long-term storage cycles may cause some geomechanical issues in the porous reservoir. The pore fluid pressure in the reservoir fluctuates due to intensive gas injection and withdrawal phases. These fluctuations in fluid pressure change the effective stresses in the reservoir and may also change the in-situ stress state outside the reservoir area [2]. These changes have implications on geomechanical phenomena related to fault stability, caprock integrity, and surface deformation. Numerical modelling e.g. 3D geomechanical modelling provides a platform to integrate lithological and mechanical heterogeneities and investigate plus predict stress state and stress path of subsurface reservoirs.

This study concentrates on a geomechanical assessment of a former gas field in the Bavarian Molasse Basin east of Munich (Germany) for which a hypothetical transformation to underground gas storage (UGS) is considered. Future scenario testing cases for long-term (seasonal) as well as short-term (weekly) gas storage are also considered to evaluate geomechanical stresses (e.g. effective stress) on reservoirs due to pressure changes with high-frequency injection/production cycles. German data for excess electricity from renewable energy sources (such as solar and wind) throughout the calendar year 2017 has also been considered in two cases to address the issues of renewable energy aspects. This implies that the surplus electricity in Germany can be stored in underground gas storage facilities with a Power-to-Gas (PtG) concept and that the stored gas can be reused for electricity generation (Gas-to-Power) or other purposes when required.

The presented modelling study is a worked example of how to set up and populate 3D coupled thermal-hydraulic-mechanical model of an underground gas storage site. This case study is very typical for the conversion of depleted reservoirs to gas storage sites as the database for mechanical earth modelling (MEM) is frequently rather old, i.e. from the exploration phase of the initial reservoir. Nevertheless, even in such cases the workflow outlined below (in the methodology section) allows generating a numerical model for testing of future injection-production schedules and assessment of maximum storage capacity.

The case study reservoir is a depleted gas reservoir located about 65 km east of Munich in the Central Molasse Basin. It is an anticlinal structural trap bounded by a normal fault. The reservoir formation is mainly Early Cenozoic Chattian Sand with 85 m thick three gas-bearing layers, found at a depth of 1770 m (1200 m below sea level). The initial gas-water contact was at 1239 m below sea level (BSL). The reservoir has produced 528 million m<sup>3</sup> of gas over 18 years from 1958 till 1976, replenishment started from 1978 till present and the reservoir has not been in operation to date. So far, the reservoir has not been used as underground gas storage. This model study would allow using the production



history of the dynamic reservoir fluid model as the foundation to build a 3D geomechanical model describing the physical evolution of the reservoir throughout its production history and future prediction by short-term scenario testing. The stress path derived from the history match provides a base to perform short-term cyclic injection and withdrawal phases and relate the results with maximum fluid pressure fluctuation of the history of the reservoir [2].

The modelling results provide information about the stress state within and around the reservoir as a result of the production and injection of each selected time step and compare it with the stress state at depletion and replenishment stages. The production history of the reservoir (porous media) was categorically useful to determine stress path within and around the reservoir, wellbore periphery as well as caprock integrity. Further, the modelling results provide information about ground surface subsidence during peak depletion and replenishment time steps which can be useful to minimize geomechanical risks to any gas storage facility, not only for methane or CO<sub>2</sub> but also for hydrogen. Finally, fault reactivation analyses are also incorporated to get a safe gas injection rate for safe storage capacity.

### 1.2 SUBI Project

This work is part of the SUBI (Safety of underground storage facilities under cyclical load: functionality and integrity of storage facilities and wells) project which is a BMBF (Federal Ministry of Education and Research) funded project (Funding Code: 03G0869) with the collaboration of various German companies and research institutes. In the course of the energy transition, the requirements for underground gas storage facilities (UGS) are increasing. Therefore, these facilities should be designed for higher frequency (frequent injection/production cycles) high amplitude (volumes) of storage operations. Therefore the main focus of the project is on the influence of such cyclic loads on the geological and technical facilities and consequently on the safety and functionality of underground gas storage facilities. To make sure the long-term protection of the managing assets, the primary processes and mechanisms must be taken into account both qualitatively and quantitatively throughout. The project, therefore, considers the holistic approach of operation-related changes in the properties of reservoirs, overburden, and their association with technical facilities (e.g. cementation - boreholes). Further, the interlinked experimental and numerical investigations form the basis for model predictions, which are validated with field observations. These models are used for scenario observations on real field modelled reservoirs to derive optimized processes for pre and post-operational phases, which increase safety even with increased cyclic loading of the reservoirs.

Gas storage facilities such as depleted oil and gas reservoirs (porous), aquifer storage facilities, and cavern storage facilities have been operating successfully in the Federal Republic of Germany for decades. Currently, underground gas storage (UGS) is mainly used in seasonal storage operations. To incorporate new technologies such as "Power to Gas", higher-frequency storage modes must be considered in the future not only for salt cavern storage facilities but also for storage in porous media. To ensure the long-term safety of UGS, an interdisciplinary and cross-scale approach is required. The processes of storage system changes in pore and cavern storage facilities under high-frequency cyclic loading are to be documented and analyzed through experimentation, modelling, and geomechanical assessment. Pore pressure changes and stress distribution can trigger the development of migration pathways through reactivation of faults, fractures, and along various discontinuities (borehole integrity) and therefore jeopardize asset facilities (e.g. drinking water) and lead to serious seismic activity [3]. The cyclic loading and unloading can also lead to both under-hydrostatic pressure conditions with migration from e.g. groundwater into the reservoir and over-hydrostatic pressure which may cause migration from the reservoir into groundwater. The main objective of the project is to avoid damage to the storage system (borehole, cementation, caprock and reservoir rocks) as a result

of cyclic loading. For cavern reservoirs, this concerns e.g. contour or cavity changes, for pore reservoirs the spatial and temporal change of hydraulic (porosity, permeability) and geomechanical properties, which affect the storage volume and the integrity of the overburden, as well as the reactivation potential of faults.

Well integrity requires stable and sealed casing cementation during operations and beyond. For this purpose, experiments have been carried out in the laboratory and multiphase simulations have been performed on different scales. The focus of the research activities is on the change in storage capacity (relevant for economic efficiency) and integrity (safety relevance) of storage systems due to cyclic loading during injection and withdrawal phases. The research project aims to create the basis for operational and design recommendations for early detection and prevention of leakages for fluids and gases due to the loss of wellbore and caprock integrity during operations and beyond. The key emphases of this part of the project area). Development of an integrated understanding of the ageing processes during cyclic loading of UGS b). Development of wellbore (casing + cementation) and reservoir (caverns and porous reservoirs) models to observe wellbore, reservoir and caprock integrity during cyclic operation. c). Observation of surface deformation (based on PSInSar) to examine the functionality or ageing of reservoir and overburden.

With a comprehensive, systemic approach, the complex rheological properties are characterized by laboratory and field experiments in such a way that they can be used for verifiable system predictions through model calculations (THM modelling and geomechanical considerations taking into account biological processes). Validation is carried out by comparing predicted and observed surface uplift and subsidence or deformation. This is intended to clarify the question of whether and how these can be used as an indication of ageing phenomena in the sense of an early warning. The contribution of this thesis in the project is about geomechanical assessment of the case study reservoir through THM modelling by building 1D and 3D mechanical earth models together with coupling with fluid flow model. The major outcomes of the modelling study are stress state in and around reservoir throughout history and future based testing scenarios of the porous reservoir, ground surface subsidence of the history of the reservoir as well as the long-term and short-term storage case scenarios, and the analyses of maximum handling pressure e.g. gas rates in injection and withdrawal phases to avoid fault reactivation and fracturing in the reservoir.

### **1.3 Thesis overview**

This section presents a short overview of all the chapters in a structured way. Chap. 1 is a brief description of the SUBI project as well as the motivation and objectives of this thesis which is an integral part of the SUBI project. Section 1.4 provides also a description of the state of the art in reservoir geomechanics in porous media along with thermal-hydraulic-mechanical (THM) coupled modelling in the underground gas storage system.

Power-to-Gas (PtG) technologies such as hydrogen injection or synthetic natural gas into the gas grid are possible using the existing gas infrastructure. Chap. 2 describes the state of the art of PtG technology, discusses the role and prospects of PtG, and gives a brief description of the systematic challenges in integrating PtG. The synergies between the gas sector and the electricity system for sector coupling are analyzed and the gas and electricity systems are compared. General background on the functions and mechanisms of the gas market is given and the injection of gas into the natural gas grid and the economic conditions of PtG in Germany are discussed.

The methodology applied in different modelling phases e.g. from 1D MEM to 3D MEM as well as dynamic fluid modelling and coupling methods of THM modelling is presented in Chap. 3. This

chapter provides detail about the scientific fundamentals (density methods, calculation of overburden stress, pore pressure, elastic properties, rock strength parameters as well as maximum and minimum horizontal stresses), which are the foundation of 1D MEM. The general description and workflow to build a 3D geomechanical model is also an integral part of this chapter.

Chap. 4 introduces the case study and describes the geographic location and geological setting of the Molasse Basin in South Germany. The stratigraphic information as well as the hydrocarbon systems in the area is also described in this chapter. The data specific to the case study reservoir such as log data, basic structural reservoir model and calibration data is included in this chapter.

Chap. 5 deals with the methods used to generate 1D MEM for all the available wells by using Techlog® software. Elastic properties (Young's modulus, Poisson's ratio, Biot coefficient, etc.) and an initial estimate for vertical and horizontal stresses at the borehole locations are derived through various empirical correlations. The calculated properties were calibrated with the available core data and the pore pressures for the caprock and the reservoir formation were calculated.

Chap. 6 presents the different aspects of 3D MEM including the advantages of geomechanical models for underground gas storage. Two main topics are discussed in this chapter: the stress state of the 3D geomechanical model, which includes not only the reservoir section but also the overburden to the ground surface and the underburden to the bedrock, and the 3D property population by interpolation method and properties from various publications applied to the model.

Chap. 7 and 8 describe the model's setup for hydraulic as well as thermal model respectively. For coupling, the same structural model (Petrel®) was used to build these models. History matching technique is applied to build a fluid flow model to compute those changes in pressure that are also the input for the geomechanical simulation. The results conclude with the calculation of the hydraulic and thermal properties and the incorporation of these properties into the coupled THM modelling.

Chap. 9 describes the modelling of the coupled thermal-hydraulic-mechanical (THM) model together with the main results. The resulting coupled THM model provides information on the effective stresses and pore pressure in the reservoir throughout the operational period. The resulting model also provides important information on the subsidence of the ground surface of the case study reservoir field. This study aims to assess the integrity of the caprock and the possible reactivation associated with gas injection and production. In addition, a parametric study will determine the pore pressure required to reactivate the fault. For numerical models, these results are crucial for information such as the safe storage capacity of the reservoir (Chap. 10). This modelling approach can be applied to any underground gas reservoir in the world.

Chap. 11 gives a summary along with a discussion. This chapter discusses the various aspects of 1D and 3D MEM, hydraulic models along with coupled THM modelling including benefits of the modelling approach in underground gas storage. Three major topics are discussed in this chapter, which is: the stress state of the 3D geomechanical model, surface subsidence of the case study reservoir field and comparison of vertical displacements of other hydrocarbon fields, the mechanical properties, and parameters studies from various publications.

Chap. 12 concludes the thesis with key findings of the study, final messages from the research and future research directions as well as the perspective and usage of the modelling results. The flowchart of the thesis is illustrated in Figure 1-1.

\*Special note: An utmost attempt has been made to use SI units throughout this thesis, but since the data from the hydrocarbon industry is used for the modelling in this study, and it is quite common in the hydrocarbon industry to use field units in the form of log data and others. This is the reason why

some of the data is still in the form of field units, which may be troublesome for the common reader, but it is important to show the original data to have a better understanding and implication on the real hydrocarbon fields for green energy such as Power-to-Gas and vice versa.

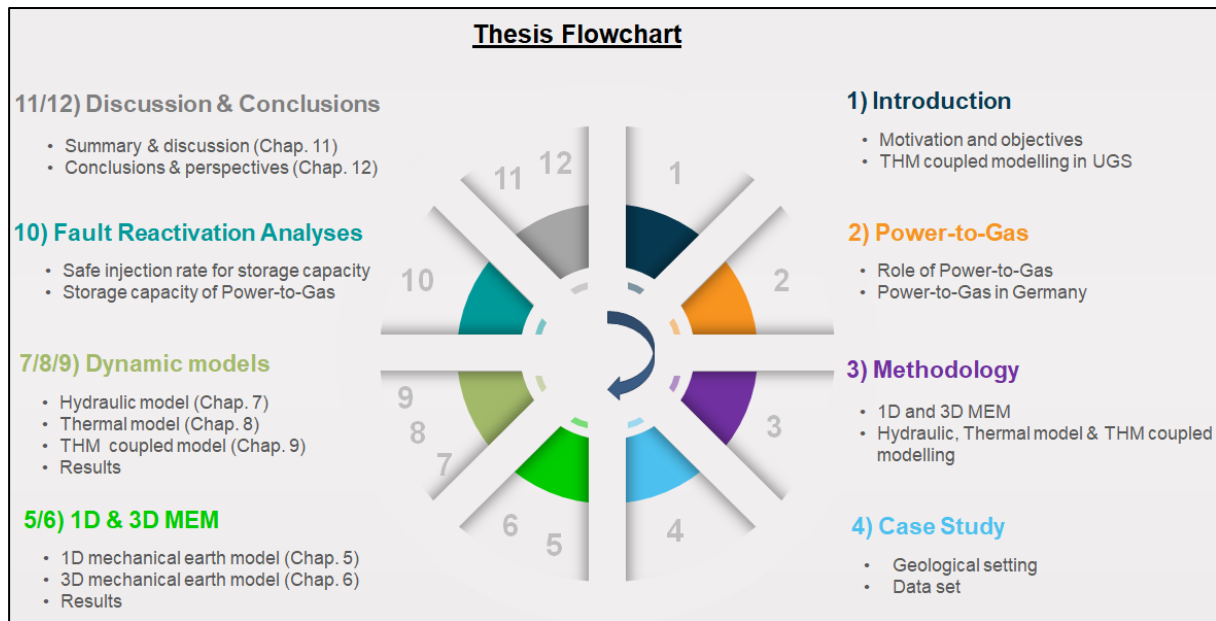


Figure 1-1: Thesis flowchart.

## 1.4 Porous UGS and importance of THM modelling

The energy demand is increasing with world's population. Natural gas is the cleanest fossil fuel and production of it from other renewable energy sources makes it a potential energy substitute, also by taking in to account the environmental concerns [4]. The data suggest natural gas will be in high demand in future as well [5]. The most popular gas storage method is underground gas storage among others such as liquefied natural gas (LNG), storage tanks and pipeline storage [6] [7]. Two important issues are associated with UGS. First, rely on gas imports due to increase in demand for power generation (Gas-to-Power) and other domestic usages. Second, any damage to infrastructure could lead to higher gas prices or disruption of supply, with unpredictable costly consequences for customers [1]. In order to address these challenges, various researches have suggested to use depleted gas/oil porous reservoirs or aquifers as UGS, where significant volumes can be strategically stored [1] [8].

Depleted hydrocarbon reservoirs particularly porous gas reservoirs are the most appropriate targets for short-term storage with frequent injection-production cycles [1] [4] [7] [9] [10]. The very first depleted gas reservoir was successfully used as underground storage of natural gas in 1916 i.e. Zoar gas field, south of Buffalo, New York (USA), where the facilities are still operational [1] [11]. Later 715 UGSs have been established globally, and the numbers are still increasing [12] [13]. As an example, various depleted gas field have been identified to be used as UGS system in Roma Shelf Australia [9]. The Roma Shelf is a structural uplift that lies within two tectonic basins of different ages; the Permian-Triassic Bowen Basin and the Jurassic-Cretaceous Surat Basin, East Australia. Hydrocarbon traps in these fields occur in a complex combination of stratigraphic and structural traps [9]. Likewise, 176 storage sites have been identified by Ramirez et al. in Netherlands which are appropriate targets for porous UGS operations [14]. The majority of these suitable porous UGS sites are depleted gas fields (79%), followed by aquifers (19%), and only few (2%) depleted oil fields [14]. The major criteria to use these fields as a UGS system are minimum storage capacity, reservoir depth, thickness, porosity and permeability as well as thickness of sealing caprocks. The total storage

capacity of these 176 Dutch offshore and onshore reservoirs is about 3.2 Gt [11]. The largest field in Western Europe, Groningen gas field, has a potential of about 7 Gt, but is not included as it is not expected to be available for UGS operations before 2050 [11]. The total estimated storage capacity of offshore depleted gas reservoirs is about 900 Mt [10] and about 1.5 Mt in offshore aquifers [15]. The largest gas fields in Netherland have a storage capacity in the order of 100 Mt and are available around 2020 [14]. Similarly, depleted oil and gas reservoirs have been transformed into underground gas storage sites in China in 2010 [16]. Out of which six depleted gas fields are in Hutubi in Xinjiang province and two oil fields are Xiangguosi and Shuang6 in the Southwest oil filed and Liaohe Oilfield respectively [16].

One of the main advantages of depleted gas reservoirs is that they allow convenient and cost-effective gas storage, as they have suitable permeability properties and pore connections [13] [17]. Some vital data such as geological and geophysical characteristics, petrophysical properties, storage capacity, pressure and production history of depleted gas reservoirs, have been thoroughly studied and well recorded during development phase of the reservoir field, which enables numerical modelling to simulate the injection-production process of underground gas reservoirs [6] [13] [18]. Additionally, the surface facilities and efficient infrastructure formerly used to produce and transfer gas from depleted fields can be utilized for storage operations. According to statistics, the working gas volume accounts for about 75% of the total working gas volume of stored gas globally in UGS in depleted gas fields [13].

Water encroachment occurs in the porous reservoir vertically and laterally during the development phase of the gas reservoir. This water invasion causes lesser porous spaces in reservoir and different fluid distribution areas are formed in the longitudinal and traverse planes of the reservoir. During the injection and production operations of the gas storage, the gas-water interface moves downward when gas is injected and the moves upward when gas is produced [19]. This phenomenon can causes changes in physical properties (e.g. porosity and permeability), mechanical properties changes (Young's modulus and Poisson's ratio etc.), capillary traps, and ageing of the reservoir especially after iteration of injection/production cycles in short-term as well as long-term storage operations [20]. Due to the intense and periodic injection/production characteristics of UGS, the multiphase fluid leakage (hydraulic) phenomena differ from reservoir exploitation. Furthermore, as the foreign gas is injected in to the reservoir which has different temperature than the reservoir actual temperature, these thermal changes in the reservoir also causes some thermal stress changes in the reservoir which is not the case in reservoir exploitation phase. Therefore, this difference leads to inaccurate numerical simulations based on gas reservoir and production history data. To date, there are few studies that provide a comprehensive and systematic understanding of the injection-production capabilities and seepage characteristics of multiphase operation of UGS in depleted gas fields [13]. Therefore, it is necessary to conduct a systematic modelling study on the changes in thermal-hydraulic-mechanical properties of UGS due to repeated water intrusion and multiphase seepage rules during high-speed injection production operation. The state-of-the-art thermos-hydro-mechanical (THM) modelling provides a platform to analyze and investigate all these issues related to porous UGS system discussed above.

A thorough understanding of the pre-production stress state and its changes with time plays an important role for the safe and economic operation of hydrocarbon reservoirs and underground storage sites. The subsurface stresses affect various operational aspects such as wellbore stability, caprock integrity, stress induced material parameter changes, fault reactivation, reservoir compaction and subsidence as well as stimulation techniques like hydraulic fracturing [21] [22] [23]. Some regional information about at least one of the components of the stress tensor, i.e., the orientation of the maximum horizontal stress, can be gathered from the World Stress Map (WSM) [24]. Magnitude information concerning the three principal stresses is generally sparse. In addition, on the scale of a

reservoir both stress magnitudes and orientations can be quite variable due to lithological heterogeneities and structural complexities [25]. Thus, a tool is required which can provide a robust prognosis of the in-situ stresses in space and time, i.e., the complete stress tensor and its changes during subsurface operations, honoring the specific conditions of the hydrocarbon reservoir and storage site, respectively. Numerical modelling and, in particular, THM modelling has proven to be a very valuable tool to integrate various data sets and to investigate the thermal-hydraulic-mechanical response of a reservoir under different operational conditions throughout its life cycle [2] [23] [26] [27] [9].

The data base for such THM modelling approach is typically derived from a wide range of geological, geophysical and engineering data including field measurements, core tests, well logs, drilling, and production data. Once the numerical model has been verified by calibration data like in situ stress measurements and historical production data, it can be utilized for testing future operational scenarios like, for example, stability of new boreholes, optimal orientation of horizontal well trajectories for multiple hydraulic fracturing and subsidence due to pore pressure reduction. With respect to underground storage, THM modelling can be used, among others, to assess the ground surface subsidence, thermal stress changes, maximum safe storage capacity and maximum threshold pressure avoiding fault reactivation and maintain caprock integrity [9] [28].

This case study is the geomechanical assessment of a former depleted gas reservoir field from Molasse Basin in South Germany. The modelling study addresses the following issue related to short-term and long-term operations of UGS: (1) material properties calculation through 1D MEM approach by using well log data (2) the construction of 3D geomechanical modelling and property modelling by upscaling the material properties from 1D MEM (3) coupling of pore pressure field from the history match as well as future testing scenario cases by using dynamic fluid flow modelling. The main results of this modelling study are stress state of the field, ground surface subsidence throughout history of the reservoir, fault reactivation and thermal stress analyses; stress path changes due to short-term injection/production cycles and safe storage capacity of the gas field.

These types of THM models, particularly short-term scheduled models, have implications on Power-to-Gas technology in which simulations help to understand excess of power from renewable resources can be stored in underground gas storage reservoir and vice versa. The following chapter addresses the issues regarding PtG technologies and repercussions of considering combination with conventional underground gas storage.

## Chapter 2 Power-to-Gas

Electricity generation from renewable energies is very volatile. There is a surplus of photovoltaic energy during the daytime because the demand is lower. However, there is not enough installed capacity to store the electricity during this surplus period. Currently, storage is expensive, which makes it difficult to solve this surplus problem, and this surplus causes an imbalance in the system. However, it is possible to store the surplus electricity via Power-to-Gas and use it in gas-fired power plants. These plants will help to replace coal-fired power plants. Consequently, the goals of security of supply and grid stability can be achieved by sharing gas and electricity [29] [30].

In the future, a connection/unification between gas and electric energy systems is possible. There are differences between the gas and electricity energy systems, but this does not mean that the differences between these two energy systems cannot be overcome. There are some areas that can promote the fusion between the gas and electricity systems. These areas are innovative information technology, improved grid capacity, the continuous increase of renewable energy and modern gas systems. In addition, it will be beneficial to eliminate market competition between gas and electricity systems. These two sectors should be considered as partners. In this way, both sectors can improve their capabilities and services [30].

When the structure is fully connected with advanced technologies and control systems, the excess electricity can be used to generate gas that can be pumped into the gas grid. In this way, energy is transferred from electricity to gas. In addition, the gas produced can be stored and is relatively cheaper than electricity. A reverse process is also possible. In this case, the gas can be used in gas-fired power plants to generate electricity, which can reduce the load on the transmission and distribution networks. This load reduction helps to increase reliability and reduce the risk of power outages [31].

### 2.1 Perceived role of Power-to-Gas and Gas-to-Power

Power-to-Gas (PtG) could be one of the solutions to the fluctuations in renewable energy system. This problem can be solved by converting surplus electricity into hydrogen or synthetic natural gas and creating a coupling interface between the gas and electricity systems [31]. The converted gas is then fed into the gas grid via the existing gas infrastructure (Figure 2-1).

This gas can be used in combined heat and power (CHP) plants to supply local and district heating networks. Exegetically, electricity should always be fed into the power grid as electricity, if possible, which represents the highest efficiency of the power grid. However, if problems occur in the electricity sector (e.g. bottlenecks, negative electricity prices or physical damage) or if there is no electricity infrastructure at the production site, the electricity can be converted into hydrogen. This hydrogen can then be fed directly into the underground gas storage or used as a gas network in the various industries (Figure 2-2). This can be stored in a hydrogen buffer to be converted back into electricity later or converted into methane. Conversion to methane can be useful whenever hydrogen injection into the gas grid is preferred but is limited by hydrogen specifications. Another reason for using Power-to-Gas could be to overcome capacity bottlenecks in continuous transmission (grid-specific) or to transport energy over long distances. In this case, the electricity is continuously converted into hydrogen or hydrocarbons. The pathways from electricity to one of the above end products are shown in Figure 2-1.

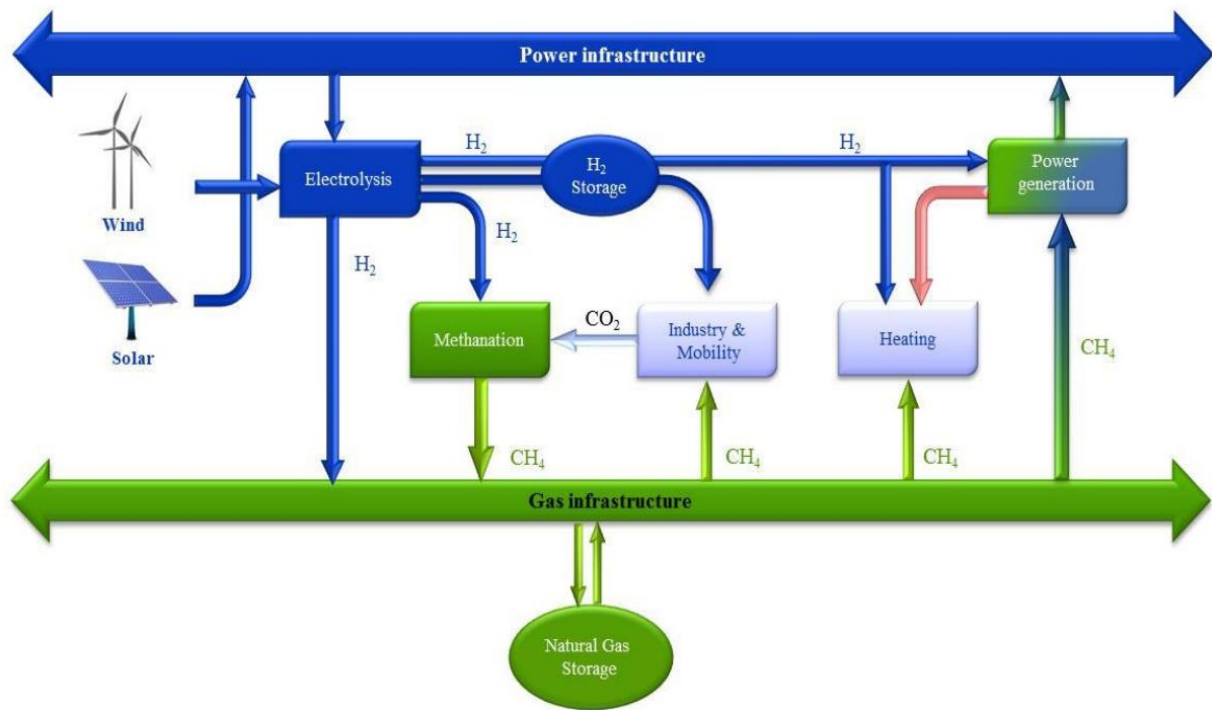


Figure 2-1: Schematic diagram of PtG concept [29].

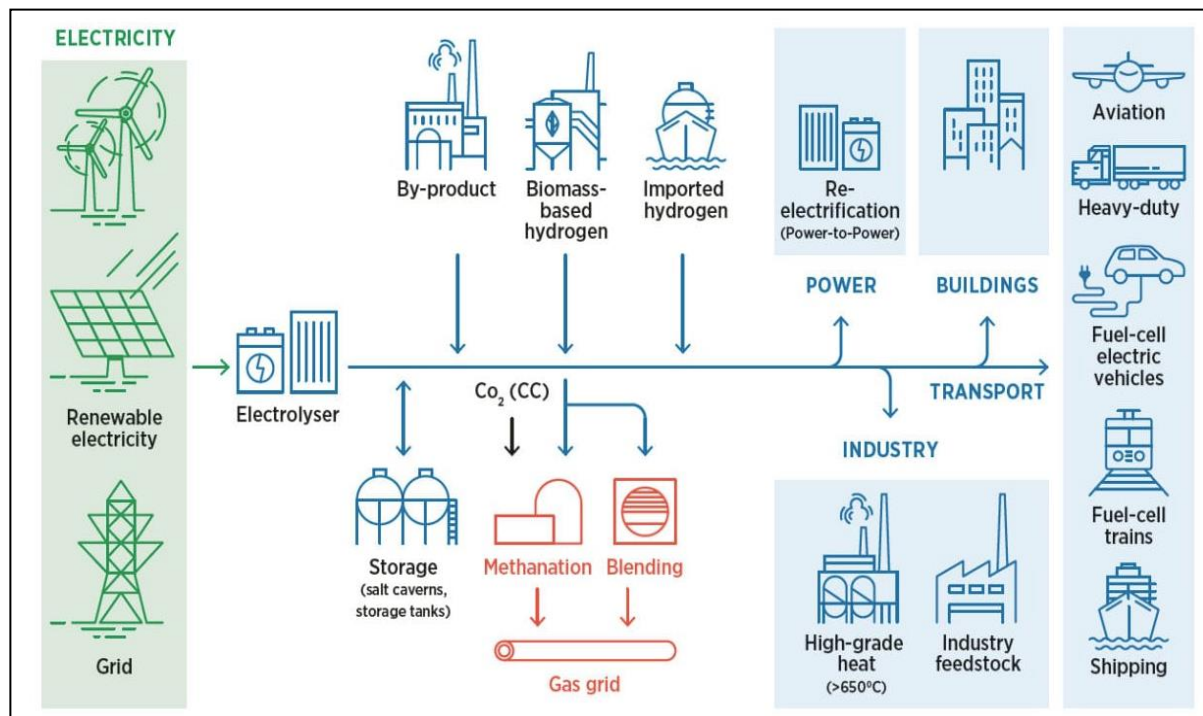


Figure 2-2: Concept of PtG and its usage in various industries [32].

Due to restrictions on the injection of hydrogen into natural gas reservoirs, the potential storage capacity of hydrogen in the gas infrastructure is significantly lower than the total storage capacity of methane [29].

Power-to-Gas differs from electricity storage technologies in that gas (hydrogen or methane) is produced as an intermediate product. This gas can then be further processed as gas or converted back into electricity. There are generally two options for re-conversion to electricity: (1) hydrogen from



electrolysis is stored and converted back into electricity by a fuel cell, or (2) hydrogen/methane is accommodated in the gas infrastructure and converted back into electricity by conventional (existing) gas power plants.

The amount of electricity required is also determined by the technologies used to electrify the individual energy sectors. The amount of energy lost when converting one type of energy into another (e.g. in PtG and GtP processes or when charging a battery) is only characteristic of the respective process. The conversion efficiency of using electricity to produce hydrogen (electrolysis) and then using this hydrogen to produce electricity is 40 %, which means that 60 % of the electricity produced is lost in the conversion process [33]. Since electricity supports the use of heat from the outside air, the ground (geothermal energy), or groundwater, an electric heat pump has an efficiency of 285 % in the heating sector. The conversion efficiency of a hydrogen fuel cell heating system is higher and is around 45 %, while the corresponding value for a heating system powered by renewable gas (methane) is 50 % [33].

### 2.2 Electrolysis and Methanation

The first step in converting electricity into hydrogen is inevitably through water electrolysis with the technology available today. The Power-to-Gas production chain consists of electrolysis and, if necessary, methanation. Electrolysis is the conversion of electricity into hydrogen. There are various possible ways of producing hydrogen. When hydrogen is converted into methane or other hydrocarbons, a carbon source (e.g. CO<sub>2</sub>) is required for the synthesis. Methanation is the synthesis of hydrogen and carbon dioxide into methane. Various synthesis methods are available, e.g. the Fischer-Tropsch process or methanol synthesis. The energy efficiency of the different processes reduces from hydrogen to methane to liquid fuels [34].

However, methane (PtG-M) is currently very expensive and uneconomical, which is a hindrance on the way to cost competitiveness with natural gas. A catalytic isothermal methanation technology is commercially marketable for methanation [35]. On the other hand, biological methanation has the potential to reduce costs but faces technical barriers to large-scale implementation. Hydrogen is produced in electrolysis, which contains water, electrodes and an electrolyte material. An electric current flows through these materials. The ion transfer from one part to the other is ensured by the electrolyte material. During this process, hydrogen and oxygen are produced independently at the cathode and the anode. The electrolyzer consists of a rectifier, a water demineralization unit, a water pump and cooling system, a hydrogen purification unit and instrumentation [35]. There are three methods for producing hydrogen by electrolysis:

1. Alkaline Electrolysis Cells (AEC)
2. Proton Exchange Membrane Electrolysis Cells (PEM-EC)
3. Solid Oxide Electrolysis Cells (SOEC).

At present, alkaline technology for water electrolysis is the most mature and economical technology for hydrogen production, while PEM electrolysis is an immature and expensive technology.

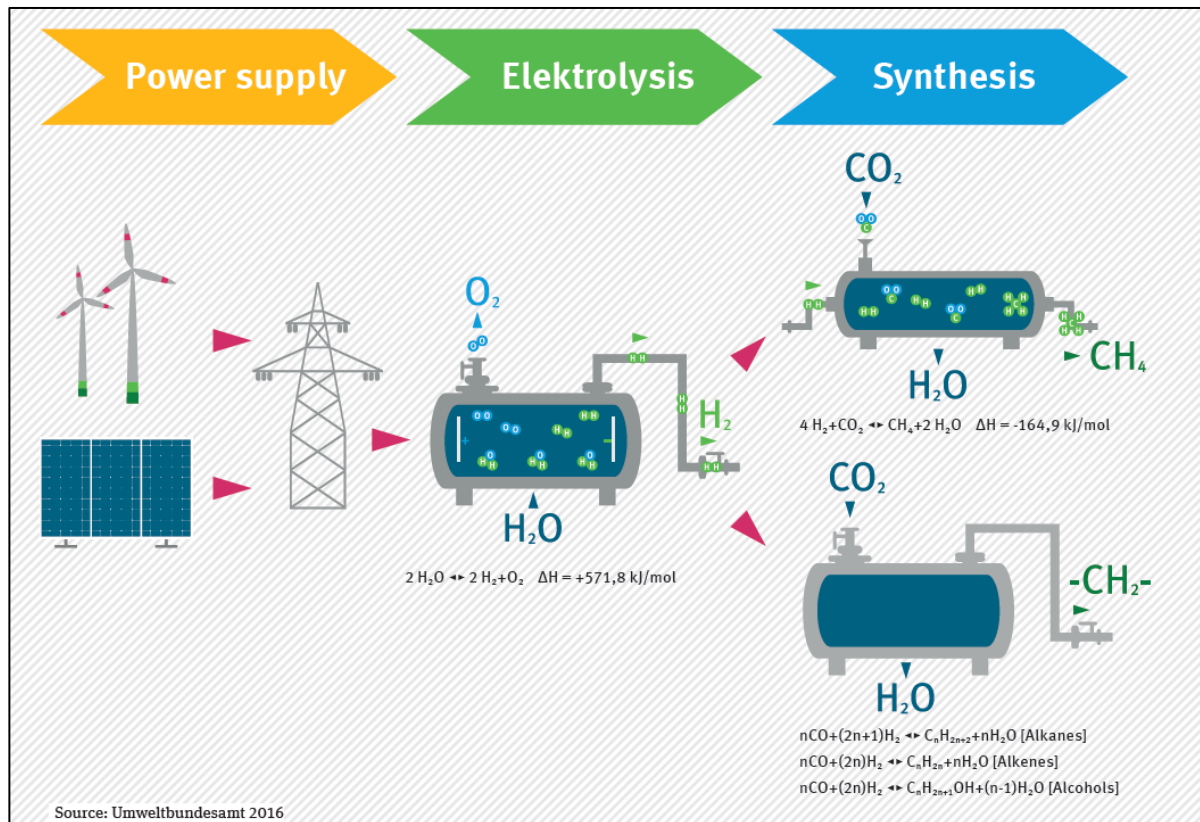


Figure 2-3: Working principle of PtG and governing chemical processes of electrolysis and methanation [35].

### 2.3 Power-to-Gas in Germany

In Germany, considerable flexibility potential is available in the national gas infrastructure and is already being used for external balancing energy. However, for a complete integration of the flexibility potential of natural gas, the balancing structures of gas and electricity must be coordinated. Moreover, the short-term exchange market, i.e. the hourly or quarter-hourly market, should also be coordinated [30].

In Germany, 17 pilot and demonstration projects have been launched since 2004 to research Power-to-Gas. The aim of the research is to link PtG with the energy transition. Currently, the "Energy Park Mainz" project (hydrogen feed-in to the grid) and the "E-Gas" project (SNG production for mobility) are the two major power-to-gas projects in Germany. The historical development of Power-to-Gas projects from concept to industrial demonstration is shown in Figure 2-4 [35].

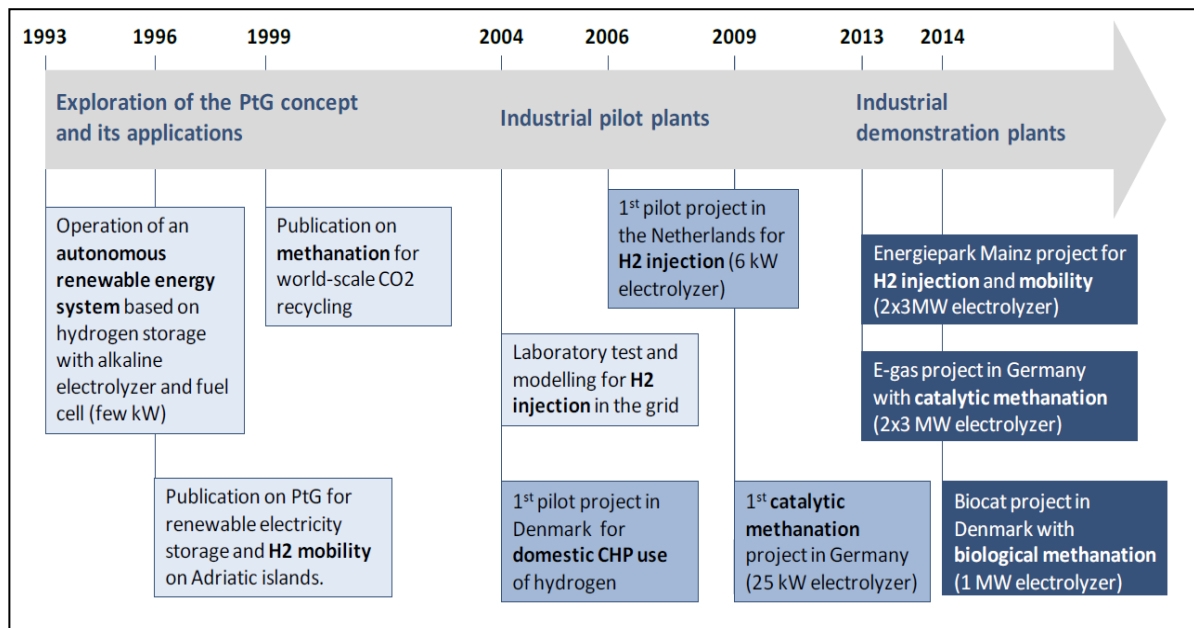


Figure 2-4: Power-to-Gas development in Europe [35].

Germany has set itself the goal of becoming a greenhouse gas neutral land (GHGND) by 2050. PtG can contribute to achieving the goal of a completely greenhouse gas neutral energy supply in the system. According to the climate protection and Umweltbundesamt (UBA) study "Germany in 2050 - A Greenhouse Gas Neutral Country" (GHGND), greenhouse gas emissions are to be reduced. The goal is to reduce them by 95 % by 2050 compared to the level of the 1990s. This goal can only be achieved if the energy supply is based entirely on renewable energies. Power-to-Gas (PtG) can be a renewable energy source. In addition, the increasing competitive pressure on biomass can be relieved through the use of PtG [36]. In the GHGND case, the final energy demand in Germany would be about 1600 TWh in 2050. This final energy demand is distributed between electricity, methane and liquid fuels (Table 2-1). To meet this final energy demand, generation capacity would need to be around 3000 TWh [34]. This target can be achieved in Germany due to the combination of the current technical capacity of installed renewable energies and the additional renewable projects planned for the future.

Table 2-1: Energy Requirements in the GHGND Scenario for Germany [36].

	Electricity in TWh	Renewable methane in TWh	Liquid renewable fuels in TWh
Private households	104.7	44.5	0
Commercial, trade and services	90.3	62.4	18.6
Industry	179.7	198	0
Transport	91.1	0	533.3
Total energy	465.8	305.7	551.9
Sum of total energies	1323.4		

Industry material use		282	
Total energy and material	1605.4		

## 2.4 Economic conditions of Power-to-Gas in Germany

At present, Power-to-Gas technology is uneconomical in Germany. This is because high investment requirements and high operating costs, conversion losses and higher taxes and levies combine to create an unfavorable scenario for Power-to-Gas [34]. Besides, power-to-gas cannot compete with natural gas. Power-to-Gas can only be profitable if the CAPEX of Power-to-Gas for grid feed-in decreases by a factor of 2 and electricity prices should be very low. Reducing CAPEX is possible to some extent through R&D efforts in electrolysis and methanation and through cost optimization (e.g. shared infrastructures, standardisation of processes and equipment), but it is still a very difficult goal [35]. Furthermore, the possibility of reducing electricity prices to as low as €15/MWh requires high shares of wind and solar energy.

Power-to-Gas plants that use renewable energy sources to produce hydrogen and methane and feed them into gas grids are granted access to the gas grid and to gas grid tariffs. This is an advantage for Power-to-Gas plants under the regulations for gas grid connections. However, the disadvantage could also come in the form of higher costs if the source of carbon input in Power-to-Gas plants is included in emissions trading, in which case the plants have to report and submit allowances under the EU Emissions Trading Scheme. This can increase the cost factor [32] [35].

Pumped water storage or compressed air storage are the types of Power-to-Gas energy storage facilities. The German law on the promotion of electricity generation from renewable energies allows exemption from the apportionment for these energy storage facilities. However, these storage facilities must pay grid fees and connection costs. These additional costs make these storage facilities uneconomical from an economic perspective [32] [35].

The cost factor plays a decisive role for PtG plants. However, these cost factors, such as future investment costs, additional costs and operating costs, depend on the demand for electricity for PtG plants. However, the demand for these plants depends on many factors, such as the global development of greenhouse gas-neutral energy supply, climate policy and its impact on carbon prices, the future technical growth of PtG plants, the development of electricity prices, the availability of sources of concentrated carbon dioxide, etc. However, the costs of PtG will be higher in the short and medium term than other technologies using renewable energy sources such as power-to-heat, etc. [34].

## 2.5 Synergy between Power-to-Gas and Gas-to-Power

A synergy and coupling interface between gas and electricity systems will enable the transmission of energy via a smart macro grid. This grid consists of a smart gas grid, a coupling interface between them and a control system. Gas Smart Grid is a dynamic gas network. It is composed of metering and control systems. This control system is integrated with remote processing systems. These remote control systems operate in real time. In addition, these systems perform functions such as connecting/disconnecting gas sources. In addition, smart gas grids should be able to control bidirectional gas flow and gas/energy storage in the future. The structure of this smart macro-grid focusing on the coupling interface is shown in Figure 2-5 [31].

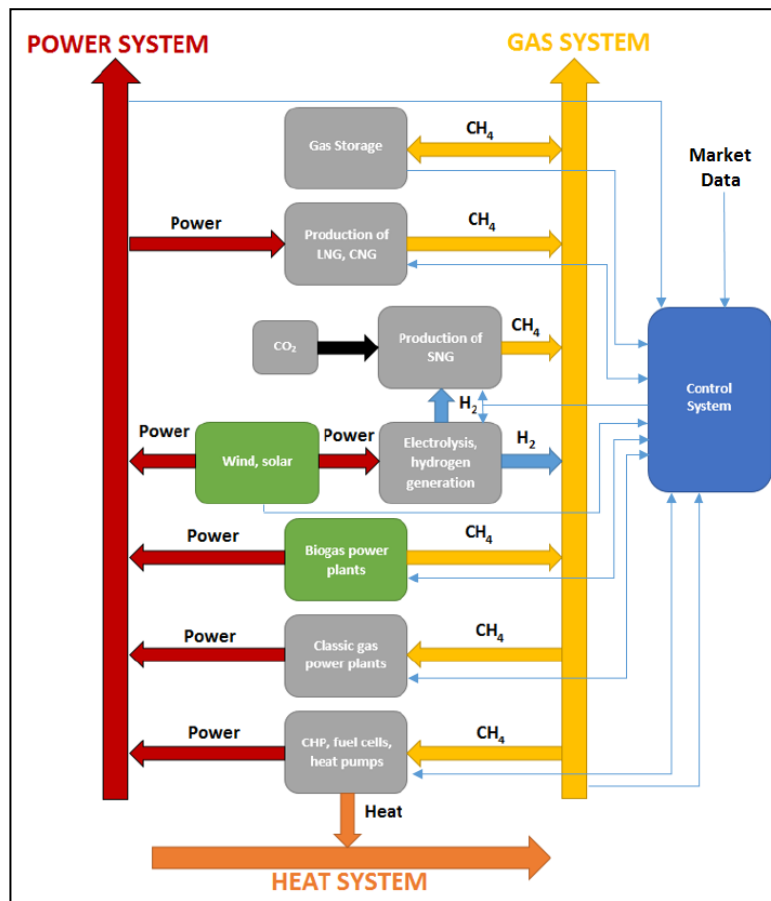


Figure 2-5: Coupling interface for gas, power and heat Systems [30].

This structure required fast communication for receiving and sending a large amount of data. Therefore, advanced network technologies such as the Internet of Things (IoT) should be used. The Internet of Things (IoT) makes it possible to connect all different types of computers, sensors and actuators, etc. and helps build the control system. This control system monitors discrepancies in the power grid (power shortage and power surplus). In case of power shortage, the control system automatically checks the amount of gas stored to generate electricity through gas-fired power plants or CHP plants. In the case of a power surplus, the control system will signal whether it is possible to inject additional hydrogen or natural gas into the gas grid. Although the focus of the control system is on balancing the electricity grid, it also helps optimize profit [31].

## Chapter 3 Methodology

The following section describes the different steps to carry out THM modelling approach. The workflow and modelling approach is based on the work of Henk et al. [26] [37] [38]. The data described in the section 4.2 have been used to achieve and validate elastic properties and stress state of the 3D geomechanical model which extends over tens of square kilometers. The aim of the different modelling approaches is to optimize the usage of different data sets. In particular, this includes the construction of 1D and 3D models using well logs and seismically derived data as well as PVT data for dynamic fluid flow model.

The entire modelling workflow for a THM coupled reservoir simulation is illustrated in Figure 3-1. It starts with 1D modelling of individual wells to calculate mechanical properties from log data. The 3D model comprising the reservoir along with underburden, overburden and sideburden formations is built using a structural/geological model which is typically based on seismic and borehole data. Upscaling of hydromechanical properties from the various 1D mechanical earth model (MEM) to the 3D MEM can be achieved through geostatistical methods such as Gaussian and Kriging interpolation methods [39]. The pore pressure field in the model domain is calculated by a fluid flow simulation which uses the same structural/geological model as the 3D MEM. Mechanical and hydraulic calculations are coupled via pore pressures and effective stresses leading to deformation which in turn affects porosity and permeability. Both the 3D MEM and the fluid flow model need to be calibrated by comparing calculation results to observational data, e.g., in situ stress measurements and historical production data. Once both approaches have been validated, the coupled model can be used to study potential future injection-production schedules like the seasonal cycles typical for underground gas storage or more frequent cycles to cover short-term variations in demand and supply.

Modelling outlines below utilize the Schlumberger software suite, i.e., Petrel for geological modelling, Techlog<sup>®</sup> for 1D MEM, ECLIPSE<sup>™</sup> for fluid flow modelling and Petrel RG (VISAGE<sup>™</sup>) for 3D MEM. Geomechanical modules of Techlog<sup>®</sup> and Petrel RG provide the user interface for geomechanical analysis and various elastic properties calculation correlations and methods. ECLIPSE<sup>™</sup> is the standard industry software to provide pore pressure evolution of the reservoir throughout its operating history and future testing scenarios. All these Schlumberger software suites can be coupled to perform THM simulations.

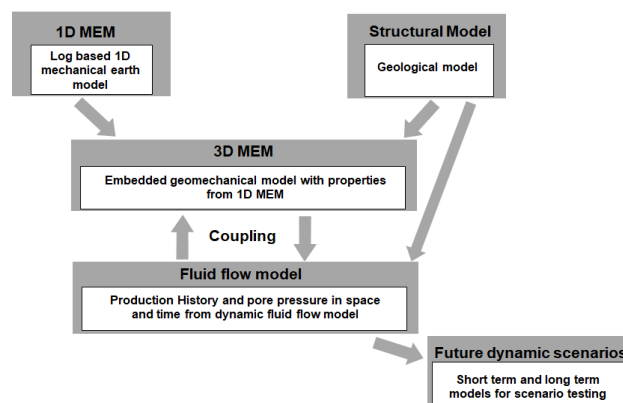


Figure 3-1: Flowchart illustrating the complete THM modelling workflow [37].

### 3.1 1D Mechanical Earth Modelling (1D MEM)

Rock mechanical properties and stress tensor with magnitude and orientation of in-situ stresses play a vital role in petroleum exploration and storage industry particularly material properties in order to control fluid flow in clastic and naturally fractured reservoir, wellbore stability and drilling operations. 1D mechanical earth modelling (1D MEM) is the numerical representation of rock mechanical properties and state of in situ stresses in a stratigraphic section of a wellbore [40]. Therefore, well log data is used to obtain various material properties and estimates for pore pressure and in situ stress along a wellbore section assuming a poro-elastic approach. The quality of a 1D MEM model depends on the availability of a large amount of well log data and the availability of laboratory tests on cores for calibration. The complete 1D MEM modelling scheme is presented in Figure 3-2 [37].

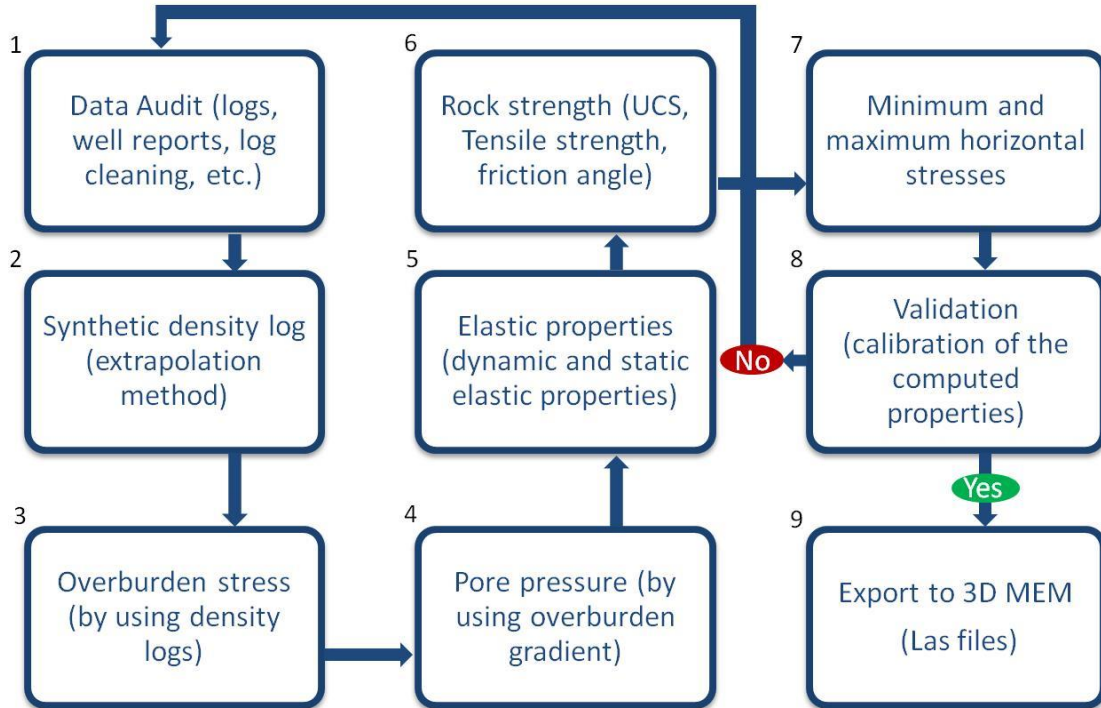


Figure 3-2: Step by step 1D MEM workflow for computing material properties, pore pressure and stresses for a single well [37].

#### 3.1.1 Vertical (overburden) stress

The 1D MEM process starts with the overburden stress calculation based on density information. The overburden stress is also an essential parameter to estimate pore pressure throughout the well section. If a density log is readily available, the vertical stress or overburden stress can be determined according to

$$S_v = \int_0^z \rho(z)g dz \approx \bar{\rho}gz \quad (1)$$

Where  $S_v$  is the vertical stress,  $\rho(z)$  is the bulk density at depth  $z$  below the earth's surface,  $g$  is the gravitational acceleration and  $\bar{\rho}$  is the average density of the total overlying rock formation [41] [27]. Thereby, well information such as elevation and air gaps must be available in order to generate a complete density curve of a well from top to bottom. In case density log data is missing or incomplete,

which frequently is the case especially for old wells, the data gaps must be filled first with synthetic densities which can be obtained by using several empirical correlations to other log parameters [41]. The extrapolation density method can be used in order to fill the air gap between bulk density logs in the computing process of overburden stress. The method provides an opportunity to make a synthetic density profile which is extrapolated up to the mudline by using information like true vertical depth (TVD), air gap and water depth (eq. 2). The combination of both extrapolated (synthetic density) and bulk densities integrate the splice density to compute the overburden stress.

$$\rho_{extrapolated} = \rho_{mudline} + A_0 * (TVD - AirGap - WaterDepth)^{\alpha_f} \quad (2)$$

Where  $\rho_{extrapolated}$  is the extrapolated synthetic density,  $A_0$  and  $\alpha_f$  are the fitting parameters,  $\rho_{mudline}$  is the density at the sea floor (offshore) or ground level (onshore) and  $TVD$  is the true vertical depth [41].

### 3.1.2 Pore Pressure

The pore pressure is a key parameter for the 1D MEM and required to determine effective stresses. The most reliable method is the direct measurement of pore pressures through wireline formation testing tools. These measurements are typically performed in reservoirs if liquid samples are taken with a wireline formation tester. Advanced technology allows the in-situ pore pressure to be measured while drilling. Using these tools on shale rock to obtain correct data is almost impossible because of their low permeability and porosity. Often the only data available before drilling is seismic data that can be used for pre-drilling estimates. These estimates are further enhanced with the data obtained from drilling. In the absence of direct measurements, empirical modelling based on well log data can be used to determine pore pressure. Various methods and correlations have been put forward to get a pore pressure profile [41], but the most popular one providing reasonable results is Eaton's method [42].

#### 3.1.2.1 Eaton's Method

The technique was originally developed for over-pressured shales in the Gulf of Mexico [42]. The method is standard in oil and gas industry to estimate pore pressure using a semi-logarithmic or linear normal trend line. This method depends on the Terzaghi's equation (eq. 3) which states that if a rock is subjected to stress, in this case vertically, the stress is counteracted by the fluid pressure of the pores in the rock, which is the pore pressure [43]. This means that the pore pressure must be subtracted to obtain the effective stress acting on the rock. The relationship between effective stress ( $S_{effec}$ ), overburden or vertical stress ( $S_v$ ) and pore pressure ( $P_p$ ) has been explained in Figure 3-3.

$$S_{effec} = S_v - P_p \quad (3)$$

Either compressional slowness from sonic logs (eq. 4) or resistivity from corresponding electric logs (eq. 5) can be used to calculate pore pressure by using Eaton's method.

$$P_p = S_v - (S_v - H_g) * \alpha_E * \left(\frac{\Delta t_n}{\Delta t}\right)^n \quad (4)$$

$$P_p = (S_v - H_g) \left(\frac{R_{log}}{R_n}\right)^n \quad (5)$$

Where,  $P_p$  is the pore pressure,  $S_v$  is the overburden gradient,  $H_g$  is hydrostatic gradient,  $\Delta t_n$  and  $R_{log}$  are compressional slowness in shales at normal pressure and resistivity log respectively, corresponding to the normal compaction trend and  $n$  is the Eaton exponent 1.2 when using the resistivity log and 3.0 for the velocity log and  $\alpha_E$  is the Eaton factor [42].



The pore pressure is determined here primarily on the basis of the deviation of the log measurements from the normal compaction trend. This trend is an estimate of how the velocity or resistivity would have been if the pore pressure had been normal, i.e. hydrostatic, hence the hydrostatic pressure gradient shown in the equations. It represents the optimally fitted linear trend of the measured data in the low permeable layers. The correct adjustment of the normal compaction trend is crucial for the result of the model [33].

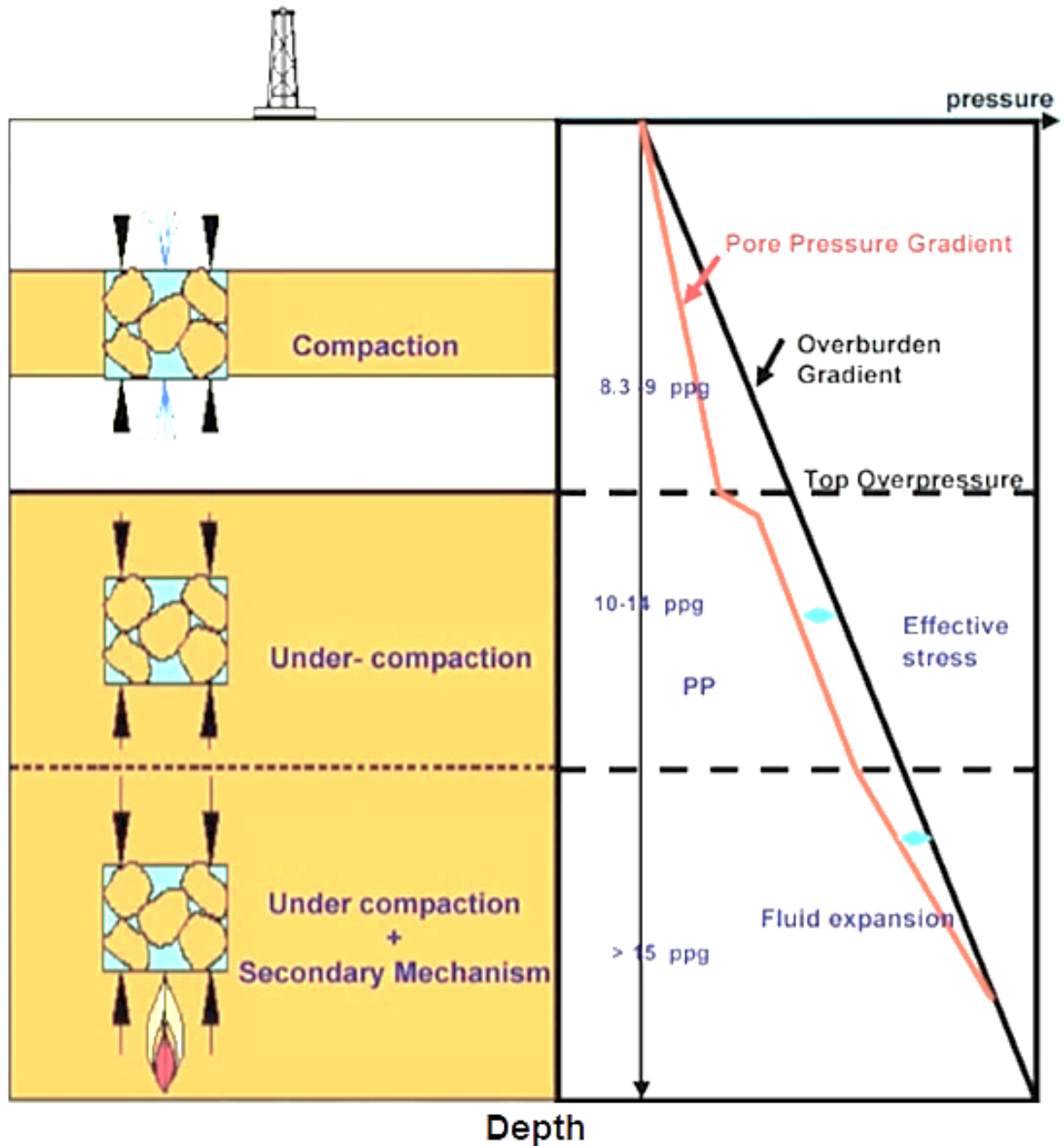


Figure 3-3: The relationship between effective stress, overburden stress and pore pressure with respect to compaction along with depth [44].

### 3.1.3 Elastic properties

Static elastic properties required for geomechanical modelling such as the Young's modulus, Poisson's ratio, shear and bulk moduli as well as the Biot coefficient have to be obtained from core analysis and laboratory measurements, respectively. However, core data is frequently very limited and – if available at all – confined to the reservoir proper and the immediate overburden (caprock). However, MEM requires information for the entire overburden and at least part of the underburden section. A continuous set of at least dynamic elastic properties can be computed from specific logging data. Though these dynamic properties do not yet reflect the static properties actually required, they can be transferred by lithology-dependent empirical correlations whose applicability can be crosschecked at calibration points (if lab tests on cores are available). As the dynamic properties are taken at high frequencies with small strain amplitudes, the dynamic elastic moduli obtained are within the elastic regime. On the other hand, large strain amplitudes have to be applied on the core during loading to measure static elastic moduli in laboratory testing. Some of these strains are irreversible therefore the moduli are not purely elastic but already comprise a certain part of plastic deformation. Hence the static moduli are always smaller than the dynamic elastic moduli because the static strains are eventually higher than dynamic strains [45].

In addition to the density data described above, computation of the dynamic elastic properties requires special sonic logs which provide compressional as well as shear wave slowness. The following equations can be used to derive dynamic elastic properties from sonic log data (eq. 6, eq. 7, eq. 8 and eq. 9) [41].

$$v_d(\Delta t_s, \Delta t_c) = \frac{\rho_b * ((3/\Delta t_c^2) - (4/\Delta t_s^2))}{\Delta t_c^2 * (1/\Delta t_c^2) - (1/\Delta t_s^2)} \quad (6)$$

$$E_d(\Delta t_s, \Delta t_c) = \frac{\rho_b * ((3/\Delta t_c^2) - (4/\Delta t_s^2))}{\Delta t_c^2 * (1/\Delta t_c^2) - (1/\Delta t_s^2)} * (10)^{-12} \quad (7)$$

$$G = \rho_b * V_s^2 \quad (8)$$

$$K = \rho_b * V_p^2 - \frac{4}{3} G \quad (9)$$

In these equations,  $v_d$  is the dynamic Poisson's ratio,  $E_d$  is the dynamic Young's modulus in Pa,  $\Delta t_c$  is compressional wave interval transit time in s/m,  $\Delta t_s$  is shear wave interval transit time in s/m and  $\rho_b$  is the bulk density in g/cm<sup>3</sup>,  $\Delta t_s$  is the shear wave slowness in s/m [41],  $G$  is the shear modulus in Pa,  $K$  is the bulk modulus in Pa and  $V_p$  and  $V_s$  are in m/s [41].

The static elastic properties are essential to calculate geomechanical deformations and can be computed by conducting empirical modelling of dynamics properties through numerous empirical correlations depending upon the lithology of the formation. These can be calculated by using various empirical correlations (Table 3-1) [46]. In these equation  $E_s$ ,  $E_d$  and  $UCS$  are in Pa,  $\rho$  is in g/cm<sup>3</sup>, and  $V_p$  is in m/s.

Table 3-1: Various empirical correlations for calculating elastic Young's modulus [46].

Lithology	Empirical Correlation	Reference
Igneous and metamorphic	$E_s = 1.263E_d - 29.5$	King, 1983
Sedimentary	$\log(E_s) = 0.02 + 0.7\log(\rho E_d)$	Eissa and Kazi, 1988
Sedimentary	$E_s = 0.018(E_d)^2 + 0.422 E_d$	Lacy, 1997
Soft rocks ( $E_s < 15\text{GPa}$ )	$\text{UCS} = 2.28 + 4.0189E_s$	Bradford et al., 1998
Hard rocks ( $E_s > 15\text{GPa}$ )	$E_s = 0.4145E_d - 1.0593$	Wang, 1999
Shale	$E_s = 0.076(V_p)^{3.23}$	Horsrud, 2001
Shale	$E_s = 0.0158(E_d)^{2.74}$	Ohen, 2003
Mudstone	$E_s = 0.103 (\text{UCS})^{1.086}$	Lashkaripour, 2002
Limestone	$E_s = 0.541E_d + 12.852$	Ameen et al., 2009

### 3.1.3.1 Shear wave velocity calculation

In the absence of shear wave slowness, i.e., if only the standard compressional sonic log is available, the Greenberg and Castagna correlation [47] (eq. 10) can be used accordingly:

$$V_s = 0.8042 V_p - 855.9 \quad (10)$$

Where  $V_s$  is the shear wave velocity and  $V_p$  is the compressional wave velocity, i.e., the inverse of the compressional wave slowness. The correlation determines the shear wave velocity for both water-saturated and dry siliclastic sedimentary rocks is almost linearly related to the compressional wave velocity [48]. Mudrocks tend to have slightly higher compressional wave to shear wave velocity ratio ( $V_p / V_s$ ) than clean porous sandstones for a given  $V_p$  [48]. The ratio is almost constant in dry sandstones. In wet sandstones and mudstones, the ratio tends to decrease with increasing  $V_p$  [48].

The water-saturated linear  $V_p$ -versus- $V_s$  trend starts with  $V_p$  a little less than water velocity and  $V_s = 0$ , and it ends at the compression and shear wave velocities of quartz [48]. The dry sandstone linear  $V_p$ -versus- $V_s$  trend starts at zero velocity and ends at the velocity of quartz. Bulk modulus and dry rigidity are about equivalent. Theoretical models based on regular packaging arrangements of spheres and on cracked solids yields  $V_p$ -versus- $V_s$ , trends consistent with observed dry and wet trends [48].

According to Castagna et. al, the observed  $V_p$ -versus- $V_s$  relation for wet siliclastic rocks result from the coincidental location of the quartz and clay points [48]. The simple sphere packing models indicate that the trends with low velocity and high porosity are largely independent of the mineral elastic properties. Since the porosity is close to zero, the velocities must essentially approach the values for the pure mineral [48].

### 3.1.3.2 Biot Coefficient

The Biot coefficient is another important parameter to describe the compressibility of rock material that can be calculated from the static bulk moduli of the dry skeletal frame and the rock material (eq. 11) [49].

$$\alpha = 1 - \frac{K_{dry}}{K_{solid}} \quad (11)$$

Where  $\alpha$  is the Biot coefficient,  $K_{solid}$  is the static bulk modulus of the rock material and  $K_{dry}$  is the static bulk modulus of the dry skeletal frame.

### 3.1.4 Strength parameters

Rock strength parameters define resistance of rock against loading and unloading. Unconfined compressive strength, tensile strength and friction angle (see below) are the significant parameters to address wellbore stability and other geomechanical problems during drilling, estimate sanding potential as well as stress magnitudes to avoid wellbore failure. The indirect estimation of these parameters is also possible by using various correlation methods (Table 3-2) [50]. In these equations,  $UCS$  is in Pa,  $V_p$  is in m/s,  $\Delta t$  is in s/m and  $E_s$  is in Pa.

Table 3-2: Various correlations to estimate unconfined compressive strength (UCS) depending upon the lithology of rock formation [50].

Lithology, location	UCS correlation
Sandstone, Thuringia, Germany	$UCS = 0.035V_p - 31.5$
Sandstone, Bowen Basin, Australia	$UCS = 1200 \exp(-0.036 \Delta t)$
Sandstone, Gulf Coast	$UCS = 1.4138 \times 10^7 (\Delta t)^{-3}$
Sandstone, Cook Inlet, Alaska	$UCS = 1.745 \times 10^9 \rho(V_p)^2 - 21$
Sandstone, Australia	$UCS = 42.1 \exp\{1.9 \times 10^{-11} \rho(V_p)^2\}$
Sandstone, Gulf of Mexico	$UCS = 3.87 \exp\{1.14 \times 10^{-10} \rho(V_p)^2\}$
Sandstone	$UCS = 46.2 \exp(0.027E_s)$
Sandstone, Worldwide	$UCS = 2.28 + 4.1089E_s$
Sandstone, Worldwide sedimentary basins	$UCS = 254 (1 - 2.7 \phi)^2$
Sandstone	$UCS = 277 \exp(-10 \phi)$
Shale, North Sea	$UCS = 0.77 (304.8/\Delta t)^{2.93}$
Shale, Gulf of Mexico	$UCS = 0.43 (304.8/\Delta t)^{3.2}$
Shale, Worldwide	$UCS = 1.35 (304.8/\Delta t)^{2.6}$
Shale, North Sea	$UCS = 2.922 \phi^{-0.96}$
Shale	$UCS = 0.286 \phi^{-1.762}$
Limestone and Dolomite	$UCS = (7682/\Delta t)^{1.82}/145$
Limestone	$UCS = 13.8 E_s^{0.51}$
Dolomite	$UCS = 25.1 E_s^{0.34}$
Limestone and Dolomite, Russia	$UCS = 276(1 - 3\phi)^2$
Limestone and Dolomite, Middle East	$UCS = 143.8 \exp(-6.95\phi)$

Bradford [51] has proposed a correlation of unconfined compressive strength with static Young's modulus (eq. 12) for soft formation (Young's modulus <12 GPa) that can be used to calculate UCS for sandstone reservoir.

$$UCS = 2.28 + 4.1089E_s \quad (12)$$

Where,  $UCS$  and  $E_s$  are the unconfined compressive strength and static Young's modulus respectively.

Tensile strength is considered to be 1/10th of the  $UCS$ , if the Bradford correlation [51] has been used to compute  $UCS$  from static Young's modulus [52]. Friction angle ( $FANG$ ) can be estimated by using Gamma ray log and porosity; it uses the Plumb's correlation (1994) (eq. 13).

$$FANG = 26.5 - 37.4(1 - \phi - V_{clay}) + 62.1(1 - \phi - V_{clay})^2 \quad (13)$$

Where  $FANG$  is friction angle,  $\phi$  is porosity and  $V_{clay}$  is volume of clay. It uses gamma ray log to estimate  $V_{clay}$ . In the absence of porosity log, compressional slowness ( $DTCO$ ) can be used to compute the porosity log by using Wyllie's correlation [53] (eq. 14).  $V_{clay}$  is in  $cm^3$  and  $DTCO$  is in s/m.

$$\phi = \frac{DTCO - 47.8549}{21371.5414 - 47.8549} \quad (14)$$

#### 3.1.5 Horizontal stresses

The stress states in the earth are quantified with the help of stress tensors. The components of these tensors are tractions acting perpendicularly or parallel to three orthogonal planes. The normal to these three planes form a Cartesian coordinate system with the axes  $x_1$ ,  $x_2$  and  $x_3$  so every point in space can be identified. There are three normal stresses out of nine components of tensors that act perpendicular to a plane ( $S_{11}$ ,  $S_{22}$ ,  $S_{33}$ ), and the other six are shear stresses acting along a plane. These relationships are shown in Figure 3-4. There is a specific alignment of the stress axes at each point in space where all shear stress components are zero. These directions are referred to as "principal stress directions". The three stresses along these directions are called principal stresses  $S_1$ ,  $S_2$  and  $S_3$  where  $S_1$  is the greatest principal stress,  $S_2$  is mean principal stress and  $S_3$  is least principal stress [54].

Among two horizontal stresses one is larger than the other and called maximum horizontal stress  $S_{Hmax}$  and smaller one is minimum or least horizontal stress  $S_{Hmin}$ . The relative magnitudes of the three principal stresses depend on the faulting regime. For instance, in the normal faulting regime the vertical stress is greater than the maximum horizontal stress which is then greater than the minimum horizontal stress. In a strike-slip faulting regime the maximum horizontal stress has become larger than the vertical stress but the minimum horizontal stress remains below it. If the horizontal input is so large that the vertical stress is the smallest principal stress, a reverse faulting regime is present. The relation of the principal stresses to the faulting regime is explained in Figure 3-5.

The horizontal stresses can be estimated based on a poroelastic approach [55]. It uses static elastic properties such as Young's modulus  $E$ , Poisson's ratio  $\nu$ , Biot coefficient  $\alpha$  as well as overburden stress  $S_v$  and pore pressure  $P_p$ . The tectonic contribution (in addition to loading by gravitation only) on the magnitude of the horizontal stresses (eq. 15 and 16) is considered applying  $\epsilon_h$  and  $\epsilon_H$  which represent the strains in the direction of the minimum and maximum horizontal stress, respectively.

Calculated maximum and minimum horizontal stresses can be calibrated by tuning both horizontal strains according to leak-off test (LOT) and wellbore stability prediction versus borehole failure observation [41] [55].

$$S_{Hmin} = \frac{\nu}{1-\nu} S_v - \frac{\nu}{1-\nu} \alpha P_p + \alpha P_p + \frac{E}{1-\nu^2} \epsilon_h + \frac{\nu E}{1-\nu^2} \epsilon_H \quad (15)$$

$$S_{Hmax} = \frac{\nu}{1-\nu} S_v - \frac{\nu}{1-\nu} \alpha P_p + \alpha P_p + \frac{E}{1-\nu^2} \epsilon_H + \frac{\nu E}{1-\nu^2} \epsilon_h \quad (16)$$

In above equations,  $S_{Hmin}$  and  $S_{Hmax}$  are minimum and maximum horizontal stress magnitudes respectively,  $\nu$  is Poisson ratio,  $\alpha$  is Biot coefficient and  $\epsilon_H$  and  $\epsilon_h$  are the maximum and minimum horizontal strain magnitudes.

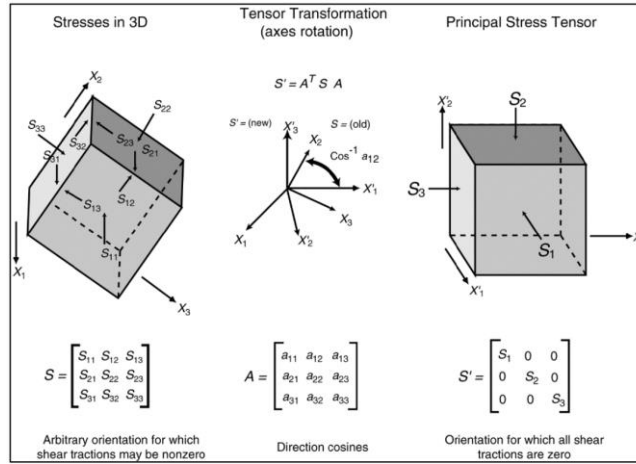


Figure 3-4: The illustration of stresses in three dimensions along with tensor transformation and principal stress tensor [54].

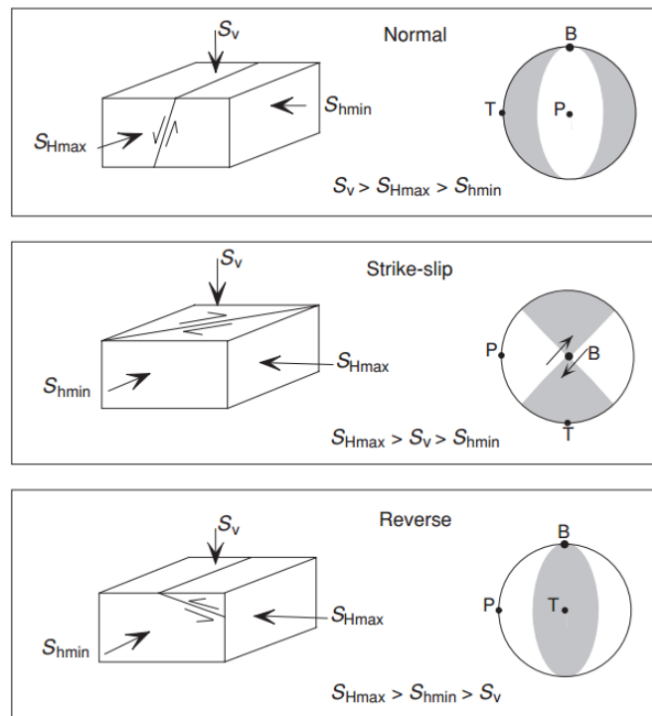


Figure 3-5: The relation of principal stresses in different faulting regimes [54].

## 3.2 3D Mechanical Earth Modelling (3D MEM)

The 3D MEM uses the workflow illustrated in Figure 3-6. The workflow requires two data sets: one for the setup of geomechanical as well as dynamic reservoir models and another for calibration of the modelling results to achieve a validated model. The input data for model setup must contain information about reservoir geometry, material properties and boundary conditions (regional stress field) and the calibration data should contain local stress measurements e.g. orientation and/or magnitudes. This could also comprise fracture data from direct measurements such as core analyses and FMI/FMS logs.

The subsurface geometry consisting of faults and lithostratigraphic layers can be adopted from the geological/structural model which in turn is usually based on seismic and well data. The model geometry can then be exported to ECLIPSE™ for dynamic fluid flow modelling. The 3D MEM can be populated with material properties i.e. elastic and fault properties can either be achieved through laboratory measurements or in absence of lab data these can be calculated from the log-based 1D MEM approach described above. This upscaling of properties from the various 1D MEM's of the individual wells to the 3D MEM can be achieved through geostatistical methods such as Gaussian and Kriging interpolation method [39]. If available, information from seismic amplitude versus offset (AVO) analysis which captures lithological changes can be used to populate the 3D MEM [27].

Finally, the regional stress field can be applied as boundary conditions of the geomechanical model including overburden stress and the magnitudes and orientations of the maximum and minimum horizontal stresses. The final 3D MEM is discretized and finite element (FE) techniques are applied to calculate stresses and strains in the model domain. The geomechanical finite element model is created and calculated by using this input data (Fig. 4-1). The simulation time depends on the total number of elements, the number of faults and the type of implementation.

The results include the principal stresses and strains at any location in the modelling domain. Further quantities such as the differential or mean stress distribution can be calculated if required. After the first calculation, the results are compared with a second set of field measurement data in the model calibration stage. The calibration data set includes local stress measurements and fracture data from various sources. In addition, hydraulic fracturing and leak-off tests can provide information on minimum principal stress as well as breakout logs and drilling-induced fractures provide information on stress orientation. In addition to stress data, image logs and core descriptions provide information on fracture patterns. A first comparison of modelling results with these field data usually shows only a partial agreement, which needs to be improved. This is done by adjusting the parameters (such as friction coefficient of the faults and maximum horizontal stress magnitudes) in the input domain. The adjustments are made iteratively and always within geologically reasonable limits. No input data should be used for calibration, otherwise this leads to futile iterations and the model uncertainty would remain the same.

In an iterative process similar to the 1D MEM, the calculated stresses are compared to observed stress data from different wells of the entire model domain. If a satisfactory fit is achieved, this model is regarded as validated in mechanical terms and can be used for coupling with the fluid flow model.

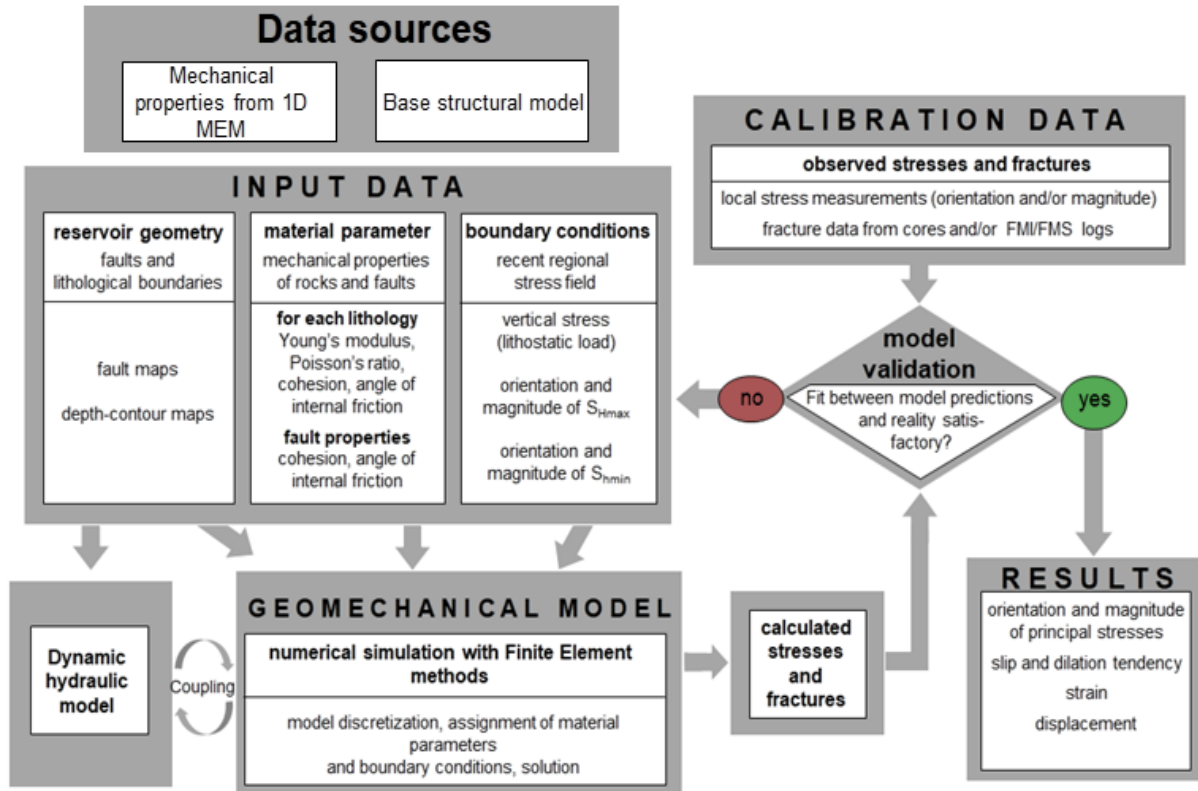


Figure 3-6: 3D geomechanical modelling workflow including input data sources, validation and calibration. Modified after Henk et al. [27] [37].

### 3.3 Hydraulic model

The flow simulation accounts for multiphase fluid flow in porous media. A hydraulic model is usually carried out by reservoir simulation, i.e. a form of numerical modelling in which physical phenomena are quantified and interpreted throughout the history of a reservoir, and beyond with the ability to extend this to future performances. Reservoir simulation is a proven and effective method for dealing with uncertainties during exploration and production [56]. It is also helpful to determine the amount of gas that can be stored in a given underground gas ( $CO_2$ , hydrogen or methane) storage reservoir [56].

The physical phenomenon behind (fluid flow) reservoir simulations is based mainly Darcy's law and mass material balance. For the flow of two immiscible fluids in a porous medium, Darcy's law and the corresponding mass balance for gas can be written as [57],

$$v_i = -\frac{K_{ij}K_r}{\mu_g} \left( \frac{\partial}{\partial x_j} P + \rho_g g h \right), \rho_g = \frac{PM}{RT} \quad (17)$$

$$-\frac{\partial}{\partial x_i} \left( \frac{1}{B} v_i \right) = \frac{\partial}{\partial t} \left( \frac{1}{B} \phi S \right) + q \quad (18)$$

Where,  $v_i$  is fluid velocity (m/s),  $K_{ij}$  is permeability tensor (md),  $K_r$  is relative gas permeability (md),



$\mu_g$  is gas viscosity (Pa.s),  $P$  is fluid pressure for gas (MPa),  $\rho_g$  is gas density (Kg/m<sup>3</sup>),  $M$  is Molar mass of air that,  $R$  is ideal gas constant that,  $T$  is absolute (thermodynamic) temperature,  $g$  is gravitational acceleration,  $h$  is fluid height (m),  $B$  is volume factor for gas,  $\phi$  is porosity,  $S$  is saturation for gas (m/s<sup>2</sup>) and  $q$  is gas source or sink. The development of reservoir and fluid properties is modelled in a series of discrete steps through space and time using finite difference techniques [58].

The composition of the fluid can be treated in different ways in reservoir simulations. Black oil simulators assume oil and gas phases as one component through space and time. The properties of this component can change with pressure and temperature, while the composition does not change [56]. Thereby, the behavior of the multiphase system can be described by complex PVT (pressure, volume, temperature) and SCAL (special core analysis) relations [56].

As a general solution method, the reservoir is divided into several cells with provided petrophysical properties such as porosity and permeability. Then, the wells are placed within cells and production rates are provided with different time steps. Lastly, the equations are solved to determine the pressure, temperature and saturation for each cell. Each cell is solved simultaneously, therefore the number of cells in the reservoir simulation is directly related to the time required to solve a time step [56].

#### 3.4 Thermal model

The thermal-flow-stress simulation model considers the proportional heat transfer in porous media when performing the multi-fluid flow concept in THM simulation. The thermal flow model is usually performed by numerical modelling where the thermal hydraulic aspects are quantified together with the geomechanical simulation and interpreted throughout the history of a reservoir and storage operations in underground gas storage facilities. The main governing law in the thermal modelling is the Fourier's law also known as the law of heat conduction. The law states that the rate of heat transfer through a material is proportional to the negative temperature gradient and to the area at right angles to that gradient through which the heat flows. The governing equation of the Fourier's law describes that the local heat flux density ( $q_h$ ) is equal to the product of the thermal conductivity ( $k_t$ ) and the negative local temperature gradient ( $-\nabla T$ ) [59].

$$q_h = -k_t \nabla T \quad (19)$$

Where,  $q_h$  is in (W/m<sup>2</sup>),  $k_t$  is in (W/m.K) and  $\nabla T$  is in (K/m).

Fourier's law can also be used in uni-dimensional form in any direction, i, j, k for that reason the equation becomes:

$$q_h = -k_t \frac{dT}{d(i, j, k)} \quad (20)$$

#### 3.5 Coupled thermal-hydraulic-mechanical (THM) modelling

The coupling of a reservoir simulator with a geomechanics module is an integral component in order to analyze hydrocarbon reservoirs in the petroleum, underground gas storage as well as geothermal industry. Conventional geomechanical simulator provides surface subsidence which is often estimated by using a simple mechanical formula without knowing the full geomechanical response. The only geomechanical parameter considered may be the pore compressibility, which is not sufficient to reproduce the changes in pore volume caused by complex pressure and temperature variations [60]

[61]. For some problems, such as primary production and linear elastic response of reservoirs, subsidence calculated by a reservoir simulator alone can produce results comparable to coupled solutions [61] [62].

In a coupled simulator, flow can be strongly influenced by the stress and strain distributions that lead to changes in porosity and permeability, but effective stress changes are ignored in conventional simulation methods. Such approaches cannot provide adequate predictions when considering a stress-sensitive reservoir (e.g. underground gas storage reservoir) [63] [60]. There are two main components of coupling: volume coupling and fluid flow coupling according to [60] [62].

In volume coupling, the changes in pore volume occur in response to variations in stress, pressure and temperature. For convergence, the calculated pore volume changes should be the same in both the fluid flow model and the geomechanical model. The pore volume changes of the geomechanical model are usually more accurate than those of the fluid flow model because they are calculated by volumetric strain via a more realistic complex material constitutive model. This method is well suited to shear and plastic deformation which involve in large changes in pore volume or porosity. These problems are common in unconsolidated heavy oils and oil sands, North Sea chalk, Californian diatomite and possibly some other materials [60] [62].

In case of fluid flow coupling, the changes in permeability and relative permeability are related to the changes in stress, shear stress and compaction. Material parameters such as permeability, relative permeability, compressibility and others change when conditions encounter a shear fracture. This is important in some reservoirs where the rock compressibility does not play a significant role in volumetric behavior, such as gas reservoirs where volume coupling is not important. Another example is the cold water/fluid injection, which leads to a thermally induced decrease in horizontal stress until the injection pressure increases the minimum horizontal stress [64].

In order to achieve the stress states of the reservoir and surrounding formations throughout history as well as during future gas storage operation, the fluid flow and the geomechanical simulation have to be coupled. The pore pressure controls the effective stresses and, hence, deformation which in turn changes rock porosity and permeability which again affects fluid flow.

Two sets of equations, one for fluid flow and one for equilibrium of forces have to be solved on the discretized model domain. There are different coupling approaches solving these sets of equations [65]. These approaches are one-way coupling, two-way coupling and full coupling. The one-way coupling scheme transfers pore pressure from the flow simulator to the mechanical model at scheduled time steps to calculate stresses and rock deformation. No modelling results are passed back to the flow simulator. In contrast, two-way coupling involves sending information on porosity and permeability changes due to rock deformation back to the flow simulator for updating the hydraulic properties there. This in turn affects fluid flow and the resulting pore pressure field which is transferred to the mechanical model. This loop is performed at each time step until convergence is reached. Full coupling or implicit coupling implicates that both simulators, i.e., the flow as well as geomechanical simulator calculate the coupling parameters by using a system of equations in which these coupling parameters would be taken as unknown assuring internal consistency [58] [66].

The following theory and background section of coupled THM modelling is adopted by the publication of Jalali et al. [62]. The response of geomechanical fluid flow coupled reservoirs to storage operations (e.g. gas injection, cold water injection, steam injection) cannot be speculated as considering them each the separate processes. Therefore, to examine the mutual interactions between temperature (T), pressure (H), and deformation (M) a coupled thermal hydraulic-mechanical (THM) model is required. The interactions of these parameters are shown in Table 3-3. When short- and long-

### 3. Methodology

term storage processes are introduced, this problem becomes more complicated because there are many ambiguities related to the thermal, hydraulic and mechanical response of the reservoir. Thermoelasticity (TM) and poroelasticity (HM) are two basic principles that combine to form (THM) coupling [62].

Table 3-3: Coupled THM processes, modified after Jalali et al. [62] [67].

	<b>Mechanics</b>	<b>Hydraulic</b>	<b>Thermal</b>
<b>Mechanics</b>	<u>Mechanical process</u> Stress, deformation, strength and failure in matrix, displacement of fractures, tectonic movement, and gravity	<u>M-H coupling</u> Stress-deformation effects on poro-elastic properties of reservoir. Fracture transmissivity and network connectivity	<u>M-T coupling</u> Mechanical conversion into heat, friction etc. (coupling effect is not well defined and usually negligible)
<b>Hydraulic</b>	<u>H-M coupling</u> Effective stress, capillary and swelling pressure-relative saturation, aperture-pressure-stiffness functions of fractures	<u>Hydraulic process</u> Darcy and Non-Darcy fluid flow in reservoir, groundwater movement, fluid injection in UGS and geothermal.	<u>H-T coupling</u> Heat convection by fluid velocity field
<b>Thermal</b>	<u>T-M coupling</u> Thermal stresses and thermal expansion of reservoir; closure, opening and irreversible deformation of fractures	<u>T-H coupling</u> Fluid viscosity and density change, thermal diffusion	<u>Thermal process</u> Heat conduction, convection and radiation due to man-made and natural heat sources, e.g. geothermal gradient, hot/cold fluid injection and production

Gough introduced thermoelectricity in the early 18th century with the concept that due to strain, the temperature in material changes [62]. The thermoelastic effect was then later described by Weber (1830) [62]. Using Biot's poroelastic approach Schiffman (1971) introduced heat transfer in materials [62] [68]. In 1985, Booker and Savvidou developed the equation of the thermoelastic concept by not considering the concept of convection, but only conductive flow. ("The mechanism of heat transfer by fluid flow") [62] [69]. The thermoelastic stress-strain relationship was developed by Aktan and Farouq Ali in 1978 by looking at the thermal stresses induced by the injection of hot water [62] [70]. With plane strain, the problem of coupling convection and heat conduction for a borehole was solved in a rational form by Hojka et al. 1993, and the stress and temperature distributions around the borehole were calculated for some steady-state flow cases [62] [71].

The effective stress for incompressible rock and the concept of one-dimensional consolidation are the fundamentals of pore elasticity formulated by Terzaghi in (1923) [62]. Successively, using the basic principles of continuum mechanics and applying the concept of coupling of stress and pore pressure in a porous medium, Biot developed a comprehensive three-dimensional theory of consolidation [62]

[72]. Biot's theory and the published papers he published are more aligned towards geomechanics than to flow models, due to which they are rarely compatible with the coupling of geomechanics and flow models. By introducing the so-called Skempton pore pressure parameters (A and B) Skempton in 1954 procure a relationship between the total stress and the pore pressure under undrained initial loading [62] [73]. Later, however, the relationship between pore pressure, stress, and volume and explaining the concept of compressibility in a porous medium is better clarified by Geerstma in 1957 [62] [74]. Later, Van der Knaap (1959) extends Geerstma's work to nonlinear elastic geomaterials only for dense and uncemented sands [62] [75]. By applying Biot theory, Geertsma in 1966 examine subsidence problems in oil fields and published prototype geomechanical modeling which is probably the first-ever coupled analysis of fluid flow [62] [72]. Nur and Byerlee (1971) demonstrated that the effective stress law proposed by Biot was far more general and precise than that proposed by Terzaghi [62] [76]. Nevertheless, there are certain limitations (one-dimensional analysis and neglect of the compressibility of fluids and rocks, etc.) that Terzaghi recognised in the assumptions he made in the 1920s to solve problems of applied rock mechanics in clay consolidation [62]. Later in the 1970s, there were further developments on coupled flow stress issues, e.g. fluid compressibility was introduced into the classical soil mechanical consolidation theory of Ghaboussi and Wilson [62] [77]. Rice and Cleary (1976) showed how poroelasticity problems could be solved by using pore pressure and stress as primary variables instead of the displacements used by Biot [62] [78].

### 3.5.1 Simulation concept and governing equations

Numerical modelling of an underground gas reservoir can contribute to the understanding of the interaction mechanisms between the injected gas and the deformation of the reservoir. The injection of cold foreign gas into the reservoir leads to thermal and mechanical disequilibrium in the reservoir by altering the transport properties, including porosity and permeability. A three-dimensional THM coupling model of a reservoir was created by incorporating the mechanical equilibrium equation, the fluid flow or seepage equation (Darcy equation), the heat transfer equation (Fourier equation) of the formation's rock matrix and the THM stress equation. These equations are based on the porosity, permeability, thermal diffusivity and other physical and mechanical parameters of the sandstone formation [79].

The mechanical equilibrium equation can be expressed as follows [79]:

$$S_{i,j,j} + f_i = 0 \quad (21)$$

Where,  $S_{i,j,j}$  is the total stress tensor ( $\text{N/m}^2$ ), and  $f_i$  is the body force ( $\text{N/m}^3$ ).

The fluid flow through the porous rock mass follows Darcy's law, as described in eq. 17 (3.3).

The equation of the continuity of the fluid flow in the rock can be written as [79]:

$$\frac{\partial \rho_l}{\partial t} + \frac{\partial(\rho_l r v_r)}{r \partial r} + \frac{\partial(\rho_l v_\theta)}{r \partial \theta} + \frac{\partial(\rho_l w)}{\partial z} = 0 \quad (22)$$

In this equation  $v_r$ ,  $v_\theta$  and  $w$  are the Darcy velocities (m/s), along radial, hoop and well-depth directions in the porous reservoir.

The relation between stress and porosity/permeability changes in porous rock can be described with the following equations [79] [80],

$$\phi = \phi_r + (\phi_0 - \phi_r) \exp(e \cdot S_M) \quad (23)$$

$$k = k_0 \exp(c \cdot (\frac{\phi}{\phi_0} - 1)) \quad (24)$$

In the above equations,  $S_M$  denotes mean effective stress,  $\phi_0$  and  $k_0$  are the porosity and permeability at zero stress, respectively,  $\phi_r$  represents the residual porosity at high stress and the exponents  $e$  and  $c$  are determined experimentally.

The heat transfer process and the total energy conservation can be express by re-writing the Fourier equation (eq. 20) [81],

$$(\rho c)_t \frac{\partial T}{\partial t} - \frac{1}{r} \frac{\partial}{\partial r} (k_t r \frac{\partial T}{\partial t}) - \frac{1}{r^2} \frac{\partial}{\partial \theta} (k_t \frac{\partial T}{\partial \theta}) - \frac{\partial}{\partial z} (k_t \frac{\partial T}{\partial z}) - q_t r = 0 \quad (25)$$

$$(\rho c)_t = (1 - \phi) c_s \rho_s + \phi c_f \rho_f \quad (26)$$

$$k_{total} = \phi k_f + (1 - \phi) k_s \quad (27)$$

In above equations, the total heat capacity of the solid and fluid phases is denoted by  $(\rho c)_t$  with units (J/(m<sup>3</sup>.°C));  $k_{total}$  is the total thermal conductivity (J/(m.s.°C)),  $q_t$  is the intensity of the internal heat source (J/(m<sup>3</sup>.s));  $c_s$  and  $c_f$  are the specific heat capacities of the formation and the fluid, respectively (J/kg.K),  $\rho_s$  and  $\rho_f$  are the density of the formation and the fluid (Kg/m<sup>3</sup>), respectively, and  $k_s$  and  $k_f$  are the thermal conductivity of the formation and the fluid (W/(m.K)) respectively [81].

Finally, the main governing equation of THM model is as follow [82],

$$2\alpha \frac{(1-2\nu)}{1+\nu} \nabla^2 p + 6\beta K_B \frac{(1-2\nu)}{1+\nu} \nabla^2 T - \nabla \cdot f - 3 \frac{(1-\nu)}{1+\nu} \nabla^2 S_{m(total)} = 0 \quad (28)$$

Where,  $S_{m(total)}$  is the mean total stress (MPa),  $\nu$  is the Poisson's ratio of the rock mass,  $\alpha$  is the Biot coefficient,  $\beta$  is the coefficient of linear thermal expansion (1/°C) and  $K_B$  is the bulk modulus of the rock (MPa). The term  $(2\alpha \frac{(1-2\nu)}{1+\nu} \nabla^2 p)$  describes the effect of poroelastic stress;  $(6\beta K_B \frac{(1-2\nu)}{1+\nu} \nabla^2 T)$  represents thermoelastic stress; and the term  $(\nabla \cdot f - 3 \frac{(1-\nu)}{1+\nu} \nabla^2 S_{m(total)})$  shows the body force [82].

### 3.6 ECLIPSE™-VISAGE™ THM modelling

THM modelling was carried out using two commercial software packages, referred to here as the ECLIPSE™-VISAGE™ coupling. ECLIPSE™ is the conventional reservoir simulator used as the flow simulator for the multiphase flow processes. In the following study, the ECLIPSE™ 100 finite difference black oil simulator is used for the flow calculations. VISAGE™ is one of the most advanced and comprehensive stress analysis simulators commercially available. It is designed for applications where nonlinear mechanics plays a greater role, for example in disciplines such as rock mechanics and geomechanics. It is flexible and can also be used in many other scientific disciplines, e.g. fluid mechanics, heat transfer, materials science, etc. The system provides high computational

power and sophisticated modelling for many analytical situations, which currently include mining, civil engineering, reservoir engineering and geothermal energy.

The advanced and comprehensive finite element code (VISAGE™) has been coupled with the ECLIPSE™ reservoir simulator to include geomechanical processes in this modelling study. Fluid flow is first calculated in ECLIPSE™ and the results are then transferred from ECLIPSE™ to VISAGE™ via the ECL2VIS interface for specified time steps. Updates of porosity and permeability can be calculated via constitutive relations, e.g. Kozeny-Carman.

The coupled THM models are based on three fundamental laws, namely Hooke's law of elasticity, Fourier's law of heat conduction and Darcy's law of fluid flow in porous media. The governing equations are discussed in section (3.5.1) above.

One way coupling is usually sufficient for THM modelling of gas reservoirs as gas compressibility dominates the bulk rock compressibility and the mass balance is mainly controlled by gas pressure rather than by the stresses of solid rock [65]. THM coupled modeled presented in this thesis is a one way coupled model. The main objective is to evaluate the stress state, ground surface subsidence and mechanical stability of faults at different points in the history of the reservoir field in relation to changes in pore pressure that occur during the production/injection phases. In this approach, pressure data is transferred from the reservoir simulator (fluid flow simulator) ECLIPSE™ to the mechanical finite element simulator (geomechanical simulator) VISAGE™ at regular and/or critical times. The fluid pressure drives the geomechanics, but mechanically induced changes in porosity and permeability are not fed back into the dynamic reservoir simulation. It is therefore assumed that permeability and porosity are the same for each time step in the modelling and are not influenced by changes in stresses or aging effects of reservoir. This type of approach is feasible in this particular case study due to the high permeability up to 80 mD characteristic of the reservoir.

## Chapter 4 Case study

The case study used to apply the workflow outlined above is a depleted gas field for which a potential conversion to an underground gas storage site is investigated. The data base was kindly provided by Uniper SE. The former gas reservoir is located about 65 km east of Munich/Germany in the northern foreland of the Alps, the so-called Molasse Basin (Figure 4-1 and Figure 4-2b). It is located in a structural trap, i.e. an anticlinal structure bounded by a north-dipping normal fault at about 1800 m depth (Figure 4-2b). The reservoir rock is of Late Oligocene age, i.e., the Chattian Hauptsand with three gas bearing layers having a total thickness of 85 m. The reservoir formation is highly porous with an average porosity of 23 % and permeability in the range from 20 mD to 500 mD [83].

The field has been produced from 1958 till 1976 and has remained in a shut-in state ever since. The initial reservoir pressure at the time of discovery was 16 MPa and dropped to a minimum level of 3 MPa during the production phase. Due to inflow of water, the present-day pressure has increased to about 15.3 MPa again.

### 4.1 Geological Setting

As the 3D MEM does not only comprise the reservoir but has to incorporate the entire overburden up to the earth's surface and part of the underburden, some information on the geological setting of the case study has to be gathered. The Molasse Basin is located to north of the Alps (Figure 4-2a), stretches about 700 km from France across Switzerland and Germany to Austria. The width of the Molasse basin reaches maximum about 130 km in the Bavarian foreland and decreases to 20 km in the western part at Lake Geneva and 10 km to the eastern part at the Vienna Basin [84] [85]. The Molasse Basin developed in Tertiary age from Late Eocene to Late Miocene. The sediments in the Molasse basin were deposited on top of a Mesozoic basement and reach a thickness of 6 km.

The Molasse Basin was formed as a result of the Alpine orogeny. The collision of European plate and African plate occurred during the Cenozoic and the subduction of European plate under African plate started in Late Mesozoic epoch. The orogenic wedge increased due to collision between two plates which pushed the lithosphere down and resulted in the formation of a deep marine foredeep. This basin was later filled with molasse sediments [86]. The Molasse basin can be divided in two essential parts. The Foreland Molasse ("Vorlandmolasse") are the flat-lying sediments north of the Alpine deformation front, whereas the Folded or Subalpine Molasse ("Faltenmolasse") (Figure 4-2b) is steeply dipping and thrust [87] [88].

The Mesozoic sediments comprise Triassic to Cretaceous limestones and sandstones. The Tertiary deposits represent the late stage of Alpine orogeny. The sedimentary rocks in the Molasse basin provide source, reservoir as well as seal rocks for hydrocarbon reservoirs [89]. However, only small oil and gas fields have been found in the German part of the Molasse basin. Most of these hydrocarbon fields have been depleted by now and can be considered for underground gas storage projects.

The wedged-shaped fill of the Molasse basin consists of Cenozoic sediments underlain by Mesozoic strata and crystalline basement rocks of the European plate (Figure 4-2b and Figure 4-3). Upper Jurassic carbonates have high permeability due to fracturing and karst structures that causes the formation pressure at about hydrostatic condition. The formation pressure of Upper Jurassic is even below over pressured Cenozoic and Cretaceous formations [90].

The Cenozoic sediments reflect the basin subsidence and reach a thickness of about 5000 m. A major

subsidence took place during Oligocene and Lower Miocene time which leads to rapid sedimentation in the basin [28]. The deposition of pelitic deposits occurred during Early Oligocene (Rupelian) due to shallow to deep marine settings. Then a subsequent sea level fall resulted in the deposition of terrestrial to coastal facies which formed Aquitanian and Chattian sand during the Late Oligocene to Lower Miocene [91]. The sea level rise during Lower Miocene resumes the marine settings again in the Molasse basin, which results in the deposition of marine and tidal deposits (Burdigalian deposits). During Middle to Late Miocene, the terrestrial and fluvial environment replaced the marine settings resulted in formation of Upper Freshwater Molasse [91].

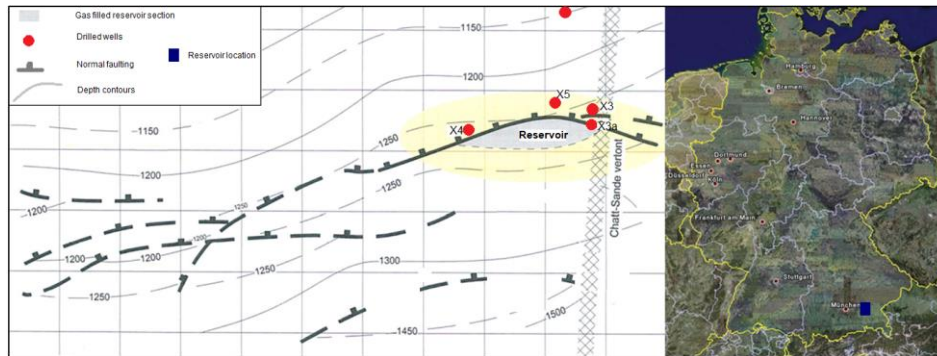


Figure 4-1: Location (blue square) and structure of the study area along with other small hydrocarbon fields in the area. Red dots indicate drilled wells in the area. (Provided by Uniper SE)

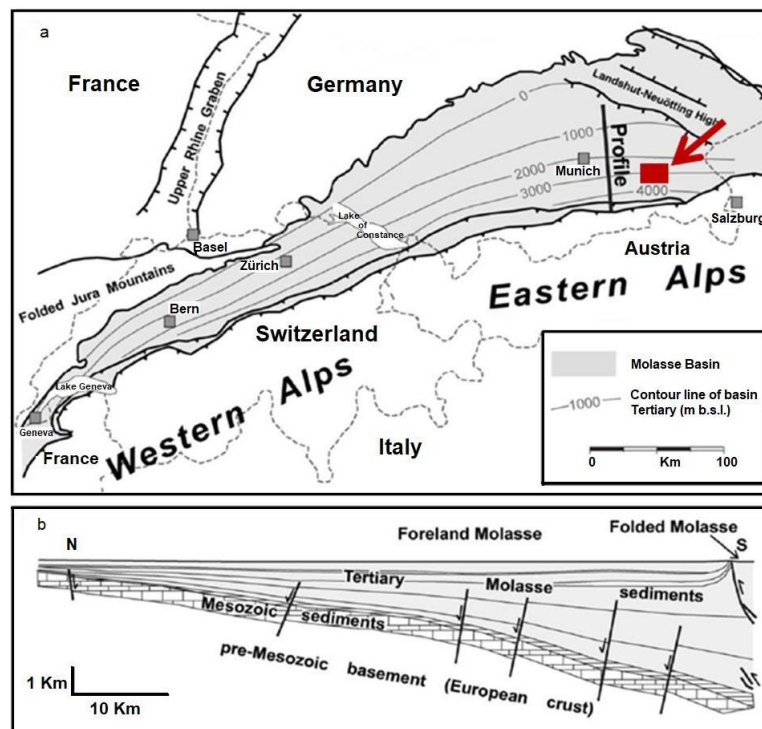


Figure 4-2: (a) Map of the Swiss-German Molasse basin along with main geological structures. Contour lines indicate the depth of the base of the Cenozoic sediments [24]. The grey area represents the Molasse Basin proper. The study area is indicated as red box. (b) N-S cross section of the profile shown in (a) representing the subsurface structures [24]. The case study reservoir is located near one of the north-dipping normal faults.



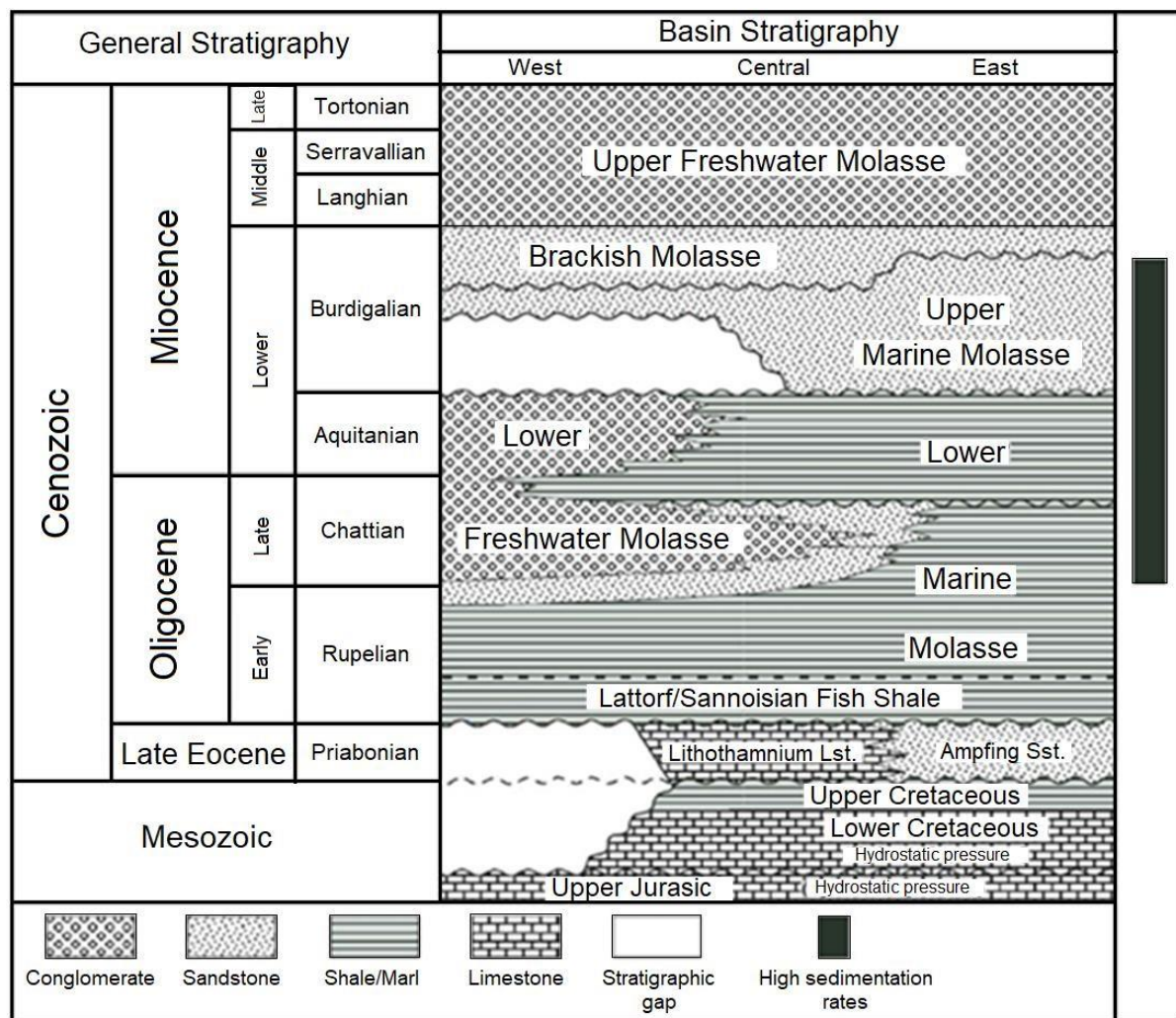


Figure 4-3: Stratigraphic overview of the Bavarian Molasse Basin along with the Mesozoic sub-Molasse succession [91]. The lithology fill and high sedimentation rates correspond to different ages and tectonic events of the Molasse Basin in Bavaria [28] [88] [92] [93].

#### 4.1.1 Hydrocarbon system

There are two hydrocarbon generation phases throughout the geological history of Molasse basin. The first one took place in Late Jurassic time in the Permo-Carboniferous sediments, which are located in graben-structures of the Variscan orogen. The other one happened during Oligocene-Miocene times in the central part of Molasse Basin adjacent to Alpine front [89]. The summary of the hydrocarbon systems in Molasse basin can be seen in (Figure 4-4).

Marine fish shale also called “Lattorfian Fish Shale” and the Lower Jurassic (Toarcian) marine Posidonia Shale are considered to be the primary source rock for oil formation in Molasse Basin, deposited during Oligocene (“Sannoisian” stage). Upper Carboniferous (Stephanian) and Lower Rotliegend (Autunian) coal seams and lacustrine shales may have yielded both gas and oil [89]. Hydrocarbon arrived upwards in the reservoir formation from deeper parts of the basin migrating along pathways with up dip direction. The main reason for the migration could be over-pressured zones close to the Alpine front. The reservoir rocks in the region are Dogger sandstones and carbonates, Cenomanian sandstone to Upper Eocene sandstones and Oligocene carbonates as well as sandstones. The case study reservoir is of Oligocene age (Chattian Sand) and represents entire range of marine environment. “From west (Bavaria) to east (Upper Austria) these are: the marine brackish Baustein sandstone, the deltaic channel deposit of the Chatt and Aquitan sandstones, and the turbiditic

Puchkirchen sandstone series" [89]. The other main gas reservoirs are Rupelian, Aquitanian and Burdigalian sandstones.

The seal formations or caprocks are the intra-formational shales of the reservoir formations. Hydrocarbons from Lattorfian Fish Shale are restricted to western to eastern German Molasse as well as Austrian part of Molasse Basin.

In order to understand the migration and accumulation process of hydrocarbons in the Molasse basin, it is important to know the location of hydrocarbon reservoirs and their connectivity to the source rock. The main driving mechanism is the excessive pressure evolution due to orogeny in the region. High pressure built up in the subalpine Molasse and depends ultimately on the overlying weight of the sedimentary and tectonic load [94]. The other driving mechanism could be squeezing out of hydrocarbons due to structural development, also lateral and vertical changes in porosity and permeability of the Molasse sediments which provided the pathways to hydrocarbon to reach out to the reservoir rock [94].

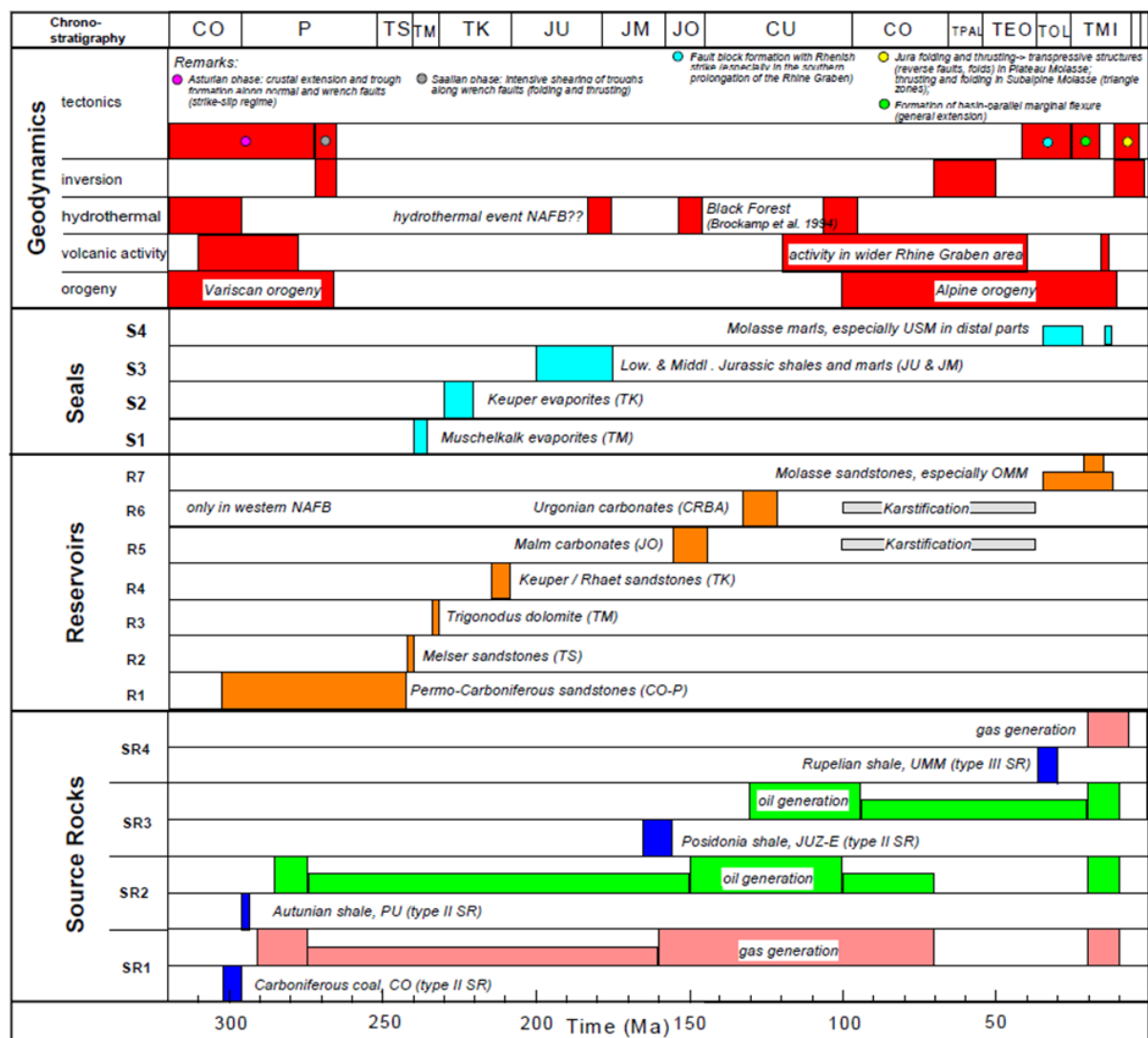


Figure 4-4: Hydrocarbon system of the Swiss-German Molasse Basin with key source rocks, reservoir formation and seal formation. The diagram represents also the hydrocarbons generation/-tectonic history as well as migration. [95].

### 4.1.2 Present day stress state in German Molasse Basin

In order to obtain boundary conditions for geomechanical modelling, the regional stress field magnitude and orientation are essential, especially for assessing the risk of fault reactivation and for drilling issues such as well stability. Present day  $S_{Hmax}$  orientation in the Molasse Basin is largely perpendicular to the strike of the Alpine front, indicating that the stress pattern is probably controlled by the potential gravitational energy of the Alpine topography and not by plate boundary forces [24]. The drilling-induced fractures (DIF's) and borehole breakouts show that the stress orientations within the Molasse Basin are very consistent and the present day  $S_{Hmax}$  orientation rotates from N-S in south-eastern Germany ( $002^{\circ}N \pm 19^{\circ}$ ) to approximately NNW-SSE in south-western Germany and the Swiss Molasse Basin ( $150^{\circ}N \pm 24^{\circ}$ ) (Figure 4-5) [24]. Some of the wells show deviation from main N-S orientation of  $S_{Hmax}$  but this can be caused by local structures such as faults.

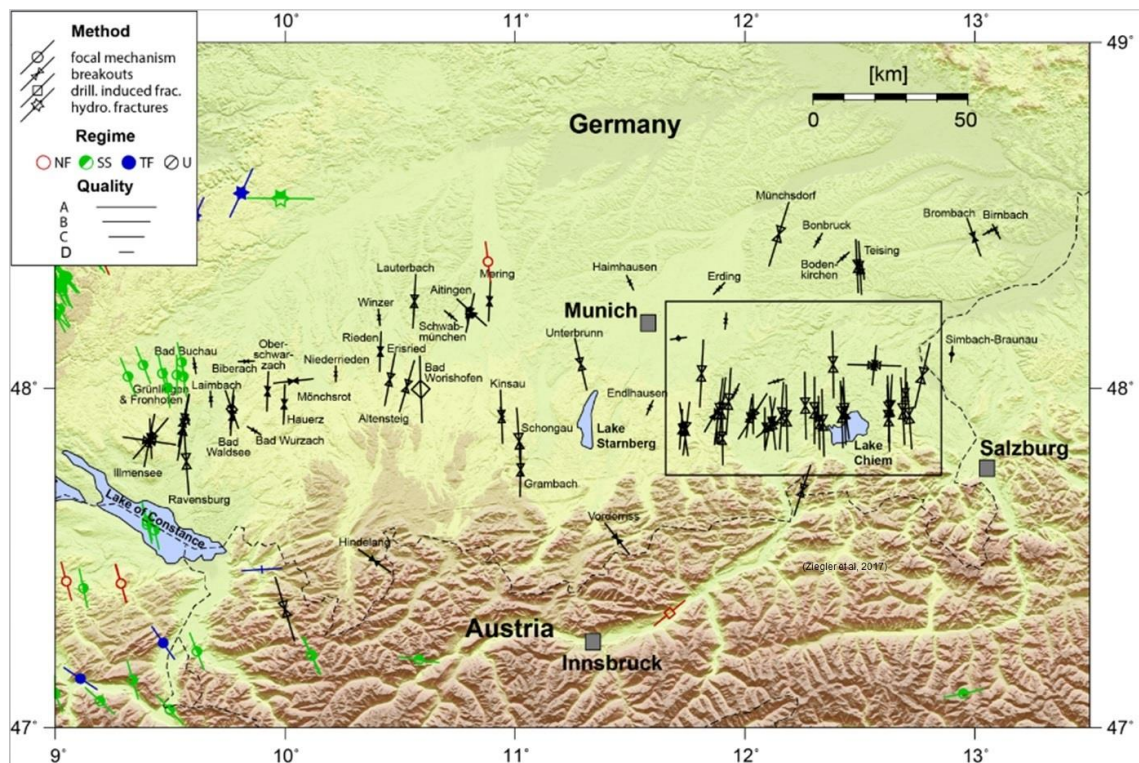


Figure 4-5: Present day orientation of maximum horizontal stresses ( $S_{Hmax}$ ) in the Molasse Basin derived from borehole breakouts and drilling induced fractures. The box represents the area of interest (modified after [24]).

## 4.2 Geology and data set

### 4.2.1 Well data

For nine wells (X1, X2, X3, X3a, X4, X5, X6, X7 and X8) some log data is available (Figure 4-7 and Table 4-1). As most of the wells have been drilled before 1980, this data is incomplete and lacks the modern logging available nowadays. However, this is the typical situation for old, depleted fields for which a conversion to storage sites is considered. In the present case, a density log is available only for well X6. It is used as a reference density log to calculate overburden and pore pressures for each of the wells. No gamma ray is available for any of the wells. Compressional sonic logs exist for seven wells; in addition, the absent shear slowness for all seven wells was calculated from the empirical modelling described in the 1D MEM section.

Table 4-1: Summary of the available well logs for all the wells.

Well name	Well tops	Mudlog	Sonic travel time log	Conductivity log	Induction log	Resistivity log	SP log	Micro-caliper log	Density log	Composite log	Mudlog
X1	✓	✓	✓	✓	✓	✓	✓	✓	x	✓	✓
X2	✓	✓	✓	✓	✓	✓	x	✓	x	✓	✓
X3	✓	✓	✓	✓	✓	✓	✓	✓	x	✓	✓
X3a	✓	✓	✓	✓	✓	✓	✓	✓	x	✓	✓
X4	✓	✓	✓	✓	✓	✓	✓	✓	x	✓	✓
X5	✓	✓	x	✓	✓	✓	✓	x	x	✓	✓
X6	✓	✓	✓	✓	✓	✓	✓	✓	✓	✓	✓
X6a	✓	✓	x	x	x	x	x	x	x	x	✓
X7	✓	x	✓	x	x	✓	✓	x	x	x	x
X7a	✓	x	x	x	x	✓	✓	x	x	x	x
X8	✓	x	x	x	x	x	x	x	x	x	x

#### 4.2.2 Calibration data

Some calibration data for the geomechanical as well as the fluid flow modelling are available. Laboratory tests such as triaxial tests were carried out on the core samples of X6 taken at reservoir level which lead to average values of 4.18 GPa for static Young's modulus ( $E_s$ ), 0.35 for static Poisson's ratio ( $\nu_s$ ) and 0.82 for the Biot coefficient  $\alpha$  [83]. While the data can be used to calibrate the empirical correlations used to find mechanical properties in 1D MEM, stress magnitudes of 38.2 MPa and 36.7 MPa observed at reservoir level of well X6a for  $S_{Hmax}$  and  $S_{Hmin}$  (Figure 4-6 and Table 4-2) [96] are used to constrain the stresses calculated by the 3D MEM. For calibration of the fluid flow simulation, the evolution of the reservoir pressure at well X6 from 1969 to present is available.

Table 4-2: Magnitude of total stresses e.g. total vertical, total maximum horizontal and total minimum horizontal stress in well X6 [24].

Well X6		Caprock	Reservoir
TVD in m		1754	1779
Total stress in MPa	max	41.3	42.2
	Inter.	37.8	38.2
	min	36.6	36.7
	mean	38.5	39.0
	vertical	41.3	42.2

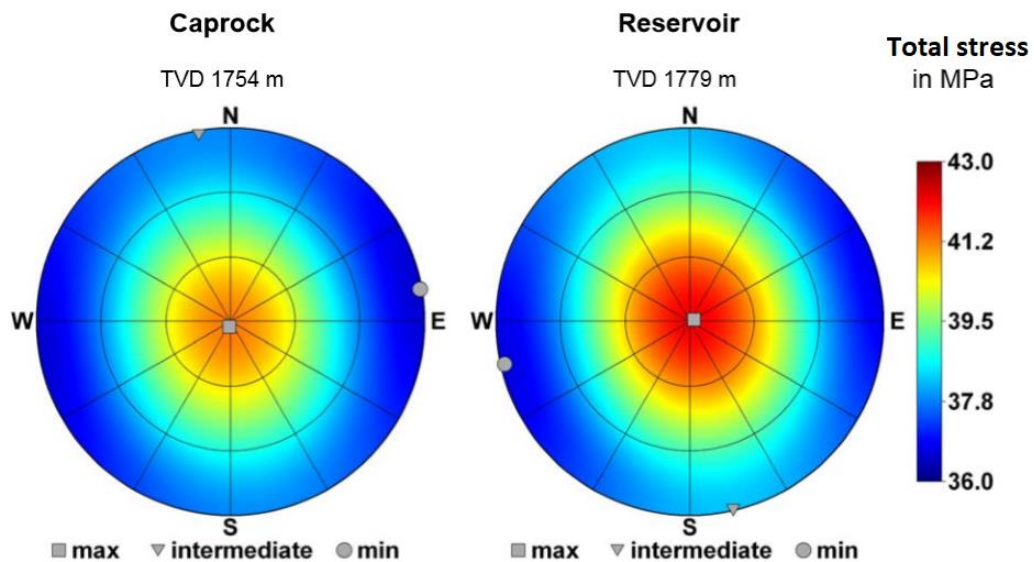


Figure 4-6: Magnitudes and orientations of the total in situ principal normal stresses at the time of core extraction in the analyzed sections of the reservoir X6 well [96].

### 4.2.3 Static geological model

The model geometry was provided by Uniper SE, which built up using seismic and well data from which depth and thickness contour maps were generated for the entire model domain. The static reservoir model is shown in Figure 4-7. The stratigraphic layers from top to bottom of the reservoir even further down to the underburden formations have been extracted from available drilling reports. The scheme of stratigraphic layers for reservoir (top and base of Chattian sandstone), overburden (Top Aquitansand, Bases Burdigal, Bases Helvet up to the earth surface) and underburden (Top Lithothamnienkalk, Top Cretaceous, Top Malm Zeta, Top Malm Gamma, Top basement down to the flat model base) formations is illustrated in Figure 4-8. The model contains three faults with the main fault which cuts through the middle of the reservoir in East-West direction. The volume of the reservoir model is about  $8 \times 4 \times 0.3 \text{ km}^3$  in X, Y and Z direction, respectively, and located at a depth of about 1200 m below sea level. The 3D grid is made up of 495720 cells which are  $162 \times 85 \times 36$  cells in X Y and Z directions respectively. The gridded part of the reservoir covers the area of  $34 \text{ km}^2$  around the anticlinal structure of the reservoir. The reservoir geometry comprises an anticlinal structure with north dipping normal faults. The Gauss-Kruger coordinate system was used to build up the model.

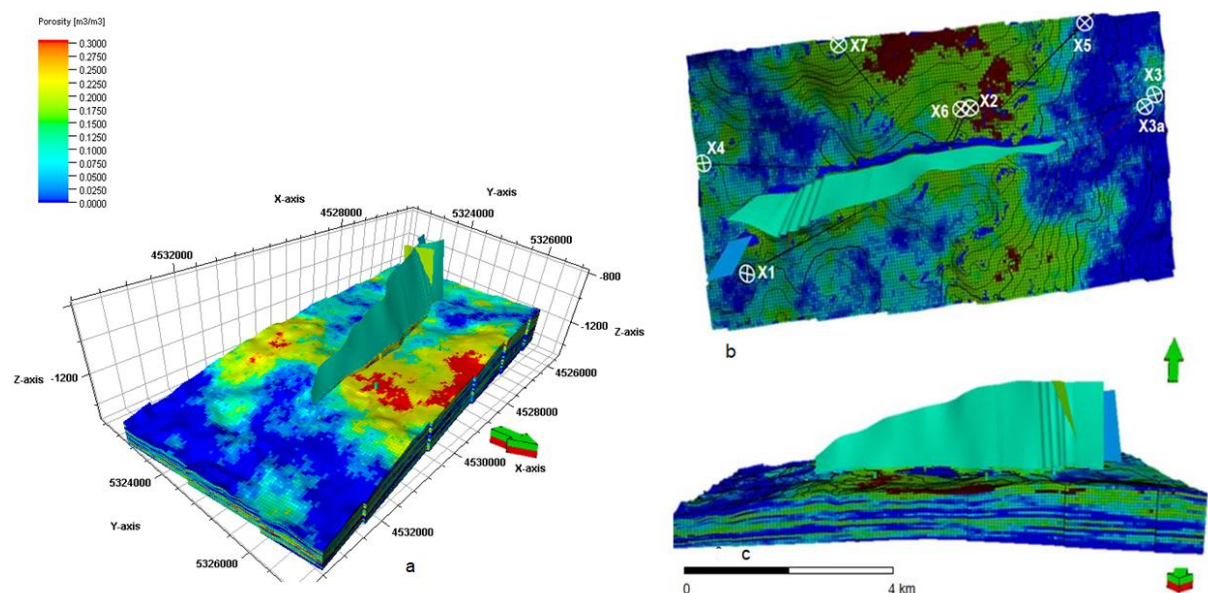


Figure 4-7: 3D structural model of the case study reservoir with three main faults. (a) is oblique view, (b) is top map view at depth of 1200 m below sea level, and (c) is east-west cross-sectional view. The model shows the porosity distribution throughout the reservoir area [37].

	Horizons		Stratigraphic units
Overburden	Earth's Surface	0 m	Quaternary, sweet-water molasse and Helvet
	Base Helvet	-801 m	
	Base Burdigal	-1442 m	
	Top Aquitansand	-1599 m	
Reservoir	Top Chatt Hauptsand	-1796 m	Aquitansand (Aquitana I) + Chatt Hangende Tonmergel
	Base Chattsand	-1977 m	Chatt Hauptsand
Underburden	Top Lithothamnienkalk	-2989 m	Chatt liegende Tonmergel, Rupel + Lattorf Fischeschiefer
	Top Cretaceous	-3387 m	Lithothamnienkalk
	Top Malm Zeta	-3533 m	Malm Zeta to Top Cretaceous
	Top Malm Gamma	-3756 m	Malm Gamma to Top Malm Zeta
	Top Basement	-4093 m	Top Basement to Top Malm Gamma
	Flat Base	-5000 m	Basement

Figure 4-8: Horizons along with intervening lithostratigraphic units used to build up the 3D MEM down to a depth of 5 km [37].

#### 4.2.4 Hydraulic model

The upscaled static geological model was exported to ECLIPSE™ for dynamic fluid flow simulations. The high-resolution reservoir model has 14 lithostratigraphic layers with individual petrophysical properties of each layer. The reservoir is highly heterogeneous with a porosity distribution of 0 to 30%

#### 4. Case study

and water saturation from 0 to 1. The porosity and permeability range are from 0 to 21 % and 0 to 80 mD respectively. The active cells cutoff is determined by a minimum pore volume of 200 m<sup>3</sup>.

The MINPV (minimum pore volume) of 200 m<sup>3</sup> has been used for the active grid of the model. There are two FIPNUM regions in the base model. The gas specific gravity at the surface condition is 0.5594. The active aquifer has been assigned to the reservoir which provides water drive mechanism. The fluids behave differently under different temperature and pressure conditions, therefore the PVT (Pressure-Volume-Temperature) relationships become significant in fluid flow simulation. PVT have a wide range of possible values, depending on whether the processes involved take place subsurface, in production facilities or in surface facilities. If gas is injected into the reservoir, it may or may not be miscible and correct PVT behavior must be predicted. The density of each phase as well as the material balance for each cell at each time steps must be calculated during fluid flow simulation. Since the density of each phase depends on the pressure and the amounts of dissolved components in each phase, the calculation of the PVT properties for each phase is the ultimate mean value to specify the fluid properties. The PVT data allow the volume produced to be translated into the state of the reservoir and then converted into mass which can be solved by the simulator as mass balance equations [56]. The general PVT (Pressure-Volume-Temperature) data of the reservoir for this study is summarized in Table 4-3 and Table 4-4.

Table 4-3: Pressure, formation volume factor and viscosity data of fluid as part of PVT data used for reservoir (flow) simulation

No.	Pressure (MPa)	Formation volume factor (FVF) m <sup>3</sup> /m <sup>3</sup>	Viscosity (cp)
1	0.1	1.183	0.01217
2	1	0.117	0.0123
3	2	0.0578	0.01247
4	3	0.038	0.01265
5	4	0.0282	0.01286
6	5	0.0223	0.0131
7	6	0.0184	0.01336
8	7	0.0156	0.01365
9	8	0.0135	0.01396
10	9	0.0119	0.0143
11	10	0.0106	0.01467
12	11	0.0096	0.01506
13	12	0.0087	0.01547
14	13	0.008	0.01589

15	14	0.0074	0.01632
16	15	0.00691	0.01676
17	16	0.00647	0.01721
18	17	0.00609	0.01767

Table 4-4: Temperature versus water viscosity data used as part of PVT data for reservoir simulation.

Temperature (C°)	Water viscosity (cp)
0	1.7259
10	1.3053
20	1.0177
30	0.8149
40	0.668
50	0.5591
60	0.4765
70	0.4127
80	0.3625
90	0.3223
100	0.2898

The water properties that have been used to get the calibrated pressure history match concluded in Table 4-5.

Table 4-5: Water properties used in the ECLIPSE™ model

Reference pressure (pref)	16 MPa
Water FVF at pref	1.005 $\text{m}^3/\text{m}^3$
Water compressibility	4.171E-4 /MPa
Water viscosity at pref	0.57 cp
Water viscosibility	0 /MPa
Water specific gravity	1.0115

In order to calculate saturate functions, information such as capillary pressure and relative



#### 4. Case study

permeability of each active cell must be provided. In this way, the upper and lower limits of saturation for each active cell can be defined. These limits are then used to determine the initial saturation of each phase in the gas and water zone. The capillary pressure in turn is used to calculate the initial transition zone saturation of each phase. Relative permeability allows the calculation of fluid mobility at different saturations of fluids (in case of multiphase flow) and the solution of the flow equations between cells and from cells to well.

The saturation function takes into account the relative permeability between gas and water and the capillary pressure to calculate the initial saturation for each phase in each cell [56]. The special core analysis (SCAL) with gas saturation functions and water saturation function for reservoir simulation of this case study have been compiled in the Table 4-6 and Table 4-7 respectively.

Table 4-6: Saturation functions for gas phase

No.	Gas saturation (Sg)	Relative permeability of gas (Krg)	Capillary pressure (MPa)
1	0.03	0	0
2	0.1	0.004743	0
3	0.2	0.11985	0
4	0.3	0.21409	0
5	0.4	0.32485	0
6	0.5	0.44699	0
7	0.6	0.57544	0
8	0.7	0.70756	0
9	0.8	0.884	0
10	0.82	0.87238	0

Table 4-7: Saturation functions of water phase

No.	Water saturation Sw	Relative permeability of water Krw	Capillary pressure (MPa)
1	0.18	0	5.94771
2	0.2	0.0001	4.04453
3	0.3	0.003	0.95074
4	0.4	0.0065	0.42817
5	0.5	0.013	0.29234
6	0.6	0.023	0.24539

7	0.7	0.035	0.19697
8	0.8	0.05	0.16447
9	0.9	0.075	0.1412
10	0.97	0.5	0.131
11	1	0.8	0.128

The equilibration data specifications are as follows (Table 4-8),

Table 4-8: Equilibration data specification for initialization

	Datum depth (m)	1235.6		Datum depth (m)	1235.6
Equilibration data for region 1	Pressure at datum depth (MPa)	15.8	Equilibration data for region 2	Pressure at datum depth (MPa)	15.8
	Water contact (m)	1235.6		Water contact (m)	1000

### 4.3 Thermal model

The same ECLIPSE™ has been used for thermal modelling as describe in the above section. Thermal modelling has been carried out by TU Clausthal in 2013 through the Schlumberger simulator ECLIPSE™ thermal E300 as well as temperature option of E100 simulator (E100-temp) [97]. E300 thermal mainly uses in heavy oil recovery especially for viscosity changes of the reservoir fluid as a function of temperature. A gas phase containing hydrocarbon and water components can be simulated on E300 thermal suit. On the other hand, the temperature effects in the reservoir can be modelled on ECLIPSE™ 100, while injecting hotter or colder fluids. E100 can also predict the viscosity anomaly in oil and water however it's not recommended for pressures up to around the critical pressure of water like E300-thermal.

#### 4.3.1 Input data for fluid and rock thermal properties

The volumetric heat capacity and thermal conductivity of 2050 KJ/m<sup>3</sup>/K and 0.8 W/m/K respectively has been taken from literature for rock [98]. The gas specific heat capacity  $c$  has been considered to be the methane specific heat capacity and can be obtained from the following formulae:

$$c_p = c_{p1} + c_{p2}(T - T_{std}) \quad (29)$$

Where,

$$c_{p2} = \frac{dc_{p1}}{dT} |_{T_{std}} = \frac{B + 2T_{pstd}C + 3T_{std}^2D + 4T_{std}^3E}{M_w} \quad (30)$$

$$c_{p1} = \frac{c_{pstd}}{M_w} = \frac{A + T_{pstd}B + T_{std}^2C + T_{std}^3D + T_{std}^4E}{M_w} \quad (31)$$

Specific heat coefficients  $A$ ,  $B$ ,  $C$  and  $D$  have been taken from the literature [99].

The initialization of the model is at the same equilibration condition as pre-described in Table 4-8. The volume of fluid initially in place is the matching criteria in different regions and even the whole reservoir. The fluid composition as a function of depth has been used for the E300-thermal model. The gas as well as water phase have been simplified by assigning only 1 component to both phases.

In order to calculate fluid Z-factor, gas density and Joule-Thomson coefficients for E300-thermal, it is necessary to match the volumes of fluid initially in place to obtain the  $Z_0$  and  $Z_1$  coefficients. The E100-temp model normally predicts the same fluid in place as the base ECLIPSE™ model (E100) without tuning the fluid and rock properties. Table 4-9 summarizes fluids in place in all regions for three models (E100, E100-temp and E300-Thermal). The reservoir pressure is 15.8 MPa and the matching volumes of the water and gas initially in places occurred in  $Z_1$  value of 0.0015 m<sup>3</sup>/Kg-mol. The average value of Joule-Thomson coefficient of 3°C/MPa has been taken [97].

Table 4-9: Reservoir fluids initially in place (predicted) [97].

Fluid in place regions	E100		E100-Temp		E300-Thermal	
	m <sup>3</sup>	m <sup>3</sup>	m <sup>3</sup>	m <sup>3</sup>	m <sup>3</sup>	m <sup>3</sup>
	Water	Gas	Water	Gas	Water	Gas
1	1.73E+8	5.80E+8	1.73E+8	5.90E+8	1.7140502E+8	5.89E+8
2	1.05E+8	61847314	1.01E+8	61847314	99551801	62517289
3	1.24E+10	0	1.24E+10	0	1.22E+10	0
4	0	0	0	0		
5	0	0	0	0		
Field	1.27E+10	6.42E+8	1.27E+10	6.42E+8	1.25E+10	6.52E+8

The difference between the fluid in place calculated by the E-100 models and E-300 model can be estimated by the following equation:

$$dev (\%) = \frac{Abs(F_{E100} - F_{E300})}{F_{E100}} \times 100 \quad (32)$$

Where,  $F_{E100}$  and  $F_{E300}$  are the fluids in place calculated with E-100 models and E-300 model respectively [69]. The resulting difference has been calculated and is about 1.5% for both gas and water phase.

The calibrated production history in the reservoir with three models (E100, E100-temp and E300-thermal) is shown in Figure 4-9. The comparison is quite clear from the production history that the production started in 1958 and produced 528 million  $m^3$  gas volume till 1976, all three models show similar pressure propagation throughout the production phase. The shut in phase then started and increased the field pressure ( up to 15.3 MPa) till 2007, it is the re-equilibration phase in which both E100 models still show same pressure propagation, however the E300-thermal model predicts about 0.3 MPa lower pressure propagation. The reason can be more of the result of difference in performance of the simulator as well as the smaller schedule time steps used for the thermal model (timesteps of all three model have been displayed in Figure 4-10) than of the temperature effects. The prominent difference in pressure propagation arises after gas cyclic process starts after 2008. Both E300-thermal and E100-temp models represent higher pressure drop during the production phase, and this higher drop in pressure propagation can be the result of higher production flow rate (Figure 4-11) as well as higher volum of fluid produced during production. As a result of higher production rate, the higher volume of injection fluid has to be injected during injection period to achieve the required reservoir pressure (Figure 4-12).

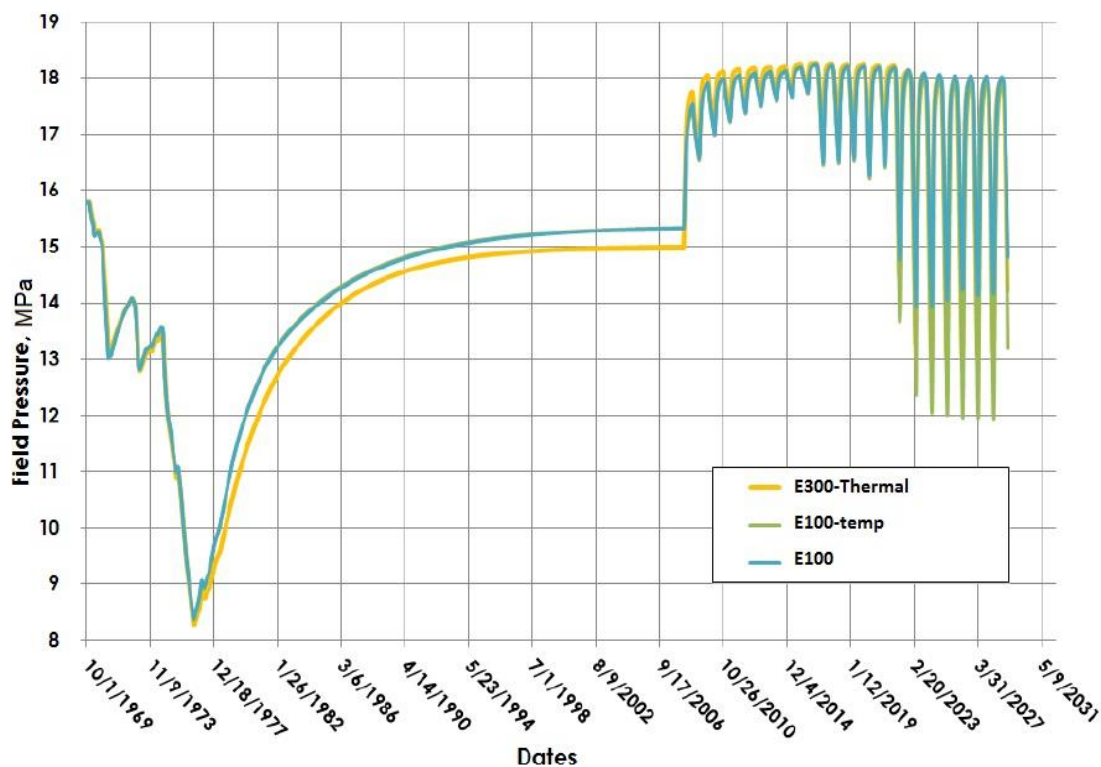


Figure 4-9: Reservoir pressure prediction with base ECLIPSE™, E100-temp and E300-Thermal models [97].

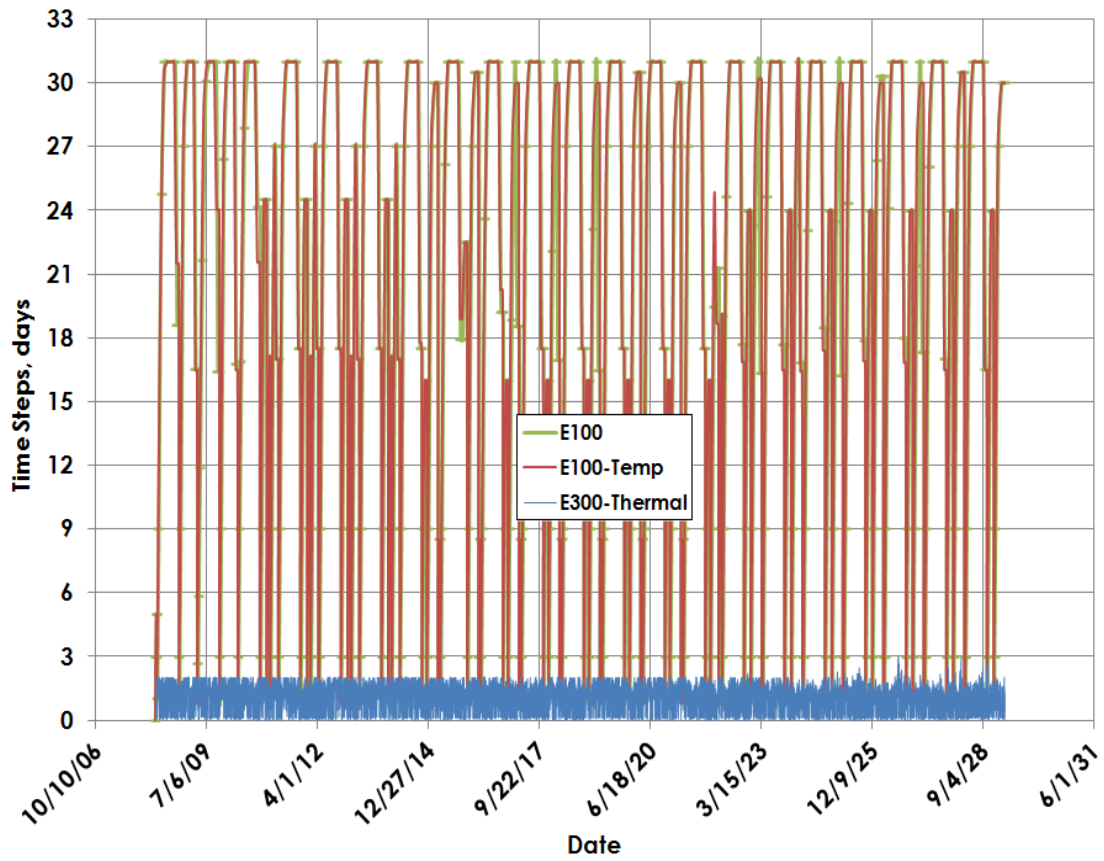


Figure 4-10: Time steps of the three models [97].

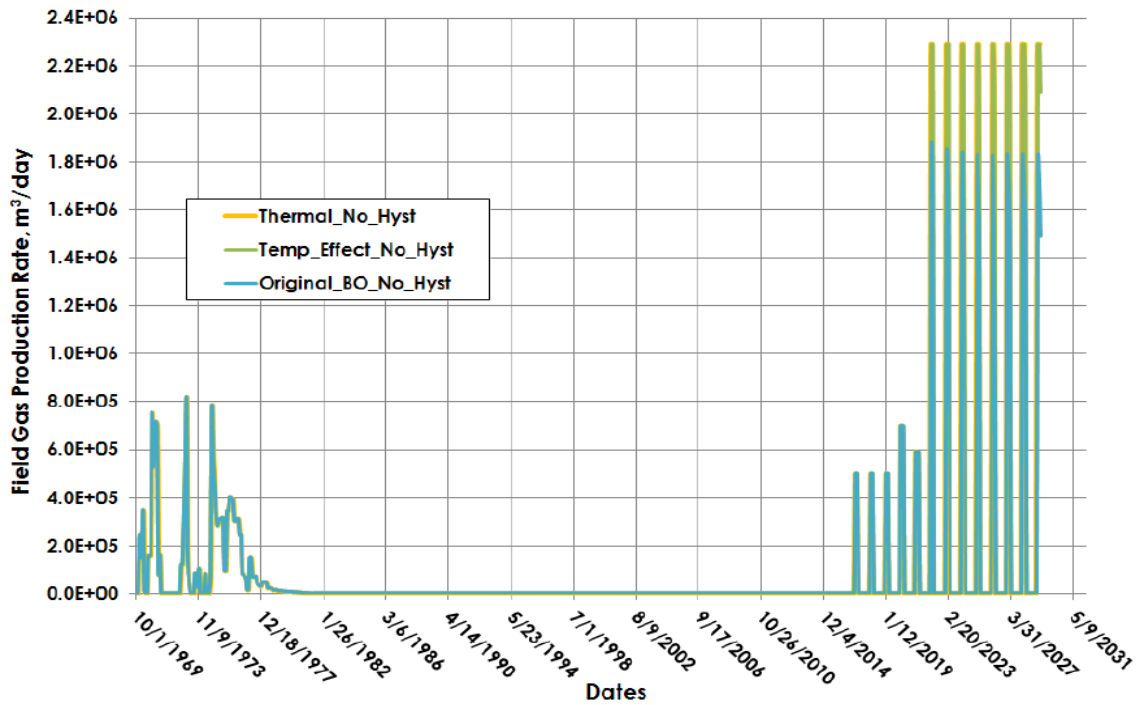


Figure 4-11: Production prediction of the gas with all three models [97].

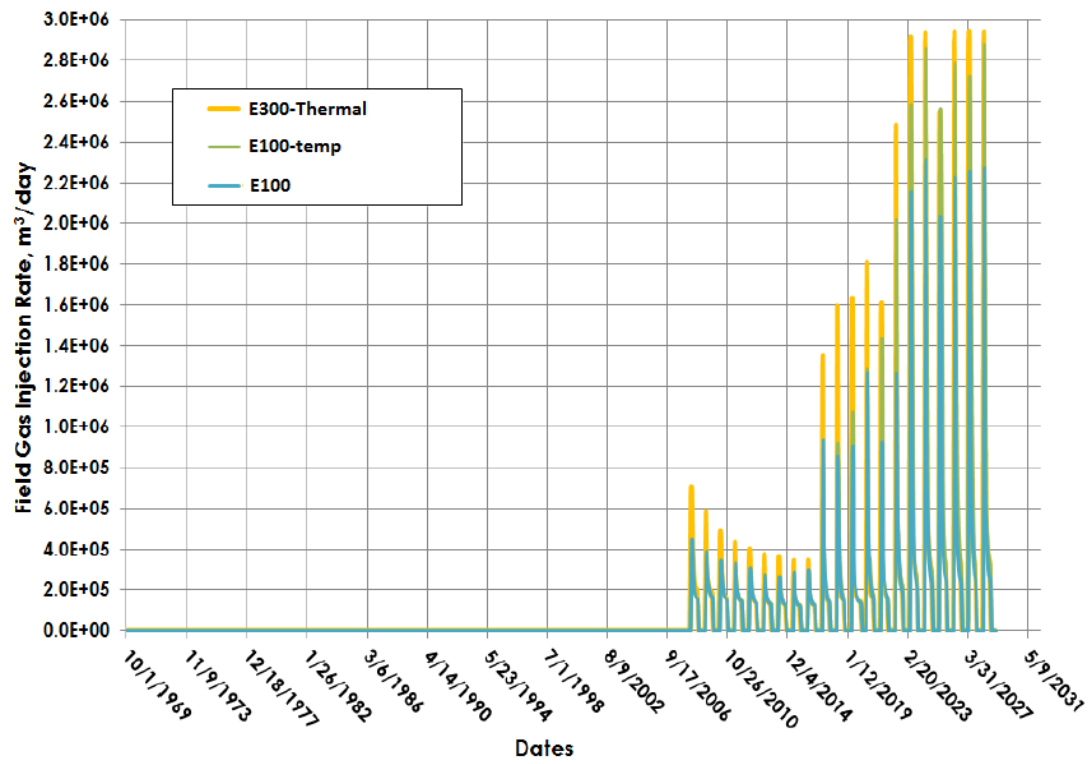


Figure 4-12: Prediction of field gas injection rate with the three models [97].

# Chapter 5 Calculation and calibration of the mechanical properties

## 5.1 1D Mechanical Earth Model

The extrapolation density method (eq. 2) is used to calculate the overburden stress in this case study (eq. 1). The pore pressure profile is acquired from the Eaton's method (eq. 3) (4). In this model study the Plumb and Bradford [40] correlation has been used to compute dynamic elastic properties and the same correlation was used to estimate static elastic properties as well as rock strength properties, calibrating the available core material properties [83]. The poro-elastic strain modelling approach is used to estimate horizontal stresses (eq. 15 and 16). The average Biot coefficient of reservoir was calculated 0.82 through 1D MEM.

## 5.2 Results

### 5.2.1 Overburden Stress

As discussed in the section 3.1.1, the overburden stress is derived from bulk density data. Bulk density was not acquired for the whole depth in this case; it is available for only two sections shown in Figure 5-1. Extrapolated density was calculated prior to overburden stress in order to get whole density profile from top to bottom of the Well X6. The combination of both bulk density and extrapolated density was used to calculate overburden stress. Where density measurements are available, they have been used; otherwise the stress was calculated using the gradient from the extrapolated density. The following Figure 5-1 shows the overburden stress profile along with extrapolated density and overburden mud weight.

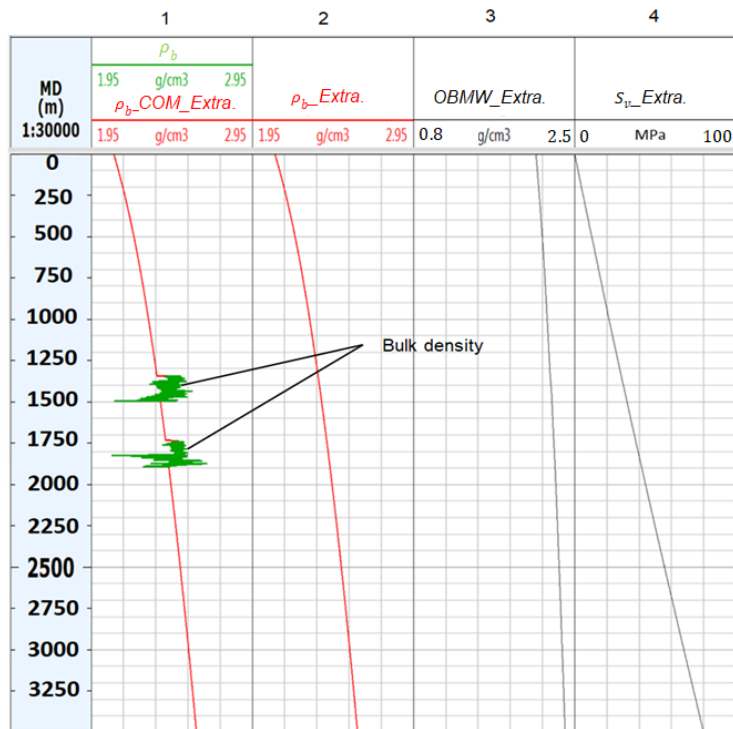


Figure 5-1: Summary of density calculations along with extrapolated overburden stress and mud weight

profiles for Well X6. Section 1 represents bulk density ( $\rho_b$ ) for two sections along with combined extrapolated and bulk density profile ( $\rho_{b\_COM\_Extra.}$ ), section 2 represent only extrapolated density profile, section 3 consists of extrapolated overburden mud weight (OBMW\_Extra.) and section 4 shows extrapolated overburden or vertical stress profile ( $S_{v\_Extra.}$ ).

### 5.2.2 Elastic Properties

Shear slowness (Figure 5-2) was calculated by using the Greenberg and Castagna correlation (10) [47]. The density log along with compressional and shear slowness were used to calculate dynamic elastic properties by using Bradford correlation, which subsequently were converted to static elastic properties by using the same correlation. The correlation requires the bulk density for the calculation of properties for the whole well section. Since, the bulk density for the whole well section was not available, therefore, by using combined extrapolated density (see section 5.2.1), the dynamic shear, bulk (Figure 5-3) and Young's moduli and Poisson's ratio (Figure 5-4) were calculated. The calculated material properties were calibrated using the laboratory measurements. Figure 5-4 shows the results of Well X6 with calibration data as an example for the 1D MEM output.

The average static elastic Young's modulus and Poisson's ratio are 4 GPa and 0.35, respectively, at X6 location at a depth of about 1786 m. The static Young's modulus decreases and Poisson's ratio increases in the reservoir section showing an increase in porosity and consequently presence of sandstone. Contrarily, the decrease in Poisson's ratio and increase in static Young's modulus indicate the presence of shale in over- and underburden sections. The similar trend can be seen Figure 5-3 for dynamic bulk and shear moduli as well as static bulk and shear moduli, which is a clear indication of presence of shale in overburden and underburden, and sand in the reservoir section.

### 5.2.3 Rock strength

In theory, unconfined compressive strength (UCS) is usually derived from published correlations for rock types using Young's modulus. The results are then calibrated using core data. If no data is available, this can lead to high deviations. Since no core data is available for calibration in this case, the reliability of the result is highly uncertain. For this reason, the calibrated static Young's modulus has been used to derive UCS (Figure 5-4). Bradford correlation is best suited for sandstone formations and the case study reservoir belongs to the same class of siliclastic sandstone formation. Since, the reservoir formation is a soft formation (Static Young's modulus <12 GPa) with Static Young's modulus of 4 GPa, the best fitting empirical model was determined using the Bradford correlation [51].

### 5.2.4 Pore pressure

The pore pressure was calibrated first to get a gradient profile matching the calibration point at corresponding depth. Both calculated and measured pressures of 16 MPa coincide at a depth of 1786 m. The pore pressure profile follows the hydrostatic pressure until the top of the reservoir section, which shows an over-pressured zone slightly surpassing the hydrostatic pressure by 5 MPa. The elastic properties at the same depth were also calibrated against measured data. At last the horizontal stresses were calculated using poro-elastic approach and calibrated against measured stresses by using strain increments, eq. (15) and eq. (16), i.e.  $\varepsilon_h = 0.0009$  and  $\varepsilon_H = 0.0012$  (Figure 6-3).



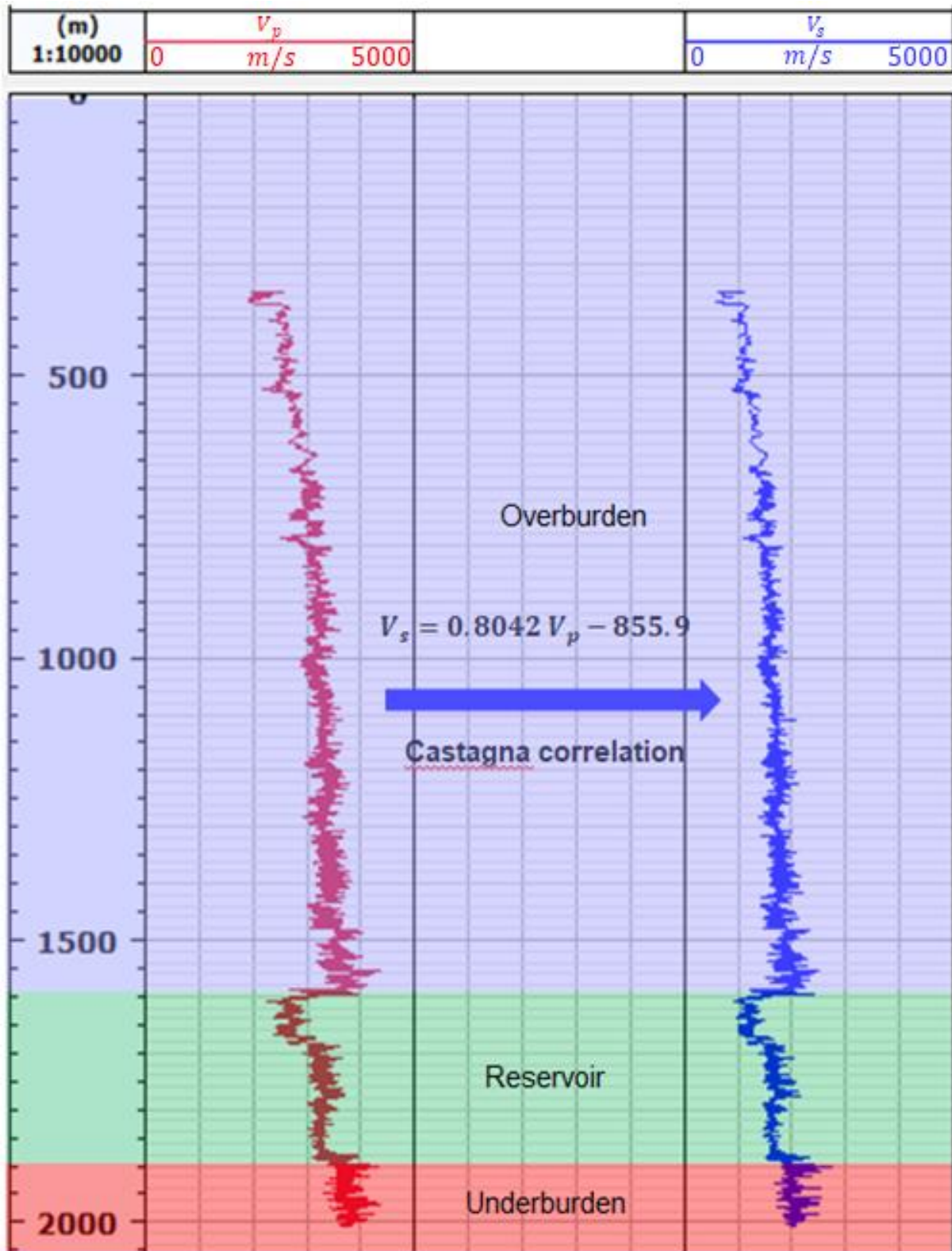


Figure 5-2: Conversion of compressional velocity ( $V_p$ ) to shear velocity ( $V_s$ ) by using Greenberg and Castagna correlation (for Well X6) [47].

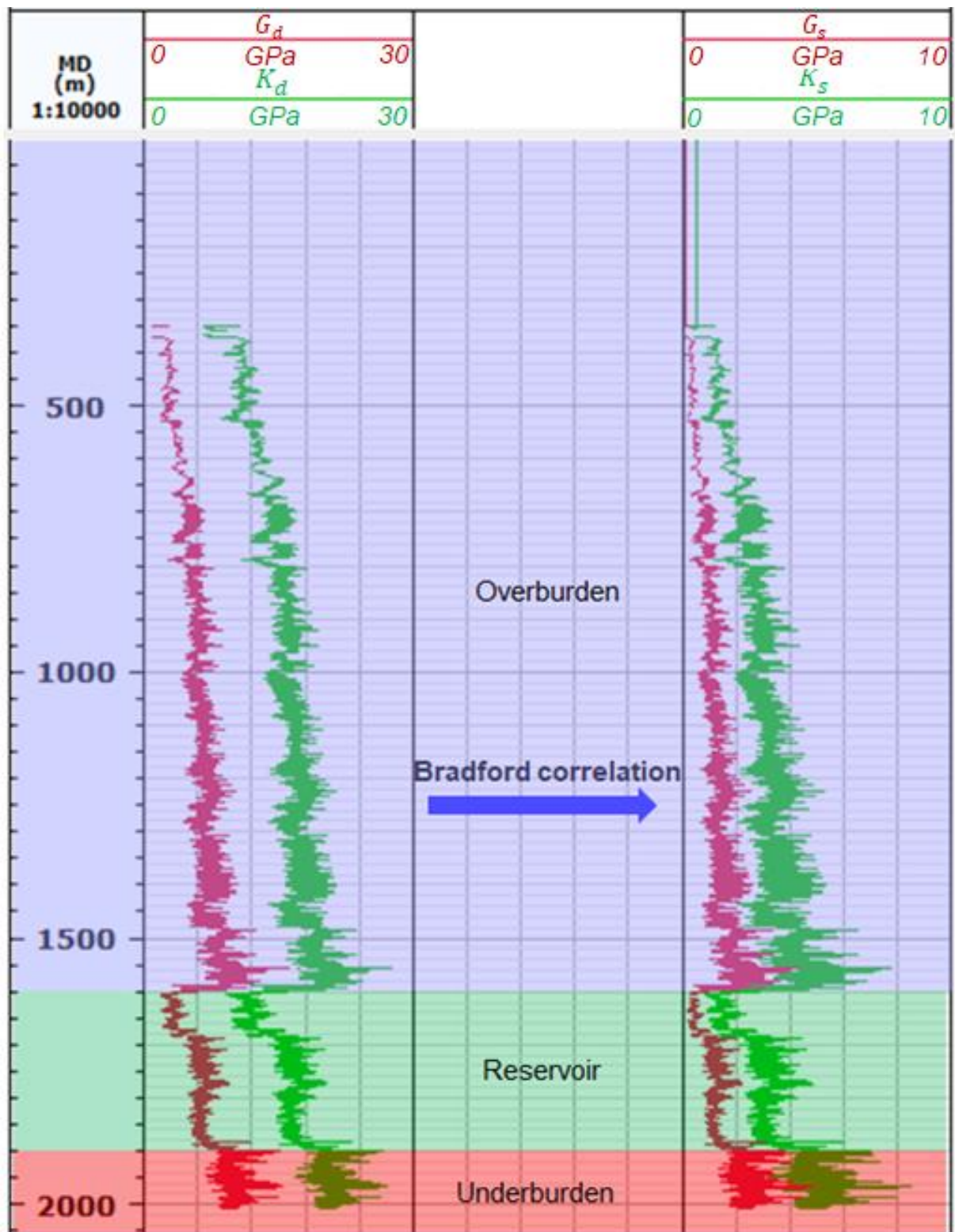


Figure 5-3: Computed dynamic Bulk modulus ( $K_d$ ) and Shear modulus ( $G_d$ ) (left) from dynamic Young's modulus and static Bulk ( $K_s$ ) and static Shear ( $G_s$ ) moduli (right) from dynamic Bulk and Shear moduli by using Bradford correlation (for Well X6).

## 5. Calculation and calibration of the mechanical properties

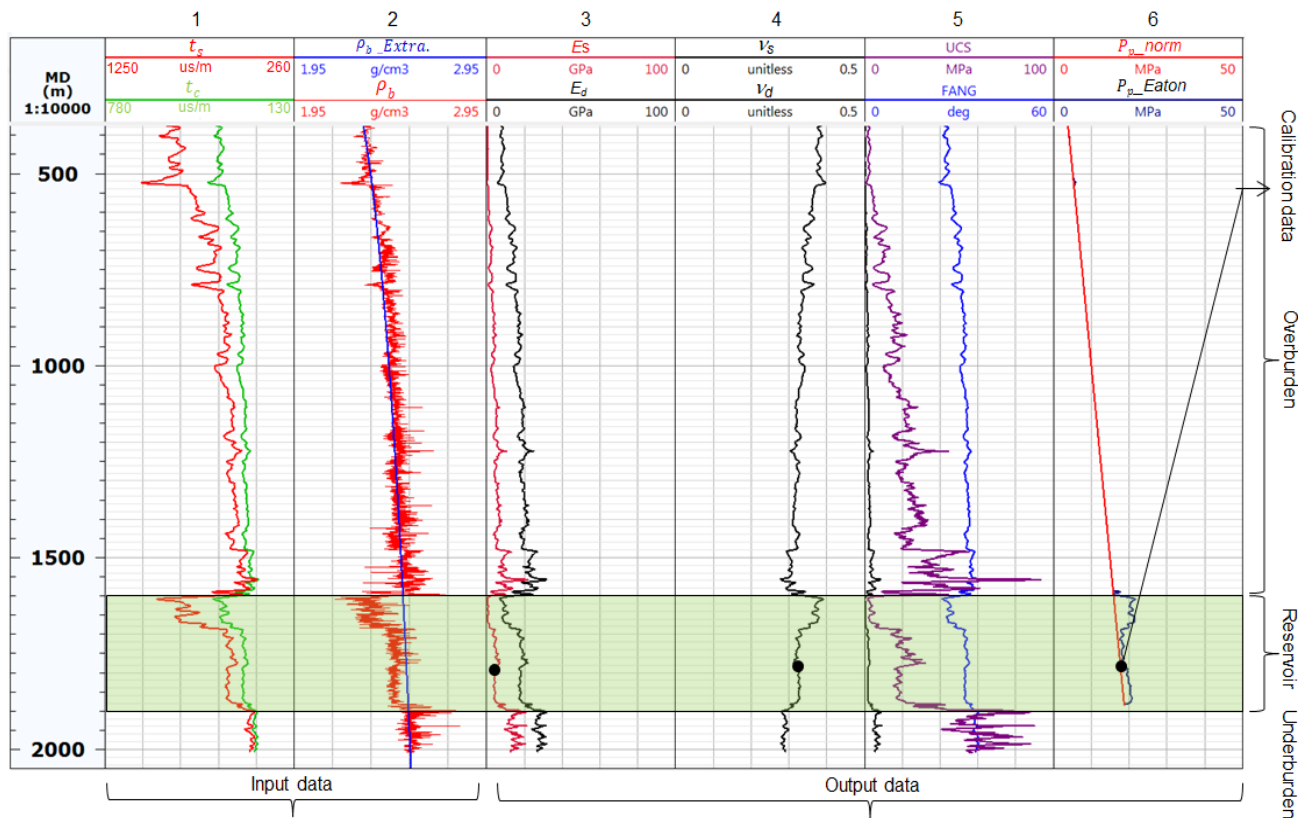


Figure 5-4: Summary of calculated mechanical properties along with input log data for Well X6. Input data comprises shear and compressional slowness as well as extrapolated density and output data includes mechanical properties and pore pressure. Section 1 contains shear slowness ( $\Delta t_s$ ) and compressional slowness ( $\Delta t_c$ ), section 2 is bulk density ( $\rho_b$ ) and extrapolated density ( $\rho_b$ \_Extra.), section 3 consists of calculated dynamic Young's modulus ( $E_d$ ) and static Young's modulus ( $E_s$ ), section 4 is dynamic Poisson ratio ( $\nu_d$ ) and static Poisson ratio ( $\nu_s$ ), section 5 shows unconfined compressive strength (UCS) and friction angle (FANG) and section 6 represents hydrostatic pressure

## Chapter 6 Calculation and calibration of the stress state

### 6.1 3D Mechanical Earth Model

3D MEM was built up using static geological model described above, which comprises a high-resolution reservoir section and regions of lower resolution away from reservoir section named as sideburden, overburden and underburden sections. Topography was extracted from the elevation maps of the ground level in order to include the top surface of the model. The horizons bounding the reservoir were used to make overburden layers and underburden layers. The basal unit of the model comprises crystalline basement rocks at a depth of about 5 km. However, as none of the wells has actually reached this depth, this information is inferred from regional geological knowledge. The final 3D geomechanical model consists of 12 horizons and 11 lithostratigraphic units with dimensions of about  $30 \times 24 \times 5$  km<sup>3</sup> in X, Y and Z direction respectively. The grid of the 3D MEM with the reservoir model embedded is shown in Figure 6-1. The higher resolution in the area of interest (reservoir) and the lower outside makes up a grid which creates balance between simulation precision and computational demand.. The calculated and calibrated log-derived properties including pore pressure, Young's modulus, Poisson's ratio and density were upscaled from the well locations to the entire model domain. Kriging, a geostatistical interpolation method that takes into count distance and degree of variation between known data points when estimating values in the areas in between these data points [39], was used to populate the 3D geomechanical model. The ranges of important material properties such as Young's modulus, Poisson ratio, bulk density and Biot coefficient of reservoir as well as over- and underburden regions are listed in Table 6-1. The precision is of course decreasing away from the wells but the model fits well with overall trends. The initial pore pressures were also upscaled and interpolated from the 1D MEM's but later in the coupling stage pore pressures of different time steps are taken from the fluid flow model.

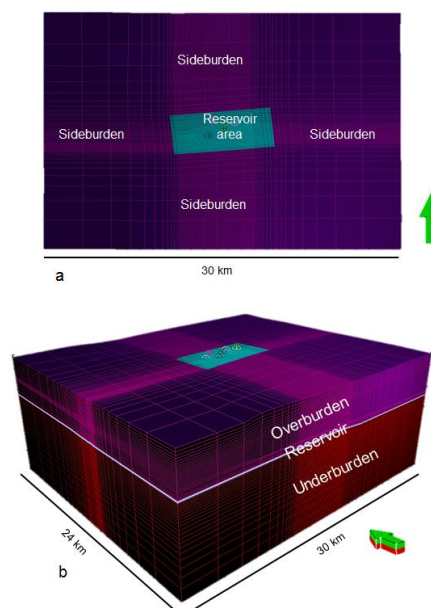


Figure 6-1: Reservoir model proper embedded in 3D geomechanical model with reservoir, overburden, underburden and sideburden zones. (a) is the top view and (b) is the oblique view [37].

## 6. Calculation and calibration of the stress state

Table 6-1: Material properties of the case study reservoir along with overburden and underburden units of 3D geomechanical model.

Stratigraphic unit	Young's modulus (GPa) (MPa)	Poisson ratio	Density (g/cm <sup>3</sup> )	Biot Coefficient
Quaternary, sweet-water molasse and Helvet	0.23-0.56 230-560	0.34-0.40	1.91-2.22	0.90-0.97
Burdigal	2.79-3.80 2970-3800	0.32-0.34	2.22-2.42	0.90-0.94
Top Aquitansand (Aquitane II) to Upper Aquitan down	1.38-4.2 1380-4200	0.32-0.36	2.43-2.47	0.89-0.95
Aquitansand (Aquitane I) + Chatt Hangende Tonmergel	2.71-3.70 2710-3700	0.32-0.35	2.45-2.49	0.90-0.92
Chatt Hauptsand	2.97-5.58 2970-5580	0.30-0.32	2.32-2.55	0.88-0.91
Chatt liegende Tonmergel, Rupel + Lattorf Fischechiefer	4.99-9.75 4990-9750	0.29-0.30	2.53-2.76	0.81-0.88
Lithothamnienkalk	3.58-16.09 3580-16090	0.29-0.34	2.77-2.85	0.77-0.90
Malm Zeta to Top Cretaceous	25-40 25,000-40,000	0.20-0.30	2.50-2.682	0.7-0.90
Malm Gamma to Top Malm Zeta	20-35 20,000-35,000	0.25-0.28	2.5-3.0	0.7-0.90
Top Basement to Top Malm Gamma	30-45 30,000-45,000	0.20-0.24	2.5-3.0	0.7-0.90
Basement	45 45,000	0.25	2.7	0.90

### 6.1.1 Boundary conditions and stress orientations

Strain increments of  $\varepsilon_h=0.0009$  and  $\varepsilon_H=0.0012$  derived from 1D modelling have been applied on the

lateral side of the model as an initial guess which provides a simulated regional stress state. Displacements in north-south direction lead to the magnitude of  $S_{Hmax}$  and displacements in west-east direction lead to  $S_{Hmin}$ . The surface of the model is a free surface which allows analysis of any movements at the earth's surface in response to pore pressure changes. The direction of the horizontal stresses can be estimated from the analysis of borehole breakouts on image logs and caliper data or earthquake focal mechanisms as well as from drilling induced tensile fractures. However, the orientation of horizontal stresses has been calibrated according to the World Stress Map (Figure 4-5 [24]).

## 6.2 Results

Petrophysical properties such as porosity and permeability were updated in the 3D geomechanical model from the dynamic fluid flow model through history matching. The mechanical properties were upscaled and populated by the Kriging method [39]. The spatial distribution of Young's modulus is presented in Figure 6-2. The mechanical properties indicate distinct vertical variations, but only slight lateral changes in lithology. The static Young's modulus in the overburden ranges from 2 GPa to ~8 GPa from top to bottom respectively. The western and eastern part of top of the reservoir indicates higher Young's modulus of about 10 to 12 GPa which increases to the east where it reaches up to 16 GPa. The average value of the Young's modulus decreases from 8 to 6 GPa in the middle of the reservoir near wells X6, X6a, and X1. The higher Young's modulus and lower Poisson ratio in the eastern part of the reservoir indicates more shally lithologies in this area. In contrast, the decrease in Young's modulus and increase in Poisson ratio in the middle and western part indicates the presence of more sandy lithologies than in the eastern part of reservoir. The higher Young's modulus in the underburden area may be due to higher compaction and presence of basement rocks close to the base of model.

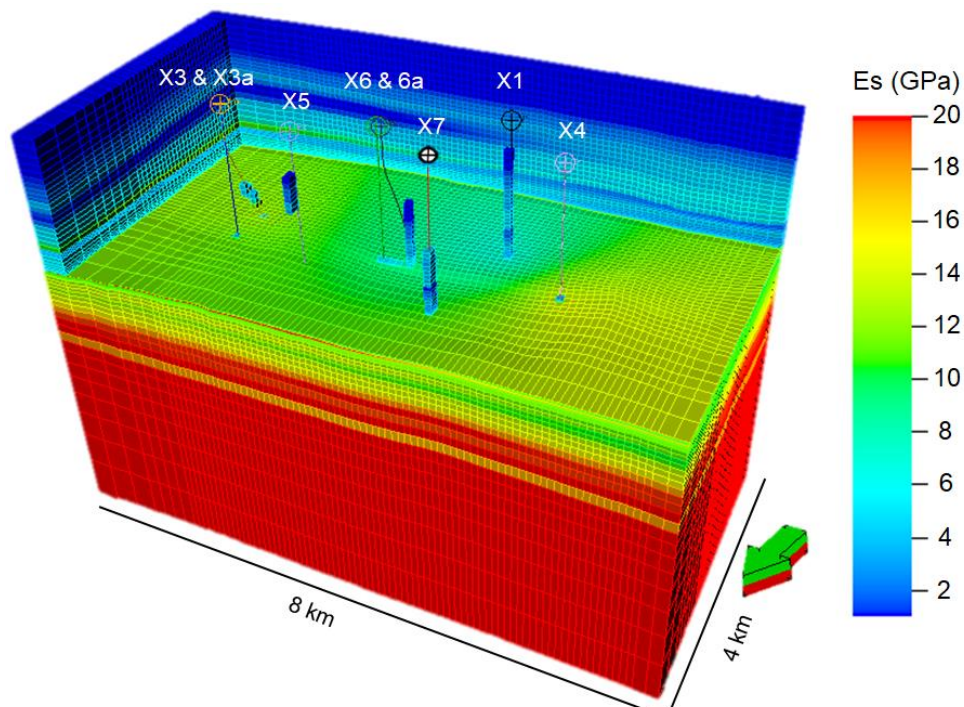


Figure 6-2: Static Young's modulus ( $E_s$ ) distribution through upscaled computed log properties (1D MEM) with wells: Oblique view of overburden and underburden of reservoir area [37].

6. Calculation and calibration of the stress state

The stress state in the 3D MEM was achieved by calibrating minimum and maximum horizontal stresses by iterative adjustment of strain increments (both minimum and maximum strains). The calibrated stresses are shown in Figure 6-3 for Well X6. The reservoir zone lies in a normal faulting regime as the vertical stress  $S_v$  is larger than the maximum horizontal stress  $S_{Hmax}$ , which in turn is larger than the minimum horizontal stress  $S_{hmin}$ . The calibration points match the calculated stresses, i.e., 38.2 MPa and 36.7 MPa for  $S_{Hmax}$  and  $S_{hmin}$ , respectively [96]. Likewise, the calculated vertical stress  $S_v = 42$  MPa in the reservoir zone which fits the observed vertical stress of 42.2 MPa from [96]. However, the vertical stress in the underburden and overburden zones becomes the smallest among the principal stresses which means a reverse faulting regime above and below the reservoir. The stress state in the section above 600 m to the surface is  $S_{Hmax} > S_v > S_{hmin}$  making it a strike-slip region. The abrupt changes in the tectonic regime with depth are a consequence of the different mechanical properties in the model domain.

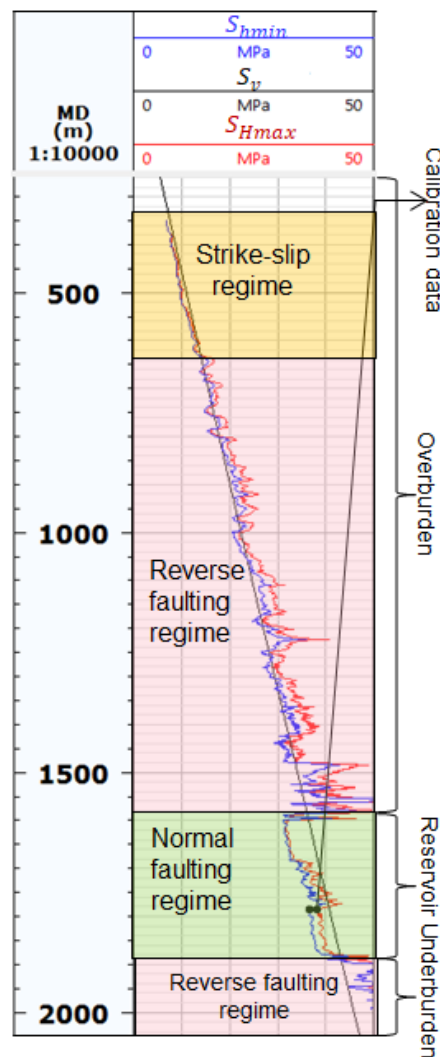


Figure 6-3: Calculated stress profile at well X6 showing vertical ( $S_v$ ), maximum ( $S_{Hmax}$ ) and minimum horizontal ( $S_{hmin}$ ) stresses with calibration data.

The magnitudes of the three stresses  $S_{Hmax}$ ,  $S_{hmin}$  and  $S_v$  in the immediate reservoir area are presented in Figure 6-4.  $S_{Hmax}$  ranges from 38 MPa to 45 MPa and tends to increase in the eastern part of the reservoir as an effect of the increase in the depth of the reservoir. Similarly,  $S_{hmin}$  and  $S_v$  are also showing this trend of increasing stresses towards the eastern side of the reservoir.  $S_{hmin}$  is in the range of 36 MPa and 44 MPa with a minimum value at 1786m depth of well X6. Moreover, the

vertical stress  $\sigma_v$  reaches up to 48 MPa to the lower eastern edge of the reservoir. The typical ratio of  $S_{Hmax}$  to  $S_v$  is about 0.91 at well X6 whereas the  $S_{hmin}$  to  $S_{Hmax}$  ratio is roughly 0.96. The  $S_{Hmax}$  orientation is similar to the data from the World Stress Map which is trending N-S in the wider region of the reservoir [24].

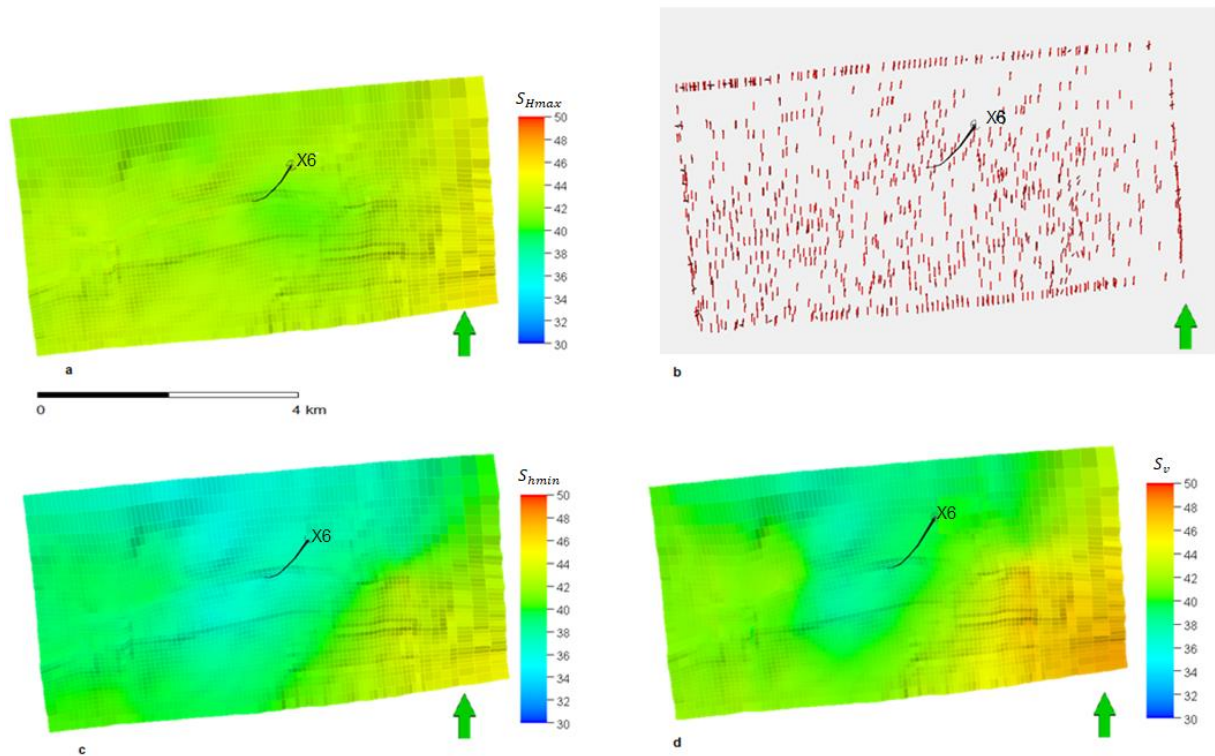


Figure 6-4: Map view of the computed principal stresses on top of the reservoir. a=magnitude of the maximum horizontal stress ( $S_{Hmax}$ ), b= orientation of  $S_{Hmax}$ , c= magnitude of the minimum horizontal stress ( $S_{hmin}$ ) and d= magnitude of the vertical stress ( $S_v$ ). Color scale is in MPa.

The validated 3D MEM gives opportunity to assess the drilling conditions (potential and risk) of a new well at any location within the model domain. Planning of well trajectory requires information on the complete stress tensor, i.e., the magnitude as well as the orientation of all three principal stresses. This information is important especially close to faults and other complexities. Such a comprehensive stress prognosis can be provided by the 3D MEM as is exemplified by the stress profile for a randomly positioned well as shown in Figure 6-5 and this stress prediction method can be used in any underground gas storage or in geothermal project anywhere in the world.



6. Calculation and calibration of the stress state

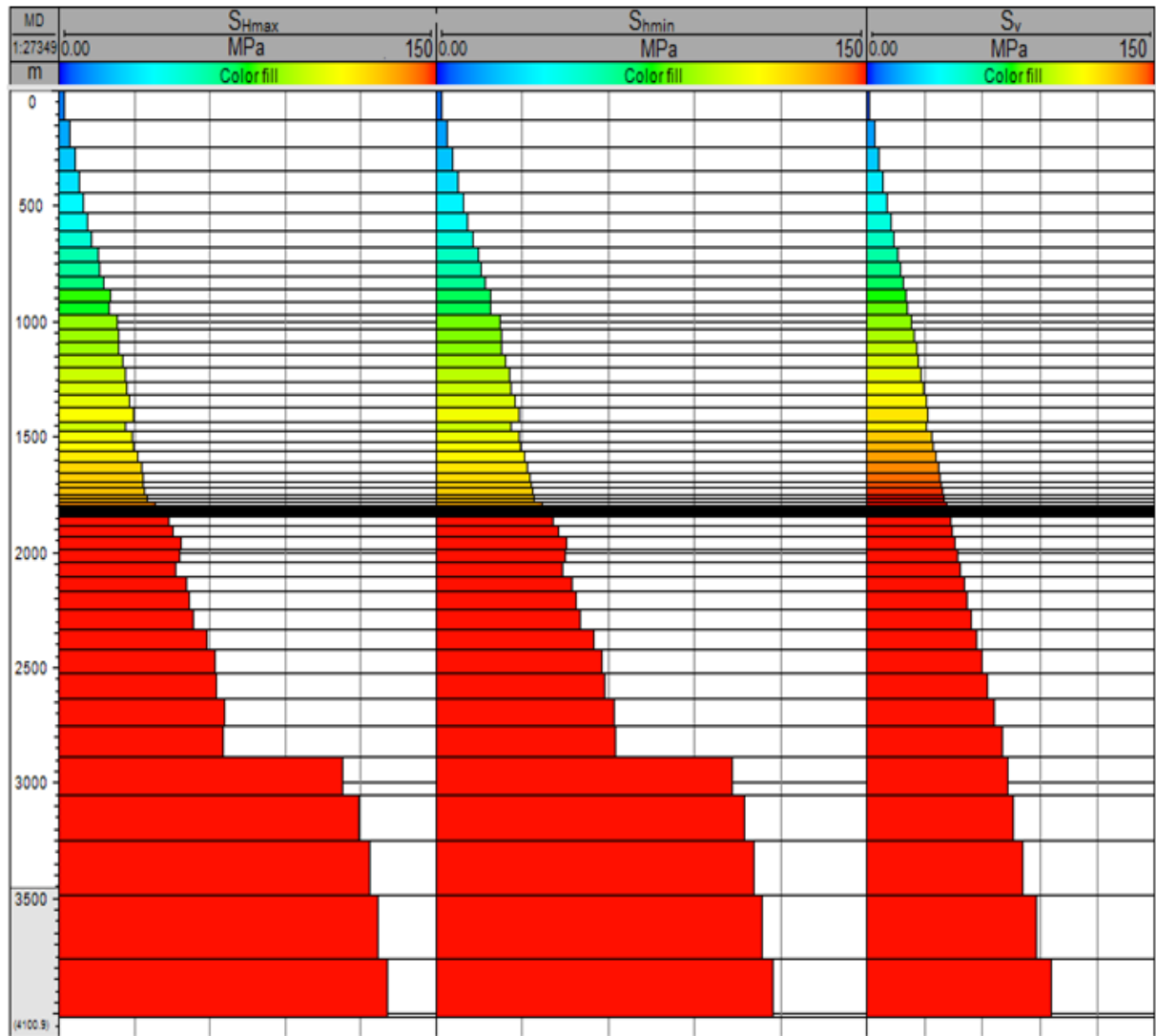


Figure 6-5: Stress state of randomly proposed well with principal stresses: maximum horizontal stress ( $S_{Hmax}$ ), minimum horizontal stress ( $S_{Hmin}$ ) and vertical stress ( $S_v$ ).

## Chapter 7 Hydraulic model

### 7.1 Model setup

Hydraulic (dynamic fluid flow) model incorporates the gas production history of the case study reservoir. The main objective of the flow model is to simulate production and injection of natural gas in the reservoir, in order to obtain pressures at different time-steps to be used as input in the coupled geomechanical simulation with VISAGE™. Pressure points computed with the ECLIPSE™ simulation (Figure 7-1) are comparable with the observed data and follow the same trend of the BHP imposed as control mode. The initial pressure of the reservoir field was ~15.8 MPa. Production started in 1969 and lasted until 1976 which caused the pressure to drop ~3 MPa at the end of the production phase i.e. on 01/12/1978. The shut-in phase then started and replenish the field pressure (up to 15.3 MPa) till 01/01/1991. The corresponding history match has been performed and the calibrated production history is shown in Figure 7-1. Five significant historic pressure points have been selected for coupled geomechanical simulation in order to analyze stress state and subsidence of the ground surface out of which: two are the pressure points during production of gas (01/12/1969 and 01/12/1974), two are during replenishment period or shut in phase (01/01/1983 and 01/01/1991), and one maximum depletion pressure point (01/12/1978) that is also the starting pressure point of shut in phase.

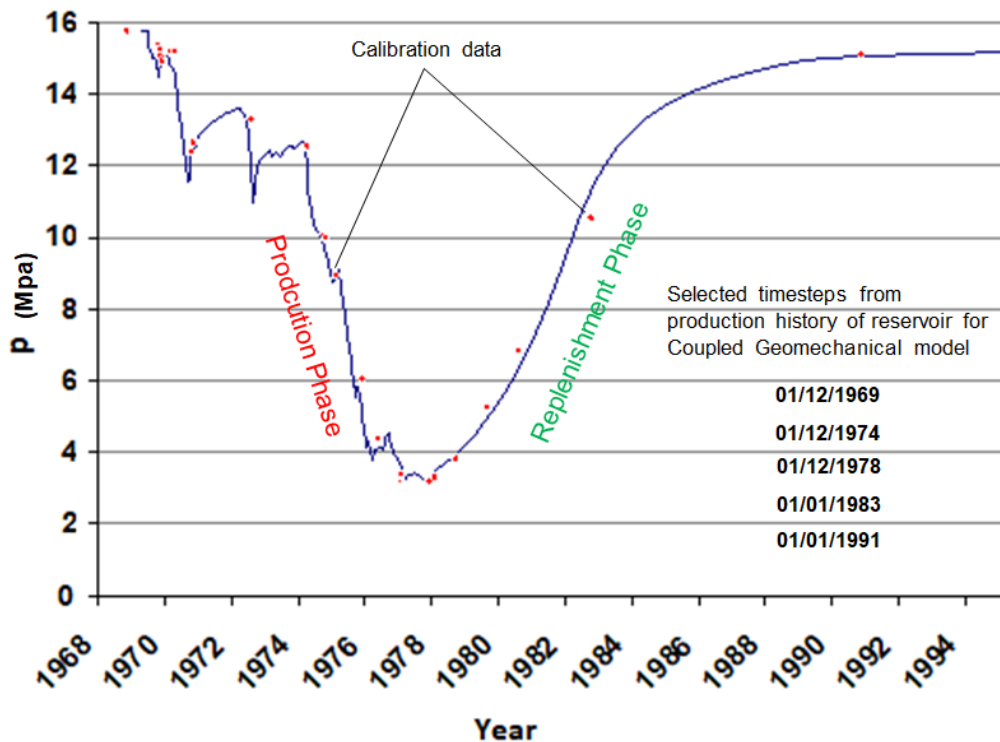


Figure 7-1: Pressure profile during production history of the case study reservoir at well X6. The curve declines during production phase and increase during shut-in phase (replenishment phase) which is present day pore-pressure and starting point of further scenario testing. Continuous blue line represents pressure profile as a result of history match from the flow simulation. Red dots are the observed pressure data which can be used as calibration points on the pressure profile.

## 7.2 Results

The following section describes the dynamic fluid flow models setup for future scenario testing cases designed for long-term (seasonal) as well as short-term (weekly) gas storage operations. The concept for these scenario testing is to evaluate geomechanical stresses on the reservoir due to pressure changes with intensive injection/production cycles. There is one fluid flow model setup for long-term seasonal storage and various models with different short-term cases. German data for excess electricity throughout the year of 2017 has also been considered in two cases to address the issues of renewable energy aspects. This implies the excess of power energy (electricity) in Germany can be stored in underground gas storage with Power-to-Gas (PtG) concept and then the stored gas can be reused for power generation (Gas-to-Power) when needed. All the cases are summarized in Table 7-1. The starting pressure point of these future scenario testing cases is the end point pressure of replenishment phase (Figure 7-1) i.e. ~15.8 MPa.

Table 7-1: All future testing scenario cases with input parameters. WBHP is well bottom hole pressure, WGIR is well gas injection rate, and WGPR is well gas production rate.

Future testing Scenario cases	Sub divisions		Input parameters			
			WBHP Upper limit (MPa)	WBHP lower limit (MPa)	WGIR (m <sup>3</sup> /day)	WGPR (m <sup>3</sup> /day)
Long-term (seasonal)			18.8	13.8	100000	100000
Short-term (weekly)	With limited water cut rate (5 m <sup>3</sup> /day)	With 1 well	18.8	13.8	10000	10000
		With 2 wells	18.8	13.8	100000	100000
		With 3 wells	18.8	13.8	100000	100000
	Without limited water cut rate	With 1 well	18.8	13.8	10000	10000
		With 2 wells	18.8	13.8	100000	100000
		With 3 wells	18.8	13.8	100000	100000
Random schedule cases	With limited water cut rate (5 m <sup>3</sup> /day)	With 1 well	18.8	13.8	100000	100000
	Without limited water cut rate	With 1 well	18.8	13.8	100000	100000

### 7.2.1 Long-term (seasonal) case

The long-term case represents the seasonal case which involves storage operations with six months

gas injection and subsequently six months production. These storage operations have been performed on Well X6. The scenario model is established for 10 years i.e. from 1<sup>st</sup> January 2020 till 1<sup>st</sup> January 2031. The first half of each year is the injection period, with a constant gas injection rate of 100,000 m<sup>3</sup>/day, and it is controlled by the upper limit of Well Bottom Hole Pressure (WBHP), which is approximately 18.8 MPa. Whereas, the second half of each year is the production period with a maximum gas rate (100,000 m<sup>3</sup>/day) controlled by lower limit of bottom hole pressure, which is approximately 13.8 MPa (Figure 7-2 b). The upper limit of WBHP (18.8 MPa) has been kept in order to avoid fault reactivation and fracture inducing phenomena. While, the lower limit of WBHP is to avoid sand production. Pre-scenario testing field pressure (~15.4 MPa) has been taken from history match obtained by the replenishment of the reservoir pressure. Field pressure (FPR) increases linearly at each injection phase until the convergence achieved after six injection-production cycles and the FPR reaches maximum of ~15.65 MPa on date 30 June 2026. Hereafter, FPR remains constant with slight deviations. On the other hand, FPR drops at each production phase to a pressure of ~15.40 MPa (Figure 7-2 a). The reason of gradual increase of FPR during the initial injection phase could be water encroachment in the reservoir. Due to this phenomena gas injection rate is lower at the initial stages and subsequently higher at later stages.

Initially, the well water production rate (WWPR) from the Well X6 is about ~10m<sup>3</sup>/day but drops to ~4m<sup>3</sup>/day after 4 injection-production cycles (Figure 7-2 c). Well gas injection rate (WGIR) and the well gas production (WGPR) rate are ~40000 m<sup>3</sup>/day at initial injection-production cycle and then linearly increase till 5<sup>th</sup> cycle reaching equilibrium (i.e. ~1E+5 m<sup>3</sup>/day) (Figure 7-2 d). Water encroachment during the long shut-in phase could be the reason for higher water cut and lower gas production rate during initial cycles.

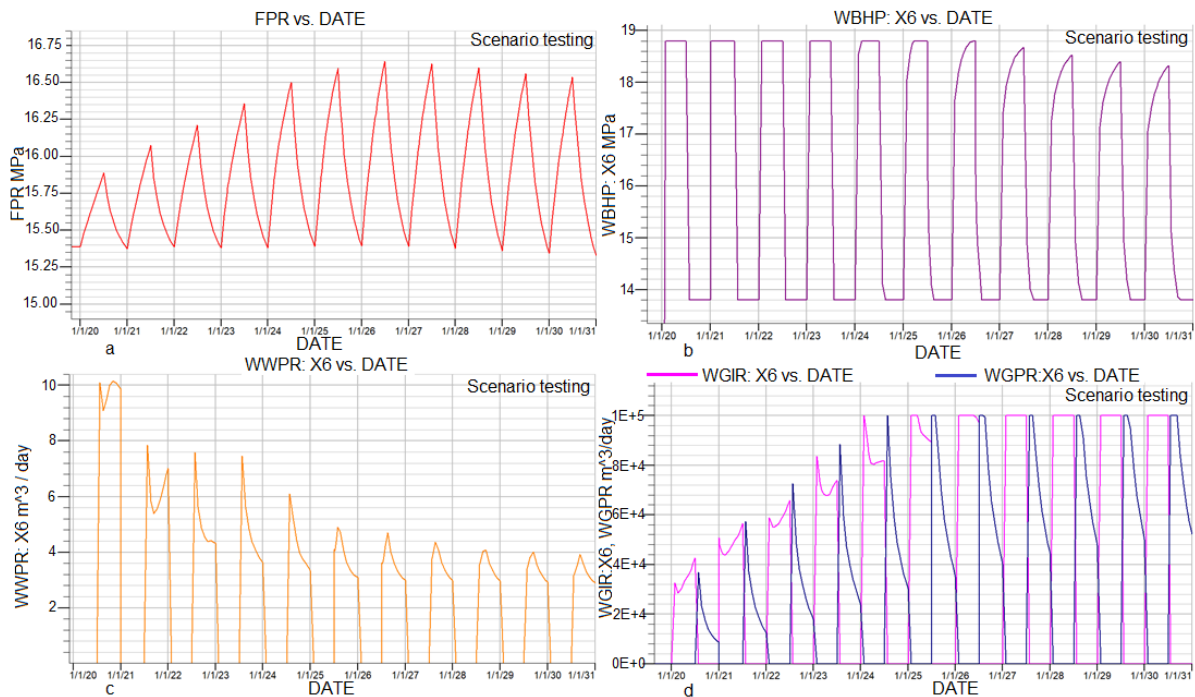


Figure 7-2: Seasonal scenario testing case that represents six months injection and six months production cycle for Well X6. (a) Field pressure (FPR) profile for these cycles, (b) Well bottom hole pressure (WBHP), (c) Well water production rate (WWPR) and (d) Well gas injection rate (WGIR) and well gas production rate (WGPR).

**7.2.2 Short-term cases**

Short-term scenario cases represent weekly storage operations. The scenario scheme has been designed to compensate excess of power produced in a season and store Power-to-Gas energy into same underground gas storage. Short-term cycle consists of 1 week injection-1 week shut in and two weeks production and 1 week shut in phases (1wkInj-1wkShut-2wkProd-1wkShut) for one year. During the injection week, gas is injected in to the reservoir which builds up field pressure (but again limited by 18.8 MPa upper limit of WBHP), and then one week shut in that maintains the pressure and then two weeks production phase to withdraw gas which drops the field pressure (lower limit constraint to 13.8 MPa) and again shut in to maintain well bore pressure.

Short-term cases are further divided in two groups: (1) with limited water cut-off and (2) without limited water cut-off. The explanation of both cases is discussed in the following section.

**7.2.2.1 Short-term cases with limited water cut-off**

These cases comprise the same schedule as discussed above but the well water production rate (WWPR) is limited to 5 m<sup>3</sup>/day in order to take into consideration the economic aspects of operating the gas storage. Commercial storage industry limits the water production rates to minimize operating costs and enhance economic returns. Therefore, this aspect has also been considered in scenario case studies.

**7.2.2.1.1 With one well**

This scenario has been performed on the vertical well X6. The same schedule scheme 1wkInj-1wkShut-2wkProd-1wkShut for 1 year has been used in this case. The well water production rate (WWPR) is restricted to 5 m<sup>3</sup>/day (Figure 7-3c). FPR in this case does not fluctuate significantly and maintains the pressure window between ~15.39 MPa and ~15.40 MPa in production and injection phases respectively (Figure 7-3a). The WBHP fluctuation is relatively smaller during the initial 3 cycles but afterwards maintains the pressure window between 16.25 MPa and 14.75 MPa with injection and production phase respectively (Figure 7-3b). The well gas injection rates (WGIR) remain constant throughout a year i.e. 10000 m<sup>3</sup>/day, but the well gas production rates (WGPR) remain lower to about 2000 m<sup>3</sup>/day during the initial 2 cycles and then increases up to 4000 m<sup>3</sup>/day at the end of the schedule cycle (Figure 7-3d). The lower WGPR compared to WGIR is due to the limited WWPR, which does not allow the well to take higher WGPR.

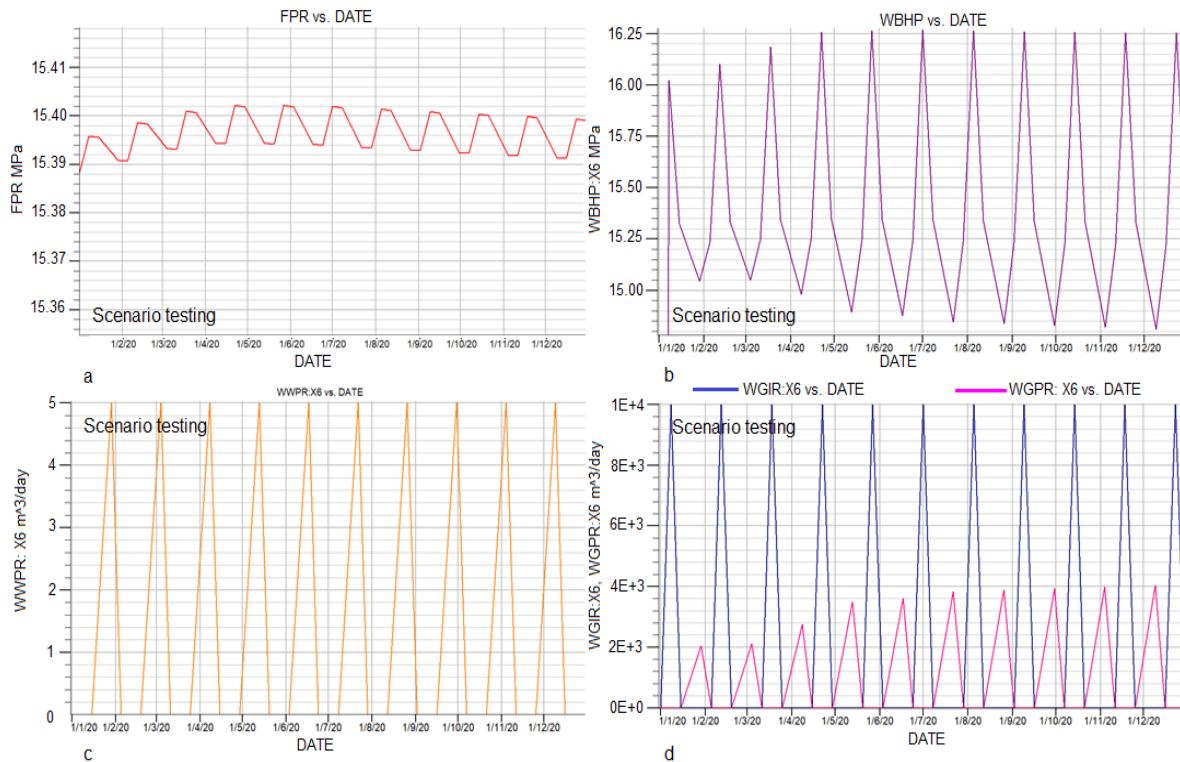


Figure 7-3: Short-term case characterizes 1 week injection-1 week shut in and two weeks production and 1 week shut in phases (1wkInj-1wkShut-2wkProd-1wkShut) for one year with one vertical well X6. (a) Field pressure (FPR) profile for these cycles, (b) Well bottom hole pressure (WBHP), (c) Well water production rate (WWPR) and (d) Injection (WGIR) and production (WGPR) gas rates.

### 7.2.2.1.2 With two wells

This short-term case has been performed on the vertical well X6 and the horizontal well H2. The same schedule scheme 1wkInj-1wkShut-2wkProd-1wkShut for 1 year has been used in this case. The well water production rate (WWPR) is restricted to  $5 \text{ m}^3/\text{day}$  (Figure 7-4c). The FPR has been shown in (Figure 7-4a). Production and injection rates for Well X6 have already been explained in above section (7.2.2.1.1). The WBHP for vertical well X6 drops in production phase when compared with horizontal well H1. WBHP behavior of both wells is exhibited in Figure 7-4b. WGPR and WGIR of horizontal well H1 is shown in Figure 7-4d, where, WGPR is far less than WGIR due to restricted WWPR. WGPR of well H1 begins at  $100 \text{ m}^3/\text{day}$  during the first cycle and reaches later at the end of the schedule year to about  $1000 \text{ m}^3/\text{day}$ . Horizontal well production rate is even less than the vertical well production rate with same water cut rate and similar lower limit of bottom hole pressure (BHP) 13.8 MPa.

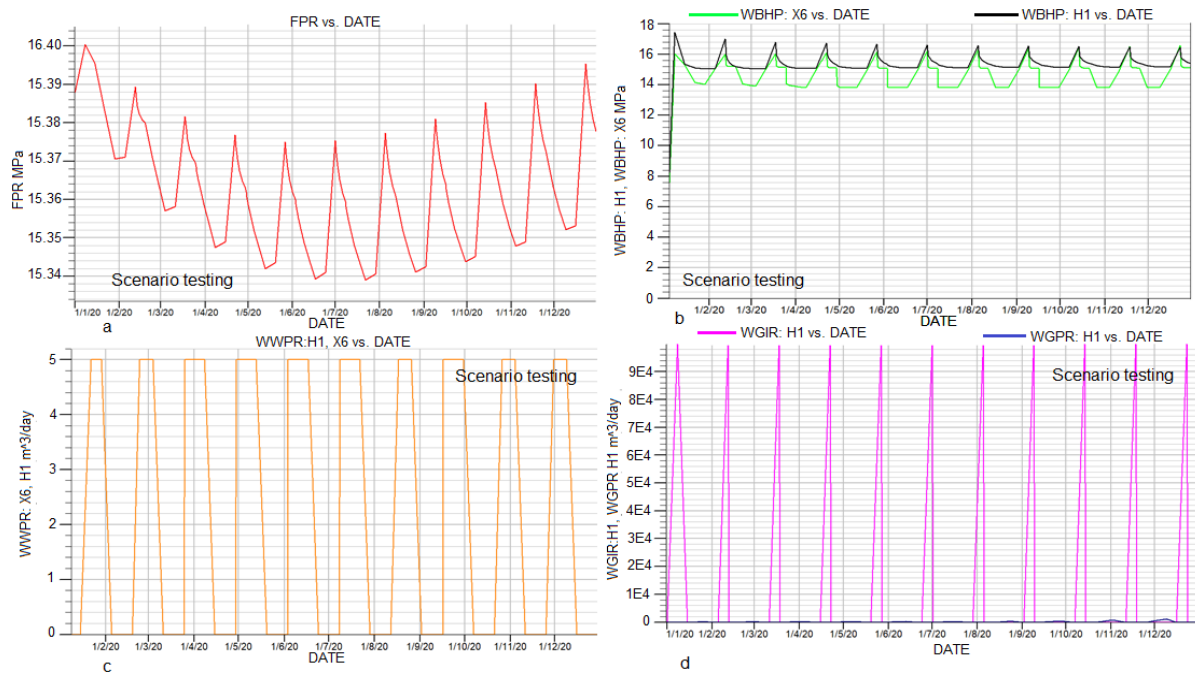


Figure 7-4: Short-term case exemplifies 1wkInj-1wkShut-2wkProd-1wkShut schedule of two wells (1 vertical well X6 and 1 horizontal well H1) for 1 year. (a) is field pressure (FPR) profile for these cycles, (b) Well bottom hole pressure (WBHP) of both wells X6 and H1, (c) Well water production rate (WWPR) for well H1 and (d) Injection (WGIR) and production (WGPR) gas rates for well H1.

**7.2.2.1.3 With three wells**

There are three wells considered for this scenario, two wells are vertical wells (X2 and X6) and one is horizontal well (H1). All the wells have been considered to have the same short-term weekly schedule as discussed above. The gas rate for injection and production both is 100,000 m<sup>3</sup>/day. Bottom hole pressure is constraint by an upper limit 18.8 MPa and lower limit of 13.8 MPa in case of injection and production respectively. Water cut-off is again 5 m<sup>3</sup>/day in production phase to limit the production of water from each well.

FPR profile for this case is shown in Figure 7-5. The progressive oscillation cycles of FPR are injection (upward) and production (downwards) phases. The overall upward trend of FPR from its initial pressure of ~15.39 MPa represents the buildup pressure with each passing schedule cycle. The upward trend of FPR throughout the schedule year is due to well water production rate (WWPR) (Figure 7-6d) and as a result, the field pressure is not stabilized in such a short time span. In order to maintain material balance in this scenario, the injection rate should be lowered down to the actual production rates of each cycle.

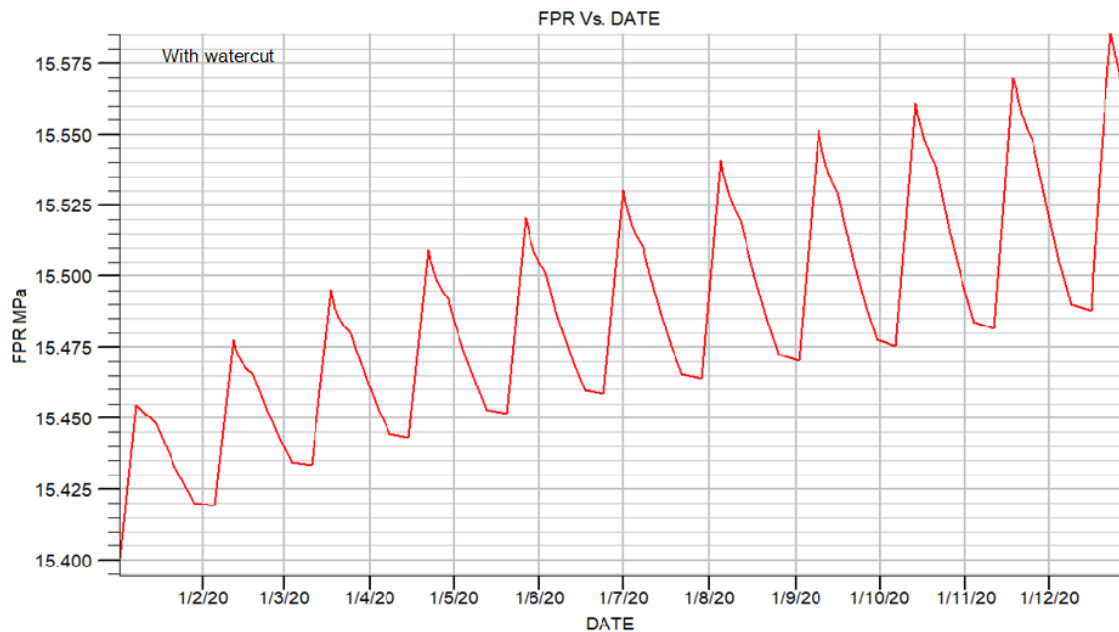


Figure 7-5: Field pressure (FPR) profile of all three well (X2, X6 and H1) with schedule 1wkInj-1wkShut-2wkProd-1wkShut for 1 year.

The comparison of the properties of all three wells is summarized in Figure 7-6. WBHP of X6 reaches the maximum limit of 18.8 MPa at the end of each injection cycle and drops back to ~15 MPa at the end of production phase. WBHP of X2 also shows similar behavior but at lower pressure e.g. it varies between 16 MPa and 17 MPa at the end of each injection phase and drops back to the same level of ~15 MPa. WBHP behavior of H1 is however different from both X2 and X6. It reaches to a maximum value of 16 MPa at the peak injection time and drops to the lowest level of ~14 MPa (Figure 7-6a). WGPR behavior of all three wells is similar with respect to linear increase with each increasing cycle. However, rates are completely different for each well. WGPR of well X2 ranges ~10,000-11,000 m<sup>3</sup>/day during the initial cycles but reaches up to 18000 m<sup>3</sup>/day at the end of the schedule. Contrarily, WGPR of well X6 ranges ~5000-6000 m<sup>3</sup>/day during the initial cycles but reaches up to ~9000 m<sup>3</sup>/day at the last cycle. An entirely different behavior of WGPR is exhibited by well H1, where it shows ~50 m<sup>3</sup>/day during the initial cycles but reaches up to ~1100 m<sup>3</sup>/day at the end of the schedule year (Figure 7-6b).

The WGIR profile of each well is completely different to the profile of the WGPR; the WGIR of well H1 shows the highest WGIR rates among other vertical wells (X2 and X6). WGIR of H1 reaches to the maximum rate of 100,000 m<sup>3</sup>/day. WGIR of well X2 and X6 reach a maximum of 40,000 m<sup>3</sup>/day and 50,000 m<sup>3</sup>/day respectively (Figure 7-6c).

The comparison shows that the horizontal well allows more gas injection and less gas production than the vertical wells and vice versa.



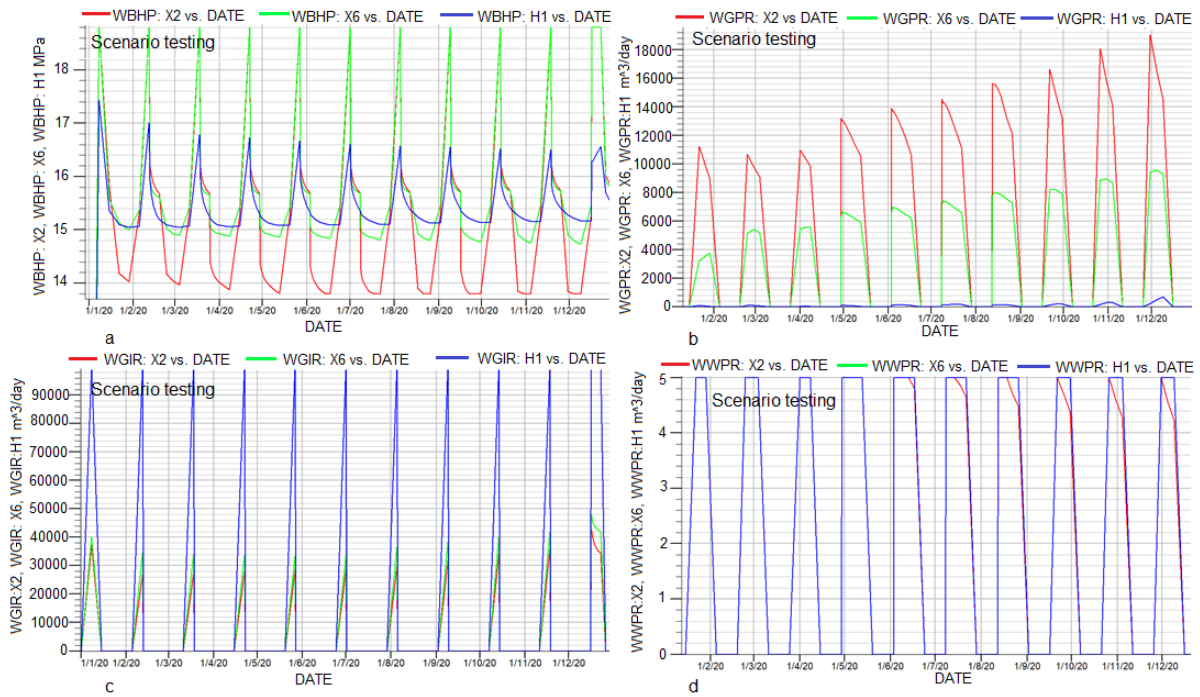


Figure 7-6: Well properties comparison of three wells case scenario with short-term schedule 1wkInj-1wkShut-2wkProd-1wkShut for 1 year. X2 and X6 are vertical wells and H1 is the horizontal well. (a) Well bottom hole pressure (WBHP) of all wells, (b) production gas rates (WGPR) for all three wells, (c) Injection gas rates (WGIR) for all three wells and (d) Well water production rate (WWPR) for all the wells.

### 7.2.2.2 Short-term cases without limited water cut-off

All the cases presented in this section have the same schedule i.e. 1wkInj-1wkShut-2wkProd-1wkShut for 1 year, but without any limit of well water production rate (WWPR) in the production phase. Therefore, all these cases have no WWPR limit of 5 m<sup>3</sup>/day.

#### 7.2.2.2.1 With one well

This scenario is carried out on a vertical well X6. In this case the same scenario schedule scheme 1wkInj-1wkShut-2wkProd-1wkShut is used for 1 year. During the initial six schedule cycles, FPR drops linearly after each phase of production cycle from ~15.39 MPa to about ~15.35 MPa. Afterwards, FPR does not fluctuate significantly and maintains the pressure window between ~15.33 MPa and ~15.35 MPa in production or injection phase (Figure 7-7a). WBHP fluctuation is constraint by the upper limit injection pressure of 18.8 MPa and lower limit production pressure of 13.8 MPa. Thus, WBHP cannot exceed upper limit of 18.8 MPa and cannot drop under lower limit of 13.8 MPa regardless of higher injection-production rates. WBHP maintains the pressure window of ~16.4 MPa during injection phase and of ~13.8 MPa during production phase of each schedule cycle (Figure 7-7b). The well water production rate (WWPR) is not restricted to 5 m<sup>3</sup>/day and is shown in (Figure 7-7c). WWPR is high at the initial cycle i.e. ~34 m<sup>3</sup>/day but decrease linearly to ~14 m<sup>3</sup>/day at the end of the schedule cycle, which indicates that the well produces more water during the initial injection operations right after long shut-in phase (i.e. starting point of schedule testing), but subsequently decreases after each passing cycle and stabilizes at 14 m<sup>3</sup>/day. The well gas injection rate (WGIR) remain constant during one year, i.e. 10,000 m<sup>3</sup>/day, but the well gas production rate (WGPR) remains unchanged during initial three cycles. Then it decreases linearly to ~6200 m<sup>3</sup>/day at the end of the schedule and remains the same afterwards (Figure 7-7d).

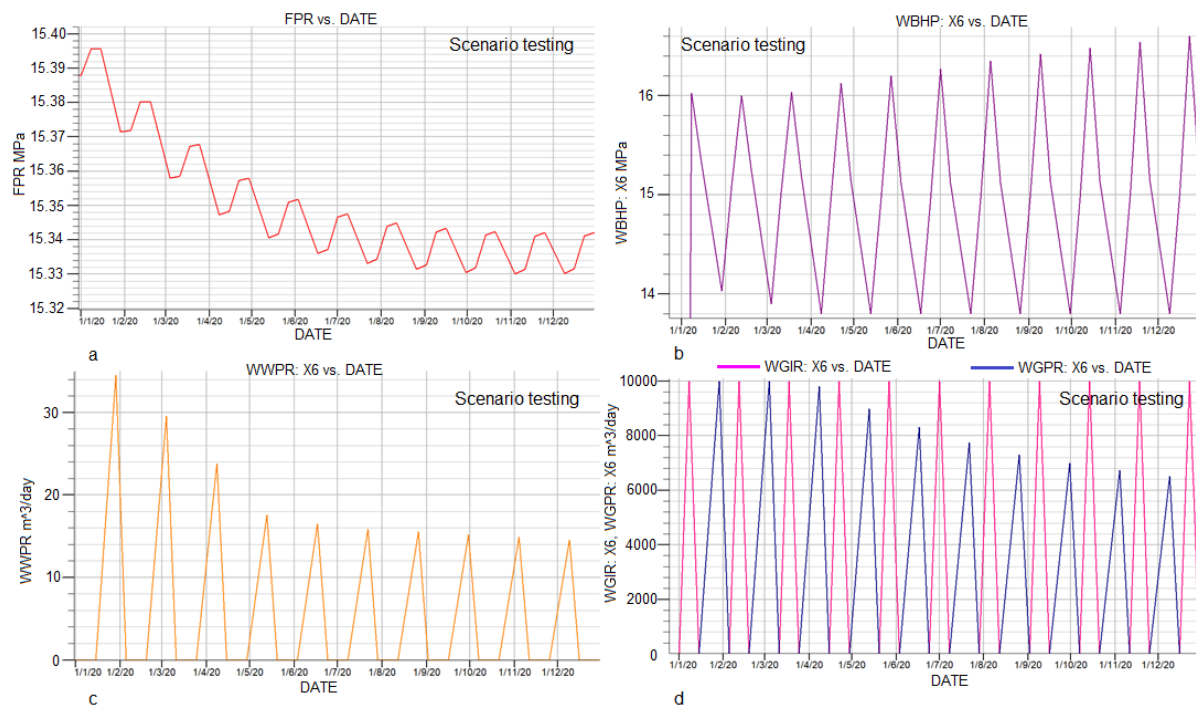


Figure 7-7: The properties of short-term case without water cut describes (1wkInj-1wkShut-2wkProd-1wkShut) schedule for one year with one vertical well X6. (a) field pressure (FPR) profile for these cycles, (b) Well bottom hole pressure (WBHP), (c) Well water production rate (WWPR) and (d) Injection (WGIR) and production (WGPR) gas rates.

#### 7.2.2.2 With two well

This short-term scenario without water cut is carried out on two wells: a vertical well X6 and a horizontal well H2. The same schedule 1wkInj-1wkShut-2wkProd-1wkShut for 1 year was used in this case. The FPR is shown in Figure 7-8a. FPR retains in the window of  $\sim 15.37$  MPa and  $\sim 15.31$  MPa in injection and production phases respectively after dropping from  $\sim 15.40$  MPa and  $\sim 15.70$  at the first cycle during injection and production phases respectively. The WBHP for well X6 and H1 reaches maximum to 16.5 MPa and 17.4 MPa respectively and drops to  $\sim 13.8$  MPa for both wells. Furthermore, the behavior of both wells is presented in Figure 7-8b. The well gas production rate (WGPR) and well gas injection rate (WGIR) as well as well water production rate (WWPR) for well X6 are already discussed in the above section (7.2.2.1). The WWPR of well H1 remains in the limit of  $250 \text{ m}^3/\text{day}$  to  $300 \text{ m}^3/\text{day}$  throughout the schedule time (Figure 7-8c). WGPR and WGIR of the horizontal well H1 are shown in Figure 7-8d. WGIR reaches maximum a value of  $10,000 \text{ m}^3/\text{day}$  during injection period and drops to  $0 \text{ m}^3/\text{day}$  during shut-in phase throughout the schedule year. WGPR of H1 remains in the range of  $1000$  to  $20,000$  during initial cycle but cross over  $60,000 \text{ m}^3/\text{day}$  at the end of the schedule cycle.

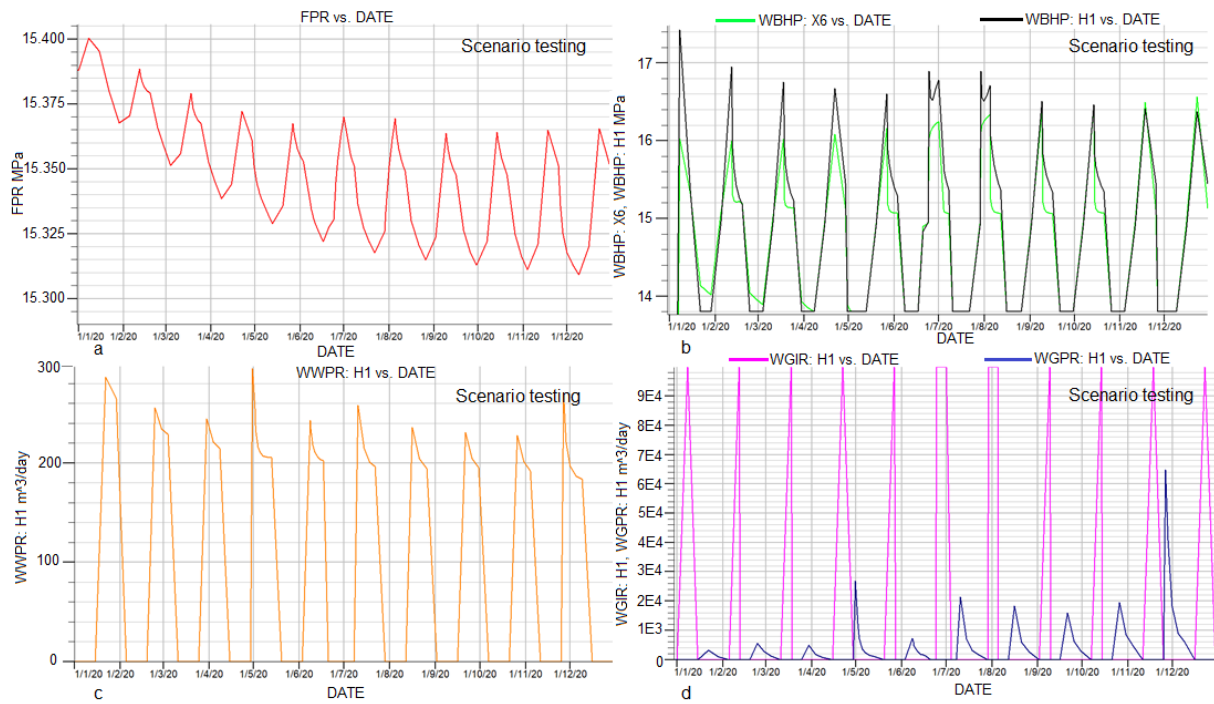


Figure 7-8: Short-term case demonstrates 1wkInj-1wkShut-2wkProd-1wkShut schedule of two wells (1 vertical well X6 and 1 horizontal well H1) for 1 year without water cut.. (a) is field pressure (FPR) profile for these cycles, (b) is Well bottom hole pressure (WBHP) of both wells X6 and H1, (c) is Well water production rate (WWPR) well water production rate (WWPR) for well H1 and (d) is Injection (WGIR) and production (WGPR) gas rates for well H1.

### 7.2.2.2.3 With three wells

Three wells are considered for this scenario, two of which are vertical wells (X2 and X6) and one horizontal well (H1). All wells were assumed to have the same short-term weekly schedule as described above. WGIR and WGPR both have same value of 100,000 m<sup>3</sup>/day; however, they are constrained by the upper limit of BHP of 18.8 MPa and the lower limit of BHP of 13.8 MPa in the case of injection and production respectively. In the production phase, WWPR is not limited to 5 m<sup>3</sup>/day from each well.

The FPR profile for this case is shown in Figure 7-9. The progressive oscillation cycles of the FPR are injection (upward) and production (downward) phases. The general trend of the FPR remains within the limit of ~15.85 MPa and ~15.375 MPa during injection and production phase respectively.

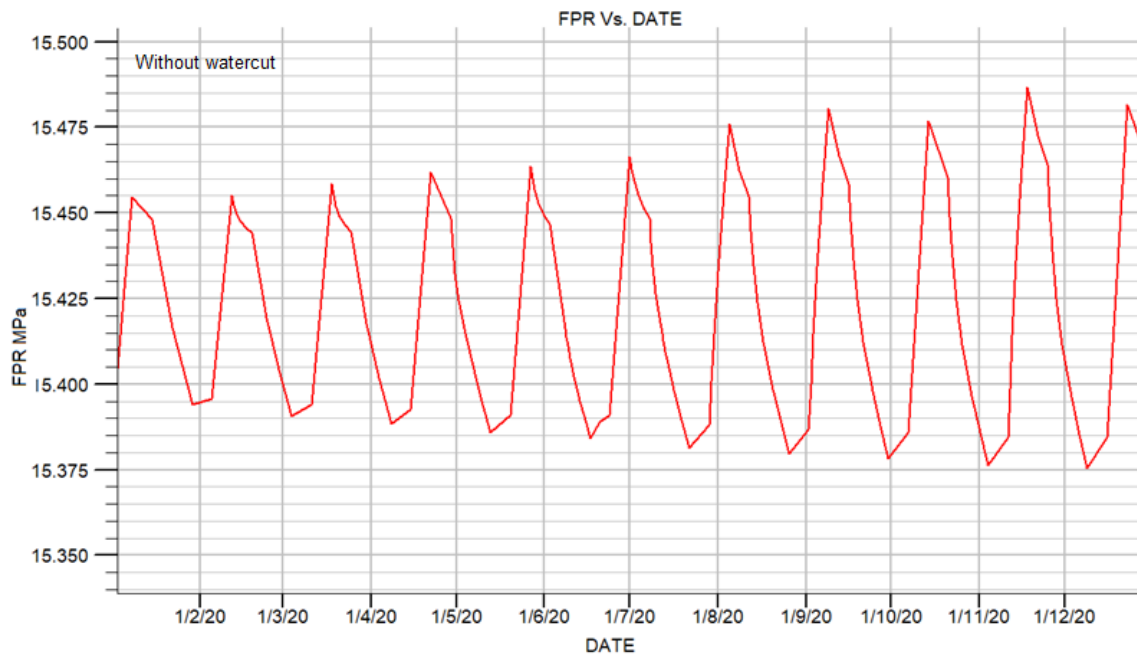


Figure 7-9: Field pressure (FPR) profile of all three well (X2, X6 and H1) with schedule 1wkInj-1wkShut-2wkProd-1wkShut for 1 year without water cut-off.

The comparison of the properties of all three wells is summarized in Figure 7-10. The WBHP of X6 reaches the maximum limit of 18.8 MPa at the end of each injection cycle and falls back to ~13.8 MPa at the end of the production phase. The WBHP of X2 also shows almost similar behavior. However, the WBHP behavior of H1 is different from both X2 and X6. It reaches a maximum value of 17.4 MPa at peak injection time and drops to the lowest level of ~13.8 MPa (Figure 7-10a). The WGPR behavior of all three wells is similar in terms of linear increase with each increasing cycle. However, the rates are completely different for each well. The WGPR of well X2 is ~12,000-16,000 m<sup>3</sup>/day during the initial cycles, but reaches up to 24,000 m<sup>3</sup>/day at the end of the schedule. In contrast, the WGPR of well X6 varies between 14,000 and 15,000 m<sup>3</sup>/day during the initial cycles, and reaches up to 22,000 m<sup>3</sup>/day at the end of the last schedule cycle. WGPR of well H1 is entirely different from other two wells, because it shows ~400-500 m<sup>3</sup>/day during the initial cycles, but reaches up to ~70,000 m<sup>3</sup>/day at the end of the schedule year (Figure 7-10b).

WGIR profile of each well is completely different to WGPR profile; WGIR of well H1 shows the highest WGIR among the other vertical wells (X2 and X6). WGIR of well H1 reaches the maximum value of 100,000 m<sup>3</sup>/day. WGIR of wells X2 and X6 reaches a maximum value of 44,000 m<sup>3</sup>/day and 45,000 m<sup>3</sup>/day respectively (Figure 7-10c). The comparison shows that the horizontal wells allow higher WGIR and WGPR than the vertical wells at the same WBHP conditions.

WWPR of well X2 allows maximum rate of 5m<sup>3</sup>/day throughout schedule year and the WWPR of well X6 also remain constant all over the schedule year with the rate of 10 m<sup>3</sup>/day. While, the WWPR of well H1 remains higher within the range of 250 m<sup>3</sup>/day and 310 m<sup>3</sup>/day (Figure 7-10d).

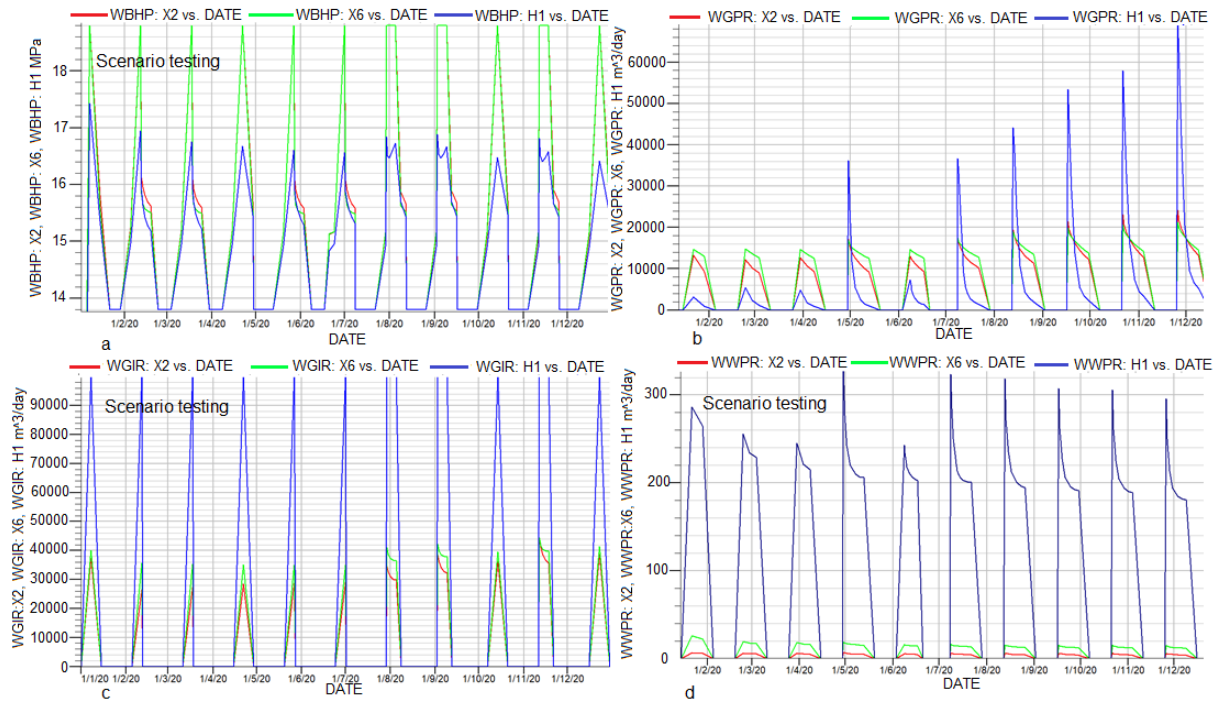


Figure 7-10: Well properties comparison of three wells case scenario with short-term schedule 1wkInj-1wkShut-2wkProd-1wkShut 1 year without water cut. X2 and X6 are vertical wells and H1 is the horizontal well. (a) Well bottom hole pressure (WBHP) of all wells, (b) production gas rate (WGPR) for all three wells, (c) Injection gas rate (WGIR) for all three wells and (d) Well water production rate (WWPR) for all the wells.

### 7.2.2.3 Random Schedule

The excess of electricity produced [100] [101] in Germany could be stored in underground gas storage by converting the power energy to gas (Power-to-Gas). PtG is a process of generation of a gas with high energy density through the electrolysis of water. The first intermediate product is power-to-hydrogen, which can be converted into synthetic methane gas power-to-methane in a subsequent methanation process that requires the injection of CO<sub>2</sub>. In this way the same seasonal underground gas storage can also be used as battery for excess energy in a calendar year. Figure 7-11 shows the Germany’s data of excess of electricity produced in a calendar year 2017. It can be seen from the data that during the summer time (from March till August) electricity produced from renewable sources such as wind and solar increases enormously. The combined wind energy (onshore and offshore) shows high variation during the first and fourth quarter of the year, meaning this high variation of electricity production from renewable sources can be stored (Power-to-Gas) and reused (Gas-to-Power) in case of excess and shortage of electricity respectively.

These scenarios have been performed on well X6. The schedule is based on the data shown in Figure 7-11. The base line of 10 GW is considered to be shut-in period. Above 10 GW base line is considered to have excess of electricity that can be used as injection periods for Power-to-Gas storage and below the limit of 10 GW is the shortage of electricity and these periods have been considered for production of gas for Gas-to-Power conversion. This data [100] [101] of excess electricity from Germany has been used to make two short-term random schedule cases: one with limited water cut-off and one without limited water cut-off. The following section considers the detailed analyses of these short-term cases.

## Stromerzeugung und Stromverbrauch 2017

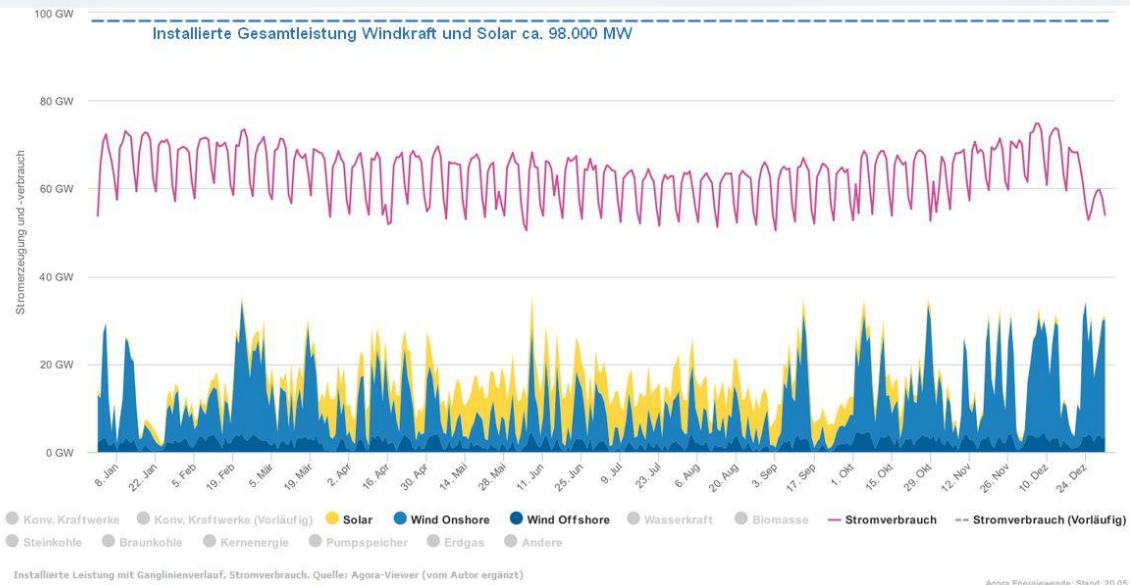


Figure 7-11: Data shows the consumption of total electricity in Germany along with electricity produced from renewable energy sources (such as wind, either offshore or onshore and solar) in the Calendar year 2017 [100] [101].

### 7.2.2.3.1 With limited water cut-off

This scenario has been performed on a vertical Well X6. The schedule timeline of 1 year has been adopted from Figure 7-11. The well water production rate (WWPR) is restricted to  $5 \text{ m}^3/\text{day}$  (Figure 7-12c). FPR eventually increases in this case up to 15.72 MPa with slight variations during the gas production cycles. Gas injection succeeds to maintain the pressure and it can be seen that it increases from  $\sim 15.39 \text{ MPa}$  and reaches approximately  $\sim 15.72 \text{ MPa}$  at the end of the one year period (Figure 7-12a). The variability of WBHP is directly proportional to the gas production cycles. As can be seen in the Figure 7-12a, as the gas production increases, well bottom-hole pressure decreases even as the gas injection continues. Maximum WBHP reaches a value of 18.8 MPa and the minimum WBHP reaches a value of 14.4 MPa and these maximum and minimum pressure values represent injection and production cycles (Figure 7-12b). Well gas injection rate (WGIR) varies during the year having a minimum injection rate of approximately  $32,000 \text{ m}^3/\text{day}$  and a maximum rate of about  $66,000 \text{ m}^3/\text{day}$ . In contrast, well gas production rate (WGPR) has a minimum and maximum value of  $4300 \text{ m}^3/\text{day}$  and  $19,000 \text{ m}^3/\text{day}$  respectively (Figure 7-12d). The lower WGPR compared to WGIR is due to the limited WWPR, which does not allow the well to produce at a higher WGPR.

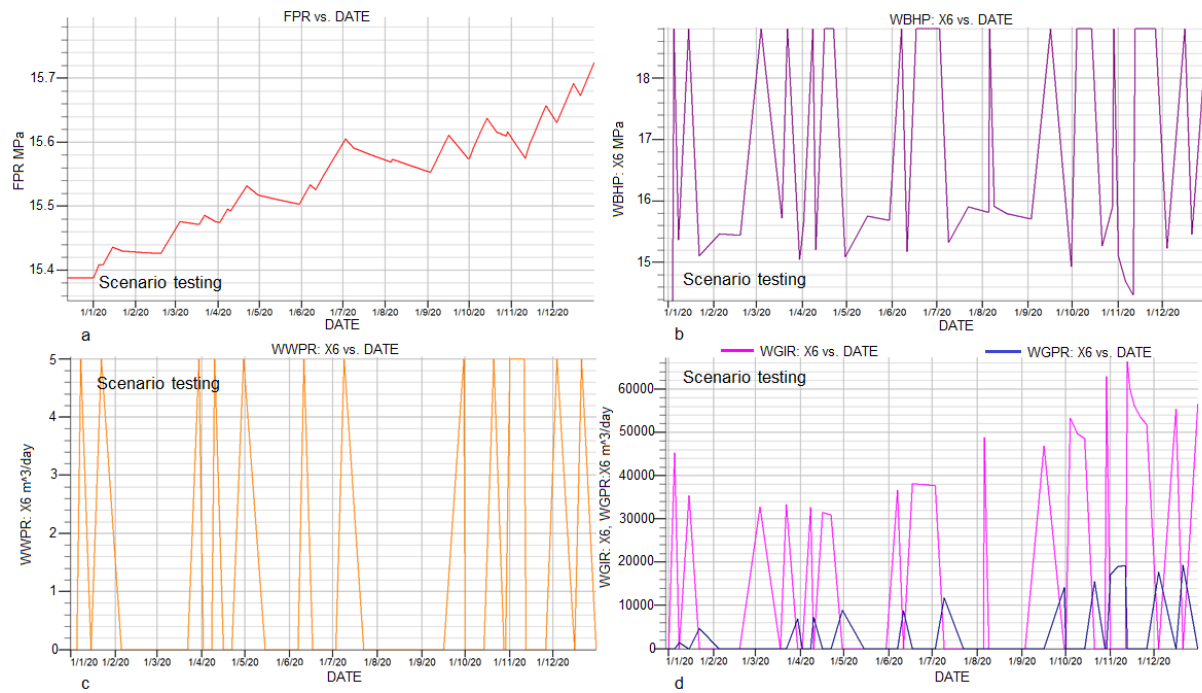


Figure 7-12: The fluctuation of electricity produced in Germany from renewable sources in 2017 is modeled in to future scenario testing case with limited water cut-off ( $5 \text{ m}^3/\text{day}$ ). The excess of energy can be stored in UGS and can be used when needed. This schedule is helpful to understand which month of the year energy can be stored as gas in UGS and in which month of the year this energy can be utilized when shortage occurs. (a) Field pressure (FPR) profile for these cycles, (b) Well bottom hole pressure (WBHP) of well X6, (c) well water production rate (WWPR) for well X6 and (d) Well gas injection rate (WGIR) and well gas production rate (WGPR) for well X6.

### 7.2.2.3.2 Without limited water cut-off

This scenario has been performed on a vertical Well X6. The schedule timeline of 1 year has been adopted from Figure 7-11. There was no water cut-off rate limit set in this scenario, hence the maximum water production rate (WWPR) increases up to  $43 \text{ m}^3/\text{day}$  and remains below  $20 \text{ m}^3/\text{day}$  throughout the production and injection period of 1 year respectively (Figure 7-13c). FPR is sustained in this case by gas injection and increases up to a maximum value of  $15.62 \text{ MPa}$  with slight variation during the gas production cycles in 1-year period (Figure 7-13a). The alteration in WBHP is directly proportional to the gas production cycles without a water cut-off limit. As it can be seen in the Figure 7-13b that WBHP reaches a maximum value of  $18.8 \text{ MPa}$  and the minimum value of approximately  $13.8 \text{ MPa}$ . Well gas injection rate (WGIR) varies during the year having a minimum injection rate of approximately  $32,000 \text{ m}^3/\text{day}$  and a maximum rate of about  $60,000 \text{ m}^3/\text{day}$ , whereas, well gas production rate (WGPR) has a minimum and maximum value of  $16,000 \text{ m}^3/\text{day}$  and  $40,000 \text{ m}^3/\text{day}$  respectively (Figure 7-13d).

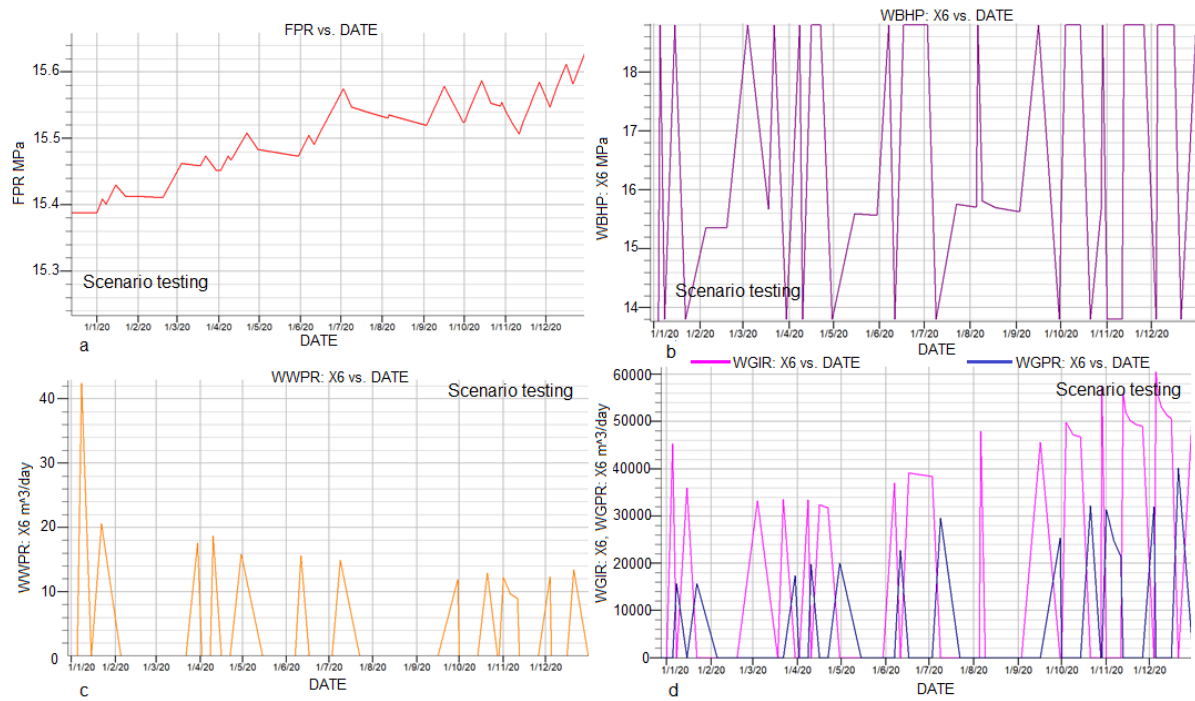


Figure 7-13: The fluctuation of electricity produced in German from renewable sources in 2017 is modeled in to future scenario testing case without limited water cut-off. The excess of energy can be stored in UGS reservoirs and can be used when needed. This schedule is helpful to understand which month of the year energy can be stored as gas in UGS and in which month of the year this energy can be utilized when shortage occurs. (a) Field pressure (FPR) profile for these cycles, (b) Well bottom hole pressure (WBHP) of well X6, (c) well water production rate (WWPR) for well X6 and (d) Injection (WGIR) and production (WGPR) gas rates for well X6.



## Chapter 8 Thermal model

### 8.1 Model setup

The same dynamic model as discussed above (section 4.2.4) has been used for thermal analyses. Since the long-term injection would impact the thermal changes in reservoir significantly, long-term seasonal case (discussed in section 7.2.1) is used to analyze the temperature changes within reservoir if a foreign gas is injected into the reservoir. The initial reservoir temperature is  $\sim 45^\circ\text{C}$  and foreign gas temperature is  $25^\circ\text{C}$ . Two cycles have been considered to analyze the temperature changes during these injection/production operations. Gas is injected into the reservoir for first half year and produced in the second half of the year 2020 and 2021 (see Figure 7-2a). Two wells X2 and X6 are considered to analyze the temperature changes around the well bore vicinity. The bottom hole pressure (WBHP) for both wells is set to an upper limit of 18.8 MPa and a lower limit of 13.8 MPa in case of injection and production phases respectively. These pressure limits are set in place to avoid fault reactivation or fracture inducing phenomena during injection phase as well as to avoid sand production or contraction of the reservoir during production phase. WGIR and WGPR are set to  $100,000 \text{ m}^3/\text{day}$  for both wells.

#### 8.1.1 Thermal stresses

Thermal stresses are the stresses that occur due to the change in temperature in the system i.e. original temperature minus final temperature. If the foreign gas is injected in to the underground gas reservoir, the temperature in reservoir changes which causes thermal related stress changes in the reservoir. The relationship of temperature changes and thermal stress is expressed by the following equation [102]:

$$S_t = E * \alpha_t(T_f - T_0) = E * \alpha_t(\Delta T) \quad (33)$$

In the above equation,  $S_t$  is thermal stress,  $E$  is the Young's modulus,  $\alpha_t$  is the thermal coefficient,  $T_f$  is the final temperature of the reservoir,  $T_0$  is the original temperature of the reservoir and  $\Delta T$  is the temperature difference in the reservoir. Less  $\Delta T$  causes less thermal stresses in the reservoir and vice versa.

### 8.2 Thermal analysis

The model setup for this case is explained in section 4.2.4. The following section describes the results i.e. temperature changes with injection of colder foreign gas ( $25^\circ\text{C}$ ) into the reservoir (i.e. about  $45^\circ\text{C}$ ) through space and time with seasonal cyclic injection/production phases. Top view of the reservoir surface is shown in the figure at different time steps (Figure 8-1). Two injection/production cycles with four time steps have been selected to show thermal changes in the reservoir with injection and production phases: t1 (01/01/20) is the pre-operational history temperature of the reservoir at well X2 and X6 (Figure 8-1a). Time step t2 (01/07/20) represents the end of the injection time of colder foreign gas ( $25^\circ\text{C}$ ) which is injected for the first half of the year 2020 (Figure 8-1b), t3 (01/01/21) is the end of production period of the cycle (Figure 8-1c) and t4 (01/07/21) is again the end of injection phase of second cycle (Figure 8-1d).

The reservoir temperature is  $45^\circ\text{C}$  at time step t1 which is the pre-operational temperature. The

temperature decreases to about 43°C at well X6 and 42.5°C at well X2 at the time step t2 after constant injection of colder gas (25°C) with a well gas injection rate (WGIR) of 100,000 m<sup>3</sup>/day for six months. The temperature increases to about 43.5°C and ~43°C at wells X6 and X2 respectively at time step t3. There is only about 0.5°C increase of temperature from t2 to t3. Temperatures at well X6 and X2 decrease to about 41.5°C and 42°C respectively, again in the second cycle of injection at t4. Thermal changes are minor and occur only at the vicinity and around the well locations. The thermal effects on the stress are not significant in the reservoir even after injection of 100,000 m<sup>3</sup>/day of colder gas for about a half year. This concludes that the thermal changes in the short-term cases are negligible to be considered to analyze the geomechanical stresses on the reservoir in storage operations.

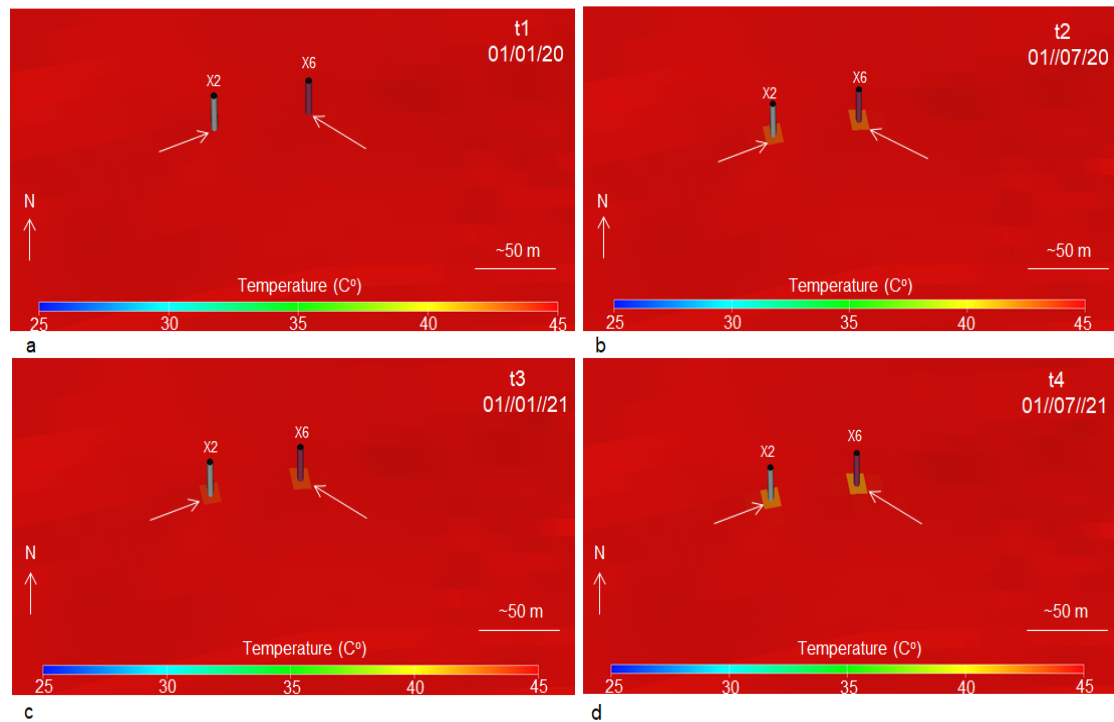


Figure 8-1: Temperature changes around Well X2 and X6 by injecting colder foreign gas at different time steps (t1, t2, t3 and t4). Time steps t1, t2, t3, t4 correspond to 01/01/20, 01/07/20, 01/01/21 and 01/07/21 respectively. The arrows show the exact location of significant temperature difference while injection/production phases. The color scale is in °C, whereas the arrows with N show northward direction.

## Chapter 9 THM coupled model

THM model accounts for both elastic as well as plastic strain. The solid rock behaves elastically under low stress conditions and plastically under high stress conditions. Therefore, the short-term (weekly) scenario testing is performed which accounts for low as well as high injection rate to predict plastic behavior of solid rock formation. Moreover, the high injection rate may also reactivate faults and even form new fracture network, which can also be predicted by dynamic geomechanical modelling. Random time schedule is also taken into account which considers the excess of electricity during low demand that can be converted into gas (PtG) and store it in the underground gas storage for short time and vice versa.

### 9.1 Results

#### 9.2 Surface displacement

Some further results from the THM models are presented in the following sections. First is presented the vertical displacement are calculated for the earth's surface throughout the production and replenishment history of the gas field. For this purpose, various parameters have been used for THM modelling at five selected time steps. Time steps correspond to initial (pre-production), production and depletion phases of the reservoir. The selected time steps with exact dates along with calibration points are shown in Figure 7-1. Maximum pressure fluctuation occurs at depletion ( $t_1$ ) and replenishment ( $t_2$ ) phases of reservoir, therefore main emphasis of this geomechanical assessment will be on these time steps. The maximum vertical displacement of the earth's surface above the reservoir was predicted at the maximum depletion time ( $t_1$ ) in 1978, i.e. nine years after production, and the maximum upheaval was observed during the maximum replenishment time ( $t_2$ ), which took place in 1990, i.e. 12 years after the maximum depletion time ( $t_1$ ). The subsidence of the ground surface at  $t_1$  is due to the compaction processes during the depletion phase, while the slight upheaval during  $t_2$  is due to increase in pore pressure by the active aquifer below the gas-bearing layers [2]. Since the displacement is a function of all cumulative displacements of all underlying cells, the vertical displacement is greatest at the ground surface directly above the reservoir area [2]. The maximum subsidence of -13 mm (negative sign stands for subsidence) at the ground surface above the reservoir is observed during  $t_1$ , which decreases laterally on each side and consequently becomes zero at the edges of the reservoir. During  $t_2$  an inverse surface behavior was observed, which led to a slight upheaval of 11 mm at the ground surface above the reservoir. The translation of the reservoir deformation to the ground surface is shown in Figure 9-1.

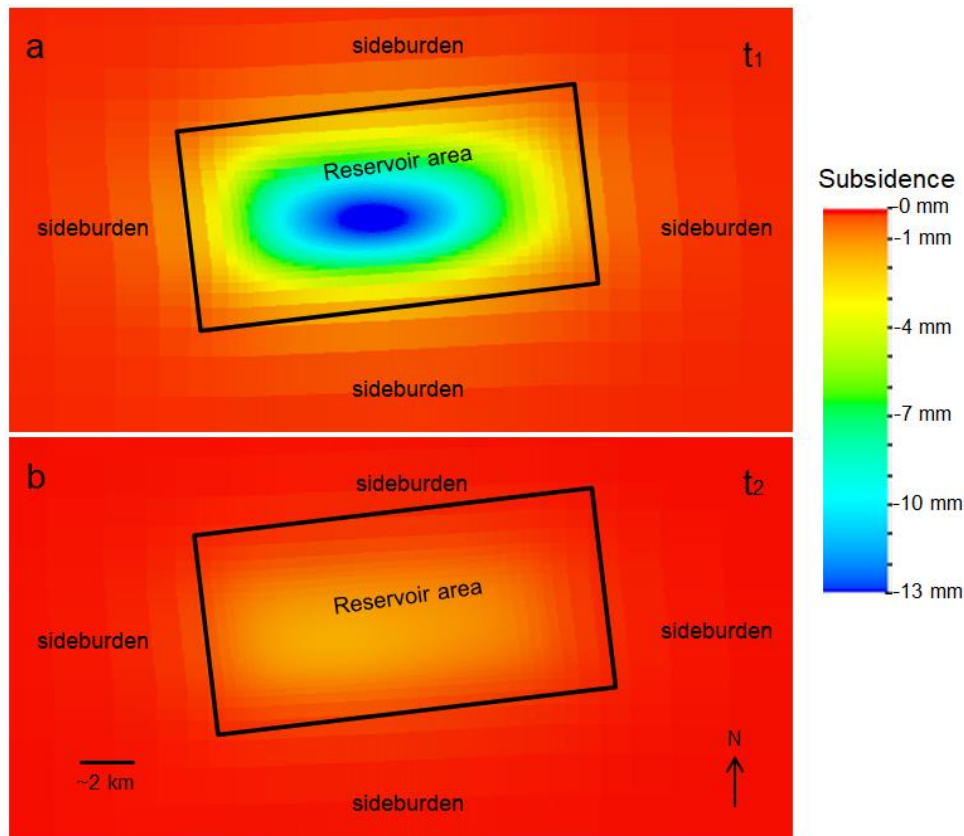


Figure 9-1: Subsidence predicted at the ground surface above reservoir during depletion ( $t_1$ ) and replenishment ( $t_2$ ) relative to pre-production time (which was 0 mm displacement). The area in the box represents the ground surface right above reservoir area and rest area is ground surface of sideburden. Color scale is in millimeters.

### 9.2.1 Future scenario testing cases

All these results are based on ECLIPSE™ models for future scenario testing cases discussed in the section 7.2. In particular, the distribution of pore pressure ( $P_p$ ) and effective stresses ( $S_{effec}$ ) through space and time are described. Decrease in effective stress was observed where there is an increase in pore pressure. All the result plots show a top view of the top layer of the reservoir, as the main focus of this dynamic geomechanical assessment is on the reservoir.

#### 9.2.1.1 Long-term (seasonal) case

Figure 9-2 describes the modelling results of the long-term case which has been discussed in the section (7.2.1). Two time steps are selected to analyze the pore pressure changes in the reservoir as well as the effects of these changes on effective stresses in reservoir. The maximum pressure drop occurs at the time step  $t_1$  (01/01/26) in response to seasonal gas withdrawal (production) and the maximum pressure rises at the time step  $t_2$  (01/07/26) in reaction to seasonal injection of gas. The comparison of pre and post gas injection phase is shown in (Figure 9-2). The change in pore pressure and effective stresses is significant around well X6 and it decreases away from the well location radially. The pore pressure of reservoir rises from ~15.3 MPa (Figure 9-2a) at  $t_1$  to ~16.7 MPa (Figure 9-2b) at the end of injection phase at  $t_2$ . This pore pressure change from  $t_1$  to  $t_2$  causes change in stress path of reservoir which in turn changes the effective stresses in the reservoir. The increase in pore pressure decreases the effective stresses acting on the reservoir. The effective stress at  $t_1$  is ~28.4 MPa at X6 well location and it decreases to ~27 MPa. Although the change in effective stresses on

reservoir is small but the significance of this change becomes more prominent with high operating gas volumes.

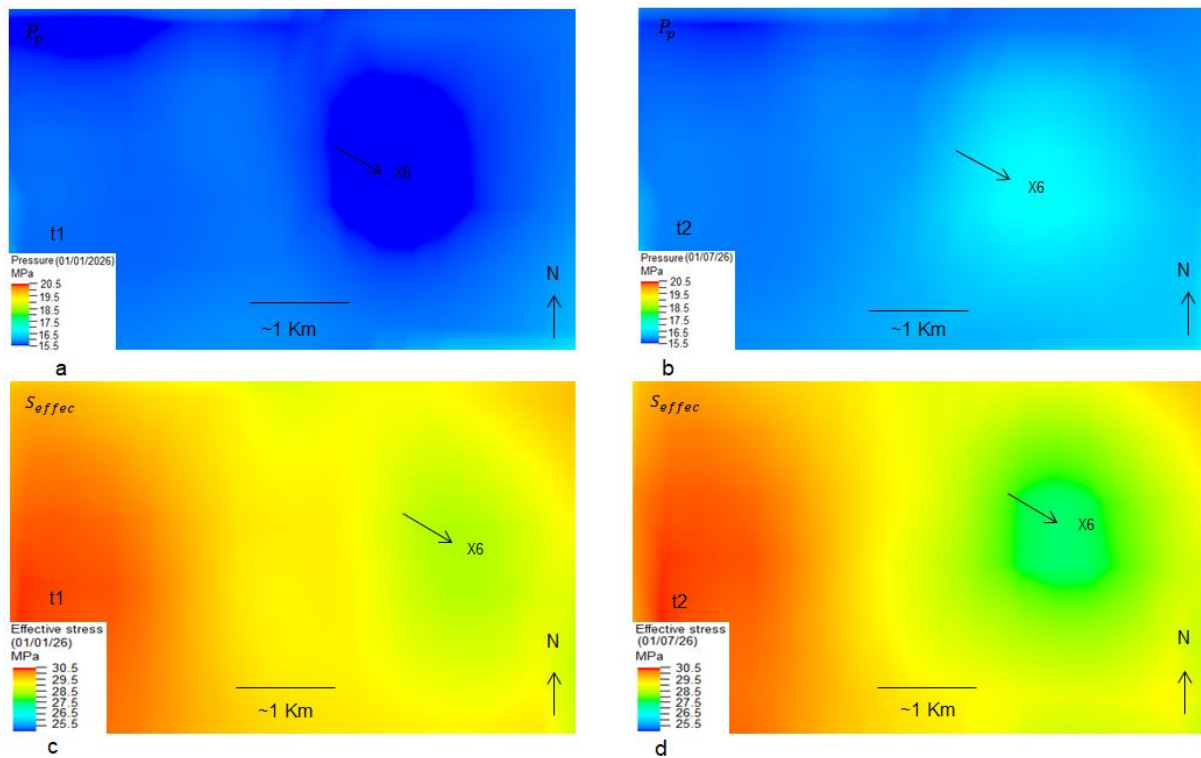


Figure 9-2: Pore pressure ( $P_p$ ) and effective stress ( $S_{effec}$ ) changes from t1 (01/01/26) to t2 (01/07/26) in long-term (seasonal) case with one well (X6). The arrows show the location of maximum observed fluctuation in  $P_p$  and  $S_{effec}$  from t1 to t2. The color scale is in MPa.

### 9.2.1.2 Short-term cases with limited water cut-off

#### 9.2.1.2.1 With one well

The fluid flow model setup of this case study has been discussed in the above section 7.2.2.1.1 with detailed description of schedule cycles as well as the operating gas rates in addition to upper and lower limit of bottom hole pressure (BHP). Figure 9-3 illustrates the modelling results of this scenario. Two time steps are considered to see the fluctuation of pore pressure and consequently effective stresses on the reservoir: t1 (01/01/20) is the lowest pressure time step and t2 (22/09/20) is the highest-pressure time step of this case. Time step t1 and t2 also show the lowest production point of pressure and the highest injection point of pressure respectively. There is a difference of about 0.02 MPa of pore pressure between t1 and t2 i.e. 15.35 MPa (Figure 9-3a) and 15.37 MPa (Figure 9-3b) respectively. The difference in pore pressure also causes the change in effective stresses acting on reservoir which are 28.15 MPa (Figure 9-3c) and 28.13 (Figure 9-3d) MPa at time steps t1 and t2 respectively. The variation in both pore pressure as well as effective stresses on reservoir is categorically minor in this modelling case.

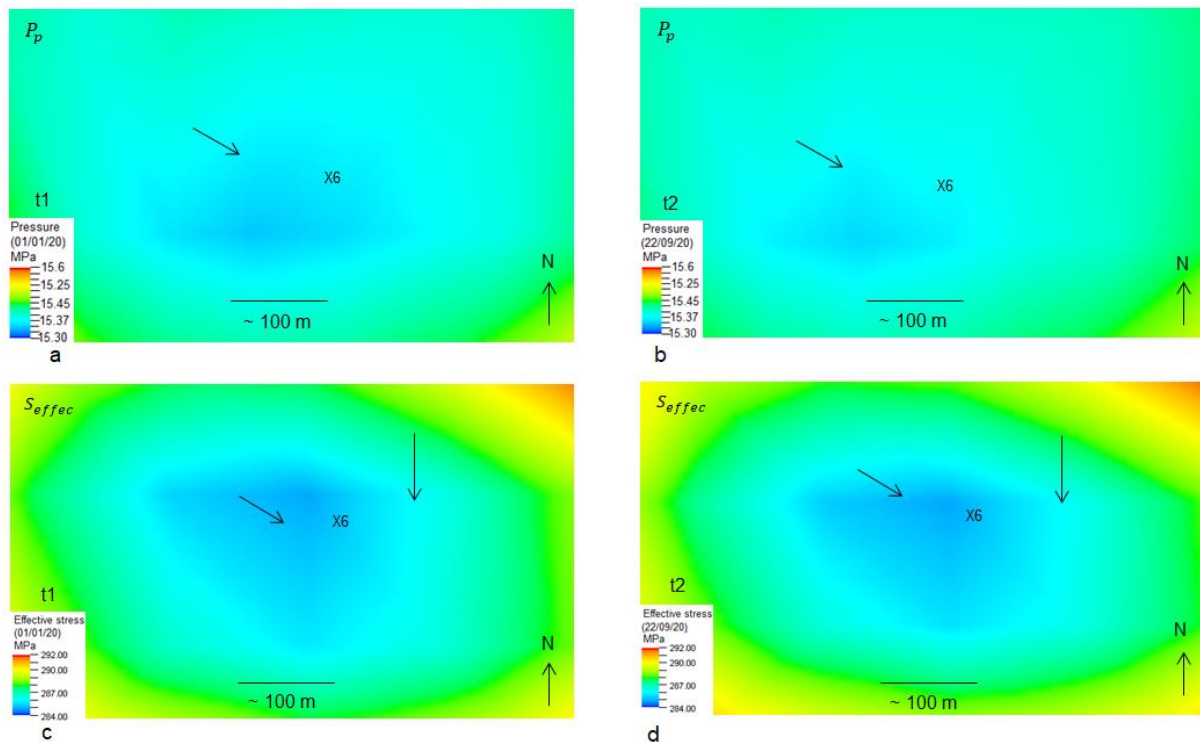


Figure 9-3: Pore pressure ( $P_p$ ) and effective stress ( $S_{effec}$ ) changes from  $t_1$  (01/01/20) to  $t_2$  (22/09/20) in short-term case with one well (X6) with water cut-off rate of  $5 \text{ m}^3/\text{day}$ . The arrows show the location of maximum observed fluctuation in  $P_p$  and  $S_{effec}$  from  $t_1$  to  $t_2$ . The color scale is in MPa.

#### 9.2.1.2.2 With two wells

The fluid flow model setup of this case study has been discussed in the section 7.2.2.1.2 with detailed description of schedule cycles as well as the operating gas rates also upper and lower limit of bottom hole pressure (BHP).

Two time steps are considered to obtain the fluctuation of pore pressure ( $P_p$ ) and effective stress ( $S_{effec}$ ) for this case study:  $t_1$  is the maximum depletion pressure (22/07/20) and  $t_2$  is the maximum injection pressure (05/08/20). Figure 9-4 shows the well location of both horizontal (H1) and vertical well (X6) along with effective stress changes with time steps.

For the well H1, the pore pressure and effective stress at  $t_1$  is observed to be  $\sim 15.7$  MPa and  $\sim 28.8$  MPa respectively and at the time step  $t_2$ , the pore pressure increased to  $\sim 15.9$  MPa, while the effective stress of the well declined to 28.6 MPa.

Whereas, at the time  $t_1$ , the pore pressure and effective stress of the well X6 is observed to be  $\sim 15.4$  MPa and  $\sim 28.6$  MPa respectively, whereas the pore pressure of the well at  $t_2$  is around  $\sim 15.5$  MPa and the effective stress decreases to  $\sim 28.5$  at this time step.

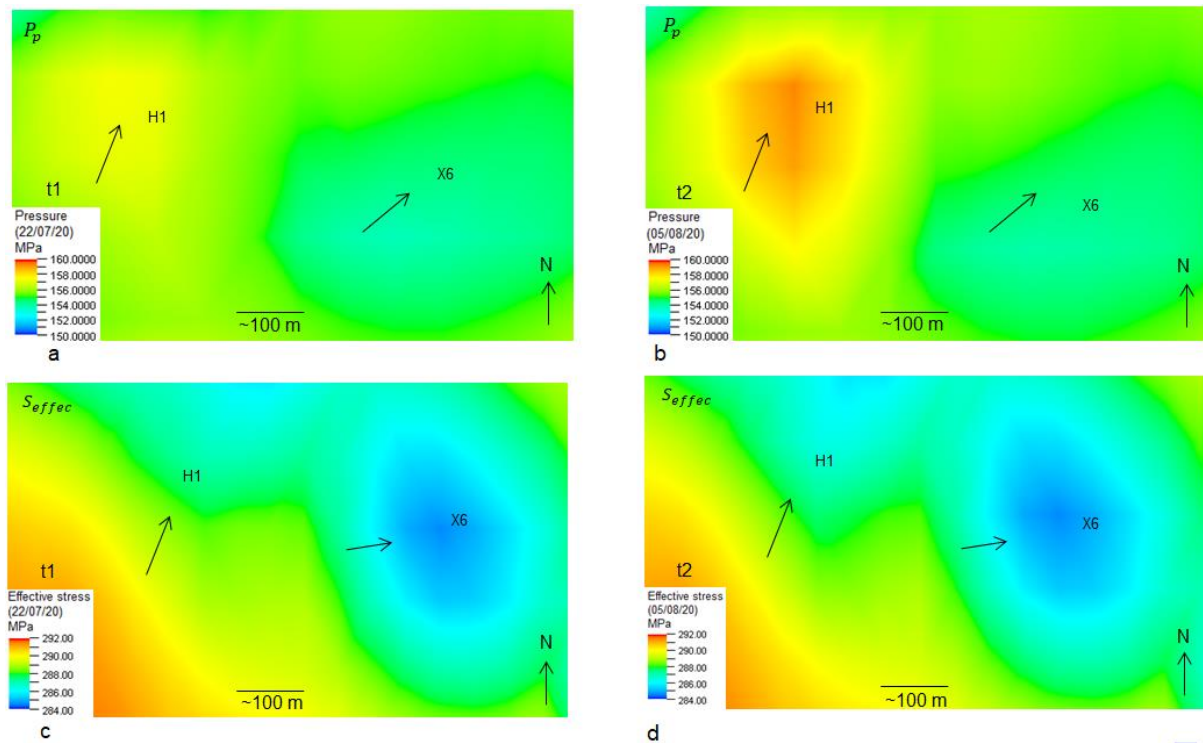


Figure 9-4: Pore pressure ( $P_p$ ) and effective stress ( $S_{effec}$ ) changes from t1 (22/07/20) to t2 (05/08/20) in short-term case with two wells (X6 and H1) with water cut-off rate of  $5 \text{ m}^3/\text{day}$ . The arrows show the location of maximum observed fluctuation in  $P_p$  and  $S_{effec}$  from t1 to t2. The color scale is in MPa.

### 9.2.1.2.3 With three wells

The ECLIPSE™ model for this case has been explained in detail in the section 7.2.2.1.3, with schedule and input data information. The result of the model is presented in Figure 9-5.

Two time steps have been selected for the analyses of change in pore pressure and effective stress acting on the reservoir. Time step t1 (16/12/20) represents the lowest pressure during production phase of the schedule cycle and t2 (23/12/20) indicates the maximum injection pressure. The fluctuations in pore pressure and effective stress on reservoir during t1 and t2 are the main results of this model.

Figure 9-5 shows the location of three wells which are denoted by H1, X2 and X6. The pore pressure at t1 and t2 for the well H1 is ~15.0 MPa and ~15.3 MPa respectively. Whereas, the effective stress values are ~29.3 MPa at t1 and about 29.0 MPa at t2. There is a difference of about ~0.3 MPa for both pore pressure and effective stress from t1 to t2.

The vertical wells X2 and X6 are close to each other, therefore, the difference in change in pore pressure and effective stress at these well locations are negligible. The value of pore pressure at both well locations at t1 and t2 are about 15.4 MPa and ~15.7 MPa respectively. The effective stress at t1 and t2 are ~28.5 and ~28.2 MPa respectively at both well locations. There is an increase in pore pressure of ~0.3 MPa from t1 to t2 and decrease in effective stress of about 0.3 MPa.

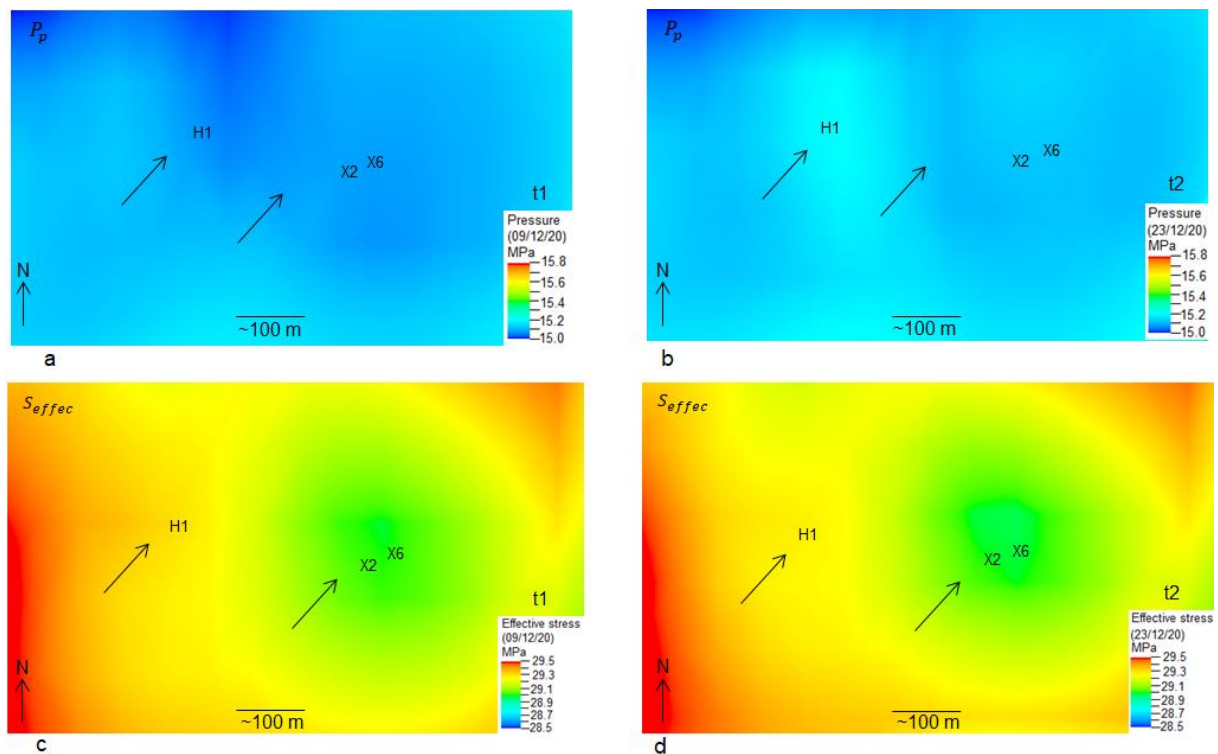


Figure 9-5: Pore pressure ( $P_p$ ) and effective stress ( $S_{effec}$ ) changes from t1 (16/12/20) to t2 (23/12/20) in short-term case with three wells (X2, X6 and H1) with water cut-off rate of  $5 \text{ m}^3/\text{day}$ . The arrows show the location of maximum observed fluctuation in  $P_p$  and  $S_{effec}$  from t1 to t2. The color scale is in MPa.

#### 9.2.1.2.4 With random schedule

The ECLIPSE™ model setup for this model is discussed in the section 7.2.2.3.1. German data for surplus energy from renewable sources has been considered in this case. The modelling results of this case are presented in the form of pore pressure and consequently effective stress changes of the top layer of the reservoir model (Figure 9-6).

Two time steps have been selected for the conclusion of results for this model. Time step t1 is the starting point of the schedule case i.e. 01/01/20, and t2 is the end schedule point (31/12/20). The pore pressure at well X6 location is about 15.2 MPa at t1 and increase to about 15.8 MPa at t2, simultaneously, the effective stresses at well X6 is about 28.6 MPa and it decreases to about 28.0 MPa at time steps t1 and t2 respectively.

There is an increase of 0.6 MPa of pore pressure and decrease of 0.6 MPa of effective stress at the top surface of the reservoir layer near well X6 from t1 to t2.



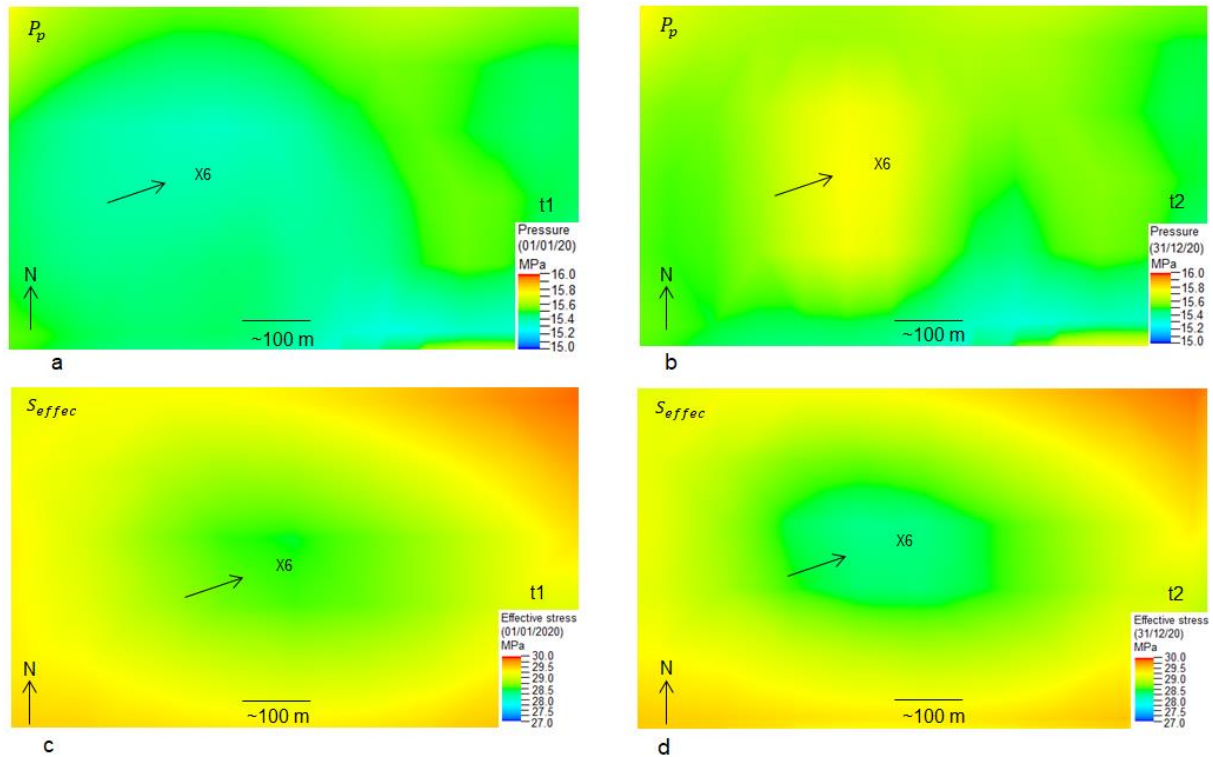


Figure 9-6: Pore pressure ( $P_p$ ) and effective stress ( $S_{effec}$ ) changes from t1 (01/01/20) to t2 (31/12/20) in short-term case with one (X6) with water cut-off rate of  $5 \text{ m}^3/\text{day}$  with random schedule. The arrows show the location of maximum observed fluctuation in  $P_p$  and  $S_{effec}$  from t1 to t2. The color scale is in MPa.

### 9.2.1.3 Short-term without limited water cut-off

#### 9.2.1.3.1 With one well

This case is described in detail in the above section 7.2.2.2.1. The change in effective stress of the reservoir with changing pore pressure is shown in Figure 9-7. Two time steps are considered for the conclusion of results for this case: t1 (22/07/20) is the lowest pressure point of the case and t2 (12/08/20) is the maximum injection pressure point of this case. It can be seen in the figure that after time period of 20 days, no significant change was observed with respect to the pore pressure and effective stress. However, at t1, the values of pore pressure and effective stress are  $\sim 15.37$  and  $\sim 28.75$  MPa, respectively. At t2, the values of pore pressure and effective stress are 15.4 and 28.72 MPa respectively.

There is only a difference of 0.03 MPa increase in case of pore pressure and 0.03 MPa decrease in effective stress at the surface of the top layer of reservoir. The intended operation of this case seems completely safe for storage operations.

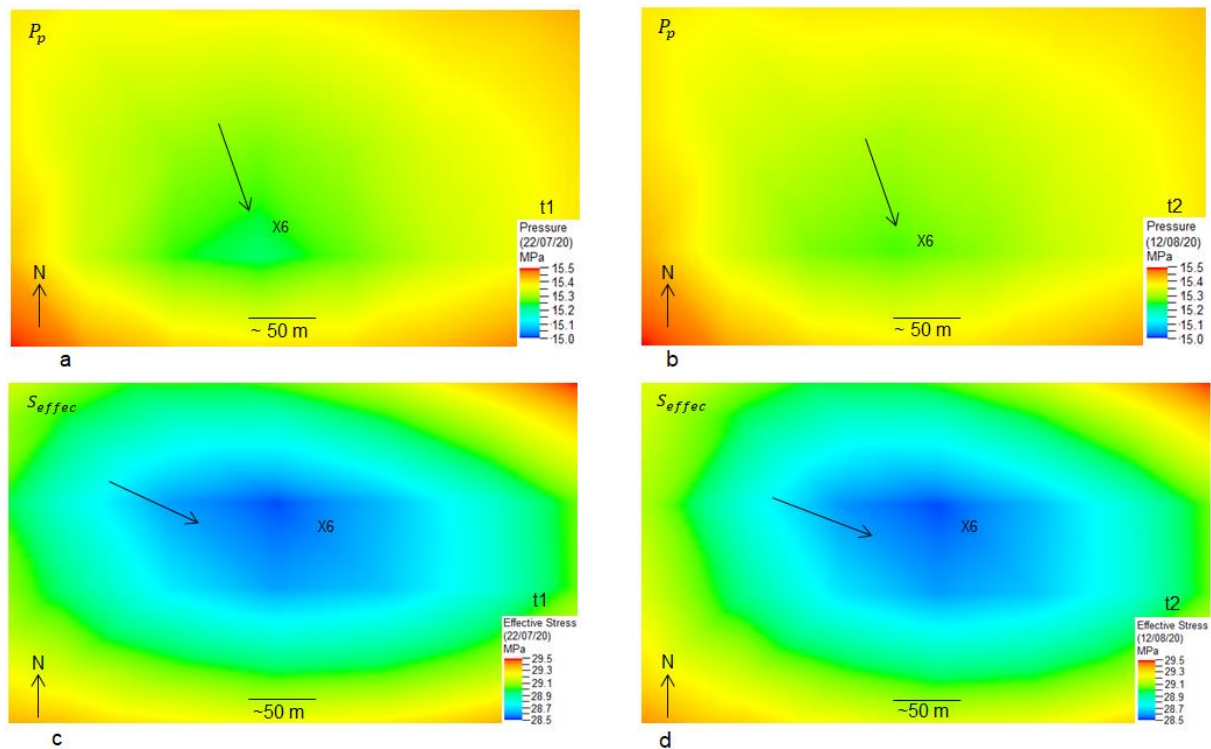


Figure 9-7: Pore pressure ( $P_p$ ) and effective stress ( $S_{effec}$ ) changes from t1 (22/07/20) to t2 (12/08/20) in short-term case with one well (X6) without water cut-off rate of  $5 \text{ m}^3/\text{day}$ . The arrows show the location of maximum observed fluctuation in  $P_p$  and  $S_{effec}$  from t1 to t2. The color scale is in MPa.

### 9.2.1.3.2 With two wells

The model setup for this case has already been explained in section 7.2.2.2.2. This case is for two wells, H1 (horizontal) and X6 (vertical). Figure 9-8 shows the location of the two wells as well as changes in effective stresses with pore pressure changes in space and time. Two time steps with lowest production pressure (t1) and highest injection pressure (t2) are considered. Time step t1 is 05/07/20 and t2 is 05/08/20. For the well H1, pore pressure and effective stress at t1 is observed to be  $\sim 15.3$  MPa and  $\sim 29.1$  MPa respectively, and the pore pressure increases up to  $\sim 15.7$  MPa, whereas the effective stress declines to  $\sim 28.7$  MPa at the well location at the time step t2. However, the pore pressure and effective stress of the well X6 at time step t1 is observed to be  $\sim 15.2$  MPa and  $\sim 28.7$  MPa respectively, while the pore pressure at the well location increases up to  $\sim 15.5$  MPa and the effective stress decreases to  $\sim 28.5$  at t2. A difference of  $\sim 0.4$  MPa in pore pressure and effective stress around horizontal well (H1) and  $\sim 0.2$  MPa around vertical well (X6) has been observed. The stress path in both cases hardly varies which indicates the safety of underground gas storage operation.

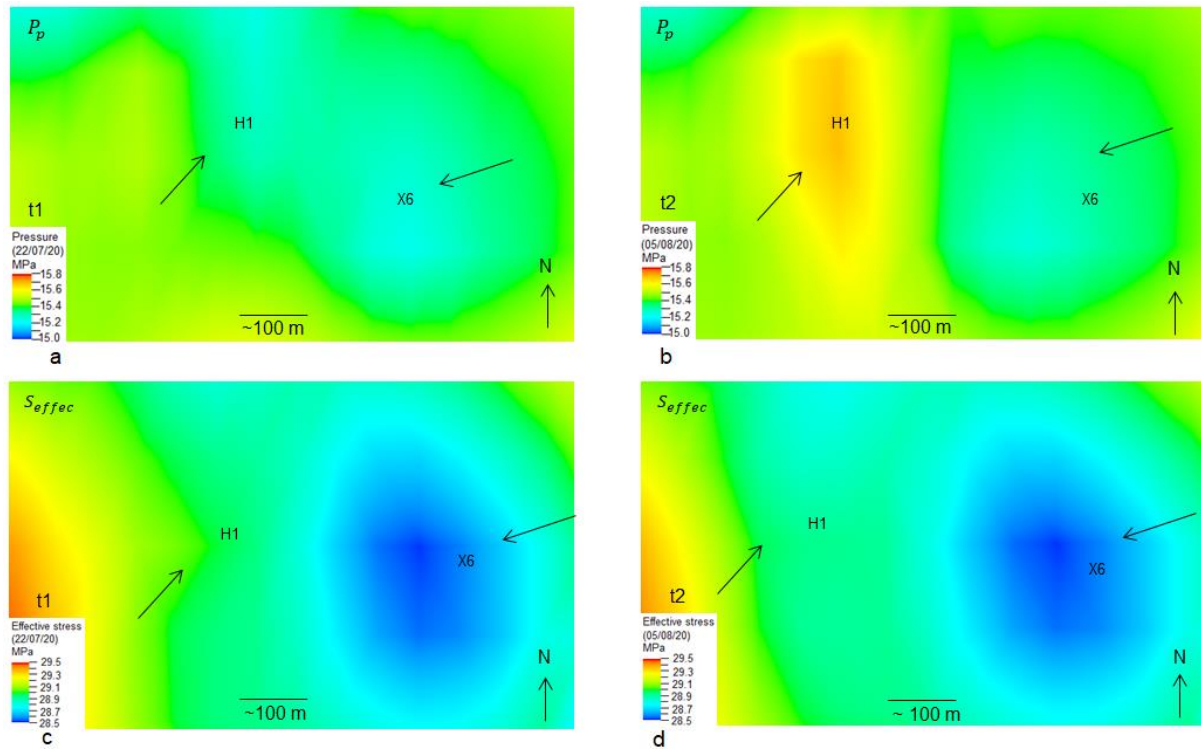


Figure 9-8: Pore pressure ( $P_p$ ) and effective stress ( $S_{effec}$ ) changes from t1 (22/07/20) to t2 (05/08/20) in short-term case with two wells (X6 and H1) without water cut-off rate of  $5 \text{ m}^3/\text{day}$ . The arrows show the location of maximum observed variation in  $P_p$  and  $S_{effec}$  from t1 to t2. The color scale is in MPa.

### 9.2.1.3.3 With three wells

The ECLIPSE™ model setup along with schedule and input data information of this scenario has been explained in detail in section 7.2.2.2.3. The results of the model are presented in Figure 9-9.

Two time steps with highest fluctuation of pore pressure have been selected. Time step t1 (09/12/20) corresponds to the lowest pore pressure point and t2 (23/12/20) corresponds to highest pore pressure point of the schedule cycle. The fluctuation in pore pressure and effective stress on reservoir during time t1 and t2 are the main results of this model.

Figure 9-9 shows the locations of three wells which are denoted by H1, X2 and X6. These three wells are the operating wells for this scenario. The main changes in pore pressure along with the effective stress occur around these wells. The pore pressures at t1 and t2 for the well H1 are  $\sim 15.5 \text{ MPa}$  and  $\sim 15.4 \text{ MPa}$  respectively. Whereas, the effective stress values are  $\sim 29.1 \text{ MPa}$  at t1 and about  $\sim 28.7 \text{ MPa}$  at t2. There is a difference of about  $\sim 0.4 \text{ MPa}$  for both pore pressure and effective stress at t1 and t2.

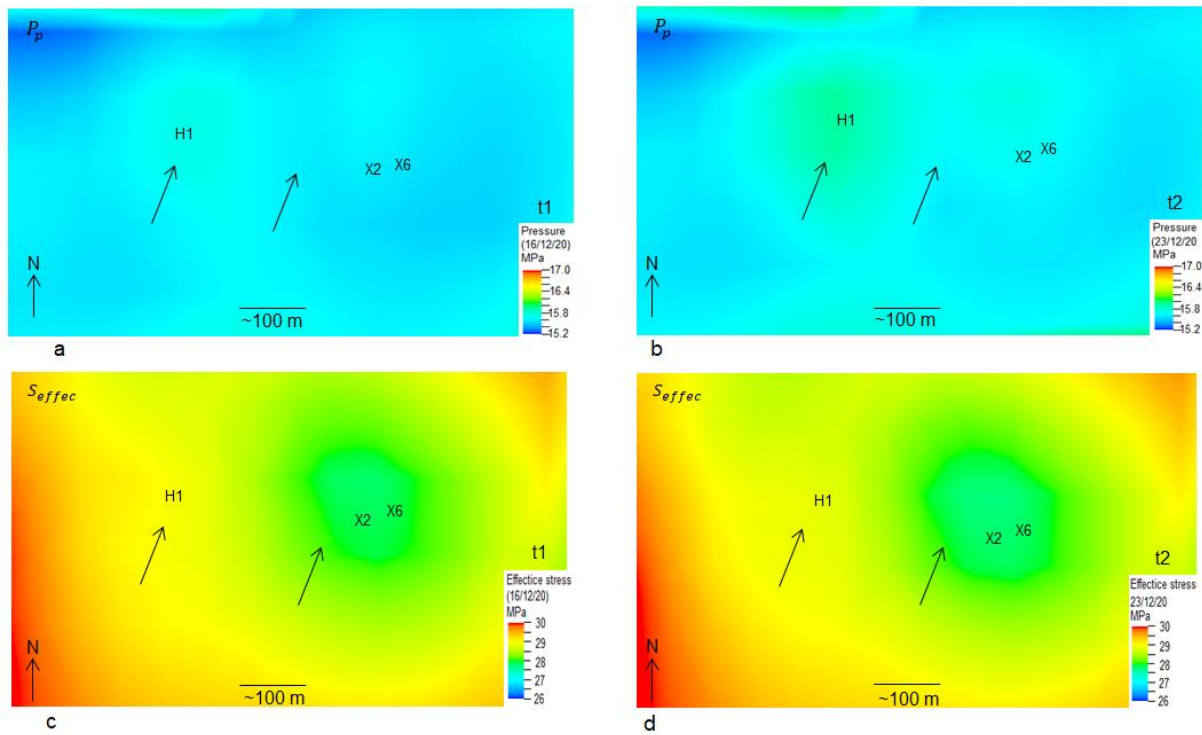


Figure 9-9: Pore pressure ( $P_p$ ) and effective stress ( $S_{effec}$ ) changes from t1 (09/12/20) to t2 (23/12/20) in short-term case with three wells (X2, X6 and H1) without water cut-off rate of  $5 \text{ m}^3/\text{day}$ . The arrows show the location of maximum observed change in  $P_p$  and  $S_{effec}$  from t1 to t2. The color scale is in MPa.

The location of the vertical wells X2 and X6 are quite close to each other, therefore, the difference in change in pore pressure and effective stress between these wells is insignificant. The value of pore pressure at both well locations at t1 and t2 is about 15 MPa and  $\sim 15.2$  MPa respectively. The effective stress values at t1 and t2 are  $\sim 29.0$  and  $\sim 28.8$  MPa respectively. There is an increase in pore pressure of  $\sim 0.2$  MPa from t1 to t2 and a decrease in effective stress of about 0.2 MPa.

#### 9.2.1.3.4 Random schedule

The ECLIPSE™ model setup for this model is discussed in section 7.2.2.3.2. German data for surplus energy from renewable sources has been considered in this case. The modelling results of this case are presented in the form of pore pressure and effective stress changes of the top layer of reservoir (Figure 9-10).

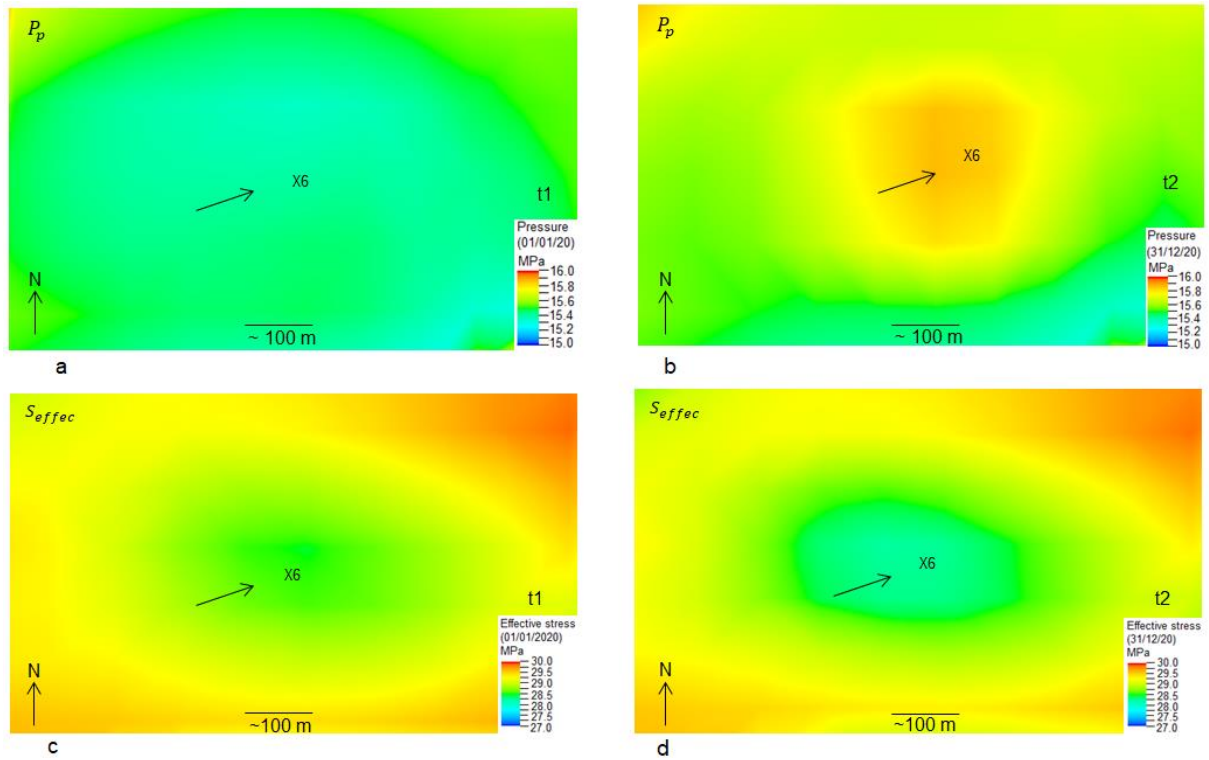


Figure 9-10: Pore pressure ( $P_p$ ) and effective stress ( $S_{effec}$ ) changes from  $t_1$  (01/01/20) to  $t_2$  (31/12/20) in short-term case with one well (X6) without water cut-off rate of  $5 \text{ m}^3/\text{day}$  with random schedule. The arrows show the location of maximum observed fluctuation in  $P_p$  and  $S_{effec}$  from  $t_1$  to  $t_2$ . The color scale is in MPa.

Two time steps have been selected for the conclusion of the results for this model. Time step  $t_1$  is the starting point of the schedule case i.e. 01/01/20, and  $t_2$  is the end schedule point (31/12/20). The pore pressure at well X6 location is about 15.1 MPa at  $t_1$  and increase to about 15.7 MPa at  $t_2$ , whereas, the effective stress at well X6 is about 28.7 MPa and it decreases to about 28.1 MPa at time steps  $t_1$  and  $t_2$  respectively. There is an increase of 0.6 MPa of pore pressure and decrease of 0.6 MPa of effective stress at the top layer of the reservoir around well X6 from  $t_1$  to  $t_2$  respectively.

The summary of all the results are compiled in Table 9-1, in order to have better understanding of pore pressure and effective stress changes of all future testing cases with time ( $t_1$  to  $t_2$ ).

Table 9-1: Summary of results for all future test scenarios. The sign + in the pore pressure changes determines the positive change or increase in pore pressure from time step  $t_1$  to  $t_2$ , while the sign - in the changes in effective stresses denotes the decrease in magnitudes of effective stresses fro time step  $t_1$  to  $t_2$ . These two quantities are inversely proportional to each other and are expressed in MPa and KPa for a better understanding of the changes.

Future testing Scenario cases	Sub divisions	Results	
		Pore pressure changes $\Delta P_p$	Effective stress changes $\Delta S_{effec}$

Long-term (seasonal)			+1.4 MPa +1400 KPa	-1.4 MPa -1400 KPa
Short-term (weekly)	With limited water cut rate  (5 m <sup>3</sup> /day)	With 1 well	+0.02 MPa +20 KPa	-0.02 MPa -20 KPa
		With 2 wells	+0.1 MPa +100 KPa	-0.1 MPa -100 KPa
		With 3 wells	+0.3 MPa +300 KPa	-0.3 MPa -300 KPa
	Without limited water cut rate	With 1 well	+0.03 MPa +30 KPa	-0.03 MPa -30 KPa
		With 2 wells	+0.2 MPa +200 KPa	-0.2 MPa -200 KPa
		With 3 wells	+0.4 MPa +400 KPa	-0.4 MPa -400 KPa
Random schedule cases	With limited water cut rate  (5 m <sup>3</sup> /day)	With 1 well	+0.6 MPa +600 KPa	-0.6 MPa -600 KPa
	Without limited water cut rate	With 1 well	+0.6 MPa +600 KPa	-0.6 MPa -600 KPa

## Chapter 10 Potential fault reactivation analyses

### 10.1 Model setup

Fault reactivation is a possibility of failure in geomechanical assessment of the reservoir which can risk operational safety, cause micro seismicity within and around reservoir and provide a leakage path for gas to escape. Fault reactivation occurs when the shear stress acting on the fault planes exceed the shear strength of the fault. Mohr-Coulomb failure criterion relationship of pore pressure and the principal stresses of this case study reservoir (lies in normal stress regime) are expressed by the equation [103].

$$P_p = \frac{1}{\alpha} \left[ \frac{1}{2} (S_v + S_{hmin}) + \frac{1}{2} (S_v - S_{hmin}) \cos 2\theta - \frac{1}{2} (S_v - S_{hmin}) \frac{\sin 2\theta}{\mu} \right] \quad (34)$$

Where  $\alpha$  is the Biot coefficient (assumed 1),  $S_v$  is the vertical and maximum principal stress,  $S_{hmin}$  is the minimum horizontal stress and  $\theta$  is the angle between dip line of the fault and the  $S_{hmin}$  direction,  $P_p$  is the critical pore pressure and  $\mu$  is the coefficient of friction.

These analyses include the calculation of the critical pore pressure with the aim of observing possible differences in pore pressure required for fault reactivation. The pore pressure derived from the history matching scenario is multiplied by a fixed factor controlled by gas rates until fault reactivation occurs. The upper limit of BHP is removed in order to get higher pore pressure. The factors used for this operation were 1.15, 1.25 and 1.5 (Figure 10-1). It is then possible to evaluate pressure change in the reservoir required to reactivate the fault as well as the safe storage capacity of the reservoir.

Figure 10-1 shows different pressure profiles based on distinct gas injection scenarios. It can be seen that  $P_p$  (history match pressure) curve exhibits a maximum value of ~16.2 MPa with 100,000 m<sup>3</sup>/day of gas rate injected for 1 year. Whereas, to reach a pressure value 1.15 times of the actual history match pressure case, 175,000 m<sup>3</sup>/day of gas is injected for 1 year. The pressure increased up to 18.6 MPa. In case  $P_p \times 1.25$ , 240,000 m<sup>3</sup>/day is injected to reach a pressure of about 20.25 MPa. Similarly, in case of  $P_p \times 1.5$ , gas volume of 560,000 m<sup>3</sup>/day is injected (for 1 year) which increases the pressure up to 24.3 MPa.

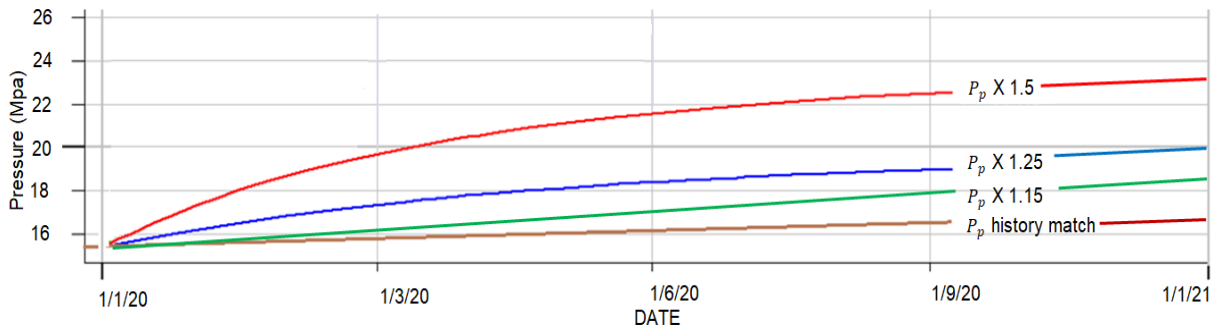


Figure 10-1: Pressure profiles for the history matching scenario and scenarios multiplied by a fixed factors ( $P_p$ ,  $P_p \times 1.15$ ,  $P_p \times 1.25$  and  $P_p \times 1.5$ ) controlled by gas injection rates until fault reactivation occurs.

### 10.2 Results

The results of this section are based on the model set up explained in the above section. The methodology follows the different cases in which the initial reservoir pore pressure is multiplied by a factor of 1, 1.15, 1.25 and 1.5, that correspond to pore pressure values of ~16.2 MPa, ~18.6 MPa, ~20.25 MPa and ~24.3 MPa respectively. The results display the oblique view of the top most layer of the reservoir (Figure 10-2 and Figure 10-3). The Mohr circles correspond to the Well X6 location which is located near the main fault (Figure 10-2 and Figure 10-3). Two time steps have been considered for all the cases: t1 (01/01/20) is the starting and t2 (01/01/21) is the end time step of the schedule year.

Fault reactivation is observed already at  $P_p \times 1.25$  (~20.25 MPa) (Figure 10-2b) at which the corresponding Mohr circle has just touched the tensile failure line. The amount of failure in the cells becomes more prominent as pore pressure increases in above pore pressure factor of 1.25 (i.e.  $P_p \times 1.5$ ), and it causes the corresponding Mohr circles to move further left (Figure 10-3 c and d). The increase in pore pressure causes decrease in effective stress which causes the Mohr circles to move to the tensile failure line. Thereafter, the material enters into the plastic regime, and therefore, in case of failure, fault reactivation occurs.

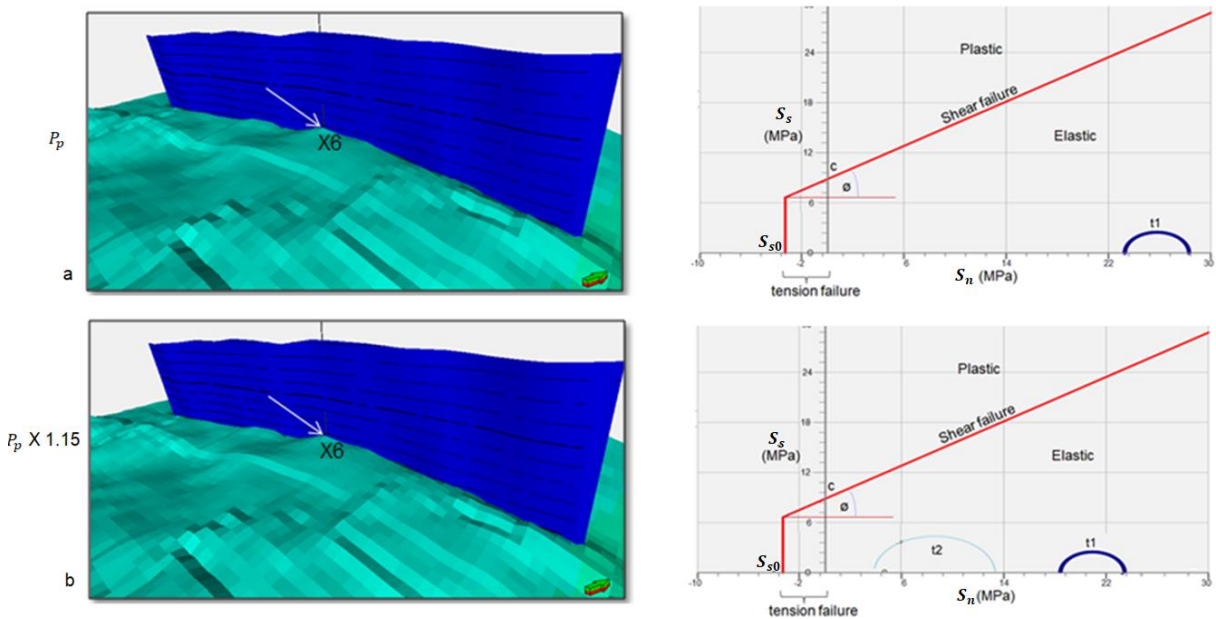


Figure 10-2: The computation of fault reactivation through numerical analysis for pressure multiplied by a factor of 1 (a) and 1.15 (b) on the left side of figure. White dots show the cells whose stress state exceeds the failure criterion (arrows show northward direction). On the right side of figure is the shear stress  $S_s$  vs. normal stress  $S_n$  diagrams, showing the Mohr-Coulomb failure criterion at well X6 location (which is



## 10. Potential fault reactivation analyses

nearest to the main fault of the reservoir). (a) is the Mohr-Coulomb diagram for  $P_p$  and (b) is the Mohr-Coulomb diagram for  $P_p \times 1.15$ . Time steps t1 and t2 correspond to starting (01/01/20) and final (01/01/21) time steps of the tested cases. An increase in pore pressure leads to a decrease in effective stresses from (a) to (b). This causes the corresponding Mohr circle to shift to the left in the direction of the tensile failure line. If the failure line is finally touched, plastic straining occurs and - in case of a fault zone - fault reactivation occurs.

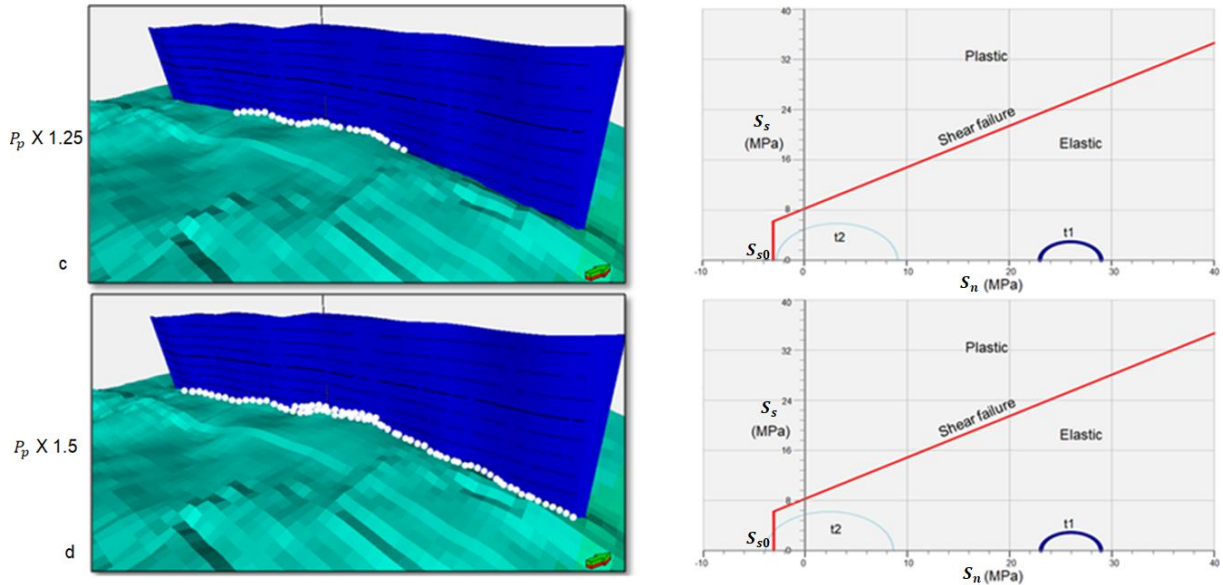


Figure 10-3: The computation of fault reactivation through numerical analysis for pressure multiplied by a factor of 1.25 (c) and 1.5 (d) on the left side of figure. White dots show the cells whose stress state exceeds the failure criterion (arrows show northward direction). On the right side of figure is the shear stress  $S_s$  vs. normal stress  $S_n$  diagrams, showing the Mohr-Coulomb failure criterion at well X6 location (which is nearest to the main fault of the reservoir). (c) is the Mohr-Coulomb diagram for  $P_p \times 1.25$  and (d) is the Mohr-Coulomb diagram for  $P_p \times 1.5$ . Time steps t1 and t2 correspond to starting (01/01/20) and final (01/01/21) time steps of the tested cases. An increase in pore pressure leads to a decrease in effective stresses from (c) to (d). This causes the corresponding Mohr circle to shift to the left in the direction of the tensile failure line. If the failure line is finally touched, plastic straining occurs and - in case of a fault zone - fault reactivation occurs.

### 10.3 Safe injection rate for safe storage capacity

The pore pressures for fault reactivation for the different scenarios calculated in the numerical modelling analysis provide an estimate of the pressure at different injection rates. The injection rate (in term of volume rate) to achieve a perfect history match (16.2 MPa) is about 100,000 m<sup>3</sup>/day and fault reactivation is already observed at  $P_p$  times 1.25 i.e. about 20.25 MPa at an injection rate of 240,000 m<sup>3</sup>/day. With the determination of the critical pore pressure, it is also possible to derive an upper limit for the injection rate to be selected for injection processes. By considering the highest safety margin, the injection rate between 100,000 m<sup>3</sup>/day and 150,000 m<sup>3</sup>/day would be considered safe injection rate for safe storage for the case study reservoir. Gas injection rate above this threshold value can have a significant impact on risk management and operational set-up of underground gas storage.

### 10.4 Storage capacity of Power-to-Gas and Gas-to-Power

Regarding the storage capacity of Power-to-Gas technologies, the case study reservoir can store

881,600 kWh/d up to maximum of 1,322,400 kWh/d of power from renewable or other resources with respect to conversion of natural gas volume of 100,000 m<sup>3</sup>/day to maximum 150,000 m<sup>3</sup>/day respectively. Power-to-Gas and Gas-to-Power convertible units are summarized in Table 10-1.

Table 10-1: Power-to-Gas and gas-to-power convertible units.

m <sup>3</sup> natural gas	kWh Power
1	8.816
0.113	1

## Chapter 11 Summary and discussion

### 11.1 1D Mechanical Earth Model

As with any numerical modelling approach, the uncertainties of the input and calibration data are critical and influence the quality and reliability of the geomechanical modelling results. Log data used in this study is very old and limited (4.2). For instance, there is only one density log available for well X6, and this density log has been used for all the wells for overburden stress calculation (5.1). The data from literature can also be used to fill the gaps in the log data; however, it provides the constant values for corresponding stratigraphic layers.

The overburden stress as well as elastic properties calculation in this study is based only on one well, therefore it can be improved if additional density and sonic logs for all the wells from top to bottom would be available. As the elastic properties were calculated by using sonic and density logs through empirical correlations, conversion from dynamic to static parameters was made more difficult by the fact that the data set was not from the same wells and did not overlap. Such overlap would have been a great improvement for the estimation of uncertainties and for the conversion of parameters. More data that sufficiently overlapped could be used, for example, to create a reservoir and/ overburden-specific conversion function. Similarly, the shear velocity logs were also absent from all the wells and were calculated by using Greenberg and Castagna correlation [48]. The acoustic logs of all the wells are just simple recording without shear slowness and the corresponding shear slowness had to be derived from empirical correlations (e.g by Greenberg and Castagna). Although it provides a set of calculated shear velocity logs for all the wells but direct shear velocity measurement would have omitted many uncertainties. This specific property calculation for all the wells simply implies that the uncertainty in these sections is high for all units and the final property results are not possible until further calibration data has been collected. This uncertainty and limitation can be overcome by planning and drilling new wells across the different parts of the reservoir in order to compare and validate the behavior of the productive zones of the reservoir formation.

In general, a broader and more solid base of material parameters is desirable, as they are important for the modelling results. Even though the elastic properties and stress data from 1D MEM have been calibrated with available measured data, however there was limited core data for calibration e.g. Young's modulus, Poisson ratio, Biot coefficient and stress data are only available for well X6 and for certain depth (4.2.2). The data basis for material properties was smaller than expected. This data set for other wells at different depths would have provided more calibration data points to omit further uncertainties in the model.

The plausibility of MEM depends on the quantity and quality of the available data. A complex 1D MEM for wells requires data from various sources. Lack of well log data limits the modelling outcomes and increases various uncertainties in the model. If a company is planning to engage in a region and drill several wells, as a first step, it should ensure that it collects all relevant data for the preparation of the preliminary MEM and uses this data to plan future wells in the region. The new data collected during the drilling of a new well can immediately be used to update the model to reduce uncertainty. The process of model generation itself should not be too expensive to offset its benefits, especially when using professional software. Most steps of the process could possibly be automated, allowing real-time application.

Although the different parameters in the MEM are associated in many ways, they all basically come

from the same basic set of log measurements. The results must always be calibrated using pressure history, core data, image logs and reports from offset drilling events. The data required for 1D MEM ranges from log data such as sonic/velocity, bulk density, gamma ray, and electric logs to core data e.g. elastic moduli, strength parameters, angle of internal friction as well as data for calibration such as pressure tests, image logs, caliper logs and major incident reports.

Some of the data set is pre-requisite for MEM such as sonic logs, density/neutron logs, gamma ray logs and core measurement data. This means that a model cannot be built if these measurements are not available because logs have not been carried out in this region or cores have not been tested or retrieved. This data is used for model calibration and absence of this data question the precision and certainty of the model. Uncalibrated models are highly uncertain because the difference between the calibrated and uncalibrated parameters (e.g. dynamic and static elastic properties) is potentially very large. Any uncertainty in the data increases the uncertainty of the model results.

## 11.2 Hydraulic Model

The results of hydraulic model show variation in gas saturation at different phases during short-term as well as long-term injection-production cycles (see section 7.2). Figure 7-2 d shows that the injection-production cycle increases the gas saturation during the later cycles as more gas produced with increasing cycles till the convergence reach. This indicates the adoption of high-speed multicycle injection-production in UGS with time. This characteristic of UGS indicates the increase of gas-containing pore space with time and explains encroachment of gas flow continuously into ground water zone for production in the pore throat development area as the injection-production cycle increases. Meanwhile, under the wetting function, the water film was concentrated in the small pore space compared to the larger pore space; the storage space occupied by the formation water and dead gas zones is released by the gas execution. Further analysis of the data shows notable findings on correlation between time and the amplitude of the gas saturation rise, as shown in Figure 11-1. The results in Figure 11-1 are based on the model discussed in section 9.2.1.1, which is long-term seasonal case.

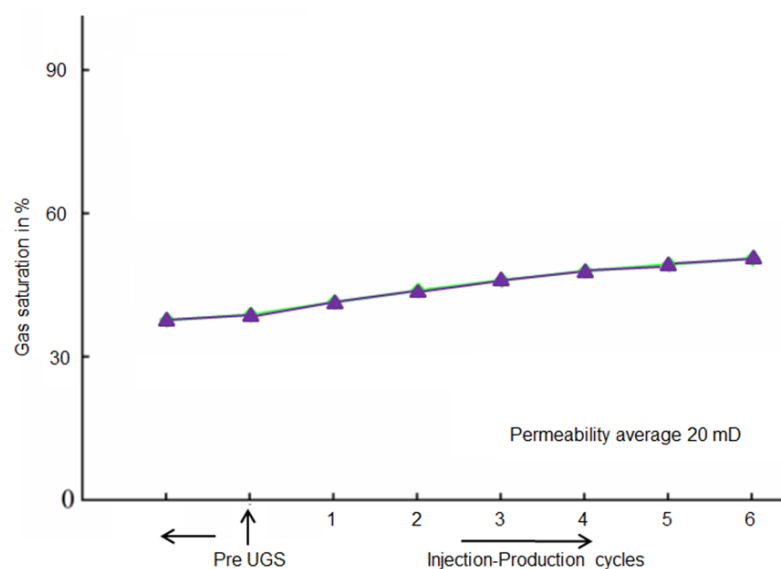


Figure 11-1: Gas saturation (%) during injection-production cycles.

During six months injection and production cycles, the increase in gas saturation from ~35% to ~50% from 1<sup>st</sup> cycle to 6<sup>th</sup> cycle respectively. Therefore, it appears that during multi-cycle injection and

production in the pre-UGS gas zone, the pore gas storage space in reservoirs with low permeability generally increases sharply, as evident from the correlation between low permeability and high initial water saturation (according to [13]). Moreover, the higher the relative quantity of liquid phase that is continuously transported and dried during high velocity development, the greater the increase in gas saturation.

The gas injection production capacity tends to improve in the UGS gas zone when the gas production is increased during the injection production cycle. Further investigation of the UGS gas zone shows that the degree of gas production also increases with the injection-production cycle, but the degree of gas production varies according to the different physical properties and connectivity of the pore spaces [13]. Strong seepage is observed in reservoirs with high permeability, and gas production and degree of gas recovery were also high under the same injection-production conditions [13].

The gas saturation first decreases in the pre UGS phase and then increases significantly during multi-cycle injection and production, showing the decrease in gas saturation and gas storage space when the gas-drive water zone (gas-water zone, where gas saturation is more dominant) was converted into gas storage. Due to the intrusion of lateral and bottom water, part of the gas storage space was occupied by water during the slow exploitation phase, and a capillary trap for the gas-containing space was also created. Further data showed that higher permeability causes water to penetrate, leading to an even greater reduction in gas saturation. During the multi-cycle injection and production phase in UGS, there was no water encroachment or the part where water encroachment occurs is displaced in the initial gas injection phase of gas storage into the gas-drive water zone. In contrast, under the influence of high velocity injection and production cycle extraction, residual water was produced that was similar to that in the gas zone before UGS [13]. The experimental analysis shows that the gas-drive water zone is the main expansion zone of the UGS, as the storage space and storage capacity is greatly increased in this gas-drive water zone [13].

The variation of gas saturation in the gas-drive water zone shows the same trends both compared to the trend in the single core experiment and the trends of average gas saturation in the parallel multicore experiment. However, in the multicore parallel experiment, the reduction in gas saturation caused by water encroachment is relatively small [13]. The distinctive feature of reservoir heterogeneity, a formation with high permeability has a great impact on the water body as it promotes water intrusion, while formations with medium and low permeability are less affected by water intrusion. During high velocity injection and production, the gas preferentially percolated into the high permeability formation, resulting in gas saturation recovery in the high permeability reservoir.

The gas permeability of the reservoir may also reduce due to clay minerals in the reservoir, which may expand when they come into contact with water, thereby occupying the pore space. For this reason, gas production and gas content are relatively low in the first injection and production cycle. Meanwhile, the gas recovery level and gas production level are low due to lower vertical permeability [13]. Furthermore, gas production and injection increase with increasing permeability.

The transition of the reservoir characteristic of the gas-water transition may indicate that water intrusion is caused not only by the exploitation of the gas field, but also by the gas storage cycle in the operational phase. In general, the gas saturation decreases both in operational zones of the reservoir and lowers in the gas-water zone. However, the effects of physical properties and heterogeneity, wettability and capillary pressure of the reservoir make the production mechanism of multicycle injection complex. The relationship between gas and water in the gas-water transition zone tends to be rational and the gas saturation tends to plateau during multicycle injection production [13]. Alternatively, residual gas and trapped gas are effectively reduced due to the back and forth movement of gas and water through the gas-containing spaces, but the changes in gas saturation are small

throughout the reservoirs. Conversely, in high-speed injection and production, water is still continuously transported into the pore throat for production, but in gas storage, the main discharge concerns water in the large pore throat because it is difficult to displace water in the microspores. For this reason, gas saturation tends to plateau in the gas-water transition zone. Due to the reduction in water intrusion energy, gas saturation increased slightly in the subsequent phases of injection and production operation.

In general, similar gas saturation is observed both during the development phase and in the gas-water gas zone. The average gas saturation values in the single-core experiment and the multi-core parallel experiment were lowered respectively by 30.62% and 16.95% [13]. However, the average gas saturation during injection production is lower in the single-core experiments than in the multicore experiments. The average gas saturation of the single core and multicore experiments during injection production were 37.25 % and 43.23 %, respectively [13]. This is due to the fact that the high permeability formation in strong heterogeneous reservoirs allows rapid infiltration of water from the edges and bottom, which results in a large amount of gas not being produced and trapped in the reservoir. Formations with low permeability, however, are protected from water intrusion [13].

These results show that low gas saturation and poor recovery are observed in the gas-water transition zone of UGS, and that effective exploitation of the gas-water transition zone is affected by reservoir heterogeneity [13]. Therefore, the effective utilization of the gas-containing pore space under the high-speed injection and production conditions of gas storage is significantly different from the utilization of the gas reservoir. For that reason, the optimal design of UGS capacity and calculation of gas storage parameters should be founded on the effective utilization of the gas-containing pore space as well as on the effective pore space of the reservoir structure in different zones [13].

### 11.3 3D Mechanical Earth Model

The field scale static geomechanical model of the case study reservoir with dimension of 30 x 24 x 5 km<sup>3</sup> is built successfully (Chap. 6.1). The model comprises 11 mechanical stratigraphic units with three faults. The model is calibrated using field data and provides novel and exclusive visualization of the in-situ stress and strain distribution of a depleted gas reservoir. The stress state of the model not only provides stress conditions around existing wells but also for undrilled parts of the reservoir as well as the overburden and underburden sections. The exposed complexity of the local stress variations underlines the need for numerical geomechanical modelling approaches.

The resolution of the reservoir model provides a good basis to construct a 3D geomechanical model with over-, under- and sideburden formations with less resolution relative to the reservoir model. The grid dimensions of the reservoir model used in geological (Petrel), hydraulic (ECLIPSE™) and reservoir section of the 3D embedded geomechanical model should match in order to perform coupling for dynamic geomechanical modelling. The robust 3D geomechanical model has been selected for the case study reservoir with appropriate dimensions of sideburden as well as under- and overburden formations.

The major lithographic units incorporated in the 3D embedded model (Figure 4-8) do not include the sub-lithostratigraphic units. 11 stratigraphic units include four overburden, six underburden and one reservoir unit. More detailed stratigraphic units with facies variations can be integrated in the model, if detailed stress modelling of the area is needed. For instance, detailed sub-lithostratigraphic units incorporation in overburden as well as reservoir section in case of planning new wells or deeper division of further stratigraphic units in underburden for geothermal applications.

Geometric information explaining the fault network is already incorporated in the case study reservoir

model provided by Uniper SE. The reservoir model contains major seismically mapped vertical faults. Due to small offsets in seismic data, some of the small faults cannot be included in the reservoir model. Subseismic faults, i.e., faults below the seismic resolution have to be omitted while considering fault modelling. However, such faults can be derived from the production behavior of neighboring wells, but their exact location will be difficult to determine. However, the origin of faults and the degree of certainty regarding their exact location is not specified in the structural model. Therefore, it was not possible to select the faults in relation to their uncertainty, and that is why all faults which are in the production area of the reservoir are considered for the geomechanical model. Only very small fault lines with hardly any offset and fault lines far outside the production area are neglected. This means that some conceptual faults are included in the geomechanical model which may follow tracks other than those defined. This has a direct impact on the modelled stress perturbations and their interaction. Furthermore, sub seismic faults, which are not detected by the production behavior, can also disturb the in-situ stress to a certain extent.

The mechanical properties of the 3D geomechanical model are derived from 1D MEM for all the wells with limited but comprehensive amount of log data. The population of the properties by interpolation methods is the only way to perform property modelling in 3D models. The precision of the property modelling by these methods can of course be challenged especially outside of the reservoir area but this is the only way to estimate properties in the area where no data or whatsoever is available. The properties are spatially distributed using the Kriging method [39], i.e. a geostatistical method that provides a deterministic model that takes into account the well properties according to a defined variogram (a spherical model was chosen).

The results of the static geomechanical model show stress state at each cell of the 3D geomechanical model. These stresses are calibrated against observed stress values provided in an internal report [96]. The observed values of all the principal stresses are limited to one well (X6). The modelling results could improve by incorporation of more calibration data across the reservoir. The calibration of the static geomechanical model is a process that is sensitive to measurement uncertainty. The results of ultrasonic wave velocity analyses (WVA) on drill cores could provide further information about the minimum principal stress magnitude along with the extended leak-off tests. However, the measurements are derived from one well (X6) in the reservoir and could therefore not be compared with any other well. More precise information about uncertainties and error ranges helps to improve the calibration procedure. It could also be improved by more measurements providing the magnitudes and orientation of all three principal stresses at a single point. If this information is reliable, it is ideal and can be obtained from methods such as ultrasonic wave velocity analysis.

### 11.4 THM coupled modelling

The geomechanical approach presented in this thesis allows characterization, from a geomechanical point of view, of the target reservoir in a very understandable way. The coupled simulation of one-way flow and geomechanics (VISAGE<sup>TM</sup>) focuses on understanding the variation of effective stresses due to pressure changes associated with gas injection into the subsurface reservoir. In other words, the focus is on the pore pressure changes during operation. The VISAGE<sup>TM</sup> model is created directly from the geological model and can therefore be considered more accurate in terms of geometry as compared to other finite element model such as ANSYS<sup>TM</sup> model. The material properties in the VISAGE<sup>TM</sup> model are scaled up from borehole logs and their population contains information about the original vertical and horizontal variations. The VISAGE<sup>TM</sup> simulator treats faults as 3D cells with different material parameters in relation to the surrounding rock. The output of the VISAGE<sup>TM</sup> model is continuous through space, and the presence of faults can be detected by an abrupt change in depth at the point of displacement, even if technically the horizon is not present at that point. Therefore,

VISAGE™ is used for ECLIPSE™-VISAGE™ coupling in order to build coupled THM model to achieve desired geomechanical results.

THM coupled modelling involves coupling of static geomechanical model with dynamic fluid (hydraulic) model. The geomechanical stresses of the reservoir change in space and time when coupled with pore pressure either from reservoir history or from future testing scenarios. In general, these dynamic models are based on the concept of effective stress to characterize the effects of pore pressure changes on reservoir and caprock integrity as well as fault stability. Simplified geomechanical models rely mainly on the concept of effective stress to distinguish the effects of pore fluid changes on reservoir integrity and fault stability. Terzaghi [43] proposed this effective stress concept for soil system, The result of the increase in pore fluid pressure is equal to the decreased effective stress on the rock mass, and conversely, this concept implies that the effective stress experienced by the rock framework is due to the changes in fluid pressure, with the absolute magnitudes of the principal in situ stresses themselves remaining unaltered.

However, there is another phenomenon that causes the minimal horizontal changes via poro-elastic interactions when the pore pressure of the reservoir changes, which is referred as stress path. The stress path is also known as pore pressure-stress coupling in a system, which describes the degree to which the minimum horizontal stress changes in response to pore pressure perturbations, either in an injection or withdrawal scenario [2] [104] [105]. Such changes of the stress tensor are important to characterize from an operational point of view, as they determine the fracture gradient as well as the pore pressure at which the fault is reactivated assuming Mohr-Coulomb failure criteria. The stress path in the reservoir and its consequences can be understood theoretically by the following statement: The pressure of the pore fluid builds up and the reservoir tries to expand in all directions when fluid or gas is injected or introduced into the reservoir. The vertical stress remains the same because the vertical direction is limited by the free surface (the earth's surface).

From a classical point of view Terzaghi [43], changes in vertical stress can be predicted as the effective vertical stress increases and decreases during withdrawal and injection, while the reservoir stress path effect can clearly distinguish the changes in the effective minimum horizontal stresses. As a result of the increased fluid pressure, the Mohr circle drifts to the left, this in turn reduces the diameter of the circle, implying that the fault is under a lower differential stress. From a theoretical treatment that consolidates only the concept of effective stress, the assumption can be made that the stress path during compression is parallel to the failure envelope rather than towards it [2]. A steeper stress path during the injection process is the result of a small Poisson's ratio, a large Biot coefficient, a large shear modulus and a shallower reservoir, further causing drift away from the failure envelope.

At case study reservoir, reactivation of the fault with increasing fluid pressure would not be possible if the stress path could be assumed to be exactly linear to higher fluid pressures. The magnitude of the stress path in the reservoir is an absolute criterion to ensure that the faults are not tapered by pressurization or depressurization. Furthermore, this linear extrapolation of the stress path is obviously only suitable for moderate fluid pressure levels. During pressurization of the system, there are some points where the horizontal stress becomes the maximum principal stress instead of the vertical stress. This shows that in the absence of stress path effects, the stress path changes and moves towards the failure criterion.

One of the main aspects of the THM modelling results is the deformation within and outside of the reservoir formation as a result of injection and withdrawal of fluid/gas in reservoir. Pressurisation and depressurisation cause deformations in both the reservoir and the overburden, which are part of the effective results of geomechanical modelling. During overpressure or underpressure, the elastic or



non-elastic expansion or contraction of the rock mass causes such deformations. The reactivation of faults and the integrity of the rock may be affected by the deformations within the reservoir. In addition, deformations associated with reservoir depletion can also pose a serious problem in terms of casing collapse and become a major obstacle to subsequent drilling [106].

The main risk related to pressurization and depressurization of a field during injection and withdrawal periods respectively is fault reactivation and associated permeable leakages. During gas injection and production phases, reactivation of the fault and associated permeable pathways is one of the main risks associated with pressurization and depressurization. The classical fault model would predict that as the fault approaches shear reactivation, there will be an increase in fluid pressure that would reduce the effective normal stress on the fault. However, the stability of the fault is significantly affected by the progression of reservoir stresses through the effects on horizontal stress magnitudes. As discussed in the above section (9.2.1), the simulation results of THM model predict decrease in effective stresses while increase in pore pressure in various short-term storage cases. If this difference in effective stresses and consequently in pore pressures is very small, no significant stress perturbations would occur. However, if this difference is large, i.e. if the pore pressure in the reservoir is large, then there is a high probability of fault reactivation with increasing pore pressure, as described in the above section (10.2) about the various fault reactivation cases. Fault reactivation occurs in the reservoir already at 1.25 times the initial pore pressure of the reservoir, which means that the Mohr circle reaches the failure line at this pressure.

Distinguishing deformations above and at the surface of the reservoir is also important for surface monitoring and for potential reactivation of faults in the reservoir section. These deformations (either elastic or sometimes plastic) occur due to contraction and expansion of the rock mass during over-pressuring and under-pressuring phases. Over- and under-pressuring of reservoir is directly related to large amount of gas injection and production rates respectively. Due to this reason, the upper (18.8 MPa) and lower (13.8 MPa) limit of bottom hole pressure (BHP) is considered, which does not allow the pressure to rise or drop below designated pressure limit as described in the above section 7.2. The deformation caused by this over-pressuring and under-pressuring of reservoir could initiate fault reactivation and may affect caprock integrity. The significant drop in reservoir pressure due to rapid depletion may damage casing and induce drilling complications for newly planned well in the reservoir [106].

The ground surface subsidence characterization is also significant factor for surface monitoring as well as for fault reactivation analysis in the overburden section. The ground surface subsidence of the case study field is -13 mm (Figure 9-1) at maximum depletion period by reduction of field pressure from 16 MPa to 3 MPa (see section 9.2) which is quite similar to Iona storage field where the ground surface subsidence is about -12 mm with reduction of field pressure from 13 MPa to 2 MPa during the maximum depletion period [2]. These values of vertical displacement are relatively smaller if compared with ground subsidence at some depleting oil and gas field in the Gulf coast region of the United States i.e. at least about 25 cm of subsidence at the ground surface. The examples from the Gulf Coast region of the United States, a sharp drop in field pressure led to the observed severe subsidence, sometimes as high as 40 MPa [107] [108].

This study does not include a sensitivity analysis to determine the stress field or displacement of the ground surface when elastic properties vary. Due to the poor correlation between the mechanical properties of the rock and the porosity in the individual wells, there can be considerable variation in the construction of the static geomechanical model, which can affect the distribution of the mechanical properties rather than the magnitudes. In contrast, the successive calibration of the sonic logs and the mechanical tests themselves appear to have close correlations, demonstrating their accuracy. However,

it is possible that the actual values for Poisson's ratio and Young's modulus may differ slightly from those used in the modelling. There are several studies have already been carried out on these parameter studies and the effects of parameter variation on geomechanical stresses and ground surface displacement [109]. Chen (2012) models the pressurization of a reservoir at 600 m depth by 1 MPa using Young's modulus and Poisson's ratio values close to our case study reservoir. This modelling study suggests reducing the stiffness of the reservoir i.e. reducing the value of Young's modulus from 5 GPa to 3 GPa, the vertical displacement increases from 0.08 to 0.12 mm [109]. Similarly, a reduction in the Poisson ratio from 0.3 to 0.2 results in an increase in the ground surface displacement from 0.11 to 0.13 mm [109]. It should be borne in mind that the sensitivity of these parameters is highly dependent on a number of different factors including the depth and size of the reservoir, stress field and the properties attributed to the surrounding formations [109]. However, the work presented by Chen gives a rough idea of the types of variations that might be expected from such modelling.

## Chapter 12 Conclusions and perspectives

### 12.1 Conclusions

For modelling and simulation of underground gas storage reservoirs, a complex multidisciplinary endeavor including fluid dynamic and geomechanical modelling predictions is needed. The results may provide helpful information regarding stress state of the reservoir area, safe storage capacity and operational pressure threshold, ground surface displacement as well as safety of reservoir and caprock. In order to incorporate all these factors, a state of the art THM modelling approach has been adopted in this study to address issues related to thermal, hydraulic, and mechanical components of underground gas storage reservoir.

A methodology is presented that uses 1D mechanical earth models (1D MEM) (Chap. 3.1) to calculate static elastic properties and pore pressures based on well log data information and provide a first approximation for the stress distribution with depth. The ideal data set for 1D MEM includes sonic-velocity logs, density/neutron log as well as core data for calibration. The absence of this data set limits the modelling results and increases various uncertainties in the model. All other data, e.g. elastic properties and pore pressure can be calculated through various correlations, such as used in this study Bradford correlation [51] for elastic properties and pore pressure from Eaton's method [42]. The 1D MEM modelling results provide a complete analysis of log, core and laboratory data leading to a detailed 1D MEM of all wells available for the case study reservoir. As an example, the calculated and calibrated Young's modulus is 4 GPa and the Poisson's ratio is 0.35 at well X6 at a depth of approximately 1786 m (section 5.2.2).

These modelling results are then used to populate a 3D geomechanical model (3D MEM) with elastic properties by using the kriging interpolation method (Chap. 6.1). This 3D finite element model (3D MEM) was built from seismic data that comprises not only the reservoir, but the entire overburden (up to the earth surface) down to the part of the basement rock as underburden. The geomechanical model is coupled with a dynamic hydraulic model (Chap. 7) to get the pore pressure field for the reservoir for certain time steps in order to simulate total and effective stresses and related deformation inside and outside of the reservoir as well as surface displacement.

The workflow was successfully applied to a case study gas reservoir (Chap. 4) located in the Molasse Basin of southern Germany. Modelling results were calibrated against various observational data sets. The validated THM model provides the complete stress state at any location in the model domain (Chap. 6.1). This information can be used for planning of future well trajectories. For example, the predicted and calibrated magnitudes of vertical stress ( $S_v$ ), maximum horizontal ( $S_{Hmax}$ ), and minimum horizontal stress ( $S_{Hmin}$ ) at well X6 at a depth of 1786 m are 42.8, 38.7 and 36.7 MPa respectively. This indicates that the reservoir lies in normal faulting regime. The modelling results also provide information about surface ground movement during depletion and replenishment times. The maximum subsidence at the ground surface above reservoir is observed to be -13 mm (negative sign represents subsidence) at ultimate depletion time which reduces sideways and eventually becomes zero at the edges of the reservoir. During replenishment period reverse surface behavior has been observed which resulted in upheaval of 11 mm at the ground surface above reservoir.

Furthermore, THM modelling results provide the starting point for future scenario testing (Chap. 7.2), e.g., conversion of the former gas field to a storage site with short-term (weekly) injection-production schedules on top of long-term (seasonal) gas storage cycles. There have been nine cases tested for

future scenarios with long-term and short-term operations. Some of the cases are with limited water cut rate ( $5 \text{ m}^3/\text{day}$ ) and others are without water cut rate. German surplus energy data from renewable energy sources (such as wind and solar energy) from the year 2017 has also been incorporated in these future testing cases in order to implement PtG technology on former gas reservoir to meet Germany's future energy demand (Chap. 2.3). The operating volumes in these cases are controlled by the upper (18.8 MPa) and lower limit (13.8 MPa) of well bottom hole pressure (WBHP). Noteworthy findings are congregated from these dynamic fluid flow cases including seepage conditions after long shut-in of the depleted gas reservoir. Due to water encroachment in the porous zone during shut-in phase, the pore volume of the gas storage plus the degree of gas recovery were low during the initial injection-production cycles, which increased later as flow conditions improved. The gas-drive-water-invaded zone proved to be the main expansion zone of the UGS. In the gas-water transition zone, the gas and water were reciprocated by the multiple injection-production cycles, resulting in a gradual deterioration of the pore and gas volume. These outcomes may contribute to a better understanding of the rules governing multi-cycle injection and production as well as UGS utilization to optimize the efficiency of the case study storage facility. The response of the reservoir to injection and production of gas was computed in terms of changes in effective stresses through a coupled simulation of fluid flow and geomechanics. The results of the coupled THM modelling of these cases (Chap. 9.2.1) show that the maximum difference of pore pressure and subsequently effective stress is observed to be 0.6 MPa among all tested cases.

The response of the reservoir to gas injection/production cycles was quantified in terms of changes in effective stresses through a coupled simulation of one-way flow and geomechanics. A flow model simulated the injection/production cycles of gas into the subsurface reservoir, and the calculated pressures were used as input to the geomechanical simulator to calculate the corresponding effective stresses. This workflow was applied to the entire development history of the reservoir, covering both production and injection operations. The calculated stress state was checked against the Mohr-Coulomb failure criterion to assess both caprock integrity and fault stability. This is made possible by including faults in the model as 3D cells with specific fault properties for which the stress state is calculated individually. The current scenario shows that the integrity of the overburden is not at risk, while possible reactivation could occur if a critical pore fluid pressure is exceeded (Chap. 10.2). Fault reactivation analyses were performed on the THM models, which evaluate various gas injection scenarios without any upper limit of WBHP. The quantified stresses are then examined against Mohr-Coulomb failure criterion to estimate fault stability. This was achieved by including faults with specific properties into the 3D geomechanical model. The stress state of the 3D cells with fault properties exceeding the shear failure line was observed against different gas injection volumes. Faults reactivation occurred at the gas injection rate of  $240,000 \text{ m}^3/\text{day}$  that gives a value of critical pore pressure. This critical pore pressure observed to be 1.25 times the original pore pressure which is equivalent to the WBHP value of 20.25 MPa (Chap. 10.2). With the determination of pore pressure, it is also possible to estimate an upper limit of gas injection rate for safe storage operation. Which in this case study was observed to be in the range between  $100,000$  and  $150,000 \text{ m}^3/\text{day}$  (Chap. 10.3).

It should be declared here that in this study the critical pore pressure is calculated at the well location, whereas the reference location for further studies can be from anywhere in the reservoir and the high permeability of the reservoir can reduce possible differences in the reference sites. Analysis of the case study numerical modelling results shows that a 4 MPa increase in pore pressure would be sufficient to trigger fault failure.

Thermal stresses depend merely upon the thermodynamic processes in the system. Therefore, one case (seasonal) has been tested for thermal stress analysis by using the same THM model. The original reservoir temperature was  $45^\circ\text{C}$  and the injected gas temperature was set  $25^\circ\text{C}$ . The thermal changes

are small ( $0.5^{\circ}\text{C}$ ) and occur only near and around the wellbore. The thermal effects on stress are not significant in the reservoir even after injecting  $100,000\text{ m}^3/\text{day}$  of colder gas for about half a year (Chap. 8.2). This suggests that the thermal changes in the short-term cases are negligible to be considered in the analysis of geomechanical stresses in the reservoir during storage operations. This is due to the low operating volumes and the short time cycles for injection production (weekly schedule) in short-term cases.

In terms of storage capacity of PtG technologies, the case study storage can store up to maximum of  $1,322,400\text{ kWh/d}$  of electricity from renewable or other resources, converting the maximum gas volume of  $150,000\text{ m}^3/\text{day}$ . This amount of energy storage can at least contribute to Germany becoming a greenhouse gas neutral country (GHGND) in 2050, which corresponds to an energy demand of  $1600\text{ TWh}$  of electricity (Chap. 2.3).

The entire workflow outlined and tested in this study is not site-specific but generally applicable to any gas storage in a porous medium including methane,  $\text{CO}_2$ , and hydrogen.

### 12.2 Perspectives

The modelling schemes described in this study provide a thermal-hydraulic-geomechanical assessment consistent with the observational data presently available. This THM modelling study can be used to assess borehole stability, which can be achieved by analyzing the hydraulic and mechanical limits of the borehole walls. Another application of the model can be a fully coupled model, where geomechanical and hydraulic models are coupled in such a way that both can receive and process the required parameters simultaneously (explained in the last paragraph). This modelling study can also serve as a benchmark for the use of UGS as a seasonal battery for PtG technologies. In this way, the excess energy can be stored as gas in the UGS and later converted back into electricity when needed.

But the modelling results and workflow can be improved by various recommendations for further work. As an example, the modelling results of both 1D and 3D MEM can be improved by more data set than currently available. This data set may include input and calibration data. More laboratory (core) data would be helpful to optimize the accuracy of the material properties, which presently depend upon the pre-established empirical correlations. Calibration would also be improved with gathering of new wellbore data e.g. availability of leak-off test and minifrac, wellbore breakout, wellbore image data would enhance the accuracy of calculated minimum and maximum horizontal stresses. New borehole data such as gamma ray, acoustic, electrical and density logs for more wells in the area would also help to improve the population of material parameters and increase the accuracy of lateral variation, which currently depends heavily on the algorithm used in this study such as kriging interpolation.

The rock properties of the reservoir have an important influence on the estimated amount of subsidence. For future modelling, it would be useful to conduct detailed rock mechanics experiments with representative samples from the deposits in the region. It is important to have as much reliable data as possible on vertical elevation changes in the region to test different hypotheses related to subsidence. Such data could come from repeated surveys of existing first-order contour lines, GPS or InSAR observations. In addition, sensitivity analyses or parameter studies to determine the stress field or displacement of the ground surface as elastic properties vary would be useful to understand the reservoir behavior in response to a change in, for example, Young's modulus or Poisson's ratio, etc.

THM modelling in this study uses a one-way coupling simulation approach. The coupling between dynamic fluid flow and geomechanical simulation can be improved by adopting two-way or even fully coupled simulation. This means that not only the pore pressure is passed from the fluid flow model to the geomechanical model, but also properties from the geomechanical model such as porosity,

permeability and rock compressibility are passed back to the fluid flow model to obtain continuously updated accurate modelling results. Two-way and fully coupled simulation approaches would also be useful to analyze ageing effects in the reservoir due to long- and short-term storage operations.

References

- [1] Teatin P., Castelletto N., Ferronato M., Gambolati G., Janna C., Cairo E., Marzorati D., Colombo D., Ferretti A., Bagliani A. & Bottazzi F., "Geomechanical response to seasonal gas storage in depleted reservoirs: A case study in the Po River basin, Italy.," *Journal of Geophysical Research, An AGU Journal*, vol. 116, no. F2, p. 21, 2011.
- [2] Tenthorey E., Vidal-Gilbert S., Backe G., Puspitasari R., Pallikathakathil Z., Maney B. & Dewhurst D., "Modelling the geomechanics of gas reservoir: A case study from the Iona gas field, Australia.," *International Journal of Greenhouse Gas Control*, vol. 13, pp. 138-148, 2013.
- [3] Altmann J. B., Müller B., Müller T. M., Heidbach O., Tingay M. & Weißhardt A., "Pore pressure stress coupling in 3D and consequences for reservoir stress states and fault reactivation.," *Geothermics*, vol. 52, pp. 195-205, 2014.
- [4] De Santis D., Mason J.A., James B.D., Houchins C., Long J.R. & Veenstra M., "Techno-economic analysis of metal-organic frameworks for hydrogen and natural gas storage.," *Energy Fuels*, vol. 31, pp. 2024-2032, 2017.
- [5] Wang X. & Economides M.J., "Purposefully built underground natural gas storage.," *Journal of Natural Gas Science and Engineering*, vol. 9, p. 130-137, 2012.
- [6] Aminian K., Brannon A. & Ameri S., "Gas storage in a depleted gas/condensate reservoir in the appalachian basin.," in *In Proceedings of the SPE Eastern Regional Meeting*, Canton, OH, USA, 2006.
- [7] Juez-Larre J., Remmelts G., Breunese J., Van Gessel S.Q. & Leeuwenburgh O., "Using underground gas storage to replace the swing capacity of the giant natural gas field of Groningen in the Netherlands. A reservoir performance feasibility study.," *Journal of Petroleum Science and Engineering*, vol. 145, p. 34-53, 2016.
- [8] Industry D. O. T. A., "Meeting the Energy Challenge: A White Paper on Energy.," Her Majesty's Stationary Off., Norwich, U. K., 2007.
- [9] Khaksar A., White A., Rahman K., Burgdorff K. Ollarves R. & Dunmore S., "Geomechanical Evaluation for Short Term Gas Storage in Depleted Reservoirs.," in *46th US Rock Mechanics / Geomechanics Symposium*, Chicago, IL, USA, 2012.
- [10] NOGEPa, "Potential for CO2 storage in depleted gas fields on the Dutch continental shelf – phase 1: technical assessment.," Google Scholar, 2008. [Online]. Available: <http://refman.energytransitionmodel.com/publications/448>.
- [11] Buschback T. C. & Bond D. C., "Underground storage of natural gas in Illinois.," Illinois Petroleum Republic. 86, Ill. State Geol. Surv., Urbana, 1967.
- [12] Zhang G., Li B., Zheng D., Ding G., Wei H., Qian P. & Li C., "Challenges to and proposals for underground gas storage (UGS) business in China.," *Nat. Gas Ind.*, vol. B, no. 4, p. 231-237, 2017.
- [13] Zhang J., Fang F., Lin W. & Gao S., "Research on Injection-Production Capability and Seepage Characteristics of Multi-Cycle Operation of Underground Gas Storage in Gas Field—Case Study of the Wen 23 Gas Storage.," *Energies, MPDI*, vol. 13, no. 3829, p. 17, 2020.
- [14] Ramírez A., Hagedoorn S., Kramers L., Wildenborg T. & Hendrics C., "Screening CO2 storage options in the Netherlands.," *International Journal of Greenhouse Gas Control*, vol. 4, no. 2, pp. 367-380, 2010.
- [15] Neele F., ten Veen J., Wilschut F. & Hofstee C., "Independent assessment of high-capacity offshore CO2 storage options.," Energy/Geological Survey of the Netherlands, Delft, the Netherlands., 2012. [Online]. Available: <http://www.globalccsinstitute.com/sites/www.globalccsinstitute.com/files/publications/35621/independent-assessment-high-capacity-offshore-co2-storage-options-opt.pdf>.
- [16] Guosheng D., Chun L. & Jieming W., "The status quo and technical development direction of underground gas storage in China.," *Natural Gas Industry*, vol. 35, no. 11, pp. 107-112, 2015.

- [17] Kuncir M., Chang J., Mansdorfer J. & Dougherty E., "Analysis and optimal design of gas storage reservoirs.," *In Proceedings of the SPE Eastern Regional Meeting*, p. 1066–1076, 2003.
- [18] Mazarei M., Davarpanah A., Ebadati A. & Mirshekari B., "The feasibility analysis of underground gas storage during an integration of improved condensate recovery processes.," *J. Pet. Explor. Prod. Technol.*, vol. 9, p. 397–408, 2019.
- [19] Dharmananda K., Kingsbury N. & Singh, H., "Underground gas storage: Issues beneath the surface.," *In Proceedings of the SPE Asia Pacific Oil and Gas Conference and Exhibition, Perth, Australia.*, p. 10–17, 2004.
- [20] Du Q., "Variation law and microscopic mechanism of permeability in sandstone reservoir during long-term water flooding development.," *Acta Pet. Sin.*, vol. 37, p. 1159–1164, 2016.
- [21] Zoback M., Moos D., Anderson R. & Mastin L., Wellbore breakouts and in situ stress., *J Geophysics*, <https://doi.org/10.1029/JB090iB07p05523>, 1985.
- [22] Herwanger J. & Koutsabeloulis N., "Seismic Geomechanics: How to Build and Calibrate Geomechanical Models using 3D and 4D seismic data.," *EAGE*, 2011.
- [23] Fischer K. & Henk A., "A workflow for building and calibrating 3D geomechanical models- a case study for a gas reservoir in the North German Basin.," *Solid Earth*, vol. 4, pp. 347-355, 2013.
- [24] Reinecker J., Tingay M., Müller B. & Heidbach O., "Present-day stress orientation in the Molasse Basin.," *Tectonophysics* 482, pp. 129-138, 2010.
- [25] Yale D. P., "Fault and stress magnitude controls on variations in the orientation of in situ-stress, in: Fracture and In-Situ Stress Characterization of Hydrocarbon Reservoirs.," *Geological Society, London*, vol. Special Publications, pp. 55-64, 2003.
- [26] Henk A., "Perspectives of geomechanical reservoir models-why stress is important.," *Oil Gas-Eur. Mag.*, vol. 35, pp. 18-22, 2009.
- [27] Guerra C., Fischer K. & Henk A., "Stress prediction using 1D and 3D geomechanical models of a tight gas reservoir-A case study from the Lower Magdalena Valley Basin, Colombia.," *Geomechanics for Energy and Environment*, vol. 19, no. [HTTP://doi.org/10.1016/j.gete.2019.01.002](http://doi.org/10.1016/j.gete.2019.01.002), 2019.
- [28] Bachmann G.H., Müller M. & Weggen K., "Evolution of the Molasse Basin (Germany, Switzerland).," *Tectonophysics* 137, pp. 77-92, 1987.
- [29] Grond L., Schulze P. & Holstein J., "Systems analyses Power to Gas: A technology review.," KEMA Nederland B.V., Groningen, 2013.
- [30] Wietschel M., Plötz P., Pfluger B., Klobasa M., Eßer A., Haendel M. & Kirchenbauer J. M., "Sektorkopplung – Definition, Chancen und Herausforderungen.," Fraunhofer ISI, 2018.
- [31] Sobczak et. al., "Analyzation of the gas sector as an option for sector coupling in the electric power system.," EIT, Magdeburg, 2017.
- [32] Patel S., "Why Power-to-Gas May Flourish in a Renewables-Heavy World.," [Online]. Available: <https://www.powermag.com/why-power-to-gas-may-flourish-in-a-renewables-heavy-world/>, 2019.
- [33] Appunn K., "Sector coupling - Shaping an integrated renewable energy system.," *Journalism for the energy transition*, 2018.
- [34] Purr K., Osiek D., Lange M. & Adlunger K., "Integration of Power to Gas/Power to Liquids into the ongoing transformation process.," *Umwelt Bundesamt Publication*, 2016.
- [35] Bucy J. D., "The potential of Power-to-Gas; Technology review and economic potential assessment.," Enea Consulting, Paris, 2016.



- [36] UBA, "Germany in 2050 – a greenhouse gas-neutral country.," 2014.
- [37] Abedin M. Z. & Henk A., "Building 1D and 3D Mechanical Earth Models for Underground Gas Storage—A Case Study from the Molasse Basin, Southern Germany.," *Energies*, vol. 13, no. 5722, p. 21, 2020.
- [38] Henk A., "Geomechanical reservoir models- a case study from the Sirte Basin, Libya.," *Oil Gas-Eur. Mag.*, pp. 18-22, 2010.
- [39] Kim M., Cha K., Lee T.H. & Choi D. H., "Kriging Interpolation Methods in Geostatistics and DACE Model.," *KSME International Journal*, vol. 16, no. 5, pp. 619-632, 2002.
- [40] Plumb R., Stephan E., Gary P., Donald & Brian S., "The Mechanical Earth Model Concept and Its Application to High-Risk Well Construction Projects.," 2000.
- [41] Schlumberger, "Techlog Geomechanics Workflow/Solution training.," 2017.
- [42] Eaton B. A., "Graphical method predicts geopressures worldwide.," *World Oil*, vol. 7, no. 76, pp. 100-104, 1972.
- [43] Terzaghi K., *Theoretical soil Mechanics.*, London: Chapman and Hall limited, 1948.
- [44] Formento J. L., "Seismic Pore Pressure Prediction.," in *EAGE*, Paris, 2004.
- [45] Adisornsuapwat K., Phuat T. C., Anis L., Vantala A., Juman R., & Boyce B., "Enhanced Geomechanical Modeling with Advanced Sonic Processing to Delineate and Evaluate Tight Gas Reservoirs.," in *SPE Middle East Unconventional Gas Conference and Exhibition*, Muscat, Oman, 2011.
- [46] Najibi A. R., Ghafoori M., Lashkaripour G.R. & Asef M. R., "Empirical relations between strength and static and dynamic elastic properties of Asmari and Sarvak limestones, two main oil reservoirs in Iran.," *Journal of Petroleum Science and Engineering*, vol. 126, pp. 78-82, 2015.
- [47] Greenberg M.L. & Castagna J.P., "Shear-wave velocity estimation in porous rocks: theoretical formulation, preliminary verification and applications.," *Geophysical Prospecting*, vol. 40, pp. 195-209, 1992.
- [48] Castagna J. P., Batzle M. L. & Eastwood R. L., "Relationships between compressional-wave and shear-wave velocities elastic silicate rock.," *Geophysics*, vol. 50, no. 4, pp. 571-581, 1985.
- [49] Biot M. A., "General solution of the equations of elasticity and consolidation for a porous material.," *Journal of Applied Mechanics*, vol. 55, pp. 91-96, 1956.
- [50] Chang C., Zoback M. D. & Khaksar A., "Empirical relations between rock strength and physical properties in sedimentary rocks.," *Journal of Petroleum Science and Engineering*, vol. 51, no. 3,4, pp. 223-237, 2006.
- [51] Bradford I.D.R., Fuller J., Thompson P.J. & Walsgrove T.R., "Benefits of assessing the solids production risk in a north sea reservoir using elastoplastic modelling.," *SPE/ISRM Eurorock*, vol. 98, pp. 261-269, 1998.
- [52] Archer S. & Rasouli V., "A log based analysis to estimate mechanical properties and in-situ stresses in a shale gas well in North Perth Basin.," *WIT Transaction on Engineering Sciences*, vol. 81, no. www.witpress.com, ISSN 1743-3533, pp. 163-174, 2012.
- [53] Wyllie M. R. J., Gregory A. R. & Gardner G. H. F., "Elastic Wave Velocities in Heterogeneous and Porous Media.," *Geophysics*, vol. 21, no. 1, pp. 41-70, 1956.
- [54] Lake L. W. & Fanchi J. R., *Petroleum engineering handbook.*, Texas: Society of Petroleum Engineers, 2007.
- [55] Hayavi M. T. & Abdideh M., "Estimation of in-situ horizontal stresses using the linear poroelastic model and minifrac test results in tectonically active area.," *Russian journal of earth sciences*, vol. 14, no. 4 doi: 10.2205/2016ES000576, 2016.
- [56] Dake L. P., "Fundamentals of Reservoir Engineering.," Amsterdam, Elsevier Scientific Pub. Co., 1978.

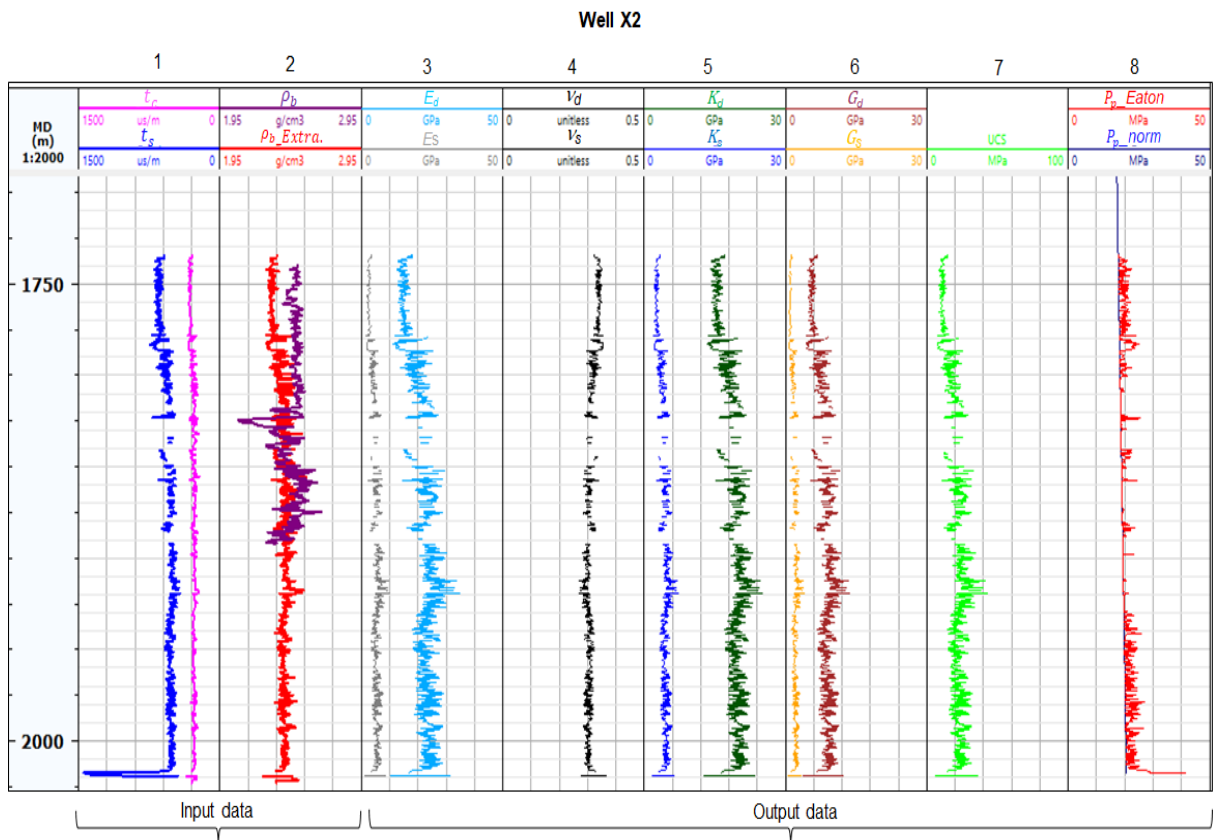
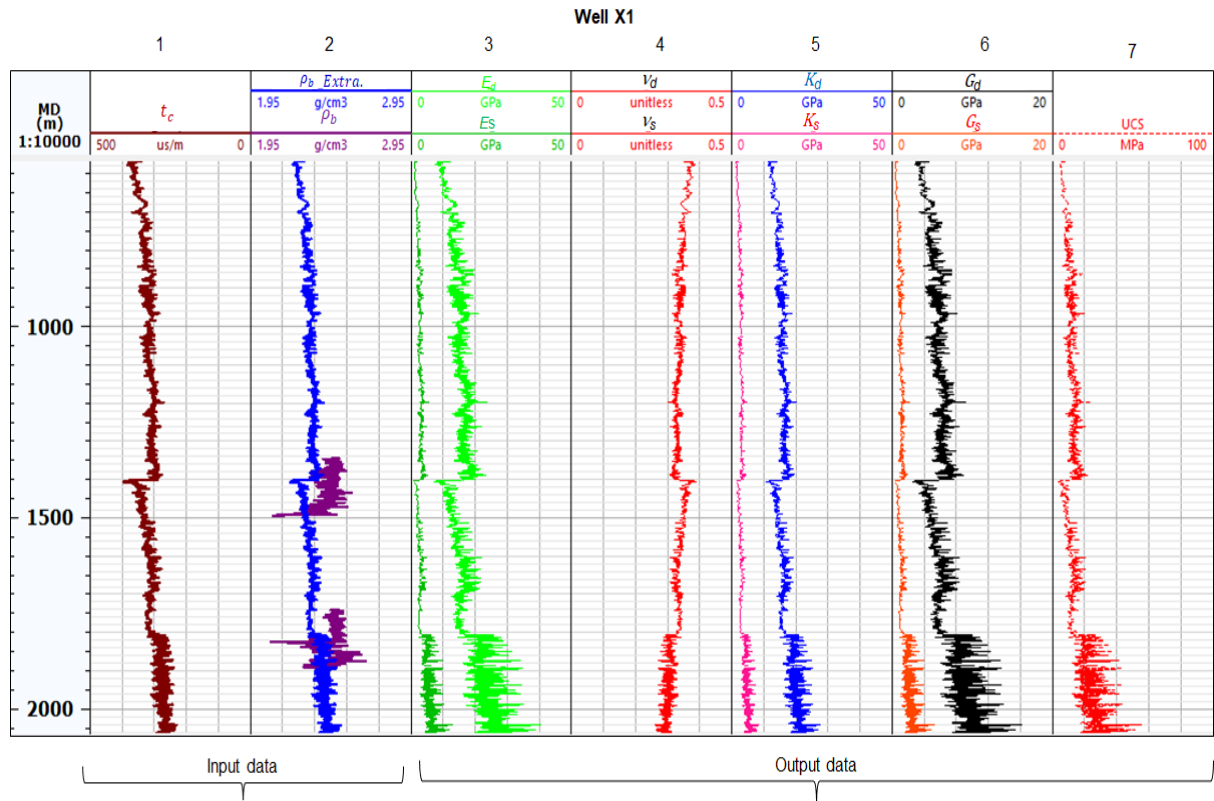
- [57] Gutierrez M., Virginia Tech., Lewis R. W. & Masters I., "Petroleum Reservoir Simulation Coupling Fluid Flow and Geomechanics.," in *Society of Petroleum Engineers*, The Hague, Netherlands, 2001.
- [58] Gutierrez M., Norwegian Geotechnical Institute, & Lewis R. W., "The Role of Geomechanics in Reservoir Simulation.," in *SPE/ISRM Eurocks'98*, Trondheim, Norway, 1998.
- [59] Dai et al., "Effective Thermal Conductivity of Submicron Powders: A Numerical Study.," *Applied Mechanics and Materials*. doi:10.4028/www.scientific.net/AMM.846.500. S2CID 114611104, vol. 846, p. 500–505, 2015.
- [60] Settari A. & Mourits F., "A Coupled Reservoir and Geomechanical Modeling System.," *SPE Journal*, vol. SPE 50939, pp. 219-226, 1998.
- [61] Tortike W. & Farouq A. S., "Reservoir Simulation Integrated with Geomechanics.," *Journal of Canadian Petroleum Technology*, vol. 5, no. 32, pp. 28-37, 1993.
- [62] Jalali M. R. & Dusseault M. B., "Coupling Geomechanics and Transport in Naturally Fractured Reservoirs.," *International Journal of Mining & Geological Engineering (IJMGE)*, vol. 46, no. 2, pp. 105-131, 2012.
- [63] Mainguy M. & Longuemare P., "Coupling Fluid Flow and Rock Mechanics: Formulation of the Partial Coupling between Reservoir and Geomechanical Simulators.," *Oil & Gas Science and Technology*, vol. 57, no. 4, pp. 355-367, 2002.
- [64] Perkins T. K. & Gonzalez J. A., "The Effect of Thermoelastic Stresses on Injection Well Fracturing.," *Society of Petroleum Engineers*, vol. 25, no. 1, pp. 78-88, 1985.
- [65] Tran D., Nghiem L. & Buchanan L., "Improved Iterative Coupling of Geomechanics With Reservoir Simulation.," in *Society of Petroleum Engineers*, Houston, Texas, USA, 2005.
- [66] Schlumberger, "Petrel Reservoir Geomechanics Fundamentals, Workflow/Solutions Training," Schlumberger Information Solutions, London, Uk, 2015.
- [67] Lanru J. & Xiating F., "Numerical Modeling for Coupled Thermo-Hydro-Mechanical and Chemical Processes (THMC) of Geological Media – International and Chinese Experiences.," *Chinese Journal of Rock Mechanics and Engineering*, vol. 22, no. 10, pp. 1704-1715, 2003.
- [68] Schiffman R., "A Thermoelastic Theory of Consolidation.," *Environmental and Geophysical Heat Transfer, ASCE*, pp. 78-84, 1971.
- [69] Booker J. & Savvidou C., "Consolidation around a Point Heat Source.," *International Journal for Numerical and Analytical Methods in Geomechanics*, vol. 9, pp. 173-184, 1985.
- [70] Aktan T. & Farouq A. S., "Finite Element Analysis of Temperature and Thermal Stresses Induced by Hot Water Injection.," *SPE 5765*, vol. 18, pp. 457-469, 1978.
- [71] Hojka K., Dusseault M. & Bogobowicz A., "Analytical Solutions for Transient Thermoelastic Stress Fields around a Borehole during Fluid Injection into Permeable Media.," *Journal of Canadian Petroleum Technology*, vol. 32, no. 4, pp. 49-57, 1993.
- [72] Geertsma J., "Problems of Rock Mechanics in Petroleum Production Engineering.," *First Congress on International Society of Rock Mechanics*, vol. 1, pp. 585-594, 1966.
- [73] Skempton A., "The Pore Pressure Coefficients A and B.," *Geotechnique*, vol. 4, pp. 143-147, 1954.
- [74] Geertsma J., "The Effect of Pressure Decline on Volumetric Changes of Porous Rocks.," *Trans. AIME*, vol. 201, pp. 331-340, 1957.
- [75] Van der Knaap W., "Nonlinear Behavior of Elastic Porous Media.," *Trans. AIME*, vol. 216, pp. 179-187., 1959.

- [76] Nur A. & Byerlee J., "An Exact Effective Stress Law for Elastic Deformation of Rock with Fluid.," *Journal of Geophysical Research*, vol. 76, pp. 6414-6418, 1971.
- [77] Ghaboussi J. & Wilson E., "Flow of Compressible Fluid in Porous Elastic Media.," *International Journal for Numerical Methods in Engineering*, vol. 5, no. 3, pp. 419-442, 1973.
- [78] Rice J. & Cleary M., "Some Basic Stress-Diffusion Solutions for Fluid Saturated Elastic Porous Media with Compressible Constituents.," *Reviews of Geophysics and Space Physics*, vol. 14, pp. 227-241, 1976.
- [79] Huan X., Xu G., Zhang Y., Sun F. & Xue S., "Study on Thermo-Hydro-Mechanical Coupling and the Stability of a Geothermal Wellbore Structure.," *MPDI, Energies*, <https://doi.org/10.3390/en14030649>, vol. 14, no. 649, 2021.
- [80] Rutqvist J., Wu Y., Tsang C. F. & Bodvarsson G., "A modeling approach for analysis of coupled multiphase fluid flow, heat transfer, and deformation in fractured porous rock.," *International Journal of Rock Mechanics*, vol. 39, p. 429-442, 2002.
- [81] Pang M., Xu G., Sun F., Xue S. & Wang Y., "Formation Damage and Wellbore Stability of Soft Mudstone Subjected to Thermal-Hydraulic-Mechanical Loading.," *Journal of Engineering and Science Technology*, vol. 12, pp. 95-102, 2019.
- [82] Hu L., Winterfeld P.H., Fakcharoenphol P. & Wu Y. S., "A novel fully-coupled flow and geomechanics model in enhanced geothermal reservoirs.," *Journal of Petroleum Science and Engineering*, vol. 107, p. 1-11, 2013.
- [83] Jahns E., "Standardtests und Sperrdruckmessungen," Gasteinlabor Dr. Eberhard, Heiligenstadt, 2009.
- [84] Ibele T., Tectonics of the Western Swiss Molasse Basin during Cenozoic times., Fribourg, 2011.
- [85] Ford M., "Foreland basin evolution around the western Alpine Arc.," *Geological Society, London*, vol. Special Publications 221, pp. 39-63, 2004.
- [86] Ziegler P., "Petroleum system of Alpine-Mediterranean foldbelts and basins.," *Geological Society, London*, vol. Special Publications 156, pp. 517-540, 1999.
- [87] Berge T.B. & Veal S.L., "Structure of the Alpine foreland.," *Tectonics* 24, pp. 1-10, 2005.
- [88] Müller M., Nieberding F. & Wanninger A., "Tectonic style and pressure distribution at the northern margin of the Alps between Lake Constance and the River Inn.," *Geol. Rundsch* 37, pp. 787-796, 1998.
- [89] Véron J., "The Alpine Molasse Basin - Review of Petroleum Geology and Remaining Potential.," *Bulletin for Applied Geology*, vol. 10, no. 1, pp. 75-86, 2005.
- [90] Lemcke L., "Übertiefe Grundwässer im süddeutschen Alpenvorland.," *Bulletin der Vereinigung Schweiz. Pet. - Geologen und -Ingenieur*, vol. 42, pp. 9-18, 1976.
- [91] Kuhlemann J. & Kempf O., "Post-Eocene evolution of the North Alpine Foreland Basin and its response to Alpine tectonics.," *Sedimentary Geology* 152, pp. 45-78, 2002.
- [92] Hay W., Wold C.N. & Herzog J.M., "Preliminary mass-balanced 3-D reconstructions of the Alps and surrounding areas during the Miocene, computer graphics in Geology.," *Lect. Notes Earth Sci.* 41, pp. 99-110, 1992.
- [93] Zweigel J., "Eustatic versus tectonic control on foreland basin fill: sequence stratigraphy, subsidence analysis, stratigraphic modelling, and reservoir modelling applied to the German Molasse Basin.," *Contrib. Sediment Geol.*, vol. 20, pp. X-140, 1998.
- [94] Schegg R., "Migration and accumulation of hydrocarbons in the Swiss Molasse Basin: implications of a 2D basin modeling study.," *Marine and Petroleum Geology*, vol. 16, pp. 511-531, 1999.
- [95] Leu W. & Oester H., "Mont Terri Project (shale research laboratory) & Hydrocarbon Potential of Western Switzerland.," [Online]. Available: <http://higherlogicdownload.s3.amazonaws.com/SPE/a6c2d780-4741-4804-b4e0->

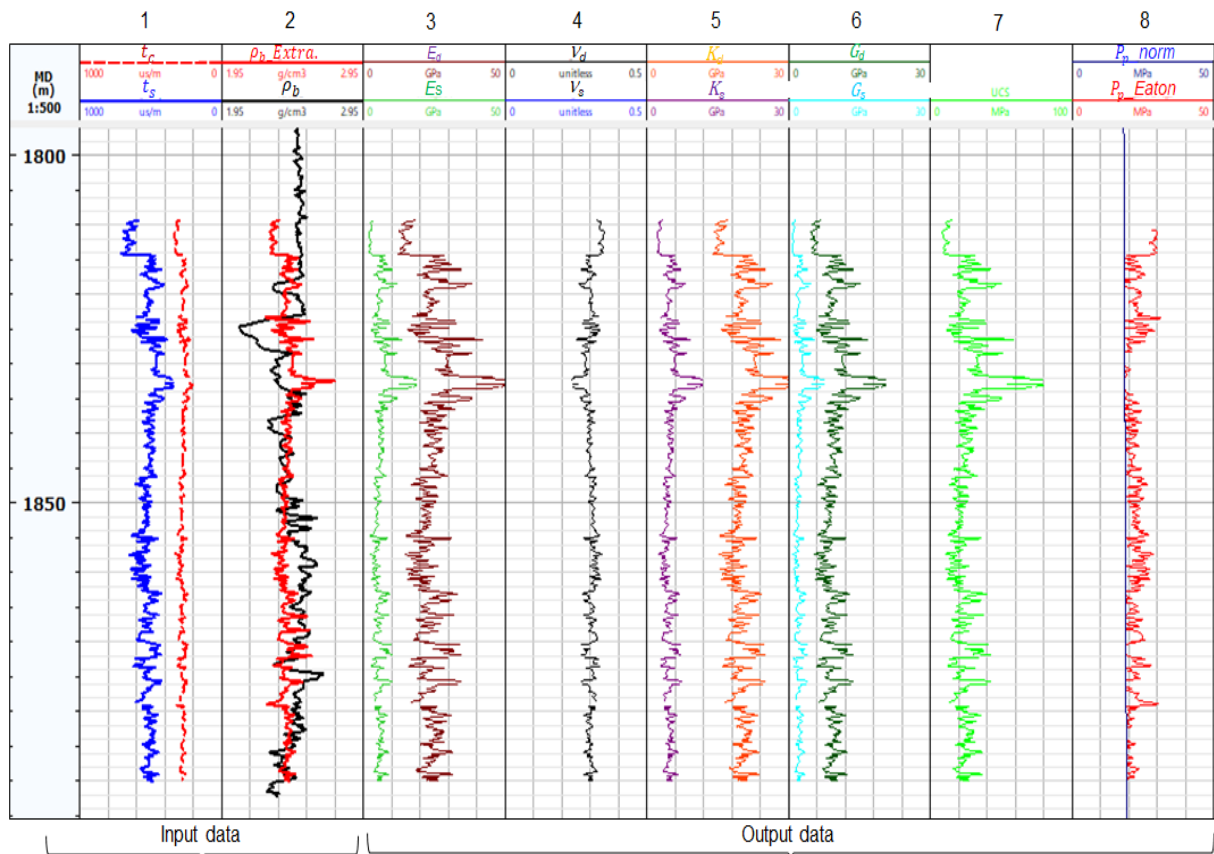
- 010e4812ddc0/UploadedImages/2012/Field%20trip%202012\_xs.pdf, 2012.
- [96] Braun R., "Einschätzung der Gasdichtheit des Deckgebirges bei Druckhöhung im Speicher.," Gebirgsmechanische Beratung, 2010.
- [97] Ganzer L. & Singhe A. T., "Investigation of Temperature Effects in a Gas Storage Reservoir and in the Storage Wells.," Institute of Petroleum Engineering (ITE), TU Clausthal, Clausthal, 2013.
- [98] Clauser C., "Thermal Storage and Transport Properties of Rocks I: Heat Capacity and Latent Heat.," in *In. Harsh Gupta (ed.) Encyclopedia of Solid Earth Geophysics*, Dordrecht, 2nd ed. Springer, 2011.
- [99] CHERIC, "Korea Thermophysical Properties Data Bank.," [Online]. Available: <http://www.cheric.org/research/kdb/hcprop/cmprch.php>. [Accessed 2012].
- [100] Frey C., "Ministerin Hendricks: Wir haben im Gegenteil sogar gigantische Stromüberschüsse.," [Online]. Available: <https://eike-klima-energie.eu/2018/01/07/ministerin-hendricks-wir-haben-im-gegenteil-sogar-gigantische-stromueberschuesse/?print=pdf>, 2018.
- [101] Burger B., "Fraunhofer ISE," Fraunhofer ISE, Freiburg, [Online]. Available: [https://www.ise.fraunhofer.de/content/dam/ise/de/documents/publications/studies/daten-zu-erneuerbaren-energien/Stromerzeugung\\_2017.pdf](https://www.ise.fraunhofer.de/content/dam/ise/de/documents/publications/studies/daten-zu-erneuerbaren-energien/Stromerzeugung_2017.pdf), 2018.
- [102] Carter G.F. & Paul D. E., *Materials science & engineering*, Materials Park Ohio: ASM International, 1991.
- [103] Fjaer E., Holt R. M., Horsrud P., Raaen A. M. & Risnes R., "Petroleum Related Rock Mechanics.," *Elsevier Science*, p. 514, 2008.
- [104] Addis M.A., "The stress-depletion response of reservoirs.," in *SPE Annual Technical Conference and Exhibition, SPE 38720*, San Antonio, Texas, 1997.
- [105] Teufel L.W., Rhett D. W. & Farrel H.E., "Effect of reservoir depletion and pore pressure drawdown on in situ stress and deformation in the Ekofisk field, North sea. Rock mechanics as a multidisciplinary science.," in *Roegiers, J. C. (Ed.), proceeding of the 32nd US Symposium.*, Balkema, Rotterdam, 1991.
- [106] Zoback M., *Reservoir Geomechanics*, Cambridge: Cambridge University Press, P. 449, 2007.
- [107] Chan A. W. & Zoback M. D., "The role of hydrocarbon production on land subsidence and fault reactivation in the Louisiana coastal zone.," *Journal of Coastal Research*, vol. 23, no. 3, pp. 771-786, 2007.
- [108] Mallman E. P. & Zoback, M. D., "Subsidence in the Louisiana coastal zone due to hydrocarbon production.," *Journal of Coastal Research*, no. Special issue No. 50, pp. 443-449, 2007.
- [109] Chen Z. R., "Poroelastic model for induced stresses and deformations in hydrocarbon and geothermal reservoirs.," *Journal of Petroleum Science and Engineering*, vol. 80, pp. 41-52, 2012.

# Appendix

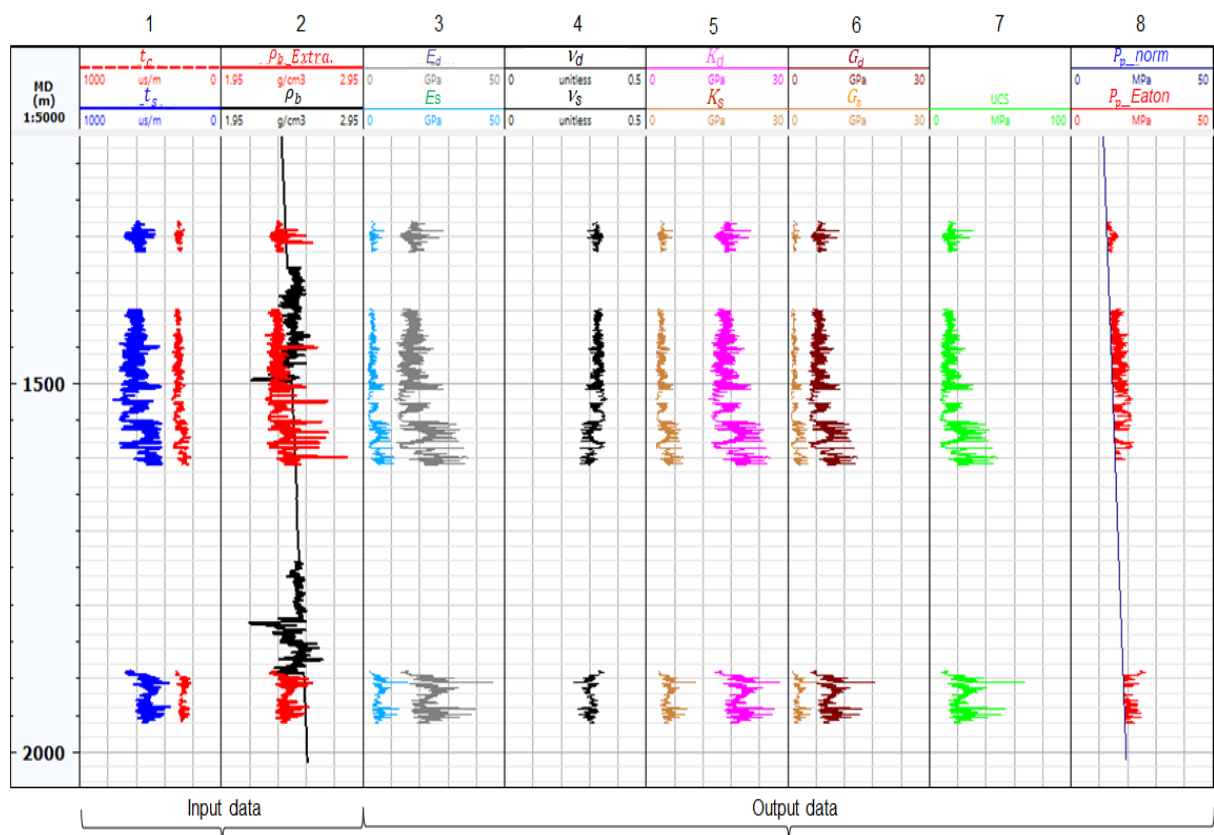
## 1D MEM for all the wells



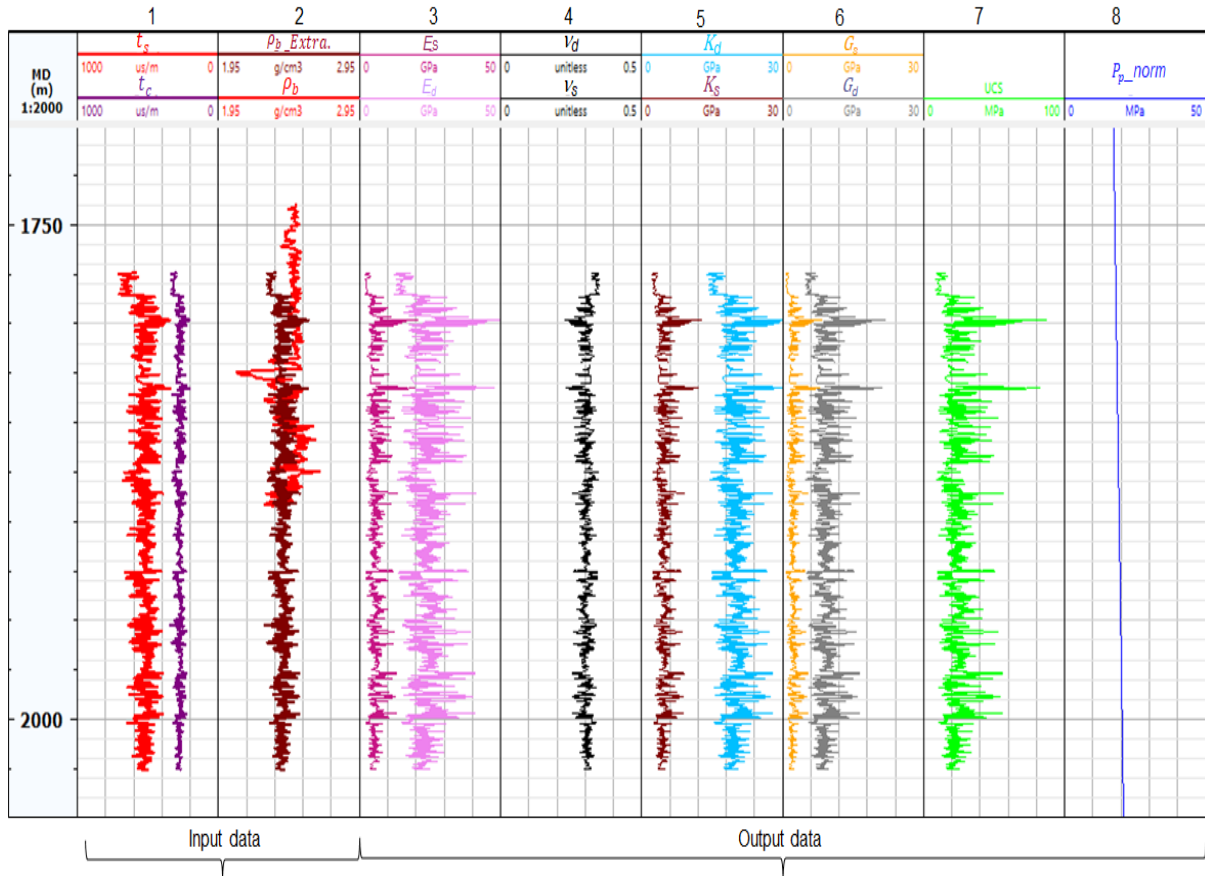
Well X3



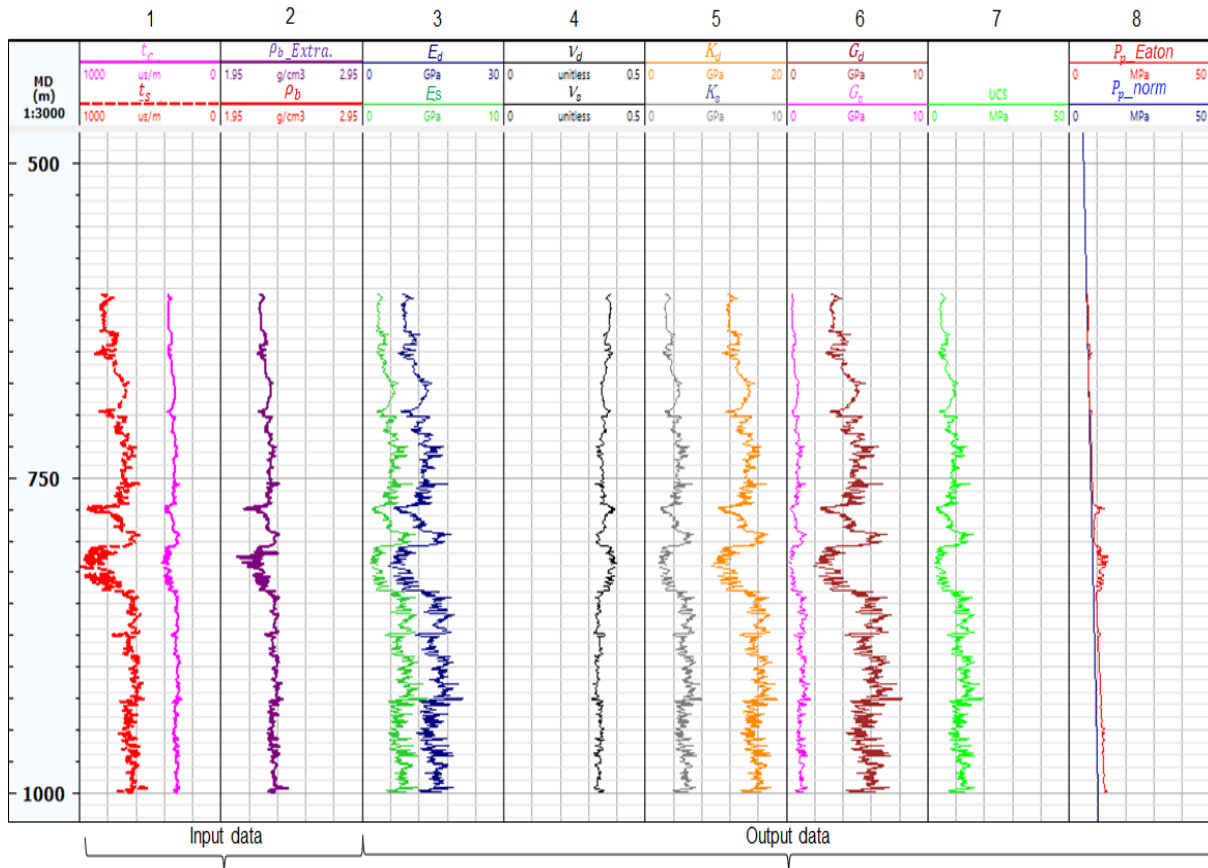
Well X3a



Well X4



Well X5







Further appendix to this thesis is provided on the attached CD. The following files are included:

**Dissertation in PDF format**

**1D Mechanical earth models for all the wells in PDF format**

**Petrel model generation 2D Map – Student guide**

**Fluid flow modelling using ECLIPSE™ 100 – Student guide**

## Statement of authorship

I hereby certify that this thesis has been composed by myself and describes my own work unless otherwise acknowledged in the text. All references and verbatim extracts have been quoted and all sources of information have been specifically acknowledged. This thesis has not been accepted in any previous application for a degree.

Hiermit versichere ich, dass ich die vorliegende Arbeit selbstständig und ohne Benutzung anderer als der angegebenen Hilfsmittel angefertigt habe. Stellen, die wörtlich oder sinngemäß aus anderen Schriften entnommen sind, sind als solche kenntlich gemacht. Die Arbeit ist in gleicher oder ähnlicher Form noch nicht als Prüfungsarbeit eingereicht worden.

Darmstadt \_\_\_\_\_ . Signature , \_\_\_\_\_

# Resume/CV

**Zain-UI-Abedin, Muhammad**

## **EXPERIENCE**

- Mar 2016-Present      Research associate at TU Darmstadt**  
 Computational geomechanics with focus on underground energy storage reservoirs  
 - Coupling methods of reservoir simulation (Eclipse) with reservoir geomechanics (Visage) With **UNIPER SE**  
 - Development of a coupled thermal-hydraulic-mechanical (THM) model for short-term gas storage by building complex 1D and 3D mechanical earth model using Schlumberger software (Eclipse, Petrel, Visage, Techlog, Python)
- October 2019            Internship at Schlumberger Oxford (United Kingdom)**
- Mar 2016-June 2017    Research assistant at TU Darmstadt on project:**  
 "Assessment of production induces stresses (APIS)" with **RWE DEA**  
 -Pore pressure field derive from dynamic modelling (Eclipse) for coupling with geomechanical model (Abaqus)
- July 2015-Dec 2015    Master thesis project at TU Clausthal with title of:**  
 "Interrelation of facies types and diagenesis with petrophysical parameters of Arab Formation Offshore Abu Dhabi"
- July 2014- Dec 2014    Master Thesis with Wintershall Holding GmbH E&P, Germany**  
 -Simulation of Volatile Oil in Naturally Fractured Carbonate Reservoir with emphasize on capillary pressure, relative permeability and wettability anomalies  
 -Field scale model dual porosity/ dual Permeability models (CMG & Eclipse Simulator) and multi-parameters sensitivities
- Feb 2014-April 2014    Group Project at TU Clausthal (RWE Dea)**  
 -Identification of IOR technologies and estimation of oil reserves  
 -Feasibility study in Hankensbuettel-Sued oil field, Germany

## **EDUCATION**

- July 2017-Present      Ph.D. at TU Darmstadt, Germany (reservoir geomechanics)**
- Oct 2012-Dec 2015    M.Sc. Petroleum Engineering (reservoir management)**
- Nov 2012-Oct 2015    M.Sc. Petroleum Geology, Clausthal University of Technology, Germany**

## **CONFERENCES AND PUBLICATIONS**

- Building 1D and 3D Mechanical Earth Models for Underground Gas Storage—A Case Study from the Molasse Basin, Southern Germany, Energies (MPDI), Published on 02.11.20 Energies (MPDI).

- "Geomechanical studies of a depleted gas reservoir for short-term gas storage-A case study from the Bavarian Molasse Basin, Germany" at 54<sup>th</sup> Rock Mechanics/Geomechanics Symposium, ARMA, 28 June- 1 July 2020 **Colorado, USA**.
- "Geomechanics of Underground gas storage" at Geoconvention, May 11-13 2020, **Calgary Canada**.
- "Coupling of flow and geomechanical simulations for short-term underground gas storage", Poster presentation at DGMK Frühjahrstagung, 25-26 April 2018, **Celle, Germany**.
- "Sedimentology of Early Cambrian Formation Salt Range, Pakistan"  
Poster Presentation at 76th EAGE Conference, June 2014, **Amsterdam, Netherlands**.
  - o Poster Presentation 75th EAGE Conference SPE EUROPEC 2013, **London, UK**.
- "Gas penetration or blocking processes in clay caprock of underground gas storage"
  - o Poster Presentation at 77th EAGE Conference, 1-4 June 2015, **Madrid, Spain**.
  - o Presentation at STC SPE, October 2013, **Wietze, Germany**.

### **COMPUTER SKILLS**

Eclipse, Petrel, Techlog, VISAGE, Python, CMG (IMEX), Ecrin Saphir, Kaapa, SurePVT, MATLAB, GIS, ANSYS, Microsoft Office Packages

### **PROJECTS AND CERTIFICATION**

**November 2018** Techlog Geomechanics by Schlumberger **La defense, France**

**March 2016** Petrel Reservoir Geomechanics by **Schlumberger, Germany**

**October, 2015** Field redevelopment Certification online by **MOL E&P**